UNIVERSIDADE DE SÃO PAULO
Instituto de Ciências Matemáticas e de Computação

Digital 3D Animation of Powder-Snow Avalanches

Filipe de Carvalho Nascimento

Tese de Doutorado do Programa de Pós-Graduação em Ciências de Computação e Matemática Computacional (PPG-CCMC)

ICMC USP SÃO CARLOS

Filipe de Carvalho Nascimento

Digital 3D Animation of Powder-Snow Avalanches

Thesis submitted to the Instituto de Ciências Matemáticas e de Computação – ICMC-USP – in accordance with the requirements of the Computer and Mathematical Sciences Graduate Program, for the degree of Doctor in Science. *EXAMINATION BOARD PRESENTATION COPY*

Concentration Area: Computer Science and Computational Mathematics

Advisor: Prof. Dr. Afonso Paiva

USP – São Carlos
January 2024

Ficha catalográfica elaborada pela Biblioteca Prof. Achille Bassi
e Seção Técnica de Informática, ICMC/USP,
com os dados inseridos pelo(a) autor(a)

d278d

de Carvalho Nascimento, Filipe
Digital 3D Animation of Powder-Snow Avalanches / Filipe de Carvalho Nascimento; orientador Afonso Paiva. -- São Carlos, 2024.
187 p.

Tese (Doutorado - Programa de Pós-Graduação em Ciências de Computação e Matemática Computacional) -- Instituto de Ciências Matemáticas e de Computação, Universidade de São Paulo, 2024.

1. . I. Paiva, Afonso, orient. II. Título.

Bibliotecários responsáveis pela estrutura de catalogação da publicação de acordo com a AACR2:
Gláucia Maria Saia Cristianini - CRB - 8/4938
Juliana de Souza Moraes - CRB - 8/6176

Filipe de Carvalho Nascimento

Animação Digital de Avalanches de Neve

Tese apresentada ao Instituto de Ciências Matemáticas e de Computação – ICMC-USP, como parte dos requisitos para obtenção do título de Doutor em Ciências – Ciências de Computação e Matemática Computacional. *EXEMPLAR DE DEFESA*

Área de Concentração: Ciências de Computação e Matemática Computacional

Orientador: Prof. Dr. Afonso Paiva

USP – São Carlos
Janeiro de 2024

To my brother.

ACKNOWLEDGEMENTS

I want to leave my true and eternal gratitude to my family, whose sacrifices paved my path. To my father, who taught me resilience; to my mother, who showed me my strength; and to my brother, always by my side.

My journey would not have been possible without my friends, who guided me in the most challenging times. In particular, I want to show my great respect and gratitude to my friend Andre Paiva, whom I consider my second brother and who has always encouraged me. My lab friends, now friends for life, Rafael Nakanishi, Camila Lages, and Matheus Tozo, for all the strength and friendship.

I want to thank my supervisor, Afonso Paiva, professor, colleague, and friend for my many years of companionship since undergrad and the many more years to come. I am also profoundly grateful for being helped by professors Paulo Pagliosa and Fabricio S. Sousa, whom I greatly admire.

Finally, I would like to acknowledge the importance of the Instituto de Ciências Matemáticas e de Computação – ICMC-USP to both my professional and character formations over these ten years. Being part of such a precious place was a true privilege.

This study was financed in part by the Coordenação de Aperfeiçoamento de Pessoal de Nível Superior – Brasil (CAPES) – Finance Code 001, under grant PROEX-6427021/D, and the São Paulo Research Foundation (FAPESP) under grant #2018/06145-4.

“You see me now, a veteran
Of a thousand psychic wars
I’ve been living on the edge so long
Where the winds of limbo roar”
(Blue Öyster Cult)

RESUMO

NASCIMENTO, F. **Animação Digital de Avalanches de Neve**. 2024. 231 p. Tese (Doutorado em Ciências – Ciências de Computação e Matemática Computacional) – Instituto de Ciências Matemáticas e de Computação, Universidade de São Paulo, São Carlos – SP, 2024.

A animação digital baseada em física de fluidos, como fumaça, água e fogo, fornece alguns dos efeitos visuais mais impressionantes da indústria do entretenimento. Porém, diversos fenômenos ainda precisam ser totalmente compreendidos, e suas formulações ainda são foco de intensa pesquisa em outras áreas, como Física e Engenharia Civil. É o caso das avalanches de neve, cuja modelagem numérica é desafiadora devido à sua dinâmica complexa. A manipulação de tais fenômenos é relativamente nova na computação gráfica e existem ainda poucos trabalhos sobre o assunto. Este projeto tem por objetivo trazer estas formulações para o campo da computação gráfica no que diz respeito à animação digital de avalanches de neve.

Palavras-chave: Computação Gráfica, simulação física, animação digital, animação baseada em física, renderização.

ABSTRACT

NASCIMENTO, F. **Digital 3D Animation of Powder-Snow Avalanches**. 2024. 231 p. Tese (Doutorado em Ciências – Ciências de Computação e Matemática Computacional) – Instituto de Ciências Matemáticas e de Computação, Universidade de São Paulo, São Carlos – SP, 2024.

Physically based animation of fluids such as smoke, water, and fire provides some of the most stunning computer graphics in the entertainment industry. However, several phenomena still need to be fully understood, and their formulations are still the focus of intense research in other fields, such as Physics and Civil Engineering. That is the case of snow avalanches, whose numerical modeling is challenging due to their complex dynamics. The manipulation of such phenomena is new to computer graphics, and few works exist. This project aims to bring such formulations to the field of computer graphics regarding the digital animation of powder-snow avalanches.

Keywords: Computer Graphics, physics simulation, Digital Animation, physically based animation, rendering.

LIST OF FIGURES

LIST OF CHARTS

LIST OF SOURCE CODES

LIST OF TABLES

LIST OF ABBREVIATIONS AND ACRONYMS

CMT	Continuum Mixture Theory
CMT	Continuum Mixture Theory
DEMs	Digital Elevation Models
DEMs	Digital Elevation Models
DILU	Diagonal-based Incomplete LU
DNS	Direct Numerical Simulation
DSL	Dense-Snow Layer
FAM	Finite Area Method
FCT	Flux Corrected Transport
FCT	Flux-Corrected Transport
FDIC	Faster version of the Diagonal-based Incomplete Cholesky
FVM	Finite Volume Method
FVMs	Finite Volume Methods
GIS	Geographical Information Systems
LES	Large Eddy Simulation
MULES	Multidimensional Universal Limiter for Explicit Solution
PBiCGStab	Preconditioned bi-conjugate gradient
PDEs	Partial-Differential Equations
PISO	Pressure Implicit with Splitting of Operators
PSA	Powder-Snow Avalanche
PSAs	Powder-Snow Avalanches
PSL	Powder-Snow Layer
RANS	Reynolds-Averaging Navier-Stokes Model
SGS	Subgrid-Scale
SH	Savage-Hutter
SIMPLE	Semi-Implicit Method for Pressure-Linked Equations
SPDEs	Surface PDEs
SPH	Smooth Particle Hydrodynamics
TVD	Total Variation Diminishing
VS	Voellmy-Salm

LIST OF SYMBOLS

$\bar{\mathbf{u}}$ — dense snow layer velocity

$\mathbf{u}_{dsl}$ — dense snow layer velocity

$\mathbf{u}_{inj}$ — injection velocity

h — dense snow layer height

ρ — density

ρ_a — air density

ρ_s — powder-snow density

ρ_c — snow cover density

α_s — powder-snow concentration of volume

α_a — air concentration of volume

p_b — basal pressure

p_{rgh} — hydrostatic pressure

τ_b — basal friction

μ — dry friction coefficient

ξ — dynamic friction coefficient

e_b — erosion energy

$\mathbf{g}$ — gravity acceleration

D_{AB} — molecular diffusivity

Sc — Schmidt number

ν_t — turbulent eddy viscosity

γ_α — mass injection factor

$\gamma_\mathbf{u}$ — velocity injection factor

L_{front} — front extension

$\omega_\star$ — entrainment noise factor

CONTENTS

CHAPTER

1

INTRODUCTION

Figure 1 – Visual effects of a snow avalanche from the movie *War for the Planet of the Apes* © 20th Century Fox.

Source: Matt Reeves (20th Century Fox) (2017).

The physically based digital animation of fluids such as smoke, water, and fire provides some of the most stunning visuals in computer graphics — see Figure 1. Several materials — e.g., snow, viscous liquids, mud — provide phenomena of great interest to visual applications but present complex physical properties that can be harder to simulate than usual simplified fluid models. These materials present solid-like resistance to deformation while also undergoing large strains characteristic of fluids. Such complexities become apparent in large-scale natural phenomena, such as snow avalanches, where multiple materials suffer enormous transformations through violent motion.

Figure 2 – The mesmerizing effect of large scale natural phenomena. (a) Snow avalanche in the Lyngen Alps of Northen Norway. (b) Mount Pinatubo eruption in 1991.

(a)

Source: Wallner, Chris (2017).

(b)

Source: Erik Klemetti (2016).

The destructive power of natural disasters produces both fear and fascination for humans. Large-scale phenomena, such as volcanic eruptions and snow avalanches, challenge our perceptions of life and death while carrying a mesmerizing effect — see Figure 2. Although fearful and harmful in real life, such events appeal to the entertainment industry (VENKATASAWMY, 2012), composing scenes in movies with great dramaticity and visual impact — see Figure 3.

Figure 3 – Visual effects of a snow avalanche from the movie *Black Widow* © Marvel Studios.

Source: Failes, Ian (2021).

Powder snow avalanches, also called dry avalanches, are particle-laden gravity currents (motions caused by gravity) formed in steep slopes, displacing vast amounts of snow down the hill. The avalanche starts with layers of packed snow detaching from the ground due to gravity. As the flow speed increases, the surrounding air gets turbulent, stirring up snow particles. Small particles may be suspended by turbulent air, thus forming a powder snow avalanche layer, which is self-accelerated by gravity. The deeper layers of dense snow suffer from fluidization, characterizing the fluid-like behavior of the avalanche.

Like any physical phenomena of diverse scales, from small grain interactions to massive mass movements, the motion of a snow avalanche obeys physical laws expressed by mathematical equations. The solution of such equations describes the snow avalanche's physical state over time, i.e., the deformation and movement on top of the terrain. The visual appearance of the avalanche body at each point in time composes the frame images of a digital animation. Hence, developing numerical methods for approximating solutions to Partial Differential Equations is crucial to achieving realistic animations.

The present text proposes a new method to produce physically based digital animations of powder snow avalanches. As pointed out in the following chapters, the mathematical modeling of a snow avalanche is still an open and challenging problem. A powder snow avalanche is a large-scale phenomenon of complex physical processes that are still not fully understood, as field measurements pose inherent difficulties. Therefore, the proposal combines different models to construct a full powder snow avalanche simulation. Figure 4 shows examples of resulting animations.

Figure 4 – Screenshots of animations produced with the proposed method. (a) A powder cloud descending a ramp. (b) A large-scale avalanche in a natural terrain.

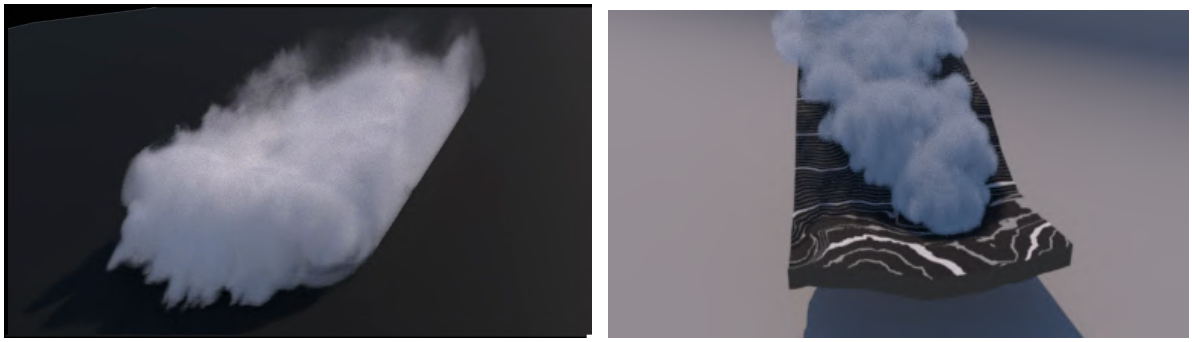

Source: Elaborated by the author.

A single avalanche presents multiple flows, called layers, interacting with one another, where snow undergoes chemical and physical transformations. Such complexity manifests in the intricate mass and energy exchanges between the layers. The relevant layers are the dense-snow layer, the transition layer, and the powder-snow layer — see Figure 5. The proposed method models each layer in a particular way with a different set of equations and simplifying assumptions:

- The overall method consists of two simulations: the dense-snow layer simulation and the powder-snow layer simulation;
- The method couples the two simulations in only one direction, where the dense snow layer influences the powder-snow layer, but the latter does not affect the former;
- The method does not simulate the transition layer. Instead, boundary conditions in the powder-snow layer model implicitly represent the transition layer.

Figure 5 – Snow avalanches consist of layers characterizing distinct flow types. The dense snow layer consists of large chunks of snow that slide over the terrain surface. As the packs of snow break, the turbulent air suspends snow particles, producing a cloud, the powder snow layer. The transition layer lies between the two layers above and represents the turbulent region that feeds the powder cloud.

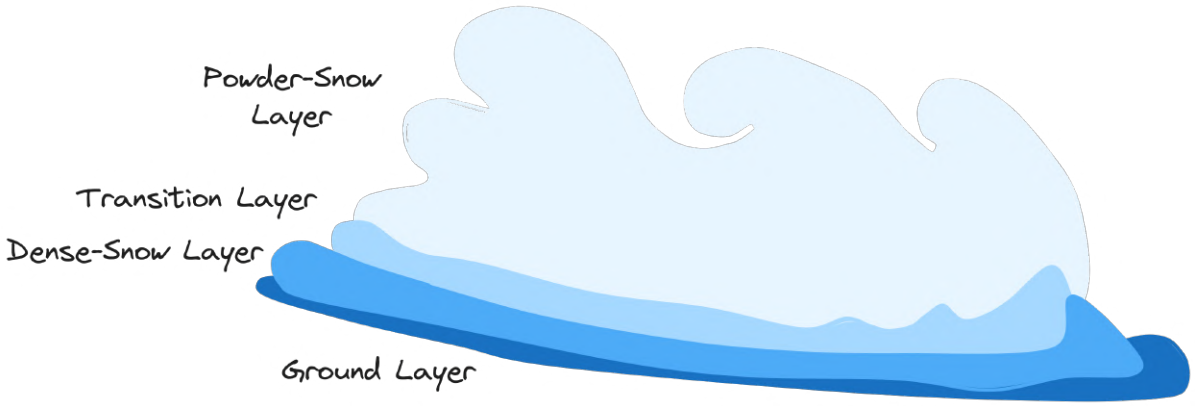

Source: Elaborated by the author.

Therefore, the method simulates both layers sequentially. In fact, given the proper boundary conditions for the powder-snow layer model, the simulation of the powder-cloud is agnostic of the method utilized for simulating the dense-snow layer. The main contributions of this work are:

- A novel method for producing physically-based digital animations of powder-snow avalanches;
- A procedural entrainment mechanism to transfer mass and energy to the powder-snow layer simulation;
- A survey on the research of snow avalanches;
- A method to compute the entrainment based on the surface distance to the leading edge of the avalanche;
- A method to compute the distance field in the avalanche based on the velocity and terrain geometry;
- A method to couple 2-dimensional to 3-dimensional simulations;
- A method to rasterize volumetric data of arbitrary cell shapes into a voxel grid;

The following section provides a brief overview of the proposed method, followed by section 1.2, outlining the text organization.

1.1 Method Outline

Figure 6 – Overall method workflow.

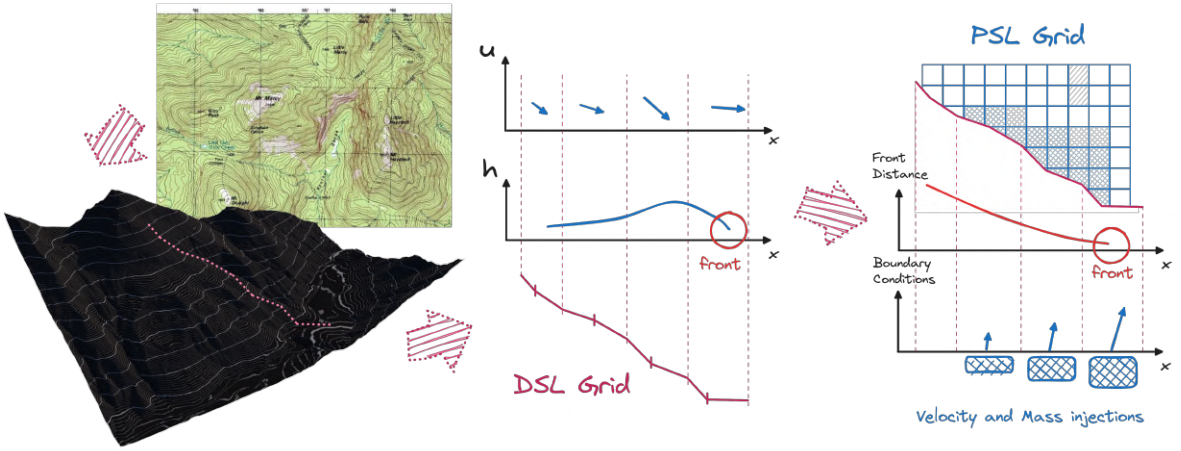

As mentioned, the method performs two sequential simulations: the dense-snow layer (DSL) simulation and the powder-snow layer (PSL) simulation. Figure 6 provides a general overview of the workflow for the whole method described by the following steps:

1. Topographic terrain data is converted into a 2-dimensional surface that determines the cell elements in the *DSL grid*. The DSL grid consists of flat polygonal cells, represented in Figure 6 as one-dimensional segments. The DSL simulation outputs two surface fields[1]: the height h and the velocity $\mathbf{u}$ for each DSL grid cell and simulation step.

2. The resulting field values of the DSL simulation get into the PSL simulation as boundary condition values for the bottom region of the *PSL grid*. The PSL grid consists of 3-dimensional cells, represented as squares in Figure 6, that decompose all the volume on the top of the terrain, on which the powder cloud will evolve. The cloud originates from the ejection of snow and air entrainment, mainly in the avalanche's front region. Therefore, the boundary conditions inject snow based on the front position, velocity, and height of the DSL. The DSL data is spatially and temporally interpolated[2] into the PSL grid's bottom faces for each time step of the PSL simulation.

3. The PSL simulation generates a volumetric density field representing the powder-snow cloud for every simulation time step. The height surface field h of the DSL simulation generates a surface mesh representing the DSL body. The resulting volumetric field for the PSL and the DSL surface mesh compose the frame data for the final animation.

[1] Here, a surface field is a scalar/vector field defined in the cells of the two-dimensional patch that composes the numerical grid. Each cell holds a value of the field.

[2] The DSL grid and the bottom surface of the PSL grid are not necessarily the same mesh. Their faces may differ in number, shape, and alignment.

1.2 Text Organization

The following items describe the contents of the chapters contained in this text. At the end of each chapter, a section of *remarks* summarizes essential information that helps maintain the overall picture. The chapters are:

- Chapter 2: An introduction to snow avalanches from the geophysical point of view, going through the physical processes that form an avalanche and the categories of such phenomena. The chapter offers the general notion of the dynamics of powder-snow avalanches and their dimensions.
- Chapter 3: A relatively extensive exploration of the scientific research on the topic. The chapter chronologically lists a series of works from the past decades and delineates the main branches of models developed in the field.
- Chapter 4: The presentation of the proposed method by detailing the mathematical models chosen for the dense-snow layer and the powder-snow layer simulations, including the transference of mass and energy between both simulations. The chapter also delves into the numerical discretizations of the equations necessary for their solutions.
- Chapter 5: The completion of the workflow, giving the final steps for producing the animations. The chapter gives examples of animations produced with the method but also explores experiments to discuss the different parameters present in the models.
- Chapter 6: Conclusions and discussions about the method and results presented in the previous chapters. The chapter also explores the limitations encountered in the current model and improvements for future work.

The end of the document contains the appendices that support the chapters:

- Appendix A: Background Concepts
- Appendix B: A brief introduction to the Finite Volume and Finite Area methods, the numerical tool utilized in Chapter 4.
- Appendix C: An introduction to the software package OpenFOAM, the code used for solving the numerical systems in Chapter 4.

CHAPTER

2

ANATOMY OF SNOW AVALANCHES

The general concept of an avalanche consists of a large amount of mass sliding down an incline due to gravity. Once friction and cohesion forces fail to hold the material over the terrain, gravity force becomes prevalent and initiates motion. The surrounding fluid may support sediment transport during motion, increasing velocity, *runout distance*[1], and mass. Many fields of science study such sediment and fluid flows and define classifications for the different avalanches.

This chapter briefly introduces the dynamics of Powder-Snow Avalanches (PSAs), a member of the family of *mixed-type avalanches*, and the different categories of natural mass motion phenomena. The chapter starts by presenting the common classification of snow avalanches, then section 2.2 on page 52 delves into the details of PSAs. The chapter finishes with a remarks section 2.3 on page 55, listing the essential concepts relevant to the rest of the text.

2.1 Gravity Flows

Physical phenomena like snow avalanches belong to the broad family of mass transport phenomena called *gravity flows*. Gravity Flows comprise the various natural phenomena characterized by the sediment transport under the action of gravity. Here, sediment means all the particulate substances, from thin snow powder to huge boulders. Due to its particulate nature, sediment will also be referred to as *granular material* throughout the text.

The *interstitial fluid*[2] plays a central role in removing friction forces, adding cohesion, causing lubrication, or supporting the motion through turbulence and buoyancy. Shortly, the following properties have a significant effect on the behavior of granular materials:

[1] The runout distance, *avalanche runout*, is the final segment of an avalanche path where the avalanche slows down and stops.

[2] The interstitial fluid is the fluid that fills the space between sediment grains, such as the mixture of water and dirt in mudflows.

- **Cohesion** creates tangential forces between grains due to humidity or electrostatic forces. For example, the thin liquid films' surface tension between two snow particles is responsible for cohesion in melting snow[3]. Cohesion is more significant in rest states, as motion may generate larger forces that overcome cohesive forces. In snow avalanches, cohesion delays the initial break-off and keeps large snow chunks from fragmenting.

- **Lubrication** reduces the friction between grains and other bodies due to the presence of another medium called the *lubricant*. In many flows, the motion produces the lubricant. In snow avalanches, the heat generated by the friction between the sliding snow and the terrain maintains a thin layer of liquid water that lubricates the flow. The presence of lubricants may increase runout distances even in low slopes.

- **Fluidization** reduces the internal friction related to grain-to-grain collisions by balancing out the gravity force with the buoyancy force generated by the interstitial fluid. The consequence is the fluid-like behavior of the granular material. In snow avalanches, fluidization generally occurs in steep slopes as the air trapped between snow grains temporarily displaces the snow. Compared to lubrication, which happens on the boundaries of the flow, fluidization happens internally. Similarly, *liquefaction* happens when the downward motion of the granular material displaces the fluid upwards (LOWE, 1976).

In many flows, the interstitial fluid is the same as the ambient fluid, which is the case for the powder cloud in PSAs. Many authors define *Sediment Gravity Flows* when the sediment's gravity-driven motion causes the fluid's motion, and *Fluid Gravity Flows* the inverse – see Figure 7 on next page. Middleton and Hampton (1973) classifies different sediment gravity flows into four categories based on the *sediment support mechanism*:

- **Debris Flows**, also referred to as mudflows, characterize flows with high cohesive strength. The cohesion originates from the nature of the constituent materials, generally water, dirt, and rocks[4]. A mixture of water and fine sediments supports sediment, allowing the motion of large blocks of mass — see Figure 8a.

- **Grain Flows** are cohesionless flows supported by direct grain-to-grain interactions. Due to grain geometries, shearing deformations lead to volume expansion[5]. The interstitial fluid is the same as the ambient fluid, which can also be water. Examples of grain flows are sand avalanches — see Figure 8b.

- **Fluidized Flows** occur under fluidization processes. In the presence of interstitial fluid, the grains disperse, and fluid motion takes into play. The injection of air in the bottom

[3] Conversely, the lack of liquid water in colder temperatures makes snow less cohesive.
[4] Debris flows have enough strength to carry much more than dirt and rocks. Due to its enormous mass and fluid behavior, the flow can take debris of large sizes, such as trees and boulders.
[5] Granular materials are also called *dilatant materials.*

of a sand tank is an example of such a phenomenon. Lowe (1979) considers a separate category called *Liquified Flow*, where support comes from the pore-fluid pressure.

- **Turbidity Currents** are particle-driven flows that generally occur on the ocean floor and are responsible for sediment transport to the deep sea. The density difference between the ambient fluid (water) and the sediment mixture drives the motion. The suspension caused by the turbulence of the fluid supports the motion, which may take even days and cover vast distances of more than 1000 km (TALLING *et al.*, 2022).

Figure 7 – Sediment Gravity Flows are motions of mass motivated by gravity. As sediment moves, the ambient fluid gets into motion as well. In the presence of an interstitial fluid, effects such as lubrication, cohesion, and buoyancy may come into play, supporting the motion (left). If sediment grains, such as sand underwater or snow powder in the air, disperse enough, the turbulence of the ambient fluid may also support the motion.

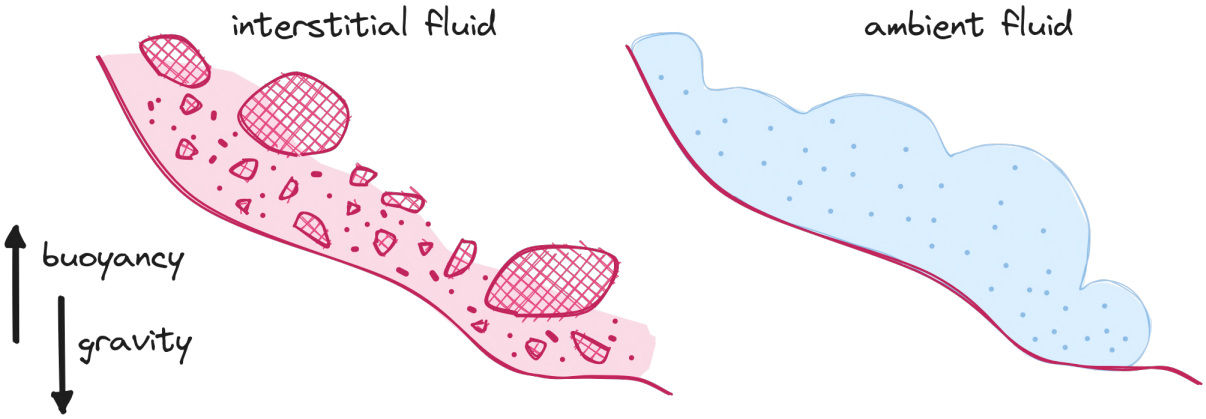

Source: Elaborated by the author.

Figure 8 – Sediment flows cover various grain flow properties, such as cohesion. For example, debris flows are highly cohesive, while sand flows are cohesionless. (a) The *1/9 Debris Flow* event on January 9, 2018, triggered in Santa Barbara County, United States. (b) Tongue-shaped grain-flow lobes on the surface of sand dunes.

(a)

Source: Hill (2019).

(b)

Source: Barale (2015).

Over the years, the classification above proved insufficient due to the diversity and complexity of gravity flows. Dasgupta (2003) suggests that the flows listed above are too different to be defined under the same category of sediment gravity flows. Moreover, the properties of lubrication, fluidization, and cohesion are not necessarily mutually exclusive, and neither the flow types are. A powder-snow avalanche, for example, contains a mixture of flow types and properties. Therefore, the gravity flows were further classified based on material type, sediment concentrations, velocity, grain size distributions, flow front speeds, shear strength, shear rate, and other criteria (VARNES, 1978; PIERSON; COSTA, 1987).

Figure 9 – Characteristics of different sediment transport/motion types.

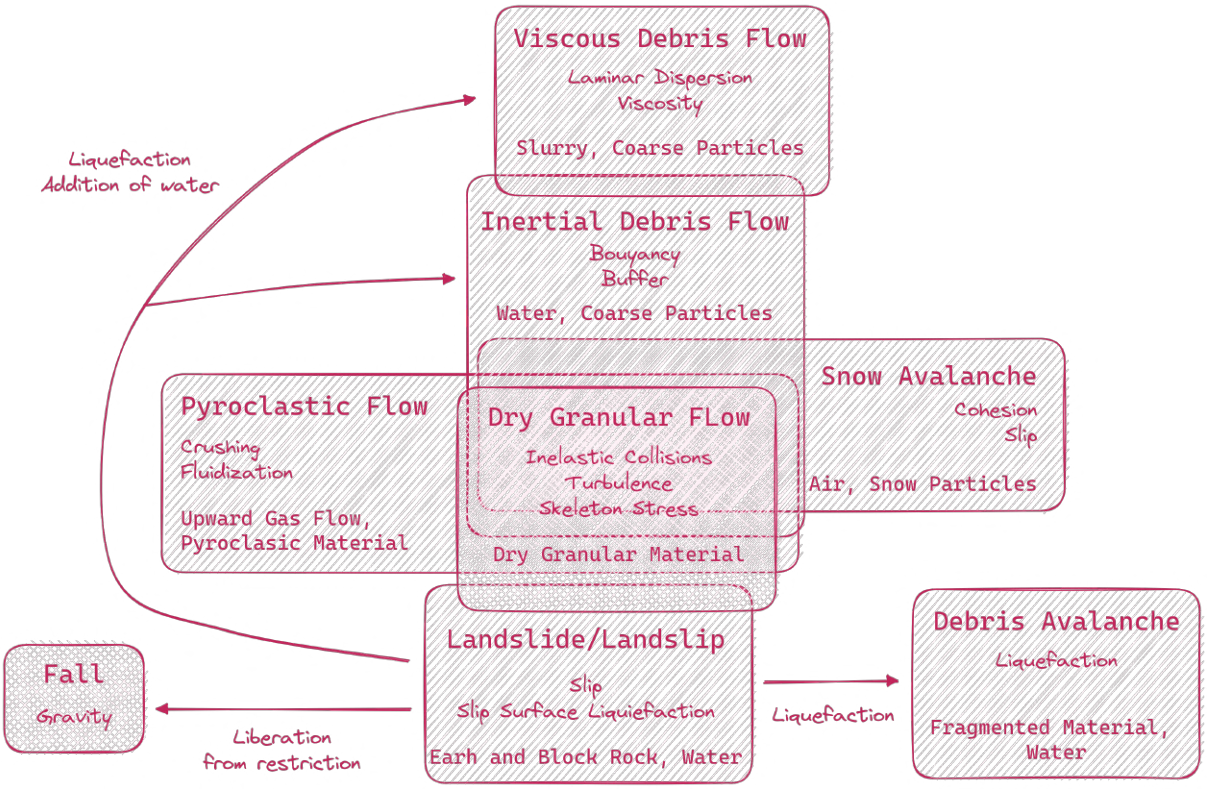

Source: Adapted from Takahashi (2014).

One important example is the classification proposed by Takahashi (2014), represented in Figure 9, focuses on particle concentration and the support mechanism. For example, particles are dispersed in the flowing body for the five upper blocks categories, while the lower three blocks present moving bodies composed mainly of agglomerates of soil and rocks. As the interaction of solid and fluid forces distinguishes debris flows physically, arrows connecting lower blocks and upper blocks on the diagram represent the water concentration. Each block lists the effects particular to each flow type that go beyond the commonly operating stresses and the participating materials.

In parallel, a *Gravity Current* is a term geologists use to characterize flows motivated by density differences between two fluids. Gravity currents, sometimes called *buoyancy currents*, are primarily horizontal flows where a fluid propagates through the ambient fluid with lesser or

greater density, such as sand storms and bores — see Figure 10. Many authors generalize gravity currents to encompass phenomena such as pyroclastic and lava streams initiated by volcanic eruptions, suspension flows, turbidity currents, and other gravity-controlled flows, including debris flows. In this context, an airborne powder-snow avalanche is considered a large-scale turbidity current.

Figure 10 – Examples of gravity currents. (a) A massive *haboob* (sand storm) hits the city of Phoenix in the United States. (b) Bores in the atmosphere making the phenomenon called the 'Morning Glory' over Australia.

(a)

Source: Stewart (2018).

(b)

Source: Petroff (2009).

In the realm of avalanches, characterized by motions of mass in mountain inclines ranging from landslides to rockfall, Pudasaini and Hutter (2007) distinguishes three large groups:

- **Flow Avalanches** are *dense gravity-driven flows* where the role of solid particles dominates, and the interstitial fluid is minor or negligible. Its particles vary with sizes ranging from sizes of clay to boulders. Such flows are present in certain types of snow avalanches, and many debris flows, having similarities with *dense granular flows*. For example, in certain dense pyroclastic flows, the solid volume fraction can be of the order of 70%.

- **Powder Avalanches** consist of light powdery grains with low or no cohesion. These avalanches are much less dense than flow avalanches and can be called *turbulent-type flows* of airborne particles. Powder avalanches are characterized by their large volume and the rapid wind that accompanies the flow. For instance, the powder avalanche formed in a PSA can move at high velocities as impressive 100 $m \cdot s^{-1}$ and form clouds of 100 m in height (SIMPSON, 1999).

- **Mixed-type Avalanches** are flow avalanches overlaid by a powder avalanche. This category of avalanches presents multiple layers in which a distinct physical behavior characterizes the layer's dominant dynamical processes. Generally, the process starts with a flow avalanche that produces enough motion and powder mass to generate a powder avalanche. The dense layer feds the powder layer as the chunks of material break into smaller pieces

and eventually into particles. The turbulent motion of the ambient fluid ejects the particles and forms the upper layer powder avalanche. Examples of mixed-type avalanches appear in turbidity currents, pyroclastic volcanic eruptions, dust clouds in the desert, and **powder-snow avalanches**.

Due to their diverse natures, flow avalanches differ significantly from powder avalanches[6]. For example, flow avalanches have significant basal friction and are bound to the terrain following small-scale features, while powder avalanches follow just the large-scale topography. Table 1 lists the fundamental differences encountered in both flows. In particular, notice the contrast in the scales for density and velocity values.

Table 1 – Table extracted from Pudasaini and Hutter (2007), showing the differences between the two type of avalanches. The values in the table are typical values measured in such flows.

		Flow Avalanches	Powder Avalanches
Flow type		Laminar	Turbulent
Velocities	$[m \cdot s^{-1}]$	$\sim 5-30$	$\sim 40-100$
Density	$[kg \cdot m^{-3}]$	$\sim 100-400$	~ 5
Flow height	$[m]$	$\sim 1-10$	~ 100

Environmental factors, such as temperature and humidity, affect the physical state of snow, creating different behaviors of snow avalanches. Therefore, snow avalanches receive further classifications that distinguish their diverse characteristics. The WSL Institute for Snow and Avalanche Research SLF (SLF, 2022) lists the following categories for snow avalanche types:

- The snow cover on the surface of a mountain is the accumulation of several snowfalls that occur over time. Throughout the days, the precipitations might bring snow in different conditions, such as particle sizes, temperature, and humidity. The stacking of different snowfalls makes the snow cover a stratified layer consisting of sub-layers of variable strength. The weight of the upper layers and the slope of the terrain impose mechanical forces that can lead to the failure of weak layers. When a weak layer of significant area lies underneath meters of snow collapses, a fracture quickly propagates throughout the snow cover. The fracture causes the sudden detachment of the whole body of snow that enters motion. The heavy snow slides freely on top of the weak layer underneath, producing the so-called **Slab Avalanches**[7] – see Figure 11a and Figure 11b.

- **Loose Snow Avalanches**, also called *sluffs* or *point releases*, generally occur during quick temperature increases. The release of loose snow starts from a single point, and the

[6] Some authors refer to PSAs as powder avalanches, which can be confusing when dealing with different classifications. Here, PSAs are mixed-type avalanches.

[7] Slab avalanches are responsible for 90% of the deaths that occur in snow avalanches because of the fast acceleration and large area they have. Skiers and mountaineers usually find themselves suddenly inside the avalanche perimeter at the time of release.

avalanche entrains snow as it fans downhill. Loose snow avalanches can reach large sizes due to wet snow entrainment – see Figure 11c and Figure 11d.

- In **Gliding Avalanches**, the entire snowpack is released, but they occur only in smooth substrata, such as flattened grass. As water penetrates the deeper layer, the friction with the ground decreases, and the avalanche is triggered.
- **Wet Snow Avalanches** generally happen in the event of rain. The main characteristic of wet snow avalanches is the presence of liquid water that wakens the snowpack.
- **Powder-Snow Avalanches** generally originate from slab avalanches. Their definition is the same as mixed-type avalanches mentioned earlier and are detailed in the next section.

Figure 11 – Slab avalanches originate from the failure of the weak layer in the snow cover. (a) The fracture line, also called the *crown line*, becomes evident after the release of a slab avalanche. (b) For persistent snow covers, the height of the slab can reach many meters. (c) Dry-loose snow avalanches start from a single point and entrain only the soft snow near the surface of the snow cover. (d) However, wet-loose snow avalanches entrain heavier snow, becoming more destructive.

(a)

Source: Vidic (2022).

(b)

Source: McGill (2023).

(c)

Source: Avalanche.org (2023).

(d)

Source: Avalanche.org (2023).

2.2 Powder-Snow Avalanches

In literature, the Powder-Snow Avalanche (PSA) usually consists of two principal layers: the Dense-Snow Layer (DSL) and the Powder-Snow Layer (PSL), representing the flow avalanche and the powder avalanche, respectively. In addition, two extra layers are used to explain the changes in mass observed in the DSL and PSL. The first layer, referred to here as the *ground layer*, consists of the static snow cover encountered in the terrain. The second layer, referred to as the *transition layer* (also called the *saltation layer*), appears above the DSL and below the PSL and is responsible for the exchange of mass and momentum between the two layers. Table 2 lists the four mentioned layers and their main characteristics.

Table 2 – Layers of a powder-snow avalanche.

Layer	Description	FLow Type
PSL	Suspension layer (fully turbulent)	Turbulent particle laden flow
Transition	Two-phase viscous wall layer	Turbulent two-phase flow
DSL	Flow avalanche layer	Laminar flow
Ground	Stagnant snow layer	Snow at rest

During a PSA, the DSL may gain mass from the ground layer by snow entrainment and lose mass from snow deposition processes. However, there are also exchanges between the DSL and the PSL. As collisions fracture large chunks of snow, the surface of the DSL becomes fluidized. The increasing wind causes particles to leave the dense layer surface in ballistic motion, creating a transition region. Some particles make their way up to the PSL, called the *suspension layer*, where collisions are less frequent and get into strong aerodynamic turbulence. Figure 12 depicts the anatomy of the avalanche described above.

Figure 12 – Powder-snow avalanches can be dissected into four main layers of different flow types. The DSL is composed of big snow packs that break into smaller pieces as the flow develops. Particles at the fluidized surface of the dense flow layer are stirred up, forming a transition layer. Small particles may be suspended by turbulent air and form the PSL, which is self-accelerated by gravity and turbulence. The DSL exchanges mass with the static snow cover that forms the ground layer by entrainment and deposition processes.

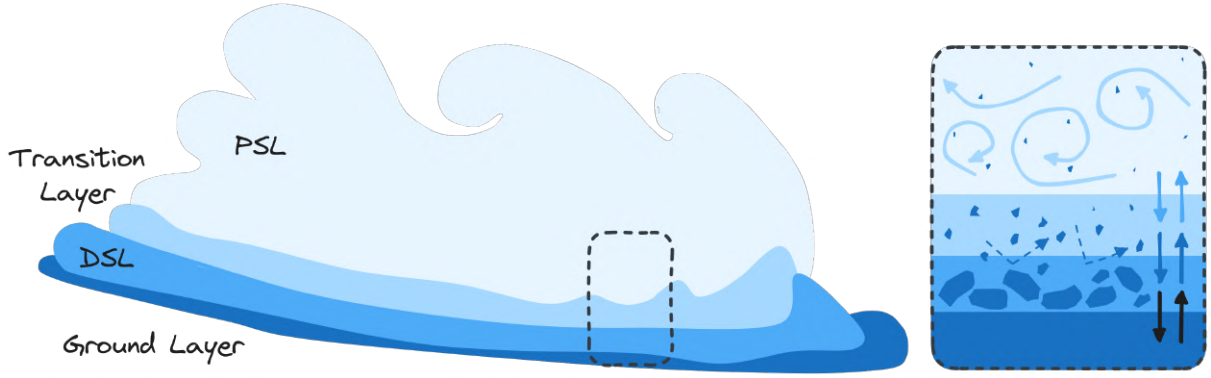

Source: Elaborated by the author.

The sequential events of a PSA happen along three distinct phases that roughly split the avalanche path into three parts: the *start zone*, the *track*, and the *runout zone*. The **start zone** is where the primary block of snow detaches from the mountain surface and starts to slide down the incline (see the slab avalanche description in the previous section on page 50). The **track** is the following section of the path where the flow develops as the avalanche accelerates and increases in size by entraining snow from the ground. The amount of entrained snow will influence how fast and long the flow will advance. In the final portion, the **runout**, the avalanche starts to slow down until it stops and the snow is deposited. Avalanches will stop depending on many factors, such as terrain topography and the decrease in entrainment.

The entrainment of snow plays a central role in the evolution of an avalanche flow, particularly in a PSA. The entrainment processes[8] feed the cloud and dictate the size of the powder cloud. Issler (2014) describes four mechanisms of entrainment in snow avalanches:

- **Plowing**, or *ploughing*, in the front of the flow occurs as the dense core incurs into the snow cover. The frontal impact pushes the snow cover forward. The amount of entrained snow (displaced snow cover) depends on the depth of the snow cover, its strength, and the speed of the avalanche.

- Depending on the strength of the snow cover, particularly in the presence of dry snow that has low cohesion, the compression force of the arriving avalanche, right in the front of the flow, creates a high pore pressure that forces the interstitial air out. The drag caused by the airflow pushes the snow upwards as an **eruption**, creating the characteristical frontline of PSAs. The process happens quickly, $0.1 \sim 2\ s$, with significant entrainment rates up to $350\ kg \cdot m^{-2} \cdot s^{-1}$ (SOVILLA; BURLANDO; BARTELT, 2006)[9].

- Between the bed and the dense core, there is a continuous **scour** of the ground layer due to the friction of the passing flow. As erodible snow loses cohesion and strength, the chunks of snow break into smaller pieces. The loose portions get trapped by the avalanche flow. Sovilla, Burlando and Bartelt (2006) relates this process to *basal erosion*, which happens away from the front and at low entrainment rates of $10\ kg \cdot m^{-2} \cdot s^{-1}$.

- The **ripping** of bed slabs occurs when the friction exceeds the shear strength of the snow cover. The sudden failure of the snow cover projects an entire slab portion into the avalanche core. Sovilla, Burlando and Bartelt (2006) describes a similar process called *step entrainment*, characterized by the failure of a resistant top layer of the snow cover. When the *crust* breaks, the flow suddenly entrains the weak layer underneath, producing entrainment rates as large as in eruption.

[8] The physical processes in entrainment processes still pose many open questions to scientists. Many challenges in field measurements limit the comprehension of entrainment mechanisms. The entrained mass results directly from the *erosion* process of the snow cover. The next chapter discusses some of these challenges.

[9] Sovilla and other authors also use *plowing* to encompass the *eruption* mechanism.

The plowing and eruption mechanisms described above are responsible for the plume formation in PSAs. The blow-out that occurs in the *leading edge* of the avalanche creates the conditions for plume formation. Bartelt *et al.* (2013) observed that after an initial plume quickly achieves 10 m of height, the growth pauses and resumes as the plume is no longer at the front ($20 \sim 50$ m behind). The air intake at the leading edge, which is velocity-dependent, expands the volume of the cloud. As the ejected heavy particles fall, the entrained air is displaced upwards, suspending the ice dust up to 100 m. This process creates vertical movement of the plumes, but not horizontal. This vertical movement of the plumes agrees that the plumes travel many times slower than the leading edge[10]. Figure 13 shows the several entrainment processes mentioned earlier.

Figure 13 – The various entrainment processes present in a PSA. Away from the front, the continuous friction forces in the ground surface cause *scour*, *basal erosion*, *ripping*, and *step entrainment*. In the leading edge, snow can be *plowed* frontwards but can also be violently ejected into the air by *eruption*. Plumes are born from the eruption and grow as heavy particles settle down and displace air upwards. The *intermittency region* includes surges of rapid flows and produces the oscillatory behavior of the PSA front.

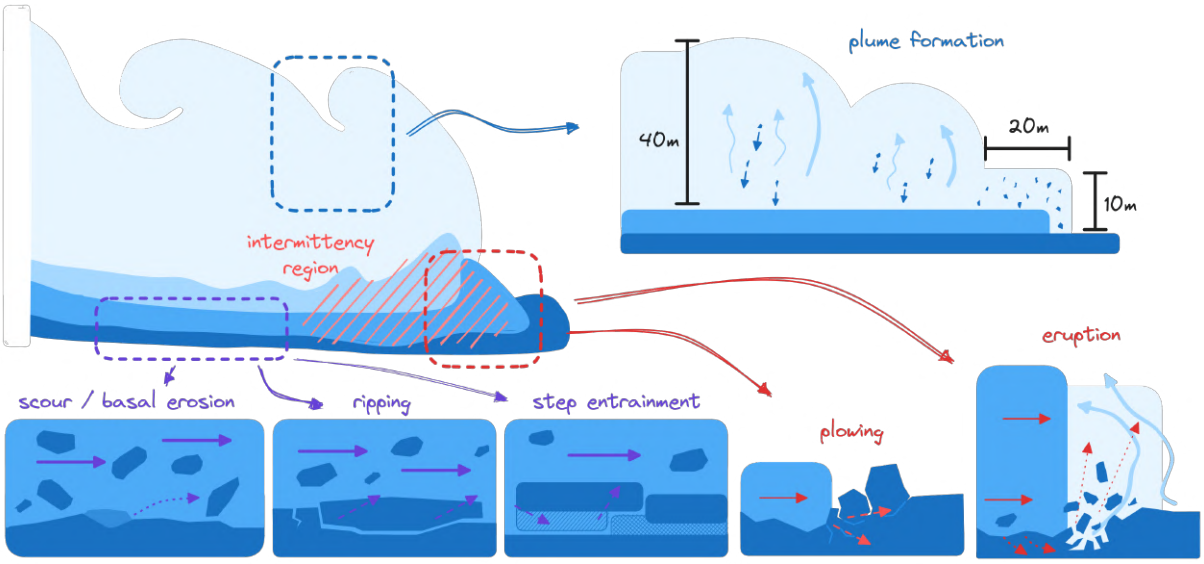

Source: Elaborated by the author.

For decades, observations indicated an oscillatory behavior occurring in the front of a PSA. The plume formation mentioned above is the direct consequence of this dynamics[11]. Such oscillations manifest as short-time streaks in radar data signatures, representing surges of velocities faster than the avalanche front. These flow structures happen in the *intermittency region* depicted in Figure 13 and quickly decelerate once they arrive at the leading edge of the avalanche. The dynamics of this *intermittent flow regime* are still poorly know (SOVILLA; MCELWAINE; KHLER, 2018).

[10] Bartelt *et al.* (2013) also observed plumes traveling at 4 $m \cdot s^{-1}$ while leading edges were traveling up to 50 $m \cdot s^{-1}$.

[11] Bartelt *et al.* (2013) observed plumes being created at approximately 0.4 Hz (plumes per second).

2.3 Remarks

- PSAs are primarily born from slab avalanches. In a fully developed PSA, many flow regimes come into play, which makes the mathematical modeling of PSAs particularly challenging. The typical approach is to divide the PSA into two layers, the DSL and the PSL, that communicate with each other through an intermediate layer, the *transition layer*.
- The DSL flow presents high densities of up to 400 $kg \cdot m^{-3}$ and depths of up to 10 m. The entrainment happens by *scour* and *basal erosion* at slow rates of 10 $kg \cdot m^{-2} \cdot s^{-1}$ but may entrain more significant amounts quickly by *ripping* and *step entrainment*.
- The PSL flow presents low densities of around 5 $kg \cdot m^{-3}$ but can reach heights of up to 100 m. Entrainment occurs primarily by the *eruption* process at the leading edge of the avalanche at incredible rates of up to 350 $kg \cdot m^{-2} \cdot s^{-1}$.
- From the many entrainment processes, the eruption is the primary source of mass for the PSL. Therefore, the dynamics at the front of a PSA need special attention when modeling PSAs.
- Plumes do not travel downhill at the same speed as the front of the avalanche. The velocity of the plumes can be as low as 4 $m \cdot s^{-1}$, with the leading edge traveling at 50 $m \cdot s^{-1}$.
- The front of a PSA presents an oscillatory behavior caused by the *intermittent region* just behind. This oscillation directly influences the formation of the plumes, which pulse from the front (e.g., 0.4 plumes per second).

CHAPTER

3

RESEARCH ON SNOW AVALANCHES

Modeling and simulating avalanche phenomena have been the goal of many researchers for decades. Research has focused mainly on avalanche prediction, hazard control, mitigation measures, and dynamics. This chapter explores the chronological advances in snow avalanche science, focusing on avalanche dynamics.

The chapter starts with an overview of the history of snow avalanche research throughout the last century in section 3.1. A complete taxonomy covering the entire period would be too extensive and beyond the purpose of this text. Consequently, the section follows the history of the leading families of models and their ramifications.

Although practical research — read observation and experimentation — goes beyond the focus of this text, measurement data plays a crucial role in numerical model validation. Field observations and laboratory experiments form the basis for physical and mathematical models. Therefore section 3.2 on page 60 briefly covers the history of field and laboratory research on the different types of snow avalanches.

The following sections delve into the history of physical and mathematical models of the two main types of snow avalanches, dense–snow and powder–snow avalanches, roughly covering the last 150 years of avalanche research. section 3.3 on page 66 explores the history of dense–snow avalanche models, and section 3.4 on page 87 treats the mixed–type models that simulate the different avalanche flow layers simultaneously, characteristic of powder–snow avalanches.

Lastly, section 3.6 on page 102 lists commercial and open-source software packages for snow avalanche simulation. section 3.7 on page 104 presents avalanche-related methods employed in Computer Graphics, which is the final goal of this project. The chapters close with relevant remarks to the subsequent chapters in section 3.8 on page 105.

3.1 General View

Since civilization spread into mountainous regions, avalanches soon became a permanent threat to human life. In the mid-20th century, mountain communities experienced considerable growth, raising the interest and urgency in avalanche research since then.

Although the first physical models appeared in the 1950s, much of their inspiration and assumptions came decades earlier. Figure 14 draws a general timeline of the scientific study of snow avalanches over the last century. The timeline depicts crucial branches of research and ideas that led to the most recent methods described in the following sections.

The first scientific study of snow avalanches dates back to 1881, pioneered by the Swiss scientist (forester) Johann Coaz (COAZ, 1881). However, only a half-century later, Seligman, Seligman and Douglas (1936) called attention to the complex nature of the phenomenon, attempting to list the multitude of physical and environmental factors that produce an avalanche. Earlier in the 20th century, Mougin (1922) calculated avalanche velocity and run-out distance by treating avalanches as sliding blocks, a solution that originated many avalanche models in use today.

Inspired by Mougin, Voellmy (1955) made the first significant attempt to formulate the dynamics of dense–snow avalanches by bringing basal friction relations to the depth-integrated hydraulic model, introduced by Barré de Saint-Venant (VENANT, 1871). Since then, Voellmy's basal friction model has been used as the starting point for most subsequent models (LACHAPELLE, 1977; ANCEY, 2016). In particular, the Voellmy-Salm (VS) model, created in the 1960s, spanned decades of influence and received many extensions and applications — being officially used by governments on avalanche hazard calculation programs (SALM, 2004). In parallel, the Russian model, referred to as the MSU model (GRIGORIAN; OSTROUMOV, 2020), also occupied an important position of influence for decades, dictating not only Eastern models but also having a significant impact on Western research.

The dense-snow avalanche research achieved its pivot point when granular flow models surged in the 1980s with the Savage-Hutter (SH) model (SAVAGE; HUTTER, 1989). The SH model brought features from VS and MSU models along with a continuum mechanics perspective, allowing the simulation of a wide range of physical processes such as entrainment, avalanche body deformation, and complex terrain flows. The SH model received great approval and is one of today's leading models for dense-snow avalanche simulations (RAUTER *et al.*, 2018). In recent years, the advance in computing resources allowed new numerical methods to offer particle-based models the capacity to handle internal flow processes and large-scale deformations on real-world terrains (GAUME *et al.*, 2018; LI *et al.*, 2021).

Models for the powder-snow cloud may follow different origins and approaches, such as the gravity currents and plume theory (ELLISON; TURNER, 1959; BARTELT *et al.*, 2013) — see Figure 14. Attempts to model the family of gravity current phenomena are contemporary to

Figure 14 – Snow avalanche research timeline. Mathematical studies on snow avalanche dynamics started approximately 150 years ago and spawned many physical models. In 1922, Mougin treated the avalanche as a single-sliding block. Over the years, the sliding block model integrated laws from 1871's Saint-Venant hydraulic equations and friction, thanks to Voellmy in 1955. Voellmy's sliding-block / hydraulic model received many extensions, and its friction models are still used today. In the 1980s, the continuum mechanics approach surged in avalanche modeling, and the analogy with granular flows produced one of the most prominent dense–snow avalanche models, the SH model. Since then, the models can handle avalanches with deformable body and flowing in complex terrains. Recently, particle-based models gained space due to computational power. Powder-snow avalanche research took a different path toward multi-phase models, concentrating on the mixture of air and ice caused by turbulence.

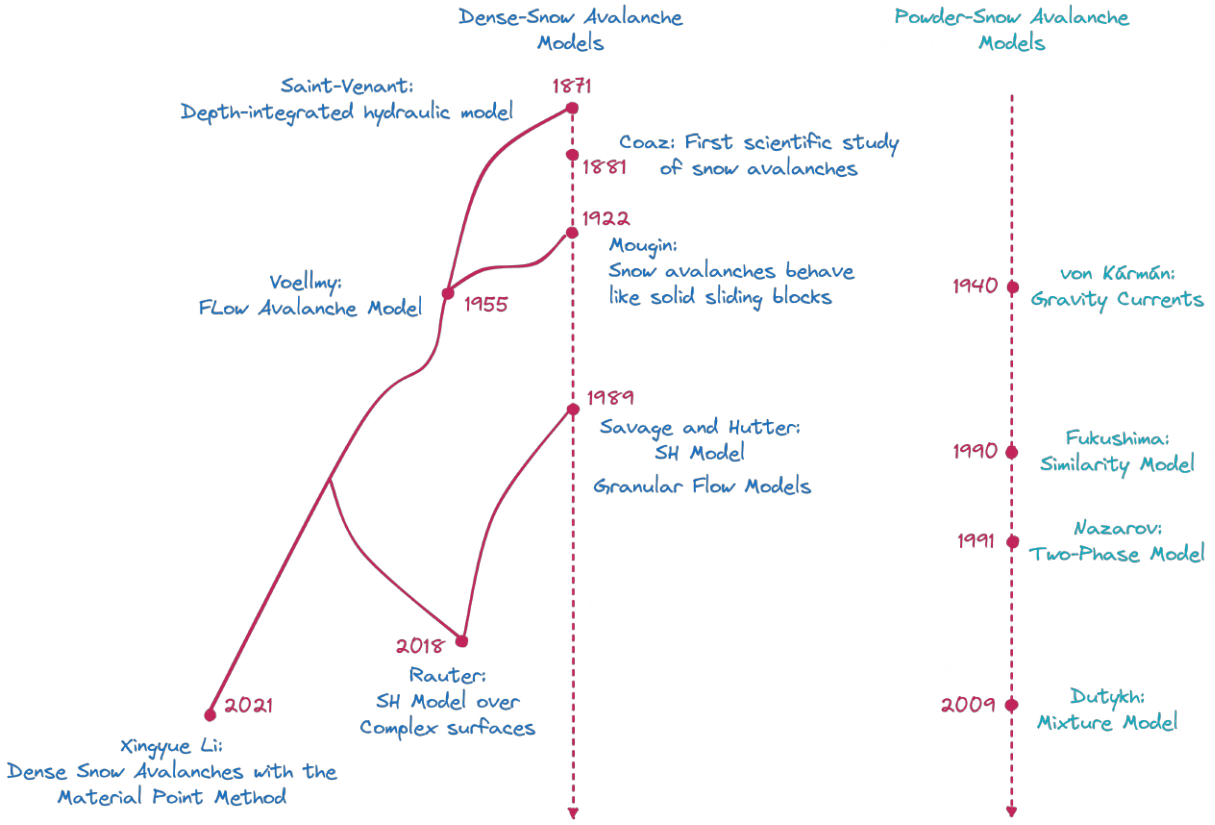

Source: Elaborated by the author.

dense avalanche studies (KARMAN, 1940; BENJAMIN, 1968). Like dense avalanche models, scientists also favored the depth-averaged models (from shallow-water theory) of powder-snow avalanches over the years. Plapp and Mitchell (1960) firstly modeled turbidity currents (siblings of powder–snow avalanches) with depth-averaged equations. Decades later, Parker, Fukushima and Pantin (1986) included equation terms for mass entrainment and turbulence. The improved model was then used to simulate powder-snow avalanches by Fukushima and Parker (1990). Recently, Ivanova *et al.* (2021) developed a shear shallow water model with turbulence applied to powder-snow avalanche simulations.

Before delving into a detailed research timeline, it is worth listing some reviews (MELLOR, 1968; MELLOR, 1978; HOPFINGER, 1983; HARBITZ, 1998; HARBITZ; ISSLER;

KEYLOCK, 1998; ECKART MCELWAINE JIM, 2012; ANCEY, 2016) and books (BOZHINSKIY; LOSEV; BARTELT, 1998; PUDASAINI; HUTTER, 2007; LOUCHET, 2021) published over the years in the general topic of snow avalanches. Likewise, a review of Russian[1] research history on snow avalanches is covered in (EGLIT; YAKUBENKO; ZAYKO, 2020).

3.2 Field Observations and Experimental Data

Field observations and laboratory experiments are the primary sources of evidence for understanding avalanche dynamics and allow researchers to design numerical models. Measurements on real large-scale PSAs[2] offer essential data for validating numerical models. Furthermore, Nishimura, Barpi and Issler (2021) calls attention to what they call the *underrated potential of field observations* by commenting "[...] the study of snow avalanches have been made in well over a dozen countries for nearly a century, with pioneering works dating back as far as 150 years [...] despite substantial progress — many fundamental questions of primary practical significance still lack a well–founded and comprehensive answer".

The knowledge about the various physical processes of snow avalanches extracted from field data over the decades is carefully discussed by Issler *et al.* (2020). Reports on field observations, such as Issler (2020) and Furdada *et al.* (2020), provide consistent conclusions about the destructive force of snow avalanches and offer valuable estimates for mass, speed, and run-out distances. For instance, data from several real avalanches helped Sovilla, Burlando and Bartelt (2006) to model the complex impact of entrainment processes on run-out distances, and Gauer (2014) to validate models dealing with front velocity.

Test sites play an essential role in the empirical study of snow avalanches. A test site is a mountain area containing avalanche paths where scientists install measurement instruments; as the famous Lautaret Pass test site in the French alps, actively in use since 1972 (THIBERT *et al.*, 2015). Over the past decades, scientists have used various equipment and methods to collect data from snow avalanches on test sites (ECKART MCELWAINE JIM, 2012). Bardolini *et al.* (2005) offers an extensive discussion and analysis of measurement techniques applied in several test sites over Europe. Measurement techniques include photogrammetry (DREIER *et al.*, 2016), radars (VRIEND *et al.*, 2013), and pylons equipped with instrumental devices containing several types of sensors (SOVILLA; SCHAER; RAMMER, 2008); see Figure 15. Chart 1 lists typical measurement techniques of relevant physical properties to snow avalanche models used in field observations.

Vallet *et al.* (2004) used videogrammetry to measure a large powder–snow avalanche triggered at the Swiss Vallée de la Sionne test site. The avalanche velocity achieved an impressive

[1] For many decades, the work of researchers from the Soviet Union and Russia was not accessible to the Occident due to translation issues and other reasons.

[2] A large data base of more then 4000 avalanche data is provided online in the website <http://www.data-avalanche.org/> (Trésorier, Marc, 2021).

Chart 1 – A list of physical quantities required by snow avalanche models and their respective measurement techniques / instrumental apparatus.

Property	Measurement	Source
Density	capacitance sensors	(DENT *et al.*, 1998)
Volume	videogrammetry and photogrammetry	(DREIER *et al.*, 2016)
Velocity	array radar systems	(VRIEND *et al.*, 2013)
Internal velocities	optical sensors	(DENT *et al.*, 1998)
Shear and normal stresses	shear plates	(DENT *et al.*, 1998)
Mass entrainment and deposition	radars	(SOVILLA, 2004)

speed of 55 $m \cdot s^{-1}$, with a cloud volume of more than 6×10^6 m^3 and 20 m of cloud height; see Table 3. Such volume measurements supported earlier plume theories (ELLISON; TURNER, 1959) — described in section 3.4. Additionally, Turnbull and McElwaine (2007) provided data supporting plume theories, showing that the front velocity is independent of slope angle due to air entrainment. Bartelt *et al.* (2013) showed that plumes decelerate quickly, obtaining measurements of $4 \sim 16$ $m \cdot s^{-1}$ — with almost stationary plumes at the tail — against front velocities of 50 $m \cdot s^{-1}$. Plumes are created at a frequency of approximately 0.4 Hz, quickly reaching 10 m of height and slowly growing up to 40 m, due to buoyancy flux, $20 \sim 50$ m behind the front; see Figure 16 on page 63.

Table 3 – A list of real scale snow avalanche measurements.

Front Speed $[m \cdot s^{-1}]$	Height $[m]$	Source
55	20	(VALLET *et al.*, 2004)
50	40	(BARTELT *et al.*, 2013)

Data collected at the Vallée de la Sionne and Monte Pizzac test sites showed avalanches growing 12 times due to snow entrainment and show that avalanches with the same speed run different distances due to entrainment mechanisms (SOVILLA; BURLANDO; BARTELT, 2006). Estimates of entrainment and deposition depth can be found in Sovilla *et al.* (2010). Sovilla (2004) extensively discusses various field measurement techniques to model mass entrainment and deposition processes with the following observations:

- On average, avalanches grow their mass by a factor of 4.6;
- The topography of the terrain has little influence on entrainment. Entrainment is also independent of avalanche size;
- On average, avalanches entrain 67% of the release snow depth (fresh snow on the ground at the moment of the release);

Figure 15 – Instrumental pylons are placed in test site avalanche paths to collect data from avalanche flow.

(a) A 20 m pylon equipped with sensors able to measure flow depth, impact pressure, cloud density and many other quantities.

Source: Sovilla, Schaer and Rammer (2008).

(b) A similar pylon being hit by a large-scale avalanche in the Vallée de la Sionne test site.

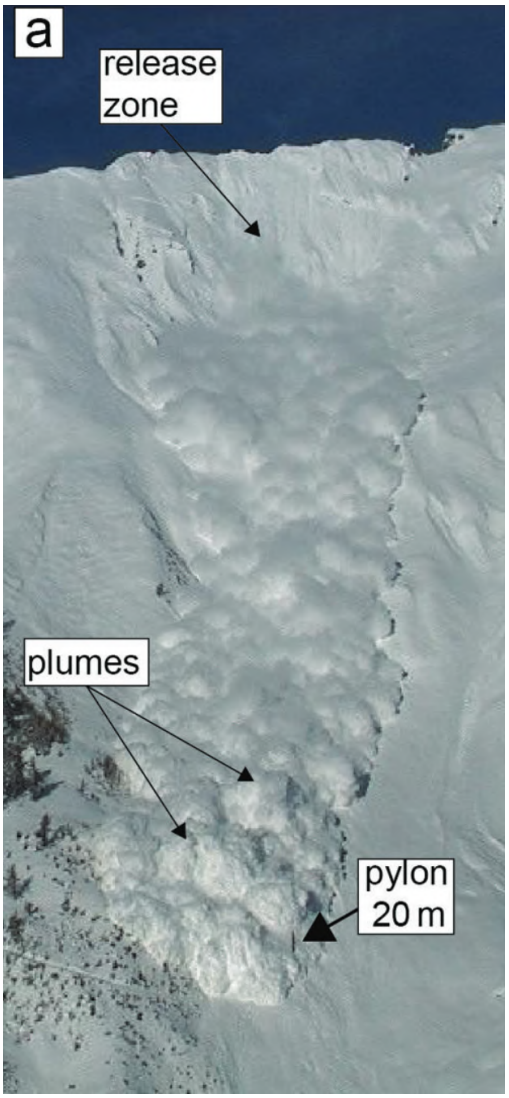

Source: Bartelt *et al.* (2016).

- The characteristics of snow directly influence entrainment. For example, high cohesion due to wet snow limits entrainment, while low cohesion leads to higher entrainment.
- High bed friction increases snow deposition and difficult entrainment due to deceleration;
- During ploughing (frontal entrainment), the entrainment rate of low-density and cohesionless snow is up to 350 $kg \cdot m^{-2} \cdot s^{-1}$ and snow cover shear strength < 1 kPa;
- During basal erosion (internal entrainment), ice crust and high-strength snow are entrained at a rate of 10 $kg \cdot m^{-2} \cdot s^{-1}$, and snow cover shear strength > 25 kPa.

Sovilla, McElwaine and Louge (2015) presented an anatomy model of the powder–snow avalanche based on field and experimental data by discussing the various profiles of density and

Figure 16 – Cross-section of plume heights and positions of an avalanche after 40 s, 45 s, and 50 s. The avalanche moves at 50 $m \cdot s^{-1}$ and plumes rise 40 m above the mountain surface.

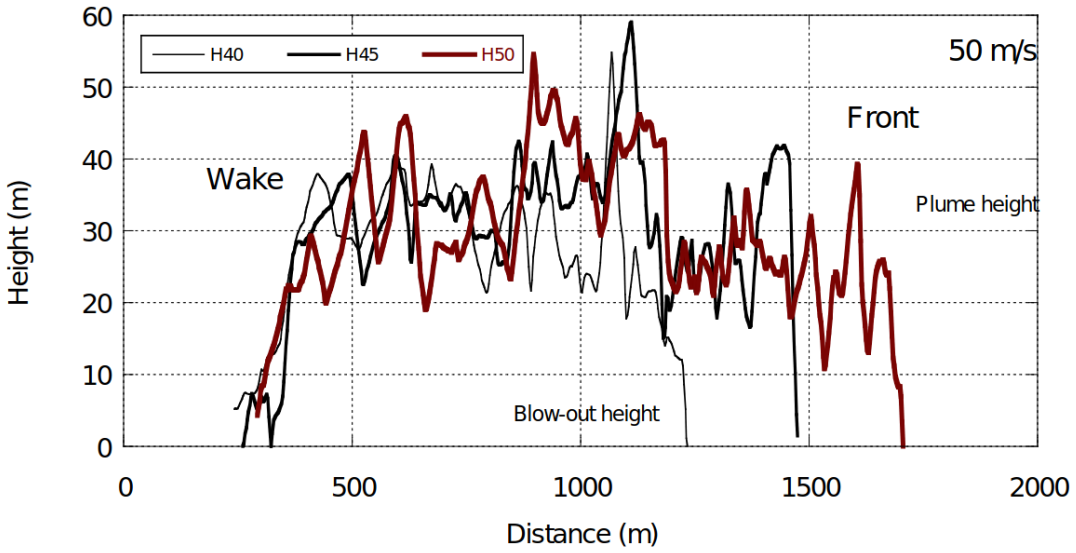

Source: Bartelt *et al.* (2013).

speed throughout the avalanche body. Later, Sovilla, McElwaine and Khler (2018) refined their earlier anatomy model by considering an *intermittency frontal region* — a highly active ≈ 10 m near front region presenting high densities of 20 $kg \cdot m^{-3}$ and velocities 60% larger than front speed. Based on radar data analysis, Köhler, McElwaine and Sovilla (2018) could distinguish seven simultaneous flow regimes in a powder–snow avalanche. The authors concluded that numerical models should handle at least 5 of those regimes. Refer to Gauer *et al.* (2008) for a previous discussion on flow regimes within powder–snow avalanches.

Despite the invaluable data collected from field observations on test sites, real-scale avalanche experiments are expensive, dangerous, unpredictable, and dependent on weather conditions. Hence laboratory experiments play a critical role in avalanche research. Controlled flow and reduced-scale experiments consist of similar flow mechanisms to real-scale avalanches. Issler (2003) examines 60 years of experimental studies over snow avalanches, discussing the similarity issues inherent to the reduced scale utilized in the laboratory.

Dimensionless numbers — refer to table 42.1 in Eckart McElwaine Jim (2012) — can be used to quantify the similarity between small and real-scale flows. Some examples of dimensionless numbers used in laboratory experiments in avalanche research are:

- **Density ratio** Δ_ρ — the density difference between the two fluids (ex. air and snow):

$$\Delta_\rho = \frac{\rho_1 - \rho_0}{\rho_0}$$

  where ρ_0 is the density of the ambient fluid (air) and ρ_1 is the density of the fluid in suspension (snow);

- **Reynolds number** Re — the ratio of inertial forces to viscous forces:

$$Re = \frac{u_f h \rho_1}{\mu}$$

where u_f is the front velocity, μ is the dynamic viscosity of the ambient fluid, and h is the front head height;

- **Richardson number** Ri — the ratio of potential energy to kinetic energy at the interface between fluids:

$$Ri = \frac{g' h \cos\theta}{u_f^2}$$

where $g' = g\Delta_\rho$, and θ is the slope angle;

- **Densimetric Froude number** Fr — the ratio of the viscous diffusion time to the convective time scale:

$$Fr = \frac{u_f^2}{g' h}.$$

Small-scale experiments can be validated by other similarity criteria as well. Faillettaz *et al.* (2002) analyzed data from more than 5000 avalanches and confirmed that slab-avalanche size distributions are scale-invariant, similar to other geophysical phenomena such as earthquakes and landslides. For powder–snow avalanches, similarity is usually borrowed from small-scale turbidity current (small Δ_ρ) tests performed in water tanks, although small-scale non-Boussinesq (higher Δ_ρ) experiments can be found in Ancey (2004), Turnbull and McElwaine (2008), Dellino *et al.* (2019), and Dai and Huang (2021).

In the case of laboratory experiments of powder–snow avalanches — emulated by small-scale turbidity currents — diverse materials are often used in place of actual snow. Examples of materials range from dry or fluidized granular materials (ROCHE *et al.*, 2011), mixture solutions of water (BEGHIN; OLAGNE, 1991) (see Figure 17a), and other sorts of materials such as glass (GREVE; HUTTER, 1993) and quartz (KELLER, 1995). Linden and Simpson (1986) used bubbling water to emulate ambient air turbulence and showed that the a gravity current can be destroyed by the background turbulence. Later, Hermann and Hutter (1991), utilized polystyrene powder and water to emulate turbulent suspension flows and achieved similarity by the Froude number; see Figure 17b. Results showing $Fr \approx 1$ explain why gravity currents speed is independent of flow angle (SHIN; DALZIEL; LINDEN, 2004). In parallel, Turnbull and McElwaine (2007) analyzed front position and volume data from test site avalanches and found values for the Froude number of 2.2 ± 0.18.

Outdoor experiments allow the use of actual snow material under natural ambient temperatures (STEINKOGLER *et al.*, 2015). Ski jump hills have also been used to simulate intermediate-scale avalanches, see (MCELWAINE; NISHIMURA, 2001) and (TSUNEMATSU; MAENO;

Figure 17 – Different mixtures can be utilized in laboratory experiments to emulate powder–snow suspensions.

(a) Dyed salt solution.

Source: Beghin and Olagne (1991).

(b) Polystyrene powder.

Source: Hermann and Hutter (1991).

NISHIMURA, 2020), where ping-pong balls serve as the granular material particles; see Figure 18.

Figure 18 – Outdoor experiment of granular flow utilizing 300000 ping-pong balls at the Miyanomori ski jump hill in Hokkaido, Japan.

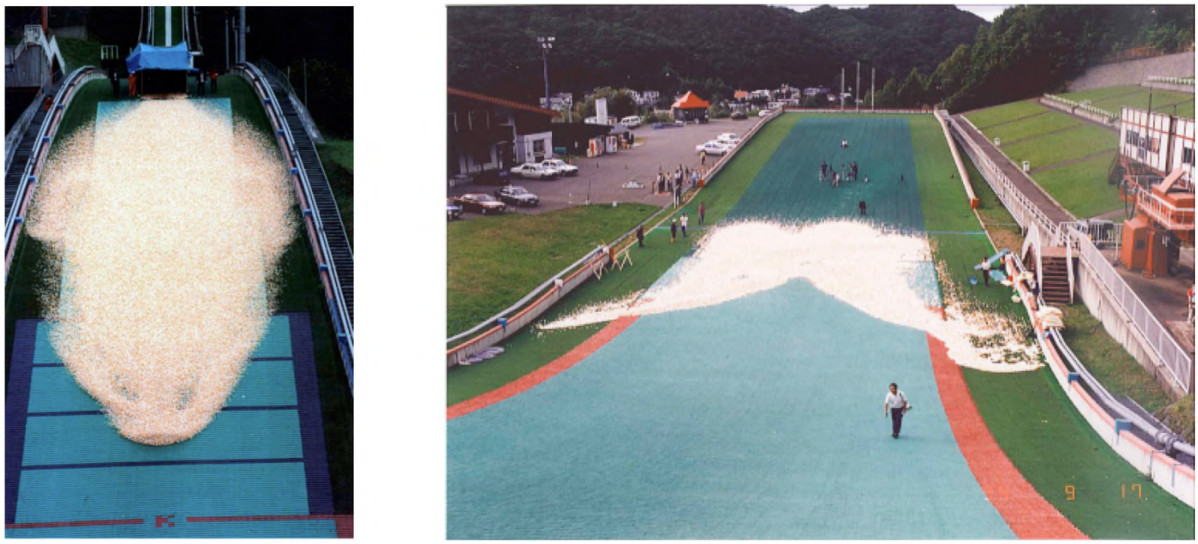

Source: Tsunematsu, Maeno and Nishimura (2020).

Internal velocities, density profiles, and stress quantities are particularly valuable to understanding the internal processes of snow avalanches. For example, an increase of internal velocity was detected by Nishimura *et al.* (1993) seconds after the passage of the front due to the arrival of the dense flow. Naaim and Martinez (1995) measured vertical profiles of particle concentration in the powder-clouds discharged in laboratory. However, due to the violent nature of such phenomena, measuring these properties is very difficult. Snow frozen at the sensors can damp signals, and physical vibrations during avalanche flow can introduce noise into

measurement data and create many other issues (KERN *et al.*, 2009). Only a few measurements were partially successful, such as in Dent *et al.* (1998).

Small-scale experiments, such as Savage and Sayed (1984) and Tiefenbacher and Kern (2004), allow the investigation of the internal flow in avalanche-like phenomena. However, the study of mass entrainment — decisive to the dynamics of powder–snow avalanche internal processes — is a complicated problem to solve in small-scale experiments. To the author's knowledge, no significant advances in mass entrainment experiments for powder–snow avalanches have been achieved — even in laboratories.

Despite the difficulty of performing measurements, research on entrainment and deposition in dense-snow avalanches has seen advances in field observations and laboratory experiments (BARBOLINI *et al.*, 2005; FARIN; MANGENEY; ROCHE, 2014; EDWARDS *et al.*, 2021). Entrainment by bed erosion directly influences avalanche motion by restricting or enhancing its mass and velocity (BARBOLINI *et al.*, 2005). Entrainment has been associated with greater runout distances (STEINKOGLER; SOVILLA; LEHNING, 2014). Observations indicate that entrainment (basal erosion) occurs mainly in the front, while deposition happens in the tail (Sovilla; Bartelt, 2002). Gauer and Issler (2004) discusses the different mechanisms of erosion in snow avalanches. Issler *et al.* (2008) observed the dominance of such mechanisms for different types of flow regimes of wet and dry snow avalanches. Issler and Jóhannesson (2011) and Issler (2014) offer a theoretical discussion about such mechanisms on various types of flows, including field observations and mathematical models presenting peaks of influx rates of up to 1000 $kg \cdot m^{-2} \cdot s^{-1}$. Issler *et al.* (2020) suggests that the eroded mass is only entrained into the avalanche.

3.3 Dense-Snow Avalanche Models

Despite the different physical properties of snow, dense snow avalanches have many similarities with other avalanches, such as debris flows and mudslides. Many mathematical models of such avalanche types share similar origins. Compared to the powder–snow avalanches, dense-snow avalanche research appears to be more extensive and explored.

Figure 19 arranges popular models of dense-snow avalanche models roughly based on the SAME (Snow Avalanche Modeling and Warning in Europe) model survey (HARBITZ; ISSLER; KEYLOCK, 1998). This text focus only on a subset of models to avoid overextending the scope of this section, concentrating on the deterministic type between the two main divisions, statistical and deterministic, as statistical models offer little detail about the internal flow dynamics of such avalanches. This section explores the dense-snow avalanche models in the same order of the following division:

- *Empirical / Statistical models* — described in subsection 3.3.1 on page 68 — apply statis-

Figure 19 – General organization of dense-snow avalanche models.

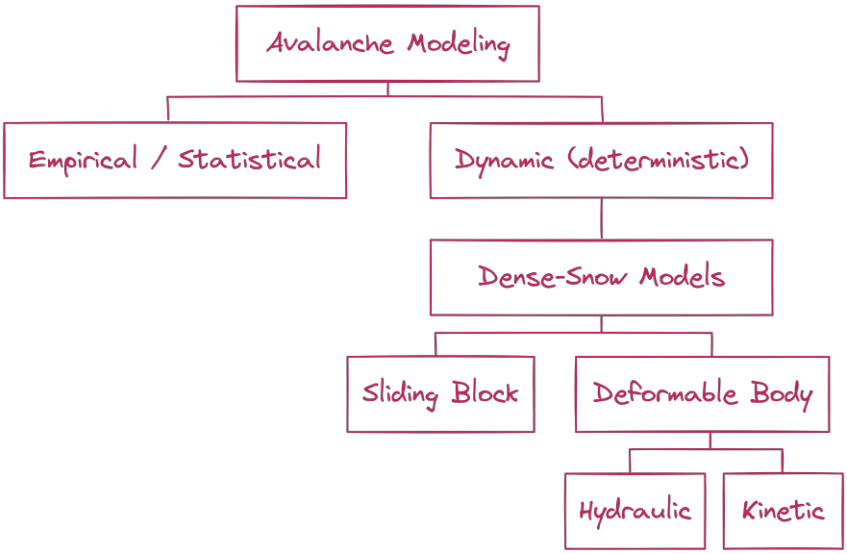

Source: Adapted from Harbitz, Issler and Keylock (1998).

tical inference methods on historical data of field observations and laboratory experiments to predict general quantities of the avalanche such as runout distances and avalanche size;

- *Deterministic models* — described in subsection 3.3.2 on page 69 — encompass all the following. Such models use mathematical equations to describe motion at different scales;
- *Sliding Block models* — described in subsection 3.3.3 on page 71 — represent the avalanche body as a single rigid (non-deformable) block that slides down over an inclined plane;
- *Hydraulic models* — described in subsection 3.3.4 on page 72 — borrow laws and relations from hydrodynamics to better reproduce the mechanical behavior of snow in sliding block models;
- *Kinetic models* — described in subsection 3.3.5 on page 76 — use balance equations from continuum mechanics to full describe the avalanche;
- *Granular Flow models* — described on page 79 — like kinetic models, stand from the continuum point of view but bring relations from the laws of motion of granular materials. Such models consider internal friction processes and other complex internal phenomena of snow avalanches, such as entrainment and deposition.

Before continuing, it is worth noticing that the above division of models is neither definitive nor inflexible since there are models that share origins and aspects of different groups simultaneously. For example, some methods combine statistical and deterministic models, while some granular flow and kinetic models borrow terms from hydraulic models. In other words,

such a division of models is not necessarily a set of disjoint groups of methods, concepts, or assumptions.

3.3.1 Statistical Models

As mentioned in section 3.2, field observations and historical data provide essential resources for understanding physical phenomena. Such data is the primary input of statistical models. *Statistical models* use historical information to predict the size of new avalanches by establishing correlations between the run-out distances and the underlying topographic parameters, such as the avalanche initiation point, stopping point, and slope angles representing the avalanche track path (MCCLUNG; LIED, 1987). Based on such parameters, the $\alpha - \beta$ model by Lied and Bakkehøi (1980) uses regression methods to estimate the run distance of an avalanche over a given terrain topography; see Figure 20 on page 68. Other examples of statistical models are the run-out ratio model by McClung, Mears and Schaerer (1989), and the space-time (ST) model by McClung (2000). Refer to Sinickas (2013) and Schweizer, Bartelt and van Herwijnen (2021) for further references and details about statistical models.

Figure 20 – Parameters used by the $\alpha - \beta$ model. The model uses the (A) starting zone location, the (B) deceleration zone location, the (C) run-out zone location, and the *average inclination angle* β. Along with regression constants γ and λ , the *stopping angle* α can be determined as $\alpha = \gamma\beta + \lambda$.

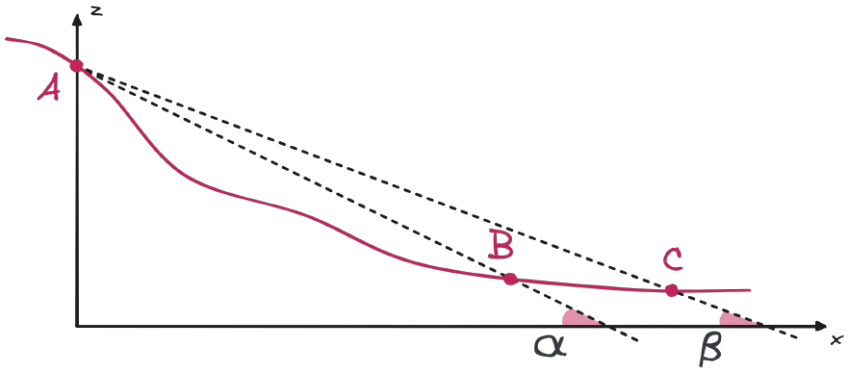

Source: Elaborated by the author.

Statistical methods have been extensively used in avalanche zoning or even in combination with deterministic methods for estimating the run-out distance of long-return period avalanches (ANCEY; GERVASONI; MEUNIER, 2004). However, such methods present several shortcomings related to issues of input data quality and the wrong assumption that avalanches' dynamic behavior is governed by topographic features (MEUNIER; ANCEY, 2004). Such limitations require the use of deterministic approaches.

3.3.2 Deterministic Models

Under the *deterministic* approach, physical and mathematical equations describe the avalanche motion. Different methods deal with different scales of representation of mass; see Figure 21 on page 69. These scales range from individual snow particles (Figure 21c) to a single sliding block representing the entire avalanche body (Figure 21a), with intermediate representations that split the avalanche body into moving columns of variable height (Figure 21b). Larger scale representations lead to simpler models and crude estimations, while more miniature scale representations offer precise flows at the cost of complicated models and computational effort.

Figure 21 – Deterministic models describe the avalanche — body in different scales of representation. Model accuracy depends on the level of representation, with more refined representations leading to higher precision on flow dynamics.

(a) A single solid block represents the avalanche body. Equations describe the movement of the center of mass, and velocity is assumed uniform throughout the block — friction forces with the inclined surface decelerate the slide.

(b) Separate columns of mass represent the avalanche body. Each column block has its center of mass and friction with the bottom surface. The height of columns varies as mass is transported between columns.

(c) Small individual blocks, called particles, describe finite volumes of the avalanche. The particles have individual properties, such as velocity and mass, and collide with each other. The collisions produce friction forces, and particles' collective movement shapes the flow.

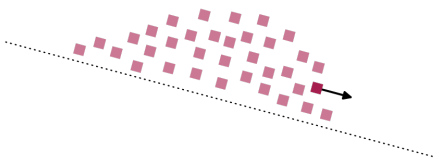

Source: Elaborated by the author.

The mathematical equations used by deterministic models may use different coordinate spaces to describe the physical quantities and the motion of avalanches. Figure 22 on page 70 depicts the two standard coordinate systems used by avalanche models: the local and global

coordinate systems. In global coordinates, the axes of the basis are aligned to the Cartesian basis and do not depend on the geometry of the domain; see Figure 22a. In local coordinates, axes vary along the geometry, and usually, the basis vectors are the bed's normal and tangential directions; see Figure 22b. Vector quantities such as the velocity and acceleration forces, in particular, are sensitive to coordinate systems and must be appropriately defined. For example, in a position in the bed surface with slope angle θ, the gravitational force $\mathbf{g}$ translates to the following projections in a local coordinate system: the tangential component along the slope, $\mathbf{g}\sin\theta$[3], and the component $\mathbf{g}\cos\theta$ along the slope normal; see Figure 22c.

Figure 22 – Models can use different coordinate systems to describe flow quantities. In the case of local coordinate systems, vector quantities must be projected onto the local basis system to guarantee consistency in equations.

(a) The global coordinates system usually uses the Cartesian coordinate system. The system does not depend on the geometry of the terrain, as all quantities follow a single coordinate system.

(b) Local coordinates follow the geometry of the domain. Each position in space spawns an aligned basis on which vectors must be projected. Such an approach can bring many simplifications to the equations.

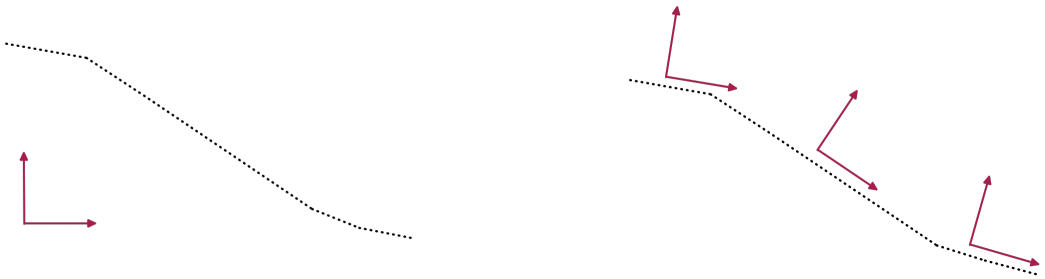

(c) Gravity acceleration vector projection onto a local coordinate system.

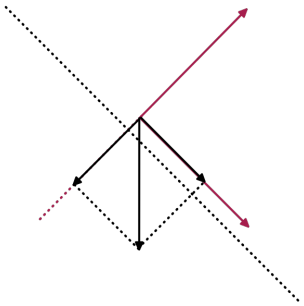

Source: Elaborated by the author.

All avalanche model equations in this section use the same local coordinates system — except for kinetic models, which use the global coordinate system. In the one-dimensional case,

[3] The projected gravitational force is common in models of flows over inclined terrains — once such models usually use local coordinates along the slope.

the horizontal direction x'[4] in the local coordinate system is tangential to the slope. Therefore, spatial derivatives along the horizontal[5] direction are defined by $\partial/\partial x'$. The dynamic variables can be functions of the time t and the position along the slope x'. For instance, the height $h'(x',t)$ of the avalanche body, measured in meters, is the height along the slope's normal direction. The velocity vector $u(x',t)$ points to the motion direction (parallel to x'). For curved slopes, the angle of the slope $\theta(x')$ is a function of the position; see Figure 23 on page 71.

Figure 23 – Common variables present in avalanche models. The height h and velocity u are functions of position x and time t. The bed slope θ varies only with position. Some models also consider the entrainable snow cover, which has depth h_0.

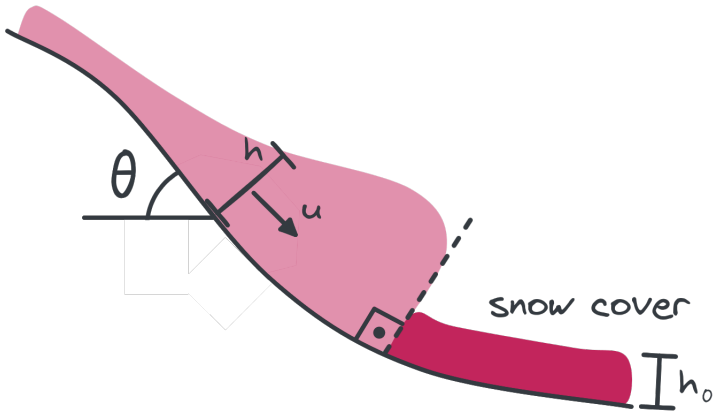

Source: Adapted from Eglit, Yakubenko and Zayko (2020).

3.3.3 Sliding Block Models

The simplest and earliest approach is the so–called *sliding block model*, introduced by Mougin (1922), and describes the avalanche as a single rigid (non-deformable) body that slides over an inclined plane representing the mountain terrain (see Figure 21a on page 69). In 1924, such early approaches were used to compute the velocity of avalanches during the Olympic Games at Chamonix (LAGOTALA, 1927). Sliding block models make the calculations relative to the center of mass of the sliding block and use specific friction forces to emulate the avalanche mechanical behavior. Typically, only one-dimensional schemes are considered and motion is described as:

$$\frac{du}{dt} = g\sin\theta - F, \tag{3.1}$$

where $u(x,t)$ is the velocity, θ is the mean slope of the inclined plane, g is the gravitational acceleration, and $F(x,t)$ is the frictional force. The mechanical behavior of the avalanche due to its interaction with the mountain soil relies on the frictional force term F, responsible for the deceleration of the flow. The most significant development in the friction term came with

[4] The prime superscript, $\bigstar'$, refers to local coordinates. However, for the sake of generality, the prime may be omitted throughout the text.

[5] Although the term *horizontal* refers to the aligned direction of left and right, as in the Cartesian coordinate system, in the context of inclined flows, the term also refers to the principal flow direction.

Voellmy (1955)'s friction model — called *Voellmy fluid* by Hungr (1995). Voellmy's model combines a dynamic friction component τ_h with a Coulomb-like dry friction (POPOVA; POPOV, 2015) component τ_d:

$$F_v = \tau_b = \tau_h + \tau_d, \quad \tau_h = g\frac{u^2}{\xi h}, \quad \tau_d = \mu g \cos\theta, \tag{3.2}$$

where ξ is the coefficient of dynamic friction related to the terrain roughness, μ is the friction coefficient related to the snow fluidity, and $h(x,t)$ is the mean flow depth of the avalanche. The letter b in τ_b stands for bed, as Voellmy's model F_v represents the bed shear stress. The term τ_h, named by Voellmy as *turbulent friction* and sometimes referred to as *shear resistance* (BARTELT; SALM; GRUBER, 1999) or *hydraulic friction* (EGLIT; YAKUBENKO; ZAYKO, 2020), is based on the Chézy resistance formula for turbulent water flow in open channels and refers to the viscous resistance — see page 170 in Kay (2017). The Voellmy's friction model is used by many generations of models today, such as debris flow models (PIRULLI; SORBINO, 2008; HUSSIN *et al.*, 2012; SCHRAML *et al.*, 2015; ABRAHAM *et al.*, 2022).

Sliding block models overcome many statistical model shortcomings but still offer few details about the flow dynamics. These models inherently consider the body of the avalanche as non-deformable. In order to account for more complex phenomena such as mass entrainment, straining, and other physical properties of an avalanche flow, avalanche models need to dive further into smaller-scale representations.

3.3.4 Hydraulic Models

The contributions of Voellmy[6] go beyond the frictional model. His analogies to hydrodynamics also brought attention to the so–called depth-integrated flow model, which has become the most prominent model for dense-snow avalanches since then (LACHAPELLE, 1977; ANCEY, 2016). The depth-integrated flow model, also called shallow water equations (SWE), is based on the works of Barré de Saint-Venant on hydraulic modeling (VENANT, 1871). Depth-integration simplifies fluid mechanics equations by neglecting vertical velocities, assuming that the flow height h is much smaller than the flow length l. The horizontal velocity at any given point is averaged over the whole depth of the flow, yielding $\bar{u}(x,t)$. In terms of scales of representation of the avalanche body, the depth-integrated flow is an intermediate scale that sees the fluid body as columns of mass that vary in height; see Figure 21b on page 69. The one-dimensional Saint-Venant's equations (SWE) are:

$$\frac{\partial h}{\partial t} + \frac{\partial}{\partial x}(\bar{u}h) = 0, \tag{3.3}$$

$$\frac{\partial h\bar{u}}{\partial t} + \frac{\partial (h\bar{u}^2)}{\partial x} = -\frac{\partial}{\partial x}(\frac{1}{2}gh^2), \tag{3.4}$$

[6] The works of Voellmy can be found in volume 73 of the series *Schweizerische Bauzeitung* at <https://www.e-periodica.ch/digbib/volumes?UID=sbz-002> (ETH, Zürich, 2022), by Wanger (2018).

where again x is the slope coordinate axis and g is the gravitational acceleration.

Notice that the hydrostatic pressure gradient dictates the flow on the right-hand side of Equation 3.4 but does not consider any friction forces. Models based on the SWE are called *hydraulic models* and can be referred to by some authors as Saint-Venant models — models using Voellmy's friction may receive this name as well. Although Voellmy popularized the depth-integration approach by using depth-averaged velocities and suggesting the use of the hydraulic model, his model lacks Equation 3.3, the continuity equation. Therefore, Voellmy assumes depth and depth-averaged velocity to be the same at all points of the avalanche, which essentially makes his model a sliding block model.

Many works extended Voellmy's model throughout the years in order to complete his equations. Particularly, the set of works made by Salm — Salm (1966), Salm (1967), Salm (1972) — are considered the most significant extensions and form the Voellmy-Salm (VS) model, with Salm and Gubler (1985) and Salm, Burkard and Gubler (1990) being referred to as the Voellmy-Salm-Gubler (VSG) model. A comparison between the VS and VSG variations can be found in Gubler (1989). The extensions incorporated by the VS model handle non-uniform flows and internal friction under the assumption that snow behaves like ideal elastoplastic cohesionless materials (like dry sand) (HEIMGARTNER, 1977), with different values for the friction coefficients of F_v. Following the *earth-pressure* definition of Rankine (1857), the VS model also adapted the hydrostatic pressure to depend on the internal friction angle ϕ replacing the momentum Equation 3.4 by

$$\frac{\partial u}{\partial t} + u\frac{\partial u}{\partial x} = g\sin\theta - F_v - \frac{\partial}{\partial x}(\lambda_{\pm} g\cos\theta\frac{h^2}{2}), \tag{3.5}$$

where the term $\lambda_{\pm} = \tan^2(45^o \pm \phi/2)$ is the active/passive[7] pressure coefficient with internal friction angle ϕ and the operation $\pm$ depends on the value of $\partial u/\partial x$ ($+$ for $\partial u/\partial x > 0$, and $-$ otherwise) (SALM, 2004). The WSL Institute of Snow and Avalanche Research SLF (SLF) (SLF, 2022) has used the VS model since earlier 1990s (SALM, 1993). Table 4 and Table 5 list the values for the coefficients of dynamic friction ξ and dry friction μ suggested by the institute (GUBLER, 2005). Software packages cited in section 3.6 use the VS model. Examples of methods based on the VS model are Sovilla and Bartelt (2002) and Christen, Kowalski and Bartelt (2010).

Table 4 – Typical values in the VS model of the dynamic friction ξ for different dense-snow avalanche conditions suggested by the SLF (GUBLER, 2005).

Dynamic friction (ξ)	Condition
> 1000	very cold dry snow, very low bed roughness
$500 \sim 600$	large bed roughness, channelled flow
400	avalanche flowing though a forest

[7] According to Salm, internal friction (plugged into the pressure term in the VS model) arises as the snow gets under a tensile (active) or compressive (passive) longitudinal strain.

Table 5 – Typical values in the VS model of the dry friction μ for different dense-snow avalanche conditions suggested by the SLF (GUBLER, 2005).

Dry friction (μ)	Condition
0.155	extreme avalanches with large volumes, flow depth of $1 \sim 2\ m$
$0.25 \sim 0.3$	smaller avalanches with volumes $< 10^4\ m^3$
0.3	wet snow avalanches of any size

Despite its success, the VS model has received many criticisms. Critics of the VS model point out several shortcomings and limitations regarding the accuracy of its predictions on runout distances and deposition heights (MCCLUNG; MEARS, 1995). Indeed, the VS model is considered by many as a sliding block model since its original formulation does not include the continuity equation (BARTELT; BUSER; PLATZER, 2006; PUDASAINI; HUTTER, 2007). Perla, Cheng and McClung (1980) derived the PCM model, which uses a calibrated mass-to-drag ratio M/D coefficient applied to the velocity squared, replacing the dynamic friction coefficient ξ - so only the dry friction coefficient μ must be estimated. An early extension of the PCM, the PLK model by Perla, Lied and Kristensen (1984), uses particles to handle snow entrainment and deposition. The PCM model offers better runout distances in complex terrains than the VS model (LIED *et al.*, 1995; JAMIESON; MARGRETH; JONES, 2008). Bartelt, Salm and Gruber (1999) solved some shortcomings of the VS model by combining characteristics from the Norwegian NIS model, by Norem, Irgens and Schieldrop (1989), and modifications to Voellmy's friction from Russian models — described on page 74.

The critical characteristic of the NIS model that puts it one step forward from sliding block models is that it considers the avalanche body as completely fluidized. The VS model, for example, alternates between three flow regimes: sliding[8], partly fluidized, and fully fluidized. Salm and Gubler (1985) adapted these flow regimes from the studies of Haff (1983) on treating the movement of granular materials from a continuum point of view. The flow regime determines the velocity profile along the depth; see Figure 24 on page 75. Non-steady and non-constant velocity profiles result from internal stresses in the avalanche body, which the previous models do not adequately handle. Allowing such velocity profiles — as in the NIS model — leads to more precise simulation results.

In parallel to western models, Russian models also have a long history. The first sliding block models in the Soviet Union appeared in the early 1930s following the same Equation 3.1 on page 71 (BOZHINSKIY; LOSEV; BARTELT, 1998). Similar to the VS model, the works of Grigorian and Eglit — Grigorian, Eglit and Iakimov (1967), Bakhvalov and Églit (1973), Grigorian and Ostroumov (1977), Eglit (1998b) — constitute the Moscow State University (MSU) hydraulic model. The one-dimensional MSU momentum equation is quite similar to VS

[8] The sliding regime, when velocity is constant accross the depth, is also called *plug flow* (LIGNEAU; SOVILLA; GAUME, 2022).

Figure 24 – Velocity profile on different flow regimes.

(a) In the sliding regime, velocity ($1 \sim 5\ m \cdot s^{-1}$) is constant across the depth and is usually characterized by high cohesive snow.

(b) As velocity increases, snow is disintegrated into clods and a partial layer becomes fluidized. The shear stress depends linearly on flow velocity.

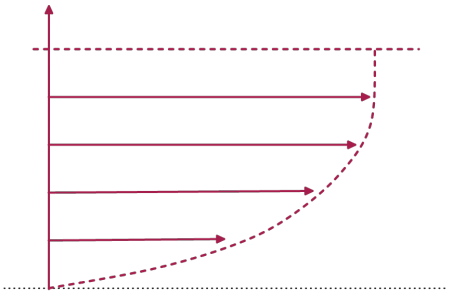

(c) At higher speeds, snow clods mobility allow changes in flow depth and deformations. The shear stress now depends on the square of the flow velocity.

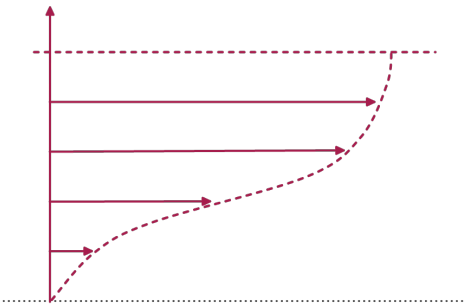

Source: Adapted from Salm and Gubler (1985).

model's Equation 3.5 on page 73:

$$\frac{\partial u}{\partial t} + u\frac{\partial u}{\partial x} = g\sin\theta - F_v - \frac{1}{2h}\frac{\partial}{\partial x}(h^2 g\cos\theta), \tag{3.6}$$

where F_v uses a modified dry friction τ_d'. The full MSU model includes the continuity Equation 3.3 on page 72 and a set of hydraulic equations to handle snow entrainment in the leading edge. Entrainment equations are treated in the subsection 3.3.7 on page 83.

From Equation 3.6, two main differences to the VS model stand out. Firstly, the MSU model discards the active/passive pressure coefficient by setting $\lambda_\pm = 1$. The second relies on the term F_v. Grigorian stated there should exist an upper limit to friction, arguing that friction cannot rise indefinitely with an increase in normal stress (GRIGORYAN, 1979). Therefore, the MSU model limits the dry friction $\tau_d = \mu g\cos\theta$ by the shear stress $\tau_\gamma = \mu p$ with a yield condition $\tau_{\gamma *}$ representing the minimal shear strength of the snow in the avalanche:

$$\tau_d' = \begin{cases} \tau_d, & h \le h_* \\ \frac{\tau_{\gamma *}}{h}, & h > h_* \end{cases}, \quad h_* = \frac{\tau_{\gamma *}}{\mu\rho g\cos\theta}. \tag{3.7}$$

In other words, the dry friction reaches a maximum value as avalanche depth h rises. In practice, larger avalanches will travel longer distances in simulations, for which Voellmy's friction model

fails to produce satisfactory results (BARTELT; SALM; GRUBER, 1999). A post-mortem paper by Grigorian was recently published with the state-of-the-art version of the MSU model, discussing updates in the friction coefficients and the handling of entrainment (GRIGORIAN; OSTROUMOV, 2020). The MSU model found its way to the west due to its snow entrainment equations with Sovilla (2004). An extensive literature in English of Russian models can be found in Bozhinskiy, Losev and Bartelt (1998) and a modern review in Eglit, Yakubenko and Zayko (2020).

Hydraulic models have been present in avalanche-like phenomena research for many decades now. Due to its simplicity and convenient analogy to hydrodynamics, hydraulic models could quickly gain space in avalanche research during the 1970s. However, the complexities of the mechanical behavior of snow during avalanche motion and the intricate relations of internal friction forces demanded new research paths and new types of models.

3.3.5 Kinetic Models

The fluid-like motion of dense-snow avalanches makes using fluid mechanics equations attractive. However, formulating a full fluid mechanics model still encounters several challenges and limitations. Most difficulties come from the inherent complexity of the dynamics of snow:

- Snow particles change in size with time and position, spanning a wide range of sizes ($0.001 \sim 1\ m$) (BARTELT; MCARDELL, 2009);
- Phenomena like erodible basal surface pose ill-known boundary conditions;
- Surge front and free surface instabilities lead to flows with abrupt changes over time;
- Dense snow flows are non-Newtonian viscoplastic flows (DENT; LANG, 1982);
- Variations in snow microstructure due to thermodynamic transformations make snow rheometry very difficult, consequently impeding the identification of constitutive relations.

Therefore, the usual fluid mechanics approach is to treat the snow material as a whole at the macroscopic scale — but far from a single piece as in sliding block models. The snow avalanche body is usually represented by a set of particles or fine numerical grids that represent small volumes of snow, as in Figure 21c on page 69. In such treatment, the bulk rheological[9] properties of snow are used instead of directly dealing with real snow particles individually at the microscopic scale. Such formulations from continuum mechanics, called *kinetic models*, combine the rheological conditions with mass, momentum, and energy balance equations (PUDASAINI;

[9] E.C. Bingham and M. Reiner defined the term *rheology* in 1929 to refer to "the science devoted to the study of the deformation and flow of matter" (BINGHAM, 1944).

HUTTER, 2007). For instance, an example of a local momentum balance equation for a bulk material is:

$$\rho \frac{d\mathbf{u}}{dt} = \rho \mathbf{g} - \nabla p + \nabla \cdot \Sigma, \tag{3.8}$$

where ρ is the bulk density, $\mathbf{u}$ is the bulk velocity, $\mathbf{g}$ is the gravity acceleration, p is the pressure, and Σ a second-order tensor called the bulk extra stress tensor[10]. In particular, the stress tensor determines the relation between stress and the different physical states or acting forces that characterize the behavior of different materials. In terms of stress-generating mechanisms during snow avalanches, Hutter (1996) gives some examples:

- The rolling of snow particles over each other, known as the *dry Coulomb rubbing friction*, that causes plastic behavior;
- The continuous and instantaneous collision of snow particles, without rubbing, transports momentum and causes viscous behavior;

where the influence of each varies on the type of the avalanche and may occur simultaneously along with other mechanisms. In dense snow avalanches for example, the dry Coulomb rubbing friction is more present. Such stress response mechanisms are represented by the material's *constitutive relations*, defined by the so–called *constitutive equations*, or *rheological models* in the present context, which describe the tensor Σ[11] components σ_{ij} in Equation 3.8 on page 77 (GONZALEZ; STUART, 2008).

The study of the relationship between stress and deformation rates traces back to the beginning of the 19th century (YU, 2002). Since then, scientists have been measuring constitutive relations for many types of materials and physical phenomena, such as debris flows (MAJOR; PIERSON, 1992) and mudflows (HUANG; AODE, 2009). Different properties of a material can also lead to different stress-strain responses, as demonstrated by Arenson, Springman and Sego (2007) for different types of frozen soil; see Figure 25a on page 78. The behavior of materials can also change depending on their stress state. For example, a material with elastic behavior can transit to plastic behavior when suffering too much of a certain type of stress. Such transitions are represented by the so–called *yield surfaces*, which define the different regions in principal stress space that represent the different material behaviors. The principal stress space is a three–dimensional spaced formed by the three princial stresses $(\sigma_1, \sigma_2, \sigma_3)$, *eigenvalues* of Σ, on which yield surfaces determine for which stress conditions, *yield conditions* or *yield stress criteria*, the material will undergo plastic deformation. Figure 25b on page 78 shows an example of a yield surface, the Mohr–Coulomb yield failure criterion that spans a six-side pyramidal

[10] The pressure p and extra tensor Σ are decomposed parts of the so–called *Cauchy stress tensor* $S = -pI + \Sigma$, where Σ is the *deviatoric stress tensor* and $-pI$ is the *spherical stress tensor* (GONZALEZ; STUART, 2008).

[11] The equations system does not has enough equations to solve all the 9 variables introduced by Σ. The consitutive equations complete the system and are usually referred to as *closure model*.

surface, for which the material undergoes plastic deformation when stresses reach any of the sides/edges (see (LABUZ JOSEPH F.AND ZANG, 2012)).

Figure 25 – Constitutive relations describe stress responses to acting forces and material deformations, such as strain. Yield surfaces define stress states of materials and yield critera characterize material behavior.

(a) The stress-strain responses for ice and frozen soil. The four curves, A, B, C, and D, represent the ductile, dilatant, brittle, and brittle failure behaviors, respectively.

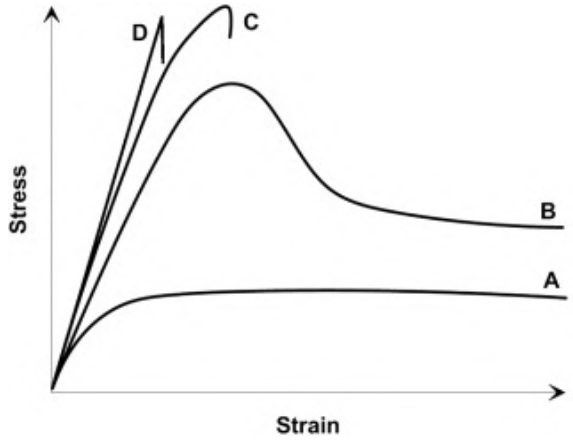

Source: Arenson, Colgan and Marshall (2015).

(b) A cross-section of the Mohr–Coulomb yield surface for an isotropic material. The surface is pyramidal with an irregular hexagonal base defined in the principal stress space (σ_1, σ_2, σ_3). The edges represent the cross-section of the surface on the π–plane — perpendicular to line $\sigma_1 = \sigma_2 = \sigma_3$.

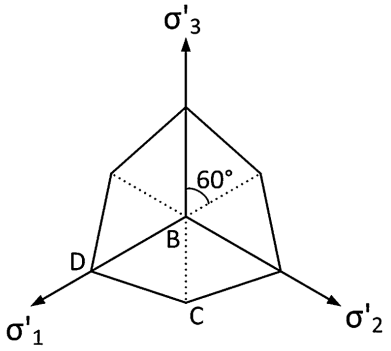

Source: Labuz Joseph F.and Zang (2012).

Examples of common constitutive equations and yield surfaces found in the literature are the Coulomb-like friction laws (IVERSON; DENLINGER, 2001), the Drucker-Prager elastoplastic model (DRUCKER; PRAGER, 1952), the Mohr-Coulomb-Cap criterion for snowpack failure (REIWEGER; GAUME; SCHWEIZER, 2015), and the nonlinear viscous law $\mu(I)$-rheology (GRAY; EDWARDS, 2014). The Voellmy's friction law described earlier is an example of constitutive equation used by kinetic models. Ligneau, Sovilla and Gaume (2022) discusses the role of friction in dense snow avalanches, and Voellmy's friction coefficients are explored in Ancey and Meunier (2004), Naaim *et al.* (2013), Sanz-Ramos *et al.* (2020).

Laboratory experiments and measurements from field observations of rheological properties help design constitutive relations of materials. However, the measurement of constitutive relations is more complicated or sometimes impossible for more complex materials like snow (ANCEY; MEUNIER, 2004). In such cases, the models borrow characteristics from other physical phenomena, such as granular and viscoplastic flows (TAI; HUTTER; GRAY, 2001; ANCEY, 2001; NICOT, 2004). Examples of rheological models used in snow applications are the Burgers model for viscoelastic materials (MELLOR, 1974), models for elastoplastic materials (SINGH *et al.*, 2022; GAUME *et al.*, 2019), models based on the micro-structural configuration of snow (St. Lawrence; LANG, 1981; MAHAJAN; BROWN, 1993), and models considering the compressibility of snow (MISHRA; MAHAJAN, 2004). Refer to Salm (1982) for more details on the earlier approaches of constitutive models for snow.

3.3.5.1 Granular Flow Models

One of the most successful approaches used by kinetic models of dense-snow avalanches is the treatment of snow as a granular material. Although the first experiments with the motion of granular materials started in 1954 with the pioneering work of Bagnold (1954), theoretical models started to appear only decades later (HAFF, 1983). Refer to Savage (1984) for a review of early models of granular flows. Complete reviews on granular flow models can be found in Campbell (1990), Hutter and Rajagopal (1994). Such models take the behavior of the granular material from a continuum point of view, which allows the use of continuum mechanics equations. Haff (1983) uses the following assumptions regarding the material grains and their analogy to fluid molecules in the continuum treatment:

- Individual grain motion follows the laws of classical mechanics;
- Different from molecules that may undergo completely elastic collisions, grain-grain collisions always involve a loss of kinetic energy (the amount of energy lost in such granular systems is significantly different from fluids);
- Although different grains have different sizes, minor differences between grain sizes do not affect the motion significantly. Therefore, such granular systems assume all particles are roughly the same size;
- Similar to the same size assumption, all grains are assumed to be roughly the same shape (spheres). Otherwise, grain-grain collisions must account for grain rotation due to torque caused by friction;
- Grains are orders of magnitude bigger than molecules, so the number density of particles in a granular flow is much smaller than the number density of molecules in a correspondent fluid. Combined with the inelastic nature of grain-grain collisions, the continuum hypothesis might not hold in some instances[12]. Thus, the model must be applied only to granular flow situations where the continuum hypothesis is valid;
- The *binary collision hypothesis* can be assumed for such granular systems, meaning that only pairwise collisions are essential for the dynamical evolution of motion;
- Unlike molecular interactions, grain-grain interactions are assumed not to have any attraction force.

The last assumption above considers only cohesionless granular materials. Aside from dry snow avalanches, dense-snow avalanches present strong, cohesive interactions. However,

[12] The continuum hypothesis considers that properties, such as velocity, density, and energy, vary continuously, even over small volumes, due to the small molecular scale. In comparison, the large-scale size of grains will lead to abrupt changes in such properties for the same small volumes.

cohesionless models for snow avalanches are widespread due to the difficulties inherent to cohesion modeling. Examples of models using cohesion can be found in Bartelt *et al.* (2015) and Valero *et al.* (2018).

The Savage–Hutter (SH) model is the first, perhaps the most famous, granular flow model for dense-snow avalanches under the continuum mechanical approach. Introduced in 1989 by S. B. Savage and K. Hutter (SAVAGE; HUTTER, 1989), the SH model considers some additional simplifying assumptions to the list above:

- The flow is density preserving, meaning that volume expansions and compactions do not happen during motion. Volume changes happen in the initiation and stop phases. Hutter and Koch (1991) reported measurements of up to 20% volume changes in sand-avalanche flows;
- The inclination slope angle θ is constant - this limitation was soon overcome by Savage and Hutter (1991), allowing mildly curved topographies;
- The avalanche body is shallow in that the height is orders of magnitude smaller than the longitudinal extensions of the body (similar to Saint-Venant's);
- The velocity is depth-averaged through the avalanche depth (also similar to the depth-integrated flow model);
- The friction is Coulomb-like dry friction with a bed friction angle δ;
- The Mohr-Coulomb yield criterion defines the constitutive behavior with internal angle of friction $\phi \geq \delta$.

According to Hutter, Savage and Nohguchi (1989), which results and physical model helped construct the SH model; the avalanche surface is assumed to be stress-free. The shearing takes place in a thin layer close to the bed, where the basal shear stress causes the sliding of the upper mass — here, the velocity profile is similar to the fluidized flow regimes in Figure 24b and Figure 24c on page 75. This way, the material behavior only needs to be known at the bottom.

Figure 26 on page 81 describes the set of stresses acting in a finite volume element of the avalanche close to the bed surface and their relations. The volume suffers pressure forces from all sides and develops shear tensions internally and externally. The normal stresses represent pressure forces due to the overburden weight of the snow above and along the path. The shear stresses come from the shear traction exerted on the sliding surfaces. Considering the local coordinate system — where x points in the slope direction, z points in the bed surface's normal direction, and y in the traverse direction — the SH model assumes that traverse sharing is negligible[13], so only shearing at the xz plane is considered ; see Figure 26a. Therefore the important stresses are the normal stresses, p_{zz} and p_{xx}, and the shear stresses τ_{xz}.

[13] Such assumption implies that p_{yy} is a principal stress.

Figure 26 – These figures show the normal and shear stresses acting in the thin basal layer of the avalanche, as assumed by the SH model. The Mohr–circle diagram relates the stress states with the acting stresses through the bed friction angle and the internal angle of friction.

(a) A volume element located at the base of the avalanche is depicted in local coordinates — x in the velocity direction and z perpendicular to the bed. The principal stresses lie in the xy plane, as traverse shearing is small and omitted. p_{yy} and p_{xx} are normal stresses and work as pressure forces due to the snow weight, and τ_{xz} are the shear stresses due to shear traction caused by sliding.

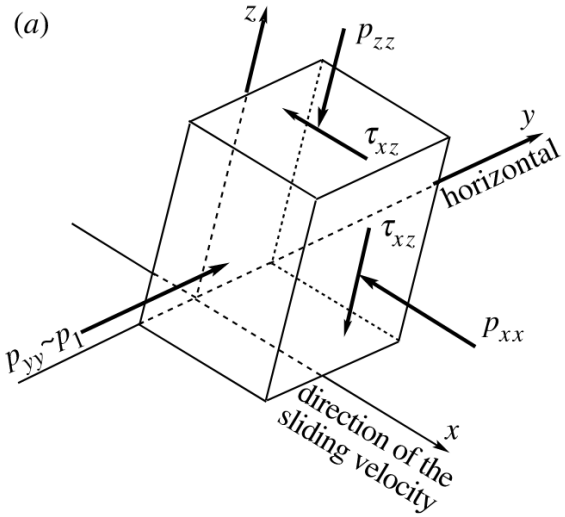

Source: Hutter, Wang and Pudasaini (2005).

(b) The figure shows a representation of the active/passive stress states. The dashed Mohr circle is the active state, while the other is the passive state. The internal friction angle ϕ bounds both circles, and the bed friction angle δ determines the transition points $(p_{zz}, \pm\tau_{xz})$ between states and, therefore, all other points.

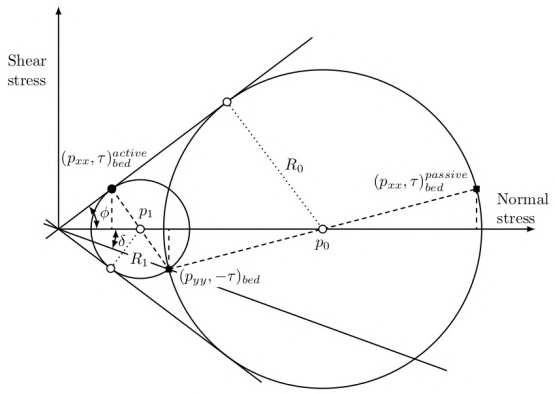

Source: Christian Kröner (2014).

The two friction angles, δ and ϕ, listed above define the constitutive behavior by prescribing the passive and active stress states $\lambda_{\pm}$. In the shear-normal stress space (p,τ), the internal friction angle ϕ bounds the possible values of shear and normal stresses by lines $\tau = \pm p\tan\phi$. The Mohr-Coulomb yield criterion defines the principal stress points for which the material transits between the active λ_+ and the passive λ_- states. The transition points are points $(p_{zz}, \pm\tau_{xz})$ and lie in lines $\tau = \pm p\tan\delta$, as shown in Figure 26b on page 81. In the figure, the two circles, called *Mohr circles*, represent the two active/passive states. The Mohr circle is a visual tool that shows the stress states of material in the (p,τ) space; the principal stresses are two diametrally opposed points on the circle — maximum normal stresses are reached when rotating the circle, so both points lie in the p–axis, and maximum shear appears on the vertical poles (notice that points $(p_{xx}, \pm\tau_{xy})$ could be obtained by rotating the circles 180^o). The SH model assumes p_{yy} equal to one of the four points depicted in the figure. Lastly, the basal normal stresses are related by earth-pressure coefficient $\lambda_{\pm}$ as $p_{xx} = \lambda_{\pm} p_{zz}$ and $p_{yy} = \lambda_{\pm} p_{zz}$.

In sum, the SH model considers an incompressible, cohesionless granular material for a dense-snow avalanche sliding down an inclined slope with small curvatures. The shallowness assumptions allow the use of depth integration along with Rankine's earth-pressure (similar to the VS model) controlled by the Mohr-Coulomb yield criterion, which classifies the SH model

as a hydraulic model. The one-dimensional equations for conservation of mass and momentum with local coordinates from Savage and Hutter (1991) are:

$$\frac{\partial h}{\partial t} + \frac{\partial}{\partial x}(\bar{u}h) = 0, \tag{3.9}$$

$$\frac{\partial h\bar{u}}{\partial t} + \frac{\partial (h\bar{u}^2)}{\partial x} = hS - \frac{\partial}{\partial x}(\frac{1}{2}\beta h^2), \tag{3.10}$$

where the terms $S(x,t)$ and $\beta(\phi,\delta)$ include the stress relations mentioned above and are described in detail in section 4.2 in Chapter 4. The term S relates to the gravitational acceleration taking into account the curvature of the terrain and momentum correction due to the drag caused by centrifugal forces. While the term $\lambda_{\pm}$ in Equation 3.5 on page 73 depends only on the internal friction angle ϕ, the term β is defined in terms of the friction angles ϕ and δ. The SH model is the first to define the earth pressure by both ϕ and δ for a granular material in an avalanche model (Christian Kröner, 2014). According to experimental data, Hutter, Wang and Pudasaini (2005) suggests the range of values for ϕ and δ are

$$30^o < \phi < 40^o, \quad 13^o < \delta < 22^o.$$

Like other models, the SH model received improvements and extensions over the years. The extension to curvilinear coordinates was expanded and tested by Hutter and Koch (1991) and Greve and Hutter (1993), which added small changes to the friction terms of the equations. Greve, Koch and Hutter (1994) and Koch, Greve and Hutter (1994) successfully extended the SH model to the three-dimensional case, later extended to curved terrains by Gray, Wieland and Hutter (1999), Wieland, Gray and Hutter (1999), Pudasaini and Hutter (2003). Hungr (1995) proposed an alternative strain-dependent (rate-dependent) constitutive law for the earth-pressure coefficient used in the SH model. See Fei *et al.* (2015) for a comparison between the SH and Hungr models. Hwang and Hutter (1995) incorporated the energy balance equation by bringing the elasticity of particles during collisions and allowing variable bulk density. Also considering inelastic collisions, Takahashi and Tsujimoto (1998) included snow flocculation and temperature to model dry and wet snow avalanches. Gray, Tai and Noelle (2003) simplified the SH model with constitutive relations inspired by the MSU model (page 75), obtaining a hydraulic model with a source term and constant earth-pressure coefficient. Their simplified version was used by Viroulet *et al.* (2017) to investigate the take-off of the granular material due to bumps in the bed. Zahibo *et al.* (2010) also used a simplified version of the SH model, but to propose multiple analytical solutions for avalanche motion over different types of inclined channels. Recently, Li and Zhang (2019) used a finite volume scheme to solve the SH model equations over unstructured grids representing arbitrary terrains. Other relevant extensions and analogous models include Iverson and Denlinger (2001), Denlinger and Iverson (2004), Luca *et al.* (2009), Gray and Edwards (2014), Zhai *et al.* (2015), Rauter *et al.* (2018). In addition to snow and ice flows, the SH model has been adapted and used for other types of materials and avalanches, such as debris flows (IVERSON, 1997; MANGENEY-CASTELNAU *et al.*, 2003; IVERSON;

GEORGE, 2014; GEORGE; IVERSON, 2014), pyroclastic flows (PITMAN *et al.*, 2003; Lê; PITMAN, 2010; DOYLE; HOGG; MADER, 2011), and landslides (LIU; HE; ONYANG, 2016).

3.3.6 Slope Treatment

The hydraulic models cited earlier and others based on Saint-Venant's equations on page 72 assume small slope terrains due to the averaged velocity condition over the flow depth. However, granular flows such as landslides and dense-snow avalanches often occur on steep slopes. Under global coordinates systems, the inherent presence of vertical velocities over a steep slope makes the pressure calculation not trivial as in the SWE (NI; CAO; LIU, 2019) — the reason why models, like the SH model, end up using local coordinates or curvilinear coordinates. Nevertheless, global coordinate systems are desired for simulating geophysical flows since the terrain is typically described by Digital Elevation Models (DEMs) defined in Cartesian coordinates systems (XIA; LIANG, 2018). Tai and Kuo (2008) used a unified coordinate system from Hui, Li and Li (1999) to account for dynamic bed curvatures and general topography. Over the years, many researchers attempted to solve the issue and adapt the SWE to arbitrary terrains with steep slopes and large curvatures (BOUCHUT *et al.*, 2003; LIANG; MARCHE, 2009; JUEZ; MURILLO; GARCíA-NAVARRO, 2013; HERGARTEN; ROBL, 2015; YUAN *et al.*, 2018; DONG; LI, 2021). Solutions include using different numerical methods, such as the Smooth Particle Hydrodynamics (SPH) and Finite Volume Method (FVM) (LEVEQUE, 2002). Rodriguez-Paz and Bonet (2005) adapted the SPH for SWE over arbitrary terrains. Vacondio, Rogers and Stansby (2012) presented a variational formulation for SWE under SPH obtaining high particle resolution in small flow depths. The flexibility of FVM for unstructured grids is the reason for its success in handling arbitrary terrain surfaces. Examples of solutions for the slope treatment with the FVM are Hubbard (1999), Begnudelli and Sanders (2006), Benkhaldoun and Sead (2010), Song *et al.* (2010), Liu *et al.* (2013), Hou *et al.* (2013a), Hou *et al.* (2013b), Duran, Liang and Marche (2013), Xia and Liang (2018), Zhao *et al.* (2018), Buttinger-Kreuzhuber *et al.* (2019). Another approach is the formulation of the equations in terms of surface partial differential equations (SPDEs) (DECKELNICK; DZIUK; ELLIOTT, 2005). The FVM adaptation to element areas called the Finite Area Method (FAM) (TUKOVI; JASAK, 2012) uses SPDEs to solve differential equations over geometric surfaces, such as thin liquid films (CRASTER; MATAR, 2009), and flows over three-dimensional surfaces (RAUTER; TUKOVI, 2018). Recently, Rauter *et al.* (2018) solved the SH model with the FAM to simulate dense-snow avalanches over natural terrains.

3.3.7 Snow Entrainment

The difficulty encountered in experimental studies of bed erosion and entrainment mechanisms led researchers to use heuristic models for snow entrainment (ISSLER; PéREZ, 2011). The typical approach appeared in the 60s along with the MSU model (page 75), considering front

entrainment and gradual entrainment (EGLIT; DEMIDOV, 2005). Refer to Eglit and Demidov (2005), Eglit, Yakubenko and Zayko (2020), Grigorian and Ostroumov (2020) for Russian models of snow entrainment and Hopfinger (1983) for early entrainment models in western research. The MSU model considers entrainment in the front resulting from the impact force of the moving snow colliding with the snow cover at rest. The impact force p_i results from the encounter of the avalanche pressure forces p and the snow cover strength p_*. After the collision, if $p_* < p$, then the snow particles at rest get into motion and join the flow. The interface between the erodible snow and the flow, called *entrainment front*, advances at speed[14]:

$$u_e = \sqrt{\frac{p_i}{\rho_0(1-\rho_0/\rho_1)}}, \quad p_i = p - p_*, \tag{3.11}$$

where ρ_0 is the snow cover density, ρ_1 is the avalanche density, p_* is the compressional strength of the snow cover, and p is the avalanche full pressure; see Figure 27 on page 85. Note that the direction of u_e is not necessarily parallel to the flow velocity u, as it is perpendicular to the entrainment front. The angle of the entrainment front $\alpha(x,t)$ is called the *abrasion angle*. According to Gauer and Issler (2004), erosion and abrasion causes a deceleration of the avalanche due to momentum transfer and hit impact. The deceleration force is given by

$$f_e = \frac{\rho_0}{\rho}\frac{\eta_e u_e u}{h}, \tag{3.12}$$

where η_e is the fraction of the eroded snow that is entrained. Gauer and Issler offer typical values for medium-size dry-snow avalanches on a $\theta = 30^o$ slope: $h \approx 1\ m$, $u \approx 30\ m \cdot s^{-1}$, $\rho/\rho_0 \approx 1 \sim 2$, and $\eta_e w_e \approx 0.05 \sim 0.10\ m \cdot s^{-1}$. Other examples of erosion speed formulas can be found in Issler (2014) — such as a version based on the abrasion angle $u_e = u \tan\alpha$ and another version based in the dry coulomb friction μ coefficient and flow velocity

$$u_e = \frac{2gh(\sin\theta - \mu\cos\theta)}{u}, \tag{3.13}$$

with $u_e \approx 10^{-3} \sim 10^{-2}\ m \cdot s^{-1}$. Issler keeps the dense–flow depth h constant by considering that mass is skimmed from the top of the flow at the same rate it is eroded from bed.

The MSU entrainment equations were incorporated into the SH model extension (BARTELT; SALM; GRUBER, 1999; SARTORIS; BARTELT, 2000) by Betty Sovilla in Sovilla, Burlando and Bartelt (2006), which also borrowed the constitutive equations from the NIS model (page 74). For a small control volume in the interface with cross-sectional area $A = wh$, where $w(x,t)$ is the flow width, the entrained mass m_e and entrainment depth d_e over a time period Δt are:

$$m_e = A u_f \rho_0 \Delta t, \quad d_e = u_f \frac{\rho_0}{\rho}\Delta t. \tag{3.14}$$

The mass balance equation is then defined as:

$$\frac{\partial A}{\partial t} + \frac{\partial Q}{\partial x} = S_e - S_d, \quad S_e = u_e \frac{\rho_0}{\rho} w, \quad S_d = C_d A, \tag{3.15}$$

[14] The details about the definition of the erosion speed u_e can be found in Grigorian and Ostroumov (2020).

Figure 27 – Scheme of the avalanche front entrainment adopted by the MSU model. The entrainment front speed u_e is not necessarily parallel to the avalanche speed, as the entrainment front has an angle α.

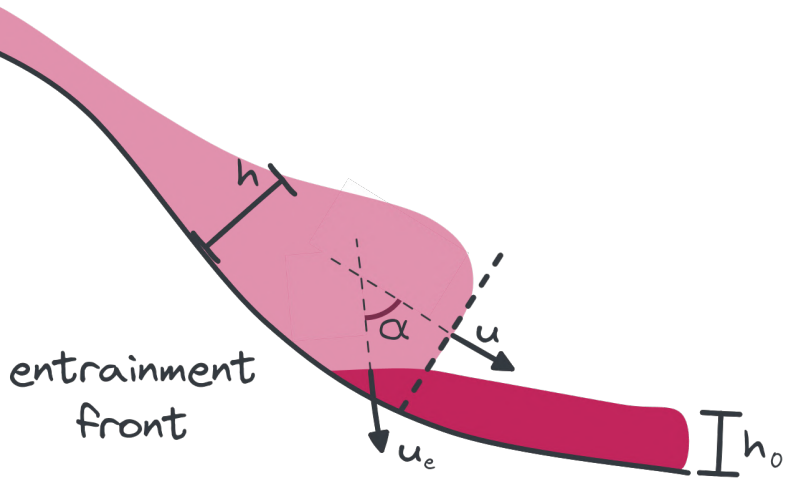

Source: Adapted from Grigorian and Ostroumov (2020).

where $C_d \in [0, 1]$ is the deposition coefficient, and S_e and S_d are the volumetric snow entrainment and deposition rates respectively. The deposition rate is considered zero if velocity is above a critical value and implementations usually consider $C_d = 1$. The term $Q = Au$ is called the *depth-averaged discharge flow*. Sovilla went further and considered multi-layered snow covers, allowing the abrasion angle to vary from layer to layer. The multilayer entrainment approach allows not only frontal plowing but also step entrainment. The collection of works of Betty Sovilla are among the most prominent and relevant studies in mass entrainment and deposition in snow avalanches (SOVILLA, 2004; SOVILLA; BURLANDO; BARTELT, 2006; SOVILLA; MARGRETH; BARTELT, 2007; LI *et al.*, 2022).

A detailed review of erosion rate formulas can be found in Iverson and Ouyang (2015), including formulas for other mass flow phenomena such as debris and pyroclastic flows (PITMAN *et al.*, 2003). Naaim *et al.* (2004) considers a thin layer, representing the entrainment front, upon which a series of forces from both sides operate. The erosion of this thin layer happens in two stages: first, the cohesion brokes up due to disintegration, and then entrainment occurs by the progressive motion of snow portions. Such an approach finds good agreement with experimental data (NAAIM *et al.*, 2013). Fischer *et al.* (2015) uses the basal shear stress τ_b to compute the entrainment rate as

$$S_e = \frac{\tau_b}{e_b} \parallel u \parallel, \tag{3.16}$$

where e_b is a parameter interpreted as specific erosion energy. Recently, Edwards *et al.* (2021) deviated from the heuristic models described above by successfully incorporating the friction coefficient from Baker, Barker and Gray (2016) to simulate erosion and deposition. For simulation validation purposes, erosion S_{er}, deposition S_d and entrainment S_e rates were quantitatively

analyzed by Li *et al.* (2022) through the following numerical measurements:

$$S_e = \frac{m_e}{A_{bed}\Delta t}, \quad S_{er} = \frac{m_{er}}{A_{bed}\Delta t}, \quad S_d = \frac{m_d}{A_{bed}\Delta t}, \tag{3.17}$$

where A_{bed} is the initial surface area of the erodible bed and m_{er}, m_e, and m_d are the eroded mass, entrained mass, and deposited mass respectively.

3.3.8 Other Models

The historical review above covered models of dense-snow avalanches considered by many researchers as the most popular in avalanche research. The relation between such models is evident; each model shares at least one aspect, and the centenary sequence of models that starts with sliding blocks in the 1920s, expanding with Voellmy's work, the VS model and its extensions, culminating along with Russian hydraulic models and the granular flow SH model represent only the main trunk of avalanche research. Therefore, this section concludes with a list of models that, although omitted above, are equally relevant.

- **Conceptual Models**

  The class of conceptual models found in-between deterministic and statistical models is investigated by Ancey, Meunier and Richard (2003). Such models use statistical and probabilistic analysis to specify coefficient parameters of deterministic models (BARBOLINI *et al.*, 2000; ANCEY; GERVASONI; MEUNIER, 2004; MEUNIER; ANCEY, 2004). The fracture mechanics theory (CORTEN, 1972) is used by Cherepanov and Esparragoza (2008) to stipulate the conditions for a fracture-entrainment regime in order to model step entrainment. The treatment of the snow avalanche as a non-Newtonian fluid was approached by Bovet, Chiaia and Preziosi (2010), Abdelrazek, Kimura and Shmizu (2014).

- **The Random Kinetic Energy Model**

  The Random Kinetic Energy model (RKE) (BARTELT; BUSER; PLATZER, 2006) describes the frictional forces acting on an avalanche from the perspective of energy production and dissipation by granular motion (BUSER; BARTELT, 2009). The RKE borrows the fluctuation-dissipation relationship of kinetic energy dissipation and the random motion of granules (LEMONS, 2003). Such an approach allows the variation of energy density (usually assumed constant) along the avalanche length, allowing more realistic modeling of entrainment and deposition (CHRISTEN; KOWALSKI; BARTELT, 2010). Valero *et al.* (2015) extended the RKE for accounting for temperature effects and thermal entrainment. A review of RKE-based models and a comparison against the classical Voellmy's friction model is provided by Issler, Jenkins and McElwaine (2018). The RKE model has been used in conjunction with the SH model equations in full — with entrainment modeling

— three-dimensional simulations of snow avalanches (FISCHER *et al.*, 2015; RAUTER; TUKOVI, 2018; RAUTER; KöHLER, 2020).

3.4 Powder-Snow Avalanche Models

Powder-snow avalanches, or airborne powder avalanches, belong to the large family of physical phenomena of particle-driven currents called gravity currents (SIMPSON, 1999). Gravity currents occur when two fluids of different densities get into motion due to gravity, promoting the intrusion and propagation of one fluid into another (UNGARISH, 2009). Gravity currents comprise a wide range of flows, from viscous magma to turbulent atmospheric currents, from heat flows inside tunnels to enormous sediment movements under the ocean. Some flows, such as katabatic winds, present minimal density ratios, while others may display more significant differences. Powder-snow avalanches are an example of complex gravity currents due to their multi-scale, non-conservative, highly-turbulent nature. Similar gravity currents include turbidity currents on ocean floors and pyroclastic flows on volcano slopes. Refer to Simpson (1999), Huppert (2006), Parsons *et al.* (2007), Ungarish (2009), Meiburg, Radhakrishnan and Nasr-Azadani (2015) for reviews on gravity current research. Particularly for powder–snow avalanches, refer to Ancey (2016).

Despite the fundamental differences between powder–snow avalanches and turbidity currents, experimental research on powder–snow avalanches has used turbidity currents as a fair analogy. Like powder–snow avalanches, turbidity currents are non-conservative, turbulent (high Reynolds number values), and particle-driven flows. Turbidity currents also present mass entrainment by deposition and suspension of particles and entrainment of ambient fluid. Early models start with the pioneering work of Bagnold (1954) on the dispersion of sediments in fluids. Turbidity currents were firstly modeled with depth-averaged equations by Plapp and Mitchell (1960). Bagnold (1962) investigated the conditions which enable a turbidity current to maintain its flow based in terms of turbulent energy. Bagnold referred this process as *auto-suspension*. Later, Pantin (1979) revisited Bagnold's work and showed that erosion and deposition of the bed material can lead to the self-acceleration of the turbidity current, for what Parker (1982) called *ignition*, but neglected entrainment of water. Refer to Wells and Dorrell (2021) for a recent detailed discussion on the relationship of turbulence and entrainment/deposition processes turbidity currents.

A crucial deviation from turbidity currents models relates to the densities of the fluids involved. Turbidity currents models (MEIBURG; RADHAKRISHNAN; NASR-AZADANI, 2015)(OUILLON; MEIBURG; SUTHERLAND, 2019) use the Boussinesq approximation (BOUSSINESQ, 1903) since the difference between sediment and water densities is sufficiently small. For powder–snow avalanches, the difference between powder–snow and air densities

invalidates the Boussinesq assumption (HOPFINGER, 1983). Non-Boussinesq[15] models for gravity currents can be found in (BIRMAN; MEIBURG, 2006; BARTHOLOMEW; LAIZET, 2019).

Since gravity current flows comprise two or more fluids with different densities, equations use indices to specify properties for each fluid, for example, densities ρ_0 and ρ_1; see Figure 28 on page 89. Typically, letters can be used instead to facilitate reading, such as a and s, standing for air and snow respectively, as in ρ_a and ρ_s. Models may use different approaches to deal with multiple fluids by considering:

- *two–phase flows* – A set of equations models the different fluid types in the flow – one balance equation for each fluid type, such as air and ice. As mentioned above, the equations use separate variables for density, velocity, and others for each fluid type. Also, such equations usually contain additional terms representing the exchange of mass and energy between fluids;
- *single–phase mixture flows* – Instead of a separate equation for each fluid type, a single set of equations models the mixture of fluids. In such an approach, some variables are combined based on the volume concentration of each fluid. For example, the final value of density becomes an interpolation of the densities of all fluids. The mixture representation reduces the number of equations drastically.

This section separate the powder–snow avalanche models into the following categories:

- *Similarity Models* – described in subsection 3.4.1 on page 89. Also called *conceptual models*, attempt to describe the flow through relations between flow quantities, such as velocity and depth, using dimensional analysis. Therefore, similarity models are more of a tool rather than a category of models since other types of models can use the same relations provided by conceptual models;
- *two–phase flows* – described in subsection 3.4.2 on page 93 and briefly introduced above;
- *single–phase mixture flows* – described in subsection 3.4.3 on page 96 and briefly introduced above.

The use of similarity theory in avalanche models refers to the use of non-dimensional numbers and variables to model the flow. The dimensional analysis produces similarity criteria to validate experiments and physical models; see section 3.2 on page 60. Also, the scaling factors allow the use of simpler models and still offer critical insights into the dynamics of such flows with large extensions in space and time (ECKART MCELWAINE JIM, 2012) —

[15] For non-Boussinesq flows, the inertia created from the density differences is not negligible since the denser fluid carries the most momentum, even with little concentrations per volume.

Figure 28 – Representation of the different densities present in a powder–snow avalanche. Particles of snow differ in density as snow is suspended and mixed with air. The snow cover contains a high density of packed particles that get compressed as the avalanche runs over it or separate into smaller clods and get incomporated into the dense flow. As turbulence and impact forces eject snow into the air, particles get mixed with air and become much less dense. Models deal with the different densities of snow by considering distinct phases or a single–phase mixture with air based on the volume concentration of particles.

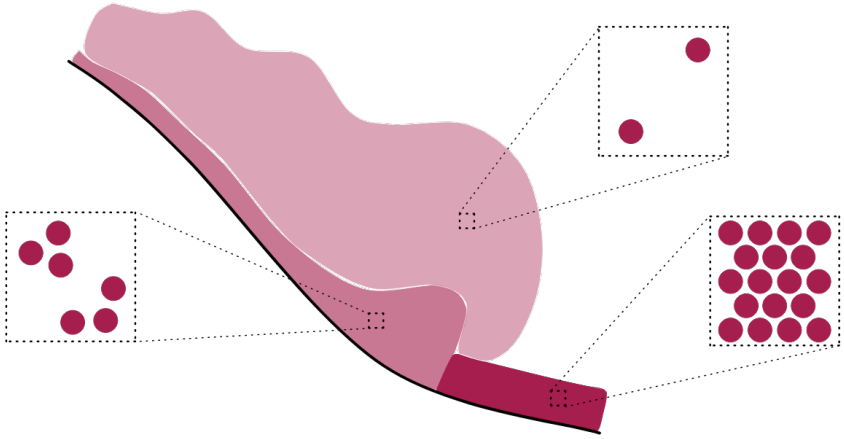

Source: Elaborated by the author.

turbidity currents, for example, can cover distances of thousands of kilometers and last for days (MOSHER *et al.*, 2017). Rottman and Linden (2002) discusses the use of dimensional analysis in gravity current models.

3.4.1 Similarity Models

The first quantitative study — towards a mathematical model — of gravity currents is attributed to von Kármán in 1940 (KARMAN, 1940); his studies of dense gas cloud propagation suggested that the velocity of the nose u_f is given by

$$\frac{u_f}{\sqrt{g'h}} = \sqrt{\frac{2}{\Delta_\rho}} = Fr, \tag{3.18}$$

where h is the front depth, $g' = \Delta_\rho g/\rho_1$ is the reduced gravity acceleration (recall the density ratio Δ_ρ from page 63), and Fr is the Froude number, related to the densimetric Froude number in page 64. Later, Benjamin (1968) revised the formulation, considering the ambient fluid's height H, see Figure 29 on page 90, and obtained the following equation:

$$\frac{u_f}{\sqrt{g'h}} = \sqrt{\frac{\alpha(1-\alpha)(2-\alpha)}{\Delta_\rho(1+\alpha)}} = Fr_H, \tag{3.19}$$

where $\alpha = h/H$ is the fractional height. Note that the Froude number is related to Benjamin's Froude number by $Fr = Fr_H \alpha^{-1/2}$. Benjamin's work is considered the base of the theory of inviscid gravity currents and has been used for gravity currents propagating with a high Reynolds

number (HUPPERT, 2006). The formulation of the Froude number as a function of height was later extended to Boussinesq flows by Borden and Meiburg (2013) and non-Boussinesq flows by Konopliv *et al.* (2016) with the relations

$$Fr_H = \sqrt{2\alpha}(1-\alpha), \text{ and } Fr_H = \sqrt{\frac{2\alpha}{\Delta_\rho}}(1-\alpha), \tag{3.20}$$

respectively. Gröbelbauer, Fanneløp and Britter (1993) proposed a correction of the reduced gravity term for higher density ratios

$$g' = g\frac{\rho_1 - \rho_0}{\rho_1 + \rho_0}. \tag{3.21}$$

Figure 29 – Visual representation of the gravity flow lock–exchange experiment considered by Benjamin: A channel with finite depth H filled with a light density fluid with density ρ_0. A gravity current of head height h advances with velocity u_f as the heavier fluid of density ρ_1 is released and moves due to the hydrostatic pressure difference.

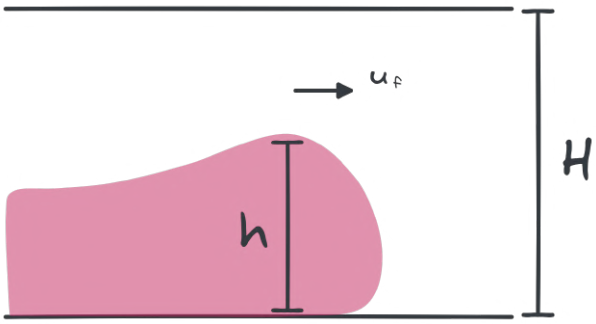

Source: Elaborated by the author.

The Froude number has also been used to determine cloud formation in powder–snow avalanches. Early studies suggest that suspension occurs due to a combination of kinematic-dynamic shocks and weak intergranular bounds (HOPFINGER, 1983). After achieving a velocity of 10 m/s and the Froude number $Fr > 2$, roll-wave formation occur. The wavelength λ of roll waves is estimated by Brock (1967) as

$$\frac{\sin\theta\lambda}{Fr^2 h} \sim 0.2 - 0.5. \tag{3.22}$$

The mechanisms of formation and dynamics of cloud lobe structures in gravity currents are the center of the study of plume theories (MORTON; TAYLOR; TURNER, 1956; ELLISON; TURNER, 1959; TURNER, 1973). Tochon-Danguy and Hopfinger (1975), Hopfinger and Tochon-Danguy (1977) extended the theory to powder–snow avalanches. Following the posterior formulation of Britter and Linden (1980), the front velocity is dependent only on the buoyancy flux $g'Q$ and defines the non-dimensional front velocity $\tilde{u}_f$ as

$$\tilde{u}_f = \frac{u_f}{(g'Q)^{\frac{1}{3}}}, \tag{3.23}$$

where $Q = u_f h_e$ is the volume flow rate of supply and h_e is the height of entrained snow cover. The plume theory for an inclined plume defines the mass continuity equation:

$$\frac{d(\bar{u}h)}{dx} = \alpha\bar{u}, \tag{3.24}$$

where $\bar{u}(x,t)$ is the mean velocity in the slope direction x and α is the air-entrainment coefficient. For steady flows, the following relation is obtained through integration

$$h = \alpha\bar{u}(t - t_0), \tag{3.25}$$

where t_0 is the start time with $h(t_0) = 0$. A semi-ellipses represent the plume with volume evolution of

$$V = E\bar{u}^3(t - t_0)^3, \quad E = \frac{\pi\alpha^2}{2}, \tag{3.26}$$

where E is the effective air-entrainment coefficient; see Figure 30 on page 91. Later, Parker, Fukushima and Pantin (1986) generalized the entrainment process from Ellison and Turner (1959) to build a system of depth-averaged equations that takes into account both sediment and water entrainment in turbidity current flows. Stacey and Bowen (1988) considered the vertical structure of the flow by studying the relations between the Richardson number and the settling velocities of suspended particles. Baines (2001) provided an extended model, along with laboratory experiments, considering the mixing process due to entrainment in gravity currents flowing down slopes. Such models consider the powder–snow avalanches similarly to other gravity current flows, particularly turbidity currents. These models can handle the multi-scale nature of gravity flows through dimensional analysis. Despite their success, internal flow properties, such as velocity profiles and turbulent motion, are often omitted or approximated by coefficient terms.

Figure 30 – Similarity models usually model the powder–snow avalanche as a geometrical shape — as the half-ellipse. The equations describe the movement of the ellipses based on the center of mass. The growth due to air entrainment is calculated through the ellipse perimeter..

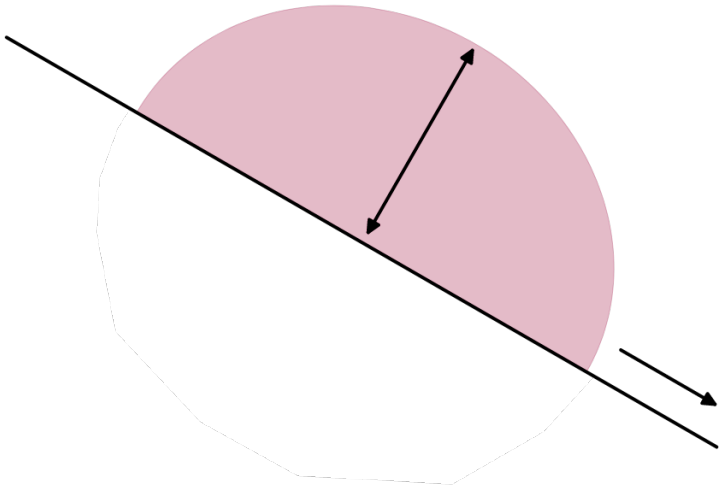

Source: Elaborated by the author.

The Kulikovskii–Sveshnikova model (KULIKOVSKII; SVESHNIKOVA, 1977), the KS model, steps forward by considering the flow as a turbulent flow of a material in suspension. The KS model includes a volume change equation and momentum conservation equations considering the kinetic energy generated from turbulence. For a two–dimensional semi-elliptic cross-section powder–snow avalanche, the KS model system of balance equations is:

$$\frac{dA_e}{dt} = \frac{P_e u_a}{2}, \tag{3.27}$$

$$\frac{d\tilde{m}}{dt} = \rho_a \dot{A}_e + \dot{\tilde{m}}_e + \dot{\tilde{m}}_d, \tag{3.28}$$

$$\frac{d(\tilde{m}u)}{dt} = \tilde{m}g\sin\theta - \rho k 2 L u^2 - \frac{c_x \rho_a H u^2}{2} - \dot{\tilde{m}}_d u, \tag{3.29}$$

$$\frac{d}{dt}\left(\frac{\partial K}{\partial \dot{H}}\right) - \frac{\partial K}{\partial H} = Q + \xi \dot{u}_a. \tag{3.30}$$

Equation 3.27 describes the change of volume due to turbulent mixing of surrounding air; A_e is the area of the semi-elliptic shape representing the cloud volume, P_e is the perimeter, and u_e the velocity of air-entrainment. Equation 3.28 represents the change of mass per unit length, $\tilde{m}$; ρ_a is the air density and the right hand side terms are respectively the entrainment of air, snow entrainment, and snow deposition. Equation 3.29 is the change of momentum defined by the gravitational acceleration, the turbulent friction, the air resistance and snow deposition; $\rho = \tilde{m}/A_e$ is the average density of the snow-air mass, c_x is the coefficient of aerodynamic resistance of the cloud, and L_e and H_e are the horizontal and vertical semi-axis of the ellipse; see Figure 30 on page 91. The last equation, Equation 3.30, relates to the internal motion in the cloud; K is the kinetic energy, Q is the generalized force, and ξ is the turbulent diffusion coefficient. Refer to Bozhinskiy, Losev and Bartelt (1998), Ancey (2001), Eglit and Demidov (2005), Eglit, Yakubenko and Zayko (2020) for comparisons and discussions on the KS model.

The KS model received many adaptations and extensions over the years. Beghin (1979), Beghin and Brugnot (1983) simplified the model by discarding entrainment and reduced the system to only one differential equation. Beghin, Hopfinger and Britter (1981) introduced the dependence of the slope angle into the growth rate of the cloud and ignored Equation 3.30 in order to model Boussinesq clouds. Decades later, Ancey (2004) combined the KS model with the simplifications introduced by Beghin, calling the extension the KSB model. Ancey used the KSB model to simulate powder–snow avalanches by adapting the KSB model to non-Boussinesq clouds and algo including an entrainment function dependent to the Richardson number[16] Ri:

$$\frac{dV}{dt} = \alpha_v \sqrt{V} u, \quad \alpha_v = \begin{cases} e^{-1.6Ri^2} & Ri \leq 1, \\ 0.2/Ri & Ri > 1, \end{cases} \tag{3.31}$$

[16] Smaller Richardson number values imply greater instabilities and therefore higher entrainment rate (ANCEY, 2016).

where α_v relates to the entrainment coefficient. Turnbull, McElwaine and Ancey (2007) further improved the KSB model by including the entrainment of snow in the volume equation to better predict densities with an extra term in

$$\frac{dV}{dt} = \alpha_v \sqrt{V} u + u_f h_e, \tag{3.32}$$

where h_e is the depth of entrained snow cover. In parallel, Parker, Fukushima and Pantin (1986) incorporated the turbulence and entrainment terms into plume theories to model turbidity currents. However, the methods of turbidity currents assume that water and sediment entrainment at the current upstream end (tail) is continuous. This assumption does not hold for powder–snow avalanches (FUKUSHIMA; PARKER, 1984). The discontinuity was handled by Fukushima and Parker (1990), that added the conservation of kinetic energy of turbulence and entrainment of snow and air, as previously mentioned, to simulate powder–snow avalanches. Their depth-averaged method was based on the important work of Fukushima (1986), which also considers the shape of the avalanche to be a cylinder of half-elliptic section and assumes the avalanche does not show significant transverse spreading. An extension of the model for arbitrary three–dimensional terrains was later proposed by Fukushima and Hayakawa (1993). The method was later applied to model the flow of suspension thermals by Akiyama and Ura (1999), Fukushima, Hagihara and Sakamoto (2000). Turnbull and Bartelt (2003) used Parker's model to study the exchange of mass due to entrainment and deposition in powder–snow avalanches. Rastello and Hopfinger (2004) included snow entrainment by proposing the rate of particle suspension as a function of the shear stress and particle Reynolds number.

All models so far model the powder–snow avalanche as a finite volume of a homogeneous turbulent suspension of ice particles. The simplified representations in similarity models, including the KSB model and its ramifications, use geometrical shapes — such as the half-ellipse — to describe the avalanche cloud. Also, such models are restricted to steady flows or only certain avalanche regimes (usually the flow regime). However, most real powder–snow avalanches contain dynamic layers of variable density. In particular, the front region and the layer close to the bed surface present much greater densities than the rarefied snow–air cloud.

3.4.2 Two-Phase Models

The class of models, called *two-phase*, *two-layer* or *mixed avalanche* models, treats the flows of the powder cloud (PSL) and dense snow (DSL) layers separately and models the intricate mechanisms of mass exchange between them — although the term two–phase[17] is usually applied to models that split the PSL into two phases, a phase for air and the other for ice.

[17] The term two–phase has a broader meaning in fluid mechanics, such as the characterization of two or more fluids with a defined interface between them. However, some avalanche models consider the mixture of fluids with no separating interface. Refer to (PROSPERETTI; TRYGGVASON, 2007) for a formal definition of multiphase flows. In this text, the terms two–phase and two–layer should clarify the distinction.

Figure 31 on page 94 depicts the general scheme of mixed snow avalanches adopted by such models; besides air, labeled by the letter a, the numbers 0, 1, and 2 label the snow cover, the dense core, and the powder cloud layers, respectively. Each layer i has density ρ_i, velocity u_i and height (depth) h_i.

Figure 31 – Representation of a multi–layered scheme of powder–snow avalanches utilized by mixed avalanche models. The snow cover has height h_0, density ρ_0, and no velocity. The only term related to air is its density ρ_a. The other layers, 1 and 2, representing the dense snow core and the powder–snow cloud, respectively, have heights h_i, densities ρ_i, and velocities u_i. A different set of equations models each avalanche layer, 1 and 2, and additional terms describe the mass and momentum exchange between both layers and include the role of air and snow cover as entrainment sources.

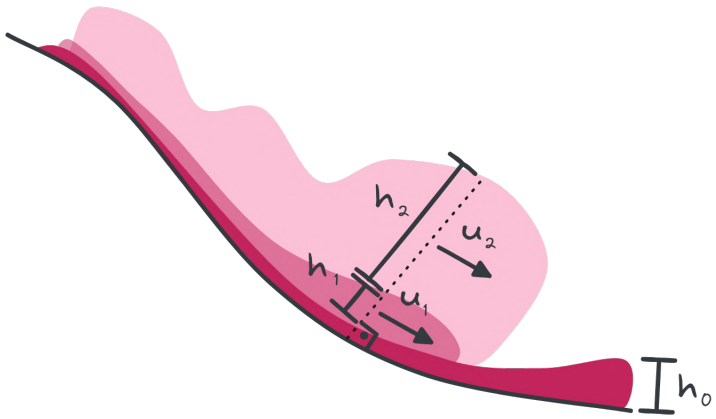

Source: Adapted from Nazarov (1991).

Early two-layer Russian models (EGLIT, 1983; NAZAROV, 1991), reviewed by Eglit (1998a), Eglit, Yakubenko and Zayko (2020), use five balance equations for the PSL and DSL and a set of variables to control mass exchange between layers. For instance, the respective continuity equations for the PSL and DSL flows are:

$$\frac{\partial h_2}{\partial t} + \frac{\partial h_2 u_2}{\partial x} = V_{2a} + V_{21} - V_s, \tag{3.33}$$

$$\frac{\partial h_1}{\partial t} + \frac{\partial h_1 u_1}{\partial x} = -V_{21} + V_{10} + V_s, \tag{3.34}$$

where $V_{i \leftarrow j}$ are rates of change in height due to transport of mass from layer j towards layer i; V_{2a} is the effect of air entrainment in the powder cloud layer, V_{21} and V_{10} are for snow entrainment into the PSL and DSL, and V_s is for snow sedimentation/deposition. The consumption of the snow cover due to entrainment is then given by

$$\frac{\partial h_0}{\partial t} = -V_{10}. \tag{3.35}$$

The terms V_{ij} are defined as

$$V_{2a} = m_a u_2 \rho^*_{2a}, \tag{3.36a}$$

$$V_{21} = m_{12} |u_2 - u_1| \rho^*_{21}, \tag{3.36b}$$

$$V_{10} = m_{01}|u_1|\rho^*_{10}, \tag{3.36c}$$

$$\rho^*_{ij} = \frac{\sqrt{\rho_i \rho_j}}{\rho_i + \rho_j}, \tag{3.36d}$$

where m_a and m_{ij} are empirical coefficients. Equations 3.36a to 3.36c mean that the rate of growth depends on the velocity difference and a combination of densities of the layers. Equations 3.36b and 3.36c work only for $h_1 > 0$ and $h_0 > 0$, respectively. The complete set of equations also include conditions for $h_j = 0$ and $x > x_f$, where x_f is the leading front of the DSL position. The momentum equations for each layer also use terms τ_{ij} to represent friction forces between layers; see Eglit (1998a).

Another approach uses the differential equations of continuum mechanics with the addition of terms of exchange of mass and momentum between phases. Scheiwiller (1986) considers the mixture of two incompressible fluids, air and powder snow cloud, occupying fractions of volume[18] $c(x,t)_i$, so density is given by

$$\rho_i = c_i \hat{\rho}_i, \quad \sum_i c_i = 1, \tag{3.37}$$

where $\hat{\rho}_i$ is the material density of phase i. Scheiwiller starts from the balance equations

$$\frac{\partial \rho_i}{\partial t} + \nabla \cdot (\rho_i \mathbf{u}_i) = 0, \tag{3.38}$$

$$\frac{\partial \rho_i \mathbf{u}_i}{\partial t} + \nabla \cdot (\rho_i \mathbf{u}_i \otimes \mathbf{u}_i) = \nabla \cdot \tau_i + \rho_i f_i + M_i, \tag{3.39}$$

$$\sum_i M_i = 0, \tag{3.40}$$

where M_i is the momentum transferred to phase i, τ_i is the Cauchy stress tensor of phase i, and f_i is the body force of phase i. Equation 3.40 dictates that no momentum is produced by transfer processes and Equation 3.38 implies ρ_i constant. Also, due to incompressibility, pressure p can be separated from the constitutive equations and the stress tensor becomes

$$\tau_i = -c_i p I + t_i, \tag{3.41}$$

where the deviatoric tensor t_i is given by a constitutive relation. Equations 3.38 and 3.39 can be rewritten as

$$\frac{\partial c_i}{\partial t} + \nabla \cdot (c_i \mathbf{u}_i) = 0, \tag{3.42}$$

$$\frac{\partial c_i \mathbf{u}_i}{\partial t} + \nabla \cdot (c_i \mathbf{u}_i \otimes \mathbf{u}_i) = \nabla \cdot \gamma_i + c_i f_i + \frac{M_i}{\hat{\rho}_i}, \tag{3.43}$$

where γ_i accounts for stresses. Scheiwiller also includes eddy viscosity and laminar viscosity into the stress tensor in order to account for turbulence by using the so–called k–ε–model

[18] The particle volume fraction c_p in a two–phase flow is the ratio between the part of the volume V_p that contains the particles of one phase and the volume V itself, i.e., $c_p = \lim_{V \to 0} V_p/V$ (ZWINGER; KLUWICK; SAMPL, 2003).

(LAUNDER; SPALDING, 1974). For a complete formulation and details refer to Issler *et al.* (2000). Naaim (1995) compared the model simulation to experimental data. Later, Naaim and Gurer (1998) modified the model to account for turbulence reduction induced by particles using the turbulence model of Chen and Wood (1985). Romanova (2017) used a similar model, which considered two-phase with the k-e model, using the Herschel-Balkley fluid model (KERN; TIEFENBACHER; MCELWAINE, 2004) to describe the constitutive relations of snow.

Recently, LEPERA (2020) proposed a complete system of equations for a two-phase model of powder-snow avalanches. The model includes thermodynamic balance equations and treats the energy transfer between phases. The equations come from granular flow models and split the stress tensor into a collisional and a frictional part. See Andreotti, Forterre and Pouliquen (2013) for details on the theory used in the model.

3.4.3 Single-Phase Mixture Models

The Continuum Mixture Theory (CMT) (ATKIN; CRAINE, 1976), briefly described in section A.1, models the mixture of fluids by considering the superposition of multiple single continua that represent the mixing fluids (constituents). Particles of all participating fluids (phases) can occupy the volume simultaneously. The occupancy of particles represented by fractions of volume becomes a central concept and determines the mass of constituents present in a particular volume.

The model of Scheiwiller, previously described on page 95, use the exact same concept. The final density given by Equation 3.37 receives the name of mixture density in the CMT context, and the same may apply to any other variable. Therefore, by assuming a mixture velocity, for example, the number of momentum equations can be reduced to one instead of using a separate equation for each constituent. One example of such an approach is the model of Dutykh, Acary-Robert and Bresch (2009), which restricted both phases to share the same velocity $\mathbf{u}$ and defined the mixture density ρ and dynamic viscosity μ as

$$\rho = c\rho_s + (1-c)\rho_a, \quad \mu = c\rho_s\nu_s + (1-c)\rho_a\nu_a = \mu_0 + \bar{\nu}\rho, \tag{3.44}$$

where $c = c_s$ is the volumetric concentration of snow particles in the cloud, the coefficients ν_i are the kinematic viscosities of air and snow, and μ_0 and $\bar{\nu}$ are

$$\mu_0 = \frac{\nu_a\rho_a\rho_s - \nu_s\rho_s\rho_a}{\rho_s - \rho_a}, \quad \bar{\nu} = \frac{\nu_s\rho_s - \nu_a\rho_a}{\rho_s - \rho_a}. \tag{3.45}$$

Fick's law dictates that the mixing of fluids follows a quasi-compressible constitutive equation

$$\nabla\cdot\mathbf{u} = -\nabla\cdot(\kappa\nabla\log\rho), \tag{3.46}$$

where κ is a coefficient related to the kinematic viscosity. In other words, the equation above accounts for diffusive effects between the consituents (phases) due to density differences. From

Equation 3.46, Dutykh, Acary-Robert and Bresch (2011) rewrites the equations into an incompressible system following the approach of Kazhikhov and Smagulov (1977) and using a new variable for velocity

$$\mathbf{v} = \mathbf{u} + \kappa \nabla \log \rho, \tag{3.47}$$

referred as *the fluid volume velocity*, and taking $\kappa = 2\bar{\nu}$ constant. The new system of equations is

$$\nabla \cdot \mathbf{v} = 0, \tag{3.48}$$

$$\frac{\partial \rho}{\partial t} + \mathbf{v} \cdot \nabla \rho = 2\bar{\nu}\Delta\rho, \tag{3.49}$$

$$\rho \frac{\partial \mathbf{v}}{\partial t} + \rho(\mathbf{v} \cdot \nabla)\mathbf{v} = -\nabla\pi - 2\bar{\nu}^t \nabla\mathbf{v}\nabla p + 2\bar{\nu}\nabla\rho\nabla\mathbf{v} + \rho\mathbf{g} + \nabla \cdot (2\mu\mathbb{D}(\mathbf{v})), \tag{3.50}$$

where $\mathbb{D}(\mathbf{v})$ is the strain rate tensor

$$\mathbb{D}(\mathbf{v}) = \frac{1}{2}(\nabla\mathbf{v} + (\nabla\mathbf{v})^T), \tag{3.51}$$

the gravitational acceleration is projected into local coordinates $\mathbf{g} = (g\sin\theta, -g\cos\theta)$, and $\pi(x,t) = p + 4\bar{\nu}\mu_0\Delta\log\rho$ is the pressure term. Notice that when $\kappa = 0$, the whole system falls back to the classical Navier-Stokes equations for incompressible fluids in u. A detailed analysis on the numerical methods and the model can be found in Calgaro, Creusé and Goudon (2015). An approximation of the mixture model to powder-snow avalanches assuming the Boussinesq regime was presented by Étienne, Saramito and Hopfinger (2004). Recently, Gurjar (2023) proposed a 2D framework extending the work of Bartelt *et al.* (2016) for the DSL and combined with the mixture modeled by Fick's law by Dutykh, Acary-Robert and Bresch (2011) mentioned above.

Some models extend dense-snow avalanche models to support the formation of the powder–snow cloud on top of the dense flow layer by coupling two separate models. For example, Bartelt, Kern and Christen (2000) uses the VS model (see page 73) to simulate the dense core but includes a term for suspension in the mass conservation equation to feed the PSL. A simplification of Parker, Fukushima and Pantin (1986) models the PSL, and the suspension term enters as a mass entrainment term in the equations. In turn, Zwinger, Kluwick and Sampl (2003) uses a modified version of the SH model (see page 82) — imposing another condition to the normal stress at the bottom — and a modification of the k–ε turbulence model for the powder–snow layer. The momentum balance is similar to Equation 3.39 on page 95, but as in the single mixture model, the particle volume fraction defines the mixture density, and the velocity is the same for both phases:

$$\frac{\partial \rho\mathbf{u}}{\partial t} + \nabla \cdot (\rho\mathbf{u} \otimes \mathbf{u}) = -\nabla \cdot p + \nabla \cdot \bar{\tau} + \nabla \cdot \tau^{Rey} + \rho\mathbf{g}, \tag{3.52}$$

where pressure and stress are split, as mentioned earlier with equation Equation 3.41, p is the static pressure. The stress tensor is also decomposed into mean values of the viscous stress $\bar{\tau}$,

and the turbulent Reynolds stresses τ^{Rey} defined as

$$\tau_{ij}^{Rey} = \mu_{tur} \cdot \left(\frac{\partial u_i}{\partial x_j} + \frac{\partial u_j}{\partial x_i} \right) - \frac{2}{3} \left(\mu_{tur} \frac{\partial u_k}{\partial x_k} + \rho k \right) \delta_{ij}, \tag{3.53}$$

$$\mu_{tur} = C_\mu \rho \frac{k^2}{\varepsilon}, \tag{3.54a}$$

where C_μ is a constant with value 0.09, δ_{ij} is the Kronecker delta function, k is related to the turbulent kinetic energy and ε to its dissipation — both variables also receive balance equations. The transfer of mass and momentum between the DSL and the PSL occurs in a thin region close to the lower bounding surface of the PSL, referred to by Zwinger et al. as the *re-suspension* layer — later named *transition layer* by Sampl and Granig (2009). The model of the transition layer is a set of boundary conditions rather than another flow layer. Such boundary conditions consider the DSL upper surface as a solid wall, and the turbulent particle volume flux at the wall j_{wall} is

$$j_{wall} = -\frac{\tau_{wall}}{\rho} \frac{1}{Sc_{tur}} \frac{\Delta c}{\Delta \mathbf{u}}, \tag{3.55}$$

where τ_{wall} is the local wall shear stress, $\Delta \mathbf{u}$ is the mean velocity difference based on the wall distance and the von Kármán constant, Δc is the volume concentration difference also based on wall distance and density, and Sc_{tur} is the turbulent Schmidt number. A brief introduction and application of the model can be found in Sampl and Zwinger (2004).

3.4.4 Entrainment

Snow entrainment and deposition play a central role in powder–snow avalanches. The roll motion of large structures causes air entrainment, which increases the volume of the cloud. In the front, the transfer of momentum due to air entrainment results in significant drag (ÉTIENNE; SARAMITO; HOPFINGER, 2004) — the cause of turbulence and suspension of snow from lower layers. In turn, snow entrainment from turbulent suspension and snow cover disintegration due to front impact is crucial to momentum transport. Deposition, on the other hand, settles down snow and dissipates energy.

Issler (1998) considers a lower saltation layer, labeled 12 following Nazarov's scheme in Figure 31 on page 94, responsible for the mass exchange in the powder–snow avalanche. The depth of the saltation layer h_{12} is given by

$$h_{12} = \beta_0^2 \frac{u_{12}^2}{2g'} \tag{3.56}$$

where $g' = g \cos\theta$, $\beta_0 = O(0.1)$ is a constant extracted from experimental data, and U is the velocity of the layer. The balance of mass for the saltation layer is governed by the rates of erosion Q_{erod}, sedimentation Q_{sed}, suspension Q_{susp}, and settling Q_{sett}:

$$\frac{\partial (h_{12}\rho_{12})}{\partial t} + \nabla \cdot (h_{12}\rho_{12}u_{12}) = Q_{erod} - Q_{sed} - Q_{susp} + Q_{sett}, \tag{3.57}$$

where $\rho_{12} = 20 \sim 50\ kg/m^3$ is the density of the saltation layer. Issler describes the mass exchange as a cycle between the suspension and saltation layers represented by particle concentrations from both layers. Such cyclic movement comes from the circling motion caused by turbulent eddies; particles keep getting ejected and settled in the saltation layer — see Figure 32 on page 99. The exchange rate terms in the right hand side are constructed from a series of constants based on the k–ε turbulent model (used in the suspension layer) — see Issler (1998) for details. A similar approach is taken by Bartelt, Kern and Christen (2000), mentioned in the end of the last section, but considering both the saltation and dense–snow layers the same. Updates including temperature changes and energy flux calculations were presented by Bartelt *et al.* (2016) and Bartelt *et al.* (2018).

Figure 32 – Representation of mass exchange between the avalanche layers employed by Issler. The turbulent eddies, represented by the circle arrows, move snow up and down through suspension and settlement through denser regions. The four processes, erosion, deposition, suspension and settling, are represented by the vertical arrows in the figure.

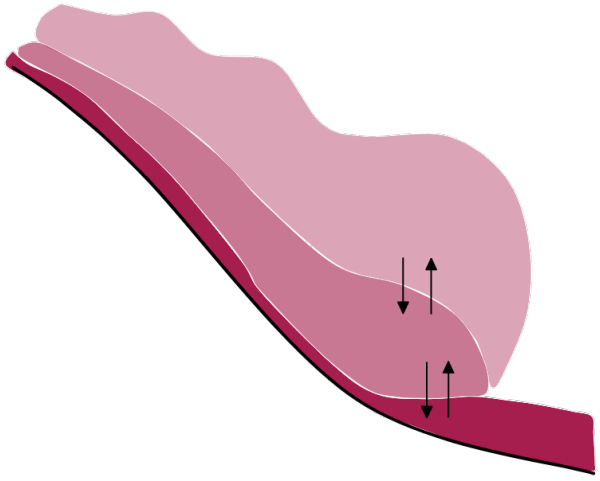

Source: Adapted from Issler (1998).

The experiments on the suspension of currents from localized front blow-out of particles performed by Carroll, Turnbull and Louge (2012) and the works of Louge, Carroll and Turnbull (2011) and Carroll, Louge and Turnbull (2013) form a detailed model for snow avalanche front dynamics. In particular, the mass flow rate of snow emerging from the front is given by

$$\frac{dm}{dt} = \rho_0(\lambda h_0 \cos\theta W)u, \tag{3.58}$$

where ρ_0 is the snow cover density, λ is the fraction of the fluidized depth that is scoured, λh_0 is the entrained depth, and W is the width of the frontal region.

Recently, Ivanova *et al.* (2021) proposed a depth-averaged model with turbulence applied to powder–snow avalanches simulations. The model splits the velocity along the depth $u = U + u'$ into mean velocity U and fluctuation velocity u' components. The mass balance for the depth-

averaged model due to entrainment is

$$\frac{\partial \hat{h}}{\partial t} + \frac{\partial (\hat{h}U)}{\partial x} = S_e + S_a, \tag{3.59}$$

where $\hat{h}$ is the cloud height with entrainment (the model distinguishes the cloud height without air entrainment h, and with air entrainment $\hat{h}$), S_e and S_a are the snow and air entrainment souce terms, respectively. The air entrainment, caused by turbulence, is described as

$$S_a = \begin{cases} (\alpha_U U + \alpha_T \sqrt{\langle u'^2 \rangle}) \frac{\hat{\rho}}{\rho}, & \hat{\rho} > 2\rho_a, U > 0 \\ 0, & otherwise, \end{cases} \tag{3.60}$$

where $\langle u'^2 \rangle = \frac{1}{h} \int_0^h u'^2 dz$ is the variance of velocity fluctuations representing the turbulent kinetic energy, $\alpha_U \in [0,1]$ is the steady entrainment coefficient, $\alpha_T \in [0,1]$ is the turbulent entrainment coefficient, and $\hat{\rho}$ is the mean density of the cloud and follows the relationship $\rho h = \hat{\rho}\hat{h}$. The snow entrainment follows an alternative approach by defining an oscillatory injection velocity $U_e(x,t)$ based on a Gaussian pulse of half-length L_0 and amplitude A_0,

$$U_e = A_0 \exp\left[-\frac{(x - x_0 - S_0 t)^2}{2 \cdot L_0^2} \right], \tag{3.61}$$

where S_0 is the propagation velocity of the pulse and x_0 is the starting position of core at time $t = 0$. The suggested values for the densities are $\rho = 7\ kg/m^3$ and $\rho_0 = 10\ kg/m^3$. The final snow entrainment term is given by

$$S_e = \frac{\rho}{\rho_0} U_e. \tag{3.62}$$

3.5 Numerical Methods

This section describes some of the different numerical approaches used to solve the mathematical models described in this chapter.

The Discrete Element Method

An example of a direct approach is the so–called Discrete Element Method (DEM), known as *molecular dynamics*. The DEM treats the avalanche body as a set of tiny volume elements called particles; recall the scale representation in Figure 21c on page 69. Simple physical laws, such as Newton's second law of motion and Euler's balance of momentum, model the motion and interactions of particles (PUDASAINI; HUTTER, 2007). The DEM has been used to compute snow fracture during the start of avalanches (GAUME *et al.*, 2014), to investigate failure behavior in weak snow (MULAK; GAUME, 2019), to compute the granular avalanche impact forces (ALBABA; LAMBERT; FAUG, 2018), to predict the internal friction of granular flows (FAVIER *et al.*, 2009), to simulate granular debris flows (ZHOU *et al.*, 2020), and to model the inter-granular bond and collision of snow particles (KABORE *et al.*, 2021). Although the DEM provides relatively more straightforward models, these models require hundreds of thousands of

elements. For large-scale 3D simulation domains, the number of elements can rise to millions of particles. In many cases, such computational effort can become a limitation. Moreover, most applications of the DEM consider only dry granular materials. On the other hand, applications where the interstitial fluid is significant, such as wet-snow avalanches and debris flows become a challenge to DEM, as cohesion plays an essential role.

The Material Point Method

Allied to the advances in computational resources, modern methods such as the Material Point Method (MPM) (SULSKY; ZHOU; SCHREYER, 1995) are becoming popular among full three-dimensional kinetic models. The hybrid nature of MPM offers an efficient framework for handling deformations through constitutive relations, making the method very attractive for avalanche applications. Recently, Li *et al.* (2021) proposed a three-dimensional and real-scale modeling covering different flow regimes for dense snow avalanches with impressive results. Their model comes along with a recent series of investigations, using the MPM, into snow failure processes and crack propagation (GAUME *et al.*, 2018; GAUME *et al.*, 2019; TROTTET *et al.*, 2022), erosion and entrainment mechanisms (LI *et al.*, 2022), detrainment in natural terrains (VÉDRINE; LI; GAUME, 2022), and flow regimes (LI *et al.*, 2020)[19]. The MPM has also been used to simulate hyperelasticity in granular flows (HAERI; SKONIECZNY, 2022), and landslides (ZHAO *et al.*, 2019).

Direct Numerical Simulations

The Direct Numerical Simulation (DNS) methods utilize fine numerical grids to capture all scale turbulent structures, as opposed to the large-scale restricted models listed below. The DNS does not use any averaging techniques and requires enormous amounts of discrete cells. Due to its unparalleled accuracy, the DNS is usually used as a ground truth solution to test the accuracy of other numerical methods (YEH *et al.*, 2013). Recently, Gurjar (2023) utilized the DNS approach to simulate powder-snow avalanches. Most methods listed in subsection 3.4.2 and subsection 3.4.3 are usually solved with DNS.

Large-Eddy Simulations

Large Eddy Simulation (LES) balances accuracy and computational efficiency by directly simulating only large-scale structures. Such structures are energy-containing large eddies. The Navier-Stokes equations are filtered in the LES approach, so only the large eddies are solved numerically (using methods similar to DNS). The small-scale turbulent structures are modeled by Subgrid-Scale (SGS) models and are referred to as subgrid-scale effects. Such SGS models appear in the equations in the stress tensor terms. LES has been used to compute flow over large areas of complex terrain (VIONNET *et al.*, 2017; ROHANIZADEGAN *et al.*, 2023). Examples of LES applications in avalanche phenomena can be found in Chawdhary *et al.* (2018), Frantz *et*

[19] The SLAB (EPFL, 2022), the EPFL Snow and Avalanche Simulation Laboratory in Switzerland, is worth mentioning, whose researchers are responsible for many recent state-of-the-art publications in avalanche research.

al. (2021), Kyrousi *et al.* (2018).

Reynolds-Averaging Navier-Stokes Model

The Reynolds-Averaging Navier-Stokes Model (RANS) decomposes the model's variables (such as velocity and pressure) into their mean and fluctuating components. The RANS provide computationally efficient solutions for Navier-Stokes problems. The variable decomposition makes this class of methods suitable for simulating turbulent flows — however, the RANS present limitations in capturing certain flow features, such as large eddy structures. Meiburg, Radhakrishnan and Nasr-Azadani (2015) lists the application of RANS in turbidity current like phenomena. Navas-Montilla *et al.* (2019) approaches such limitations on simulating turbulent shallow flows. Recently, extending from Gavrilyuk, Ivanova and Favrie (2018), Ivanova *et al.* (2021) used RANS to simulate powder-snow avalanches under the shallow water model.

3.6 Software Packages

The crucial importance of snow avalanche models in natural hazards leads to developing software for research or use in hazard mapping by governmental institutions and companies. Over the decades, governments and institutions collaborated on developing such software, as in the case of the Austrian government and the Swiss Federal WSL[20] Institute for Snow Avalanche Research (SLF). This section contains a brief list of software packages and libraries, commercial and open source, used for the simulation and study of snow avalanches. A discussion on the limitations and calibration of some packages in the list can be found in Jamieson, Margreth and Jones (2008).

3.6.1 Proprietary & Commercial Software

- **AVAL-1D**: Developed by the SLF, the AVAL–1D (CHRISTEN; BARTELT; GRUBER, 2002) is a software package consisting of two modules, the FL–1D for dense-snow avalanche simulations and the SL–1D for powder–snow avalanches. AVAL–1D is commonly used by avalanche practitioners to predict runout distances and flow velocities Based on the VS model, the details of the models can be found in the works presented by Issler (1998), Bartelt, Salm and Gruber (1999), Issler *et al.* (2000). The package employs the finite difference method to solve equations. Oller *et al.* (2010) discusses its applications with real avalanche cases and offers several values for the parameters of the VS model. Figure 33a shows a screenshot of the software. More information is available at AVAL-1D, WSL (2022).

[20] The Swiss Federal Institute for Forest Snow and Landscape Research (WSL) monitors and studies forest, landscape, biodiversity, natural hazards and snow and ice. WSL is a research institute of the Swiss Confederation and part of the ETH Domain (SLF, 2022).

- **SAMOS-AT**: Developed in 1999 and introduced by Zwinger, Kluwick and Sampl (2003), the Snow Avalanche MOdelling and Simulation (SAMOS) tool (SAMPL; ZWINGER, 2004) was developed for the Austrian Federal Ministry for Agriculture, Forestry, and Environment for avalanche risk assessment. SAMOS is a simulation tool for powder–snow avalanches and uses a two–layer model to simulate the DSL and PSL. SAMOS uses the SH model for dense snow flows and a single mixture phase for the PSL.

  In 2007, an improved version of the software, named SAMOS–AT (SAMPL; GRANIG, 2009) (AT stands for Advanced Technology), brought significant modifications to the model. SAMOS–AT solves the DSL with a Lagrangian set of particles representing columns of variable height containing volumes of the dense flow over the bed surface, similarly to the SWE approach. A two–phase model represents the PSL, with separate mass and momentum balances for air and powder snow. A discussion and analysis of the parameters of the software can be found in Fischer (2013), Fischer *et al.* (2015).

- **RAMMS**: Introduced by (CHRISTEN; KOWALSKI; BARTELT, 2010) and developed in SLF, the RApid Mass Movements Simulation (RAMMS) software package offers simulations for three phenomena: avalanches, rockfalls, and debris flows. RAMMS is currently used for hazard mapping in Switzerland and therefore follows the Swizz guidelines. The system combines the VS and the RKE models (subsection 3.3.8 on page 86) and can simulate full three–dimensional dense flows. Figure 33b shows a screenshot of the software. Information about RAMMS is available at RAMMS, WSL (2022).

Figure 33 – Examples of graphical user interfaces of commercial software packages for snow avalanche simulation.

(a) Simulation of a one-dimensional snow avalanche in the AVAL-1D software package.

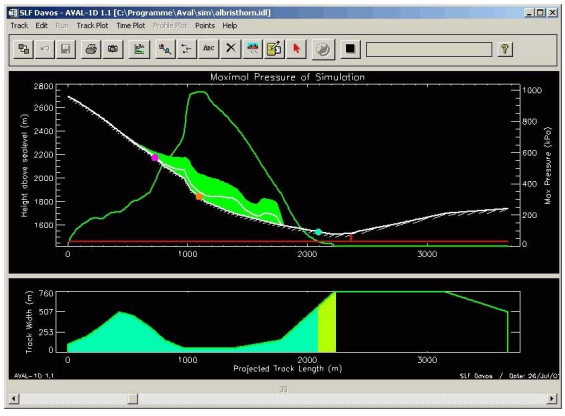

Source: AVAL-1D, WSL (2022).

(b) Simulation of a dense-snow avalanche over a three-dimensional terrain in the RAMMS software package.

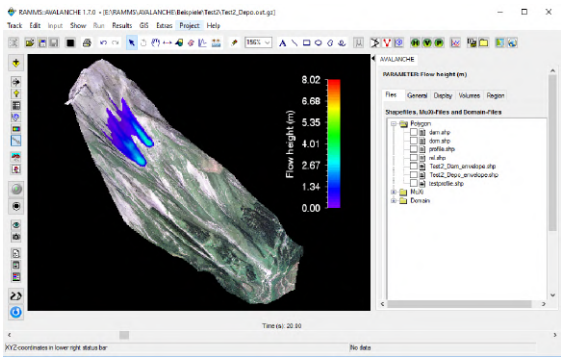

Source: RAMMS, WSL (2022).

3.6.2 Open Source / Free Software

- **Xcompact3d**: Xcompact3d and its modules is a framework of high-order finite-difference flow solvers dedicated to the study of turbulent flows (BARTHOLOMEW *et al.*, 2020) — in particular, DNS and LES simulations. Introduced by Frantz *et al.* (2021) on the simulation of turbulent gravity currents under the Boussinesq regime, the software has found many applications worldwide by many research groups, such as wake and jet flows. The software is available at <https://www.incompact3d.com/about.html> (LAIZET; LAMBALLAIS, 2022).

- **TRENT2D**: Originating from Armanini, Fraccarollo and Rosatti (2009), the TRENT2D package provides accurate solutions for two-dimensional dense snow avalanche simulations. The package models the equations in a global coordinate system, making it suitable for complex terrains. Refer to Zugliani and Rosatti (2021) for a complete description of the models and methods utilized by the software.

- **TITAN2D**: Introduced by Patra *et al.* (2005), TITAN2D simulates granular flows over large-scale natural terrains. Its roots track back to the simulation of volcanic avalanches based on the SH model (PITMAN *et al.*, 2003). Information about the methods implemented by the package can be found in Simakov *et al.* (2019), Patra *et al.* (2020). The source code is available at <https://github.com/TITAN2D/titan2d>.

3.7 Avalanche-Like Phenomena in Computer Graphics

The numerical methods cited in the previous sections are also present in Computer Graphics research and applications, with various adaptations and optimizations for computational efficiency. For instance, aside from water simulation, the particle-based method SPH found many applications over the years, such as the solution of SWE (SOLENTHALER *et al.*, 2011; CHLDEK; URIKOVI, 2015; XIA; LIANG, 2016), the animation of lava flows in volcano eruptions (ZHANG *et al.*, 2017), viscoplastic materials (PAIVA *et al.*, 2009), granular flows (BELL; YU; MUCHA, 2005; ALDUáN; OTADUY, 2011), snow avalanches (YNDESTAD, 2011; JONTHAN; DANIEL, 2021), and snow compression (GISSLER *et al.*, 2020).

Eulerian methods based on adaptive grids were used to animate debris flow (WANG *et al.*, 2015) and real-time granular flows for sand animation (ZHU *et al.*, 2019). Other relevant numerical methods are the APIC (JIANG *et al.*, 2015), Power Particles (GOES *et al.*, 2015), and (ZHU *et al.*, 2013) for large-scale domains.

Since the debut of MPM into the graphics community by Stomakhin *et al.* (2013) on the animation of snow for Disney's *Frozen* movie, MPM has rapidly become the state-of-the-art for many types of material simulations. The flexibility of MPM has allowed the simulation of cloth (JIANG; GAST; TERAN, 2017), elastoplastic materials (GAO *et al.*, 2017), *fase-*

changing materials (STOMAKHIN *et al.*, 2014), plastic flow for foam (YUE *et al.*, 2015; RAM *et al.*, 2015), *multi-species* materials and fluid mixtures (TAMPUBOLON *et al.*, 2017; GAO *et al.*, 2018), and fracture of materials (WOLPER *et al.*, 2020). In the realm of avalanche-like phenomena, Zhao *et al.* (2019) recently used MPM to animate landslides, and Gaume *et al.* (2018) produced incredible animations of slab avalanches using MPM.

Due to its complexity and high computational demand, alternative approaches solve the turbulent features of flows. In particular, procedural techniques for emulating turbulent motion and generating turbulent patterns became very successful. A few examples are Bridson, Houriham and Nordenstam (2007), Narain *et al.* (2008), Kim *et al.* (2008a), Wang *et al.* (2020).

Over the years, people in the entertainment industry have been using graphics tools and usual fluid simulation techniques to emulate snow avalanches (KAPLER, 2003; KIM; FLORES, 2008; imageworks, 2020; Failes, Ian, 2021). Tsuda *et al.* (2010) is the first to bring physical properties of snow into account by producing a mixed simulation of dense snow flow and powder–snow layers, followed later by Güçer and ÖZGÜÇ (2014), which applies molecular dynamics to the flow. Cordonnier *et al.* (2018) proposed a method for generating visual landscapes covered by snow that considers the effect of avalanches over time using a hydrostatic model. Tillgren (2020) used a procedural scheme based on Voronoi meshes to generate slab fractures on snow avalanches. Recently, Liu *et al.* (2021) presented a Position-based Dynamics (PBD) framework combined with the Bingham viscoplastic model to simulate snow avalanches. To the author's knowledge, these few references are the only publications directly or indirectly related to the digital animation of snow avalanches.

3.8 Remarks

- Plumes are almost stationary, with horizontal velocities of 4 $m \cdot s^{-1}$, compared to the front velocities of up to 55 $m \cdot s^{-1}$.
- The plume velocity is independent of slope angle due to air entrainment.
- The air intake is velocity-dependent at the leading edge and is responsible for the cloud growth.
- Avalanches can grow their masses up to five times on average.
- Laboratory experiments show that slab-avalanche size distributions are scale-invariant.
- The Voellmy friction model combines a dynamic friction component τ_h with a Coulomb-like dry friction component τ_d:

$$\tau_h = g\frac{u^2}{\xi h}, \qquad \tau_d = \mu g \cos\theta.$$

The dry friction for large avalanches is $\mu = 0.155$, and the dynamic friction $\xi > 1000$;

- The SH model is a granular flow, depth-integrated model for dense-snow avalanches under the continuum mechanical approach.
- The entrainment rate in the dense-snow avalanche can be defined as

$$S_e = \frac{\tau_b}{r_b} \parallel u \parallel .$$

  A common assumption is that mass detaches from the top of the dense layer at the same rate that mass is entrained in the bottom.

- The mixture model provides a way to model the powder-snow avalanche as a single-phase flow, although the air phase is also considered. The model uses the concentration of volumes α_s and α_a to represent the simultaneous occupancy of the snow and air phases in space. However, the equations are written only in terms of α_s.
- Under the mixture model, the mixture quantities are defined in terms of the constituent occupancies, $\alpha_\bigstar \in [0,1]$, such as the mixture density:

$$\rho = \rho_s \alpha_s + \rho_a \alpha_a .$$

- Although both phases can be simplified as incompressible fluids, the mixture of both fluids is compressible.

CHAPTER

4

SIMULATION METHOD

This chapter delves into the details of the overall method. Here, a set of separate numerical methods simulate a mixed-type powder-snow avalanche. In particular, the workflow completely decouples the powder-snow layer from the dense-snow layer. Both layers are treated as separate simulations that communicate with each other numerically.

Refer to Appendix B on page 205 for a brief introduction to the numerical methods used in this chapter, such as the Finite Volume Method (FVM), and Appendix C on page 223 for a description of the software package OpenFOAM, the framework utilized to implement the models.

The first section gives a complete overview of the method, followed by section 4.2 on page 110 and section 4.3 on page 116, discussing the details of each separate method for the Dense-Snow Layer (DSL) and Powder-Snow Layer (PSL) simulations, respectively. The chapter ends with a list of remarks in section 4.4 on page 129.

4.1 Method Pipeline

As described in section 2.2 on page 52, the powder-snow avalanche consists of four main layers, from bottom to top: a ground layer representing the static snow cover, the DSL, a transition layer, and the PSL. Like Sampl and Granig (2009), this method takes the following assumptions:

Assumption 1. *The layers' physical characteristics are sufficiently different to justify a different set of equations to explain their respective motion.*

Assumption 2. *The transition layer is considered a rough wall that coincides with the surface of the DSL. The wall moves at the same speed as the DSL.*

The first assumption is more of a necessity in front of the complexity of the whole phenomenon; it allows the application of more appropriate models for each type of flow. On the other hand, Assumption 2 enormously simplifies the method by removing the explicit representation of the *transition layer*, which is particularly challenging to model. In practice, the method simulates only the DSL and PSL flows, as boundary conditions for both numerical models could implicitly represent the *transition layer*. However, a third assumption further simplifies the overall setting:

Assumption 3. *Neither the turbulent air nor the deposition processes of the PSL are significant enough to have any effect on the motion or mass of the DSL. Thefore the role of the PSL in the DSL is negligible.*

The direct consequence of Assumption 3 is that the system becomes a one-way coupling system of simulations, meaning that the resulting data of the first simulation serves as input for the second one. Schematically, the main algorithm performs both layer simulations in sequence and *glues* them together by converting the DSL output quantities into boundary conditions for the PSL equations. Figure 34 depicts the final decomposition of the powder-snow avalanche after the abovementioned assumptions.

Figure 34 – The simulation method considers the following decomposition of the powder-snow avalanche. The method simulates only the DSL and the PSL flows. The transition layer is an interface that translates to boundary conditions for the PSL. The snow cover is static and serves as the source of mass for the upper layers.

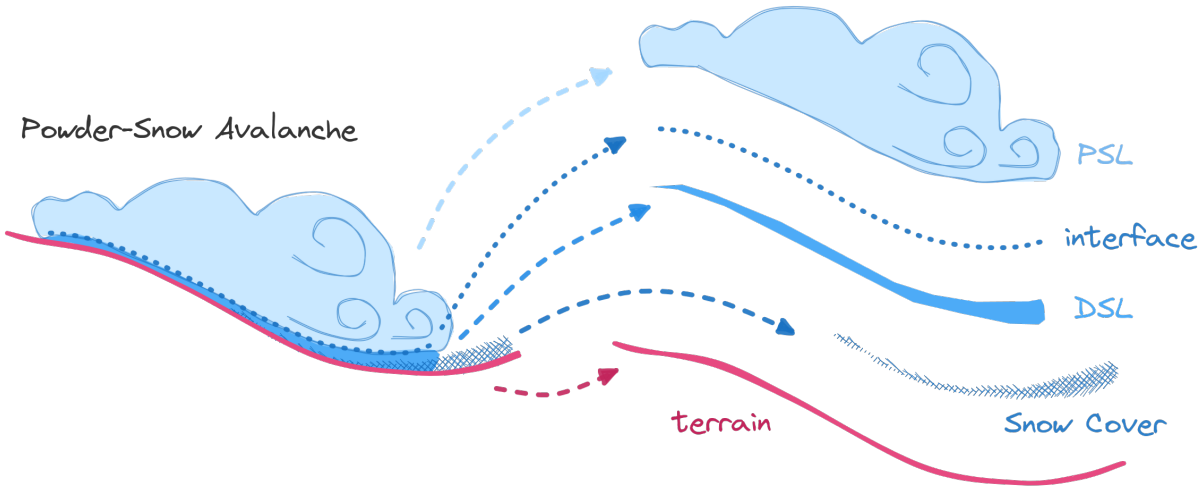

Source: Elaborated by the author.

The pipeline consists of three main steps that conduct the numerical information transport from the lower to the upper layers. The middle step converts the output data from the DSL flow simulation into input quantities for the PSL flow simulation. The details will become clear in the next sections. Figure 35 represents the following sequential steps:

- **Step 1**: Since it is a one-way coupling system, the full simulation of the DSL flow can be executed without any dependency. The two essential resulting quantities are the height h and the velocity $\mathbf{u}$ of the DSL. The velocity vector is parallel to the terrain surface. The final height of the snow cover h', after its erosion, is also passed forward.
- **Step 2**: The resulting data from the previous step are converted into boundary conditions for the bottom faces of the PSL flow. The output is the amount of injected mass into the powder cloud and the velocity of the injection $\mathbf{u}_{inj}$. The injection velocity vector is perpendicular to the terrain surface. The computation of the injection quantities requires an extra field representing the distance to the front region of the DSL.
- **Step 3**: The final step simulates the PSL flow. The injection information computed in *step 2* generates mass for the cloud, and the governing equations take care of the motion. The final data is a *density field* representing the occupancy of snow powder in the simulation domain.

Figure 35 – The visual representation of the three steps described in the text. The output data from the DSL flow simulation representing tangential velocity and DSL height is converted into an amount of injected mass with parallel velocity. The injection intensity depends on the distance to the front of the DSL flow. The final result is a volumetric field representing the powder snow cloud.

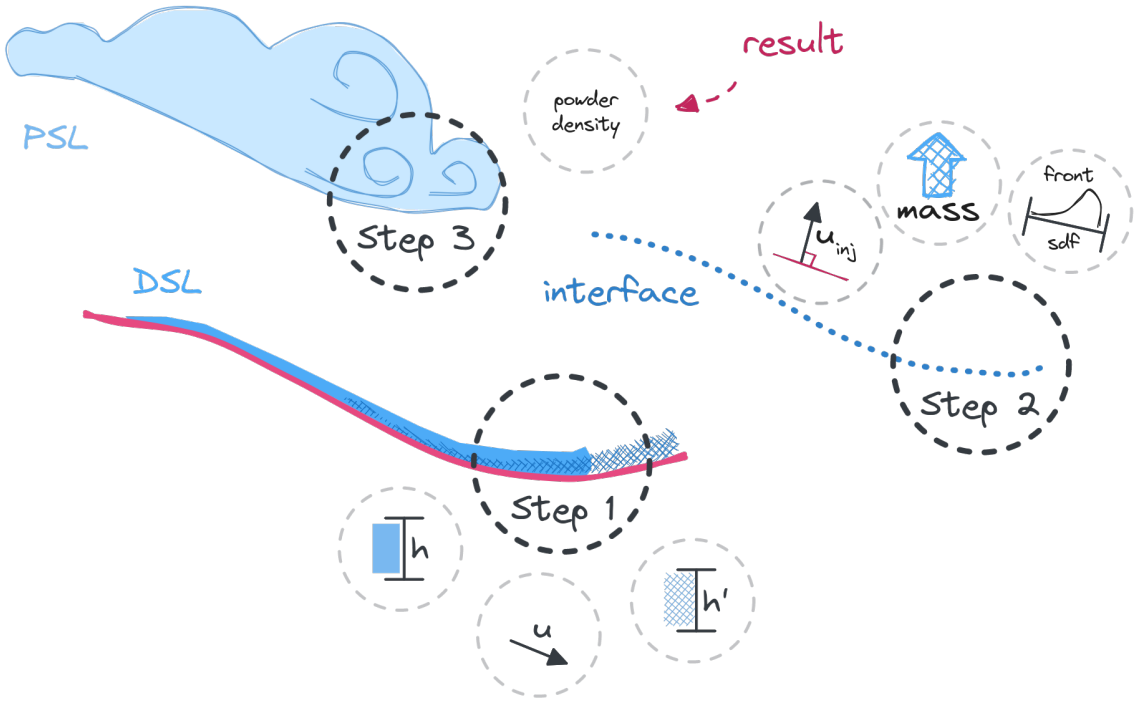

Source: Elaborated by the author.

This chapter focuses only on the mathematical models that describe the DSL and the PSL. However, the simulations run over discrete meshes representing the numerical grid for the FVM. The details regarding the generation of the numerical grids from topographical data, the

computation of the DSL front distance field, and other computational aspects are discussed in Chapter 5 on page 131.

4.2 Dense-Snow Layer Model

This section describes a method for simulating the dense flow avalanche corresponding to the DSL in the powder-snow avalanche. The core assumption is that the DSL behaves as a granular material that undergoes high deformation. The steep slope of the terrain tests the bed friction against the force of gravity. The internal friction also determines the motion of the granular flow by generating heat and resisting deformations.

The method resorts to the successful family of Saint-Venant Equations derived models to reduce the problem to two dimensions, particularly the well-known Savage-Hutter model (SAVAGE; HUTTER, 1991). As introduced in subsubsection 3.3.5.1 of Chapter 3, the SH extends the Shallow Waters Equations (SWE) by introducing a Coulomb-like dry friction for bed friction and a Mohr-Coulomb yield criterion to handle the internal friction. Additionally, the SH tackles the inherent limitation of the SWE for steep slopes by describing its equations with local curvilinear coordinates (x', y', z') – see Figure 36. In the curvilinear setting, the vector quantity $\mathbf{v}$ is described as $\mathbf{v}' = (v'_x, v'_y)^T$, where the prime superscript $(\bigstar)'$ denotes the curvilinear coordinates[1].

Figure 36 – The SH model describes the equations in the local curvilinear coordinates (x', y', z'). The directions of x' and y' are parallel to the terrain, where x' follows the slope, and the direction of z' points to the normal direction $\mathbf{n}$. The height h' represents the height of the avalanche in the normal direction. The model takes the averages $\bar{\mathbf{u}}$ of the vertical variation of the velocity $\mathbf{u}$.

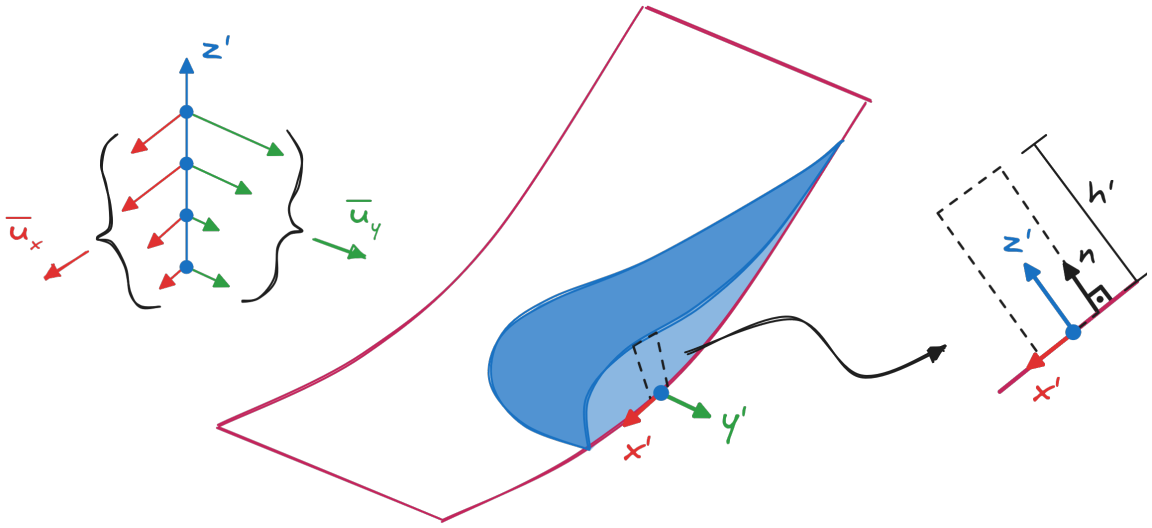

Source: Elaborated by the author.

[1] Note that the vectors for the following equations are two-dimensional vectors since the SWE removes one dimension by averaging the values along the vertical direction.

For a simple ramp, as shown in Figure 36, curved only in the x' direction, Koch, Greve and Hutter (1994) applies the SH equations as the following:

$$\frac{\partial h'}{\partial t} + \nabla' \cdot (h' \bar{\mathbf{u}}') = 0, \tag{4.1}$$

$$\frac{\partial (h' \bar{\mathbf{u}}')}{\partial t} + \nabla' \cdot (h' \bar{\mathbf{u}}' \otimes \bar{\mathbf{u}}') = \frac{\tau_b'}{\rho} + \mathbf{g}_{xy}' h' - \frac{k}{2\rho} \nabla' (h' p_b), \tag{4.2}$$

$$\bar{\mathbf{u}}(\mathbf{x}) = \frac{1}{h'(\mathbf{x})} \int_0^{h'(\mathbf{x})} \mathbf{u}(\mathbf{x} - \mathbf{n}(\mathbf{x}) z') dz' \quad [m \cdot s^{-1}], \tag{4.3}$$

where h' is the height of the flow normal to the surface (in the direction of z'), $\bar{\mathbf{u}}' = (\bar{u}_x, \bar{u}_y)^T$ is the average velocity in the z' direction, $\nabla' = (\frac{\partial}{\partial x'}, \frac{\partial}{\partial y'})^T$ is the spatial derivatives in curvilinear coordinates, τ_b' is the basal friction term (based on the Coulomb friction), k is the curvature of the x' curved axis, $\mathbf{g}_{xy}'$ is the tangential components of the gravitational acceleration, and p_b is the basal pressure defined as

$$p_b = \rho h' g_z' + \rho h' k \bar{u}_x'^2 \quad [kg \cdot m^{-1} s^{-2}], \tag{4.4}$$

where the first term represents the gravitational influence and the second term relates to the centrifugal force.

For more complex terrains, the computation of the curvature k is challenging. Alternatively, Rauter and Tukovi (2018) offers an approach based on thin liquid film methods that solves Surface PDEs (SPDEs)[2] and can handle mildly curved terrains. In contrast to the SH, their method describes the equations in Cartesian coordinates and relates the vertical component of the velocity to the basal pressure. The solution splits the momentum equation into *surface-tangential* and *surface-normal* parts:

$$\frac{\partial h'}{\partial t} + \nabla \cdot (h' \bar{\mathbf{u}}) = 0 \quad [m \cdot s^{-1}], \tag{4.5}$$

$$\frac{\partial (h' \bar{\mathbf{u}})}{\partial t} + \nabla_S \cdot (h' \bar{\mathbf{u}} \otimes \bar{\mathbf{u}}) = -\frac{\tau_b}{\rho} + h' \mathbf{g}_S - \frac{1}{2\rho} \nabla_S (h' p_b) \quad [m^2 \cdot s^{-2}], \tag{4.6}$$

$$\nabla_n \cdot (h' \bar{\mathbf{u}} \otimes \bar{\mathbf{u}}) = h' \mathbf{g}_n - \frac{1}{2\rho} \nabla_n (h' p_b) - \frac{1}{\rho} \mathbf{n} p_b \quad [m^2 \cdot s^{-2}], \tag{4.7}$$

where, for a surface with normal vector $\mathbf{n}$, the surface-tangential gradient operator ∇_S and the surface-normal gradient operator ∇_n are defined as

$$\begin{aligned} \nabla_n &= (\mathbf{n} \otimes \mathbf{n}) \cdot \nabla, \\ \nabla_S &= (\mathbf{I} - \mathbf{n} \otimes \mathbf{n}) \cdot \nabla. \end{aligned} \tag{4.8}$$

The respective gravitational components, $\mathbf{g}_S$ and $\mathbf{g}_n$, are defined in the same way. Note that Equation 4.6 and Equation 4.7 are very similar, distinguished only by the strictly normal and tangential terms. Essentially, both equations represent a decomposition of Equation 4.2 in a

[2] See Deckelnick, Dziuk and Elliott (2005).

velocity equation and a *basal pressure equation*[3], respectively. The boundary condition $\bar{\mathbf{u}} \cdot \mathbf{n} = 0$ ensures that the fluid motion is tangential to the surface and helps to solve Equation 4.7. Therefore, the solution for the basal pressure p_b can solve the velocity field $\bar{\mathbf{u}}$.

In order to account for entrainment processes, Rauter *et al.* (2018) extends the model above with the entrainment model provided by Fischer *et al.* (2015). The extension modifies the mass conservation equation Equation 4.5 to include the entrainment rate q_e defined as

$$q_e = \begin{cases} \frac{\tau_b \cdot \bar{\mathbf{u}}}{e_b}, & h'_c > 0, \\ 0, & h'_c = 0 \end{cases} \quad [kg \cdot m^{-2} \cdot s^{-1}], \tag{4.9}$$

where $e_b[m^2 \cdot s^{-2}]$ is the specific erosion energy and h'_c is the height snow cover encountered by the avalanche, defined as

$$h'_c(z) = (H'_c(z_0) + \frac{\partial H'_c}{\partial z}(z - z_0)) \cos\Theta \quad [m], \tag{4.10}$$

where $z[m]$ is the mountain elevation and $\cos\Theta = \mathbf{g} \cdot \mathbf{n}$. The other terms are user parameters, $z_0[m]$ is the elevation reference, $H'_c(z_0)$ is the base value, and $\frac{\partial H'_c}{\partial z}$ is the growth rate. Equation 4.5 then becomes

$$\frac{\partial h'}{\partial t} + \nabla \cdot (h' \bar{\mathbf{u}}) = \frac{q_e}{\rho} \quad [m \cdot s^{-1}], \tag{4.11}$$

and the consumption of the snow cover due to entrainment over time is

$$\frac{\partial H'_c}{\partial t} = -\frac{q_e}{\rho} \quad [m \cdot s^{-1}]. \tag{4.12}$$

Finally, the basal friction τ_b follows the Voellmy friction model, see subsection 3.3.3 of Chapter 3, and is defined as

$$\tau_b = \mu p_b \frac{\bar{\mathbf{u}}}{|\bar{\mathbf{u}}| + u_0} + \frac{\rho g}{\xi} |\bar{\mathbf{u}}| \bar{\mathbf{u}} \quad [kg \cdot m^{-1} \cdot s^{-2}], \tag{4.13}$$

where $\mu[\cdot]$ and $\xi[m \cdot s^{-2}]$ are constant values, and $u_0[m \cdot s^{-1}]$ is a regularization value to avoid the division by near zero velocities.

4.2.1 Numerical Model

This section describes the method employed by Rauter *et al.* (2018) to solve the governing equations described in the previous section. The numerical method, described in section B.2 on page 220, is called the Finite Area Method (FAM) and is a specialization of the FVM for curved surfaces. The FAM discretizes the equations over the decomposition of the surface domain into cells called finite areas, flat polygonal areas bounded by straight edges — left side of Figure 37. Moreover, the FAM is constructed to solve SPDEs by discretizing the differential operators in the tangential and normal directions, fitting Equation 4.6 and Equation 4.7, respectively.

[3] The basal pressure equation relates to Equation 4.4 but does not require the calculation of the curvature the surface curvature k.

Figure 37 – The FAM solves PDEs on curved surface domains by discretizing the domain into a surface mesh. Each cell The discretization process uses the fluxes passing through the edges of each cell. The flux in an edge is defined by $(h\mathbf{u})_{e_c} \cdot \mathbf{L_e}$, where $\mathbf{L_e} = |\mathbf{L_e}|\mathbf{m}_e$ is the edge length vector pointing outward the cell, and h is the DSL height transported by the velocity $\mathbf{u}$. Note that $\mathbf{m}_e$ is not necessarily orthogonal to the surface normal $\mathbf{n}$ at the cell center.

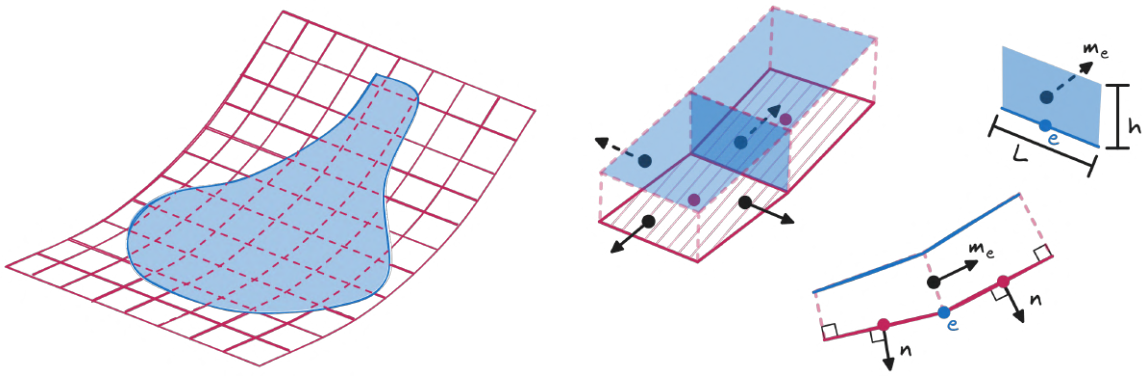

Source: Elaborated by the author.

The equations are solved sequentially by an iterative method, represented by Source code 1, that repeats the sequence until convergence is achieved. The sequence is composed of three steps:

1. Use Equation 4.7 to compute a new value for the basal pressure p_b;
2. Use Equation 4.6 to compute a new value for the velocity field $\bar{\mathbf{u}}$;
3. Use the new velocity $\bar{\mathbf{u}}$ to compute a new value of h' with Equation 4.11.

Source code 1 – DSL Algorithm.

```
1:      u = u_0; pb = pb_0; h = h_0;
2:      for(t = t_0; t < t_final; t += dt) {
3:          while(residual > threshold && ) {
4:              pb = computePb(u, h, pb);
5:              u = computeU(pb, u, h);
6:              h = computeH(u, pb);
7:          }
8:      }
```

The following details consider a finite area cell C, with area C_A and center point C_c. The cell is bounded by a set of edges $e_i \in E$ that may be shared with neighboring cells N_i. The flux of any rank tensor field Ψ through each edge e_i is defined by $(\Psi)_{e_{ci}} * \mathbf{L_e}_i$, where $\mathbf{L_e}_i$ is the edge length vector pointing outwards the cell, and $*$ is an appropriate product operation.

In the following discretization equations, *implicit*[4] terms are terms localized in the center points, $(\bigstar)_{C_c}$, associated with the system matrix entries. *Explicit* terms are all the remaining quantities that happen to be on the right hand side of the equations. The superscript $(\bigstar)^o$ denotes the current known value of $\bigstar$ in the current time step. The steps of the algorithm above are:

- $p_b \leftarrow \texttt{computePb}(\bar{\mathbf{u}}^o, h^o, p_b^o)$

  The new value of p_b is computed explicitly from Equation 4.7:

$$p_b = -\rho(\nabla_n \cdot (h^o \bar{\mathbf{u}}^o \otimes \bar{\mathbf{u}}^o)) \cdot \mathbf{n} + (\rho h^o \mathbf{g}_n)_{C_c} \cdot \mathbf{n} - \frac{1}{2}(\nabla_n (h^o p_b^o)) \cdot \mathbf{n}$$

  where

$$\begin{aligned} \nabla_n \cdot (h^o \bar{\mathbf{u}}^o \otimes \bar{\mathbf{u}}^o) &\approx (\mathbf{n} \otimes \mathbf{n}) \cdot \sum_{e_i \in E} (h^o \bar{\mathbf{u}}^o \otimes \bar{\mathbf{u}}^o)_{e_{ci}} \cdot \mathbf{L}_{\mathbf{e}i}, \\ \nabla_n (h^o p_b^o) &\approx (\mathbf{n} \otimes \mathbf{n}) \cdot \sum_{e_i \in E} (h^o p_b^o)_{e_{ci}} \mathbf{L}_{\mathbf{e}i}. \end{aligned} \tag{4.14}$$

- $\bar{\mathbf{u}} \leftarrow \texttt{computeU}(\bar{\mathbf{u}}^o, h^o, p_b^o)$

  The new value for the velocity field $\bar{\mathbf{u}}$ comes from the solution of the system

$$\mathbf{A}\bar{\mathbf{u}} = \mathbf{b} \tag{4.15}$$

  constructed from the discretization of Equation 4.6

$$\underbrace{\frac{\partial (h^o \bar{\mathbf{u}})}{\partial t}}_{1} + \underbrace{\nabla_S \cdot (h^o \bar{\mathbf{u}}^o \otimes \bar{\mathbf{u}})}_{2} = \underbrace{-\frac{\tau_b}{\rho}}_{3} + \underbrace{h^o \mathbf{g}_S}_{4} \underbrace{- \frac{1}{2\rho} \nabla_S (h^o p_b^o)}_{5},$$

  where each numbered term translates into the system as:

  1. $\boxed{\dfrac{\partial (h^o \bar{\mathbf{u}})}{\partial t}}$

     The transient term is descritized by the second-order implicit Euler:

$$\frac{C_A}{2\Delta t}\left(3(h^o \bar{\mathbf{u}}) - 4(h\bar{\mathbf{u}})^{n-1} + (h\bar{\mathbf{u}})^{n-2}\right)_{C_c}, \tag{4.16}$$

     where the superscripts $(\bigstar)^{n-1}$ and $(\bigstar)^{n-2}$ denote known values from previous time steps.

  2. $\boxed{\nabla_S \cdot (h^o \bar{\mathbf{u}}^o \otimes \bar{\mathbf{u}})}$

     The convective term is discretized via the *upwind scheme*[5]:

$$(\mathbf{I} - \mathbf{n} \otimes \mathbf{n}) \cdot \sum_{f_i \in S} \Phi_{e_{ci}} \bar{\mathbf{u}}_{e_{ci}}, \tag{4.17}$$

[4] See implicit and explicit term definitions in section C.2.

[5] See advection schemes in subsection B.1.5 on page 216.

where

$$\Phi_{e_{ci}} = (h\bar{\mathbf{u}})^o_{e_{ci}} \cdot \mathbf{L}_{\mathbf{e}i},$$
$$\bar{\mathbf{u}}_{e_{ci}} = \begin{cases} (\bar{\mathbf{u}})_{C_c}, & \Phi_{e_{ci}} \geq 0, \\ (\bar{\mathbf{u}})_{N_{ci}}, & \Phi_{e_{ci}} < 0. \end{cases} \tag{4.18}$$

3. $\boxed{-\frac{\tau_b}{\rho}}$

The basal friction term is given by Equation 4.13:

$$\tau_b = \mu p_b^o \frac{\bar{\mathbf{u}}}{|\bar{\mathbf{u}}^o| + u_0} + \frac{\rho g}{\xi} |\bar{\mathbf{u}}^o| \bar{\mathbf{u}},$$

so the term is implicitly solved by the system as

$$C_A \left(\left(\mu p_b \frac{1}{|\bar{\mathbf{u}}| + u_0} + \frac{\rho g}{\xi} |\bar{\mathbf{u}}| \right)^o \bar{\mathbf{u}} \right)_{C_c}. \tag{4.19}$$

4. $\boxed{h^o \mathbf{g}_S}$

The source term is directly translated into the system as

$$(\mathbf{I} - \mathbf{n} \otimes \mathbf{n}) \cdot (h^o \mathbf{g}) C_A. \tag{4.20}$$

5. $\boxed{\frac{1}{2\rho} \nabla_S (h^o p_b^o)}$

The last term is also explicitly solved by the system as

$$(\mathbf{I} - \mathbf{n} \otimes \mathbf{n}) \cdot \frac{1}{2\rho} \sum_{e_i \in E} (h^o p_b^o)_{e_{ci}} \mathbf{L}_{\mathbf{e}i}. \tag{4.21}$$

- $h \leftarrow$ `computeH`$(\bar{\mathbf{u}}^o, h^o, p_b^o)$

The DSL height is given by the numerical system

$$\mathbf{A}_h[h] = \mathbf{b}_h, \tag{4.22}$$

constructed from the discretization of Equation 4.11:

$$\underbrace{\frac{\partial h}{\partial t}}_{1} + \underbrace{\nabla \cdot (h\bar{\mathbf{u}}^o)}_{2} = \underbrace{\frac{q_e}{\rho}}_{3},$$

where each numbered term translates into the system as:

1. $\boxed{\dfrac{\partial h}{\partial t}}$

   The transient term is descritized by the second-order implicit Euler:

$$\frac{C_A}{2\Delta t}\left(3h - 4h^{n-1} + h^{n-2}\right)_{C_c}. \tag{4.23}$$

2. $\boxed{\nabla \cdot (h\bar{\mathbf{u}}^o)}$

   The convective term is discretized via the *upwind scheme*:

$$\sum_{f_i \in S} \Phi_{e_{ci}} h_{e_{ci}}, \tag{4.24}$$

   where

$$\begin{aligned} \Phi_{e_{ci}} &= (\bar{\mathbf{u}})^o_{e_{ci}} \cdot \mathbf{L}_{\mathbf{e}i}, \\ h_{e_{ci}} &= \begin{cases} (h)_{C_c}, & \Phi_{e_{ci}} \geq 0, \\ (h)_{N_{ci}}, & \Phi_{e_{ci}} < 0. \end{cases} \end{aligned} \tag{4.25}$$

3. $\boxed{\dfrac{q_e}{\rho}}$

   The right-hand side term accounts for snow entrainment into the DSL and uses Equation 4.9. In the presence of a snow cover, q_e is defined as:

$$q_e = \left(\frac{\tau_b \cdot \bar{\mathbf{u}}}{e_b}\right)^o,$$

   and the complete term is explicitly solved as

$$\left(\frac{\tau_b \cdot \bar{\mathbf{u}}}{\rho e_b}\right)^o C_A. \tag{4.26}$$

4.3 Powder-Snow Layer Model

The miscible nature of the turbulent movement of snow and air in the powder-snow layer appeals to mixture models. Therefore, we consider the family o models originated from the Continuum Mixture Theory (CMT) — see section A.1 on page 203. In particular, our model contemplates the two main mixture constituents, $\mathscr{C}_s$, and $\mathscr{C}_a$, representing respectively snow[6] and air phases[7]. Therefore, the terms in the following equations indexed with the subscript $(\bigstar)_s$ refer to field quantities of snow, and those indexed with the subscript $(\bigstar)_a$ refer to field quantities of air. The model then combines snow and air property quantities to describe the final mixture.

[6] Recall that the snow phase consists of airborne particles of ice.

[7] The terms *phase* and *constituent* are interchangeable throughout the text.

Moreover, allied to the superposition assumption of the CMT, the mixture is characterized by the fraction of volume $\alpha_\bigstar \in [0,1]$ occupied by the constituent $\mathscr{C}_\bigstar$ for any given volume occupied by the mixture. The mixture density ρ, for example, is defined by

$$\rho = \alpha_s \rho_s + \alpha_a \rho_a, \quad \alpha_s + \alpha_a = 1. \tag{4.27}$$

The CMT conveniently introduces a mean velocity $\mathbf{u}$ for the mixture, interpreted as the velocity of the center of mass of the constituents. Thus, we can simplify our model using the mean velocity instead of handling $\mathbf{u}_s$ and $\mathbf{u}_a$ explicitly. Additionally assuming incompressibility for both phases and the mixture, the continuity equation is

$$\nabla \cdot \mathbf{u} = 0, \tag{4.28}$$

imposing ρ_s and ρ_a constant densities. The momentum equation for the mean velocity can be derived directly from the linear momentum balance law:

$$\frac{\partial \rho \mathbf{u}}{\partial t} + \nabla \cdot (\rho \mathbf{u} \otimes \mathbf{u}) = \nabla \cdot \mathbf{S} + \rho \mathbf{g}, \tag{4.29}$$

where $\mathbf{S}$ is the Cauchy stress field and $\mathbf{g}$ the gravitational acceleration. The Cauchy stress field is composed by a *reactive* part $\mathbf{S}^r$ and an *active* part $\mathbf{S}^a$:

$$\mathbf{S} = \mathbf{S}^r + \mathbf{S}^a. \tag{4.30}$$

For incompressible fluids, the reactive stress field is spherical and its multiplicative term p is interpreted as the pressure:

$$\mathbf{S}^r = -p\mathbf{I}. \tag{4.31}$$

The reactive stress field $\mathbf{S}^r$ would be sufficient to model ideal fluids. However in the case of Newtonian fluids, the Cauchy stress field carries the active term $\mathbf{S}^a$, defined as[8]

$$\mathbf{S}^a = \mathbf{S} - \frac{1}{3}\mathrm{tr}(\mathbf{S})\mathbf{I}. \tag{4.32}$$

The active term $\mathbf{S}^a$ is related to the shear-rate stresses and is represented by the shear-rate tensor τ, also called *viscous stress tensor* or *deformation-rate tensor*, given as

$$\mathbf{S}^a = \tau = 2\mu\mathbf{D} - \frac{2}{3}\mu\mathrm{tr}(\mathbf{D})\mathbf{I}, \tag{4.33}$$

where $\mathbf{D} = \frac{1}{2}(\nabla \otimes \mathbf{u} + (\nabla \otimes \mathbf{u})^T)$ is the strain-rate tensor and μ is the mixture viscosity[9]

$$\mu = \alpha_s \mu_s + \alpha_a \mu_a. \tag{4.34}$$

[8] The decomposition of $\mathbf{S}$ splits a matrix $\mathbf{S}$ into a hydrostatic $\mathbf{S}^H$ part and a deviatoric $\mathbf{S}^D$ part, $\mathbf{S} = \mathbf{S}^H + \mathbf{S}^D$. The hydrostatic part is defined as $\mathbf{S}^H = \frac{1}{3}tr(\mathbf{S})\mathbf{I}$, which is particularly interpreted as the negative pressure $-p\mathbf{I}$. The deviatoric part is simply given by $\mathbf{S}^D = \mathbf{S} - \mathbf{S}^H$.

[9] If $\mu = 0$ and $\rho = \rho_0$ constant, the system is reduced to the known Euler equations: $\nabla \cdot \mathbf{u} = 0$ and $\rho_0 \frac{\partial \mathbf{v}}{\partial t} + (\nabla \cdot \mathbf{u})\mathbf{u} = -\nabla p + \rho_0 \mathbf{g}$.

The development of the trace operator in Equation 4.33 yields

$$\begin{aligned} \mathrm{tr}(\mathbf{D}) &= \mathrm{tr}\Big(\frac{1}{2}(\nabla \otimes \mathbf{u} + (\nabla \otimes \mathbf{u})^T)\Big) \\ &= \nabla \cdot \mathbf{u}, \end{aligned} \tag{4.35}$$

therefore the tensor τ can be written as

$$\tau = 2\mu\mathbf{D} - \frac{2}{3}\mu(\nabla \cdot \mathbf{u})\mathbf{I}. \tag{4.36}$$

Note, however, that by the continuity equation Equation 4.28, $\nabla \cdot \mathbf{u} = 0$, the equation above reduces to

$$\tau = 2\mu\mathbf{D}. \tag{4.37}$$

The expansion of Equation 4.30 in Equation 4.29 results into the momentum equation found in the Navier-Stokes equations

$$\frac{\partial \rho\mathbf{u}}{\partial t} + \nabla \cdot (\rho\mathbf{u} \otimes \mathbf{u}) = -\nabla p + \nabla \cdot \tau + \rho\mathbf{g}. \tag{4.38}$$

For numerical purposes, it is also convenient to use a change of variable for the pressure term. The pressure field is modified to account for the hydrostatic pressure p_{rgh} and is defined as:

$$p_{rgh} = p - \rho\mathbf{g} \cdot \mathbf{h}, \tag{4.39}$$

where $\mathbf{h}$ is the position vector read as the height. The substitution of p by p_{rgh} proceeds by applying the gradient on both sides of Equation 4.39:

$$\begin{aligned} \nabla p_{rgh} &= \nabla p - \nabla(\rho(\mathbf{g} \cdot \mathbf{h})) \\ -\nabla p &= -\nabla p_{rgh} - \rho\mathbf{g} \cdot \nabla \otimes \mathbf{h} - \mathbf{h} \cdot \nabla(\rho\mathbf{g}) \\ -\nabla p &= -\nabla p_{rgh} - \rho\mathbf{g} \cdot \mathbf{I}_z - \mathbf{g} \cdot \mathbf{h}\nabla\rho - \cancelto{0}{\rho\mathbf{h} \cdot \nabla\mathbf{g}} \\ -\nabla p &= -\nabla p_{rgh} - \rho\mathbf{g} - \mathbf{g} \cdot \mathbf{h}\nabla p \end{aligned} \tag{4.40}$$

where the term $\nabla \otimes \mathbf{h}$ reduces to the tensor $\mathbf{I}_z$ with diagonal $(0,0,1)^T$ and null non-diagonal elements. The final linear momentum equation is written as

$$\frac{\partial \rho\mathbf{u}}{\partial t} + \nabla \cdot (\rho\mathbf{u} \otimes \mathbf{u}) = -\nabla p_{rgh} - \mathbf{g} \cdot \mathbf{h}\nabla\rho + \nabla \cdot \tau. \tag{4.41}$$

The remaining equations describe the conservation of mass and use the concentration of volume α_s instead of ρ. Using α in the equation requires only one set of equations since $\alpha_a = 1 - \alpha_s$ (Equation 4.27). Notice that, in principle, the transport equation for α_s would be

$$\frac{\partial \alpha_s}{\partial t} + \nabla \cdot (\mathbf{u}\alpha_s) = 0, \tag{4.42}$$

which conserves α_s along the motion. However, the turbulent motion in the PSL causes the mixing of both phases and therefore Equation 4.42 gets a source term on the right-hand side. The

additional term takes into account the kinetic energy, produced by turbulence, that composes the stress tensor for the field α_s and models the mixing effect of the turbulence:

$$\frac{\partial \alpha_s}{\partial t} + \nabla \cdot (\mathbf{u}\alpha_s) = \nabla \cdot \left(\left(D_{AB} + \frac{\nu_t}{Sc} \right) \nabla \alpha_s \right). \tag{4.43}$$

The constant Sc is called the Schmidt number and is the ratio of the momentum diffusivity to mass diffusivity[10]. ν_t is the turbulent eddy viscosity, which comes from the transfer of energy due to moving eddies produced by turbulence. The molecular diffusivity, D_{ab}, describes the velocity of diffusion of molecules from the snow phase into the air phase.

A further simplification takes the turbulent energy out of the equation, $\nu_t = 0$, yielding the final form

$$\frac{\partial \alpha_s}{\partial t} + \nabla \cdot (\mathbf{u}\alpha_s) = \nabla \cdot \left(D_{AB} \nabla \alpha_s \right). \tag{4.44}$$

4.3.1 Transition Layer Model

The previous section detailed the model equations for linear momentum and mass transport. The set of equations describes the evolution of the powder-snow cloud over time due to gravity. The gravity force causes the acceleration of heavy snow particles in regions where the density difference is high. Besides the gravitational acceleration, mass transport manifests through molecular diffusion between both phases. However, none of the terms in the equations consider the mass exchange between the powder-snow cloud and the sources of snow particles. Moreover, the volume of the cloud also varies due to air drag and air intake, which are also not accounted for by the equations.

As described in previous chapters, the powder-snow layer gains mass from the processes in the interface layer between the DSL and the PSL, called the *transition layer*. This section explores a couple of models for the transition layer and considers the eruption entrainment type, described in section 2.2, as the principal source of mass and momentum injections in the PSL.

Here, boundary conditions in the PSL model system implicitly represent the transition layer. In this sense, a Dirichlet boundary condition for mass and velocity imposes snow injection at the bottom region of the PSL. Since the equations describe the powder-snow mass in terms of concentration of volume $\alpha_s \in [0,1]$, the transition layer model must define an injected volume concentration α_{inj} driven by an injection velocity $\mathbf{u}_{inj}$.

Consider a volume V localized at the bottom region of the PSL. During the eruption entrainment process, the total injection flux F_{inj} passing through the bottom surface area A is given by:

$$F_{inj} = \Phi_{inj} \cdot \mathbf{S_f} = \rho_s \mathbf{u}_{inj} \cdot (A\mathbf{n}_b) \quad [kg \cdot s^{-1}], \tag{4.45}$$

[10] Physically, the Schmidt number has a direct relation to the flow strength. The increase in Sc means higher momentum diffusivity leading to an increase in the flow strength.

where $\Phi_{inj} = \rho_s \mathbf{u}_{inj}$ is the mass flux and $\mathbf{S_f} = A\mathbf{n}_b$ is the surface area vector pointing at the normal boundary vector $\mathbf{n}_b$ outwards the volume. Note that writing the mass in the equation above by terms of concentration of volume inevitably requires the volume V. In the following, the superscript $(\bigstar)^v$ will associate $\bigstar$ to the volume V, such as in the equation of the total powder-snow mass m^v inside the volume V:

$$m^v = \alpha_s^v \rho_s V. \tag{4.46}$$

Figure 38 – The injection of powder snow happens principally through the eruption entrainment process. For a control volume V, represented in the figure by the square/cube, in the bottom region of the PSL, mass flows upwards through the bottom surface area A. The volume concentration of the powder snow inside V increases with the mass inflow.

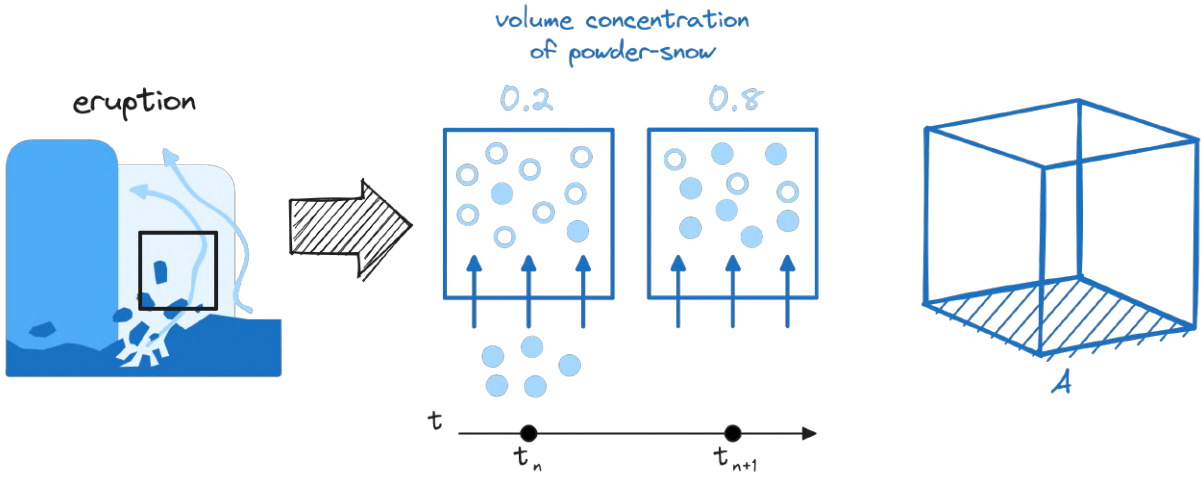

Source: Elaborated by the author.

Take the injection example in Figure 38, representing an increase of 0.6 in the value of α_s^v over time $\Delta t = t_{n+1} - t_n$. From Equation 4.45, the total amount of injected mass m_{inj}^v in this case is

$$m_{inj}^v = \alpha_{inj}^v \rho_s V = \Delta t F_{inj} = \Delta t (\rho_s \mathbf{u}_{inj}) \cdot (A\mathbf{n}_b), \tag{4.47}$$

which implies

$$\alpha_{inj}^v = \frac{A\Delta t}{V} \mathbf{u}_{inj} \cdot \mathbf{n}_b. \tag{4.48}$$

Over the years, researchers proposed models to compute m_{inj}^v and $\mathbf{u}_{inj}$. In particular, Carroll, Louge and Turnbull (2013) defines the mass flow rate in the two-dimensional eruption entrainment process as

$$F_{inj} = \rho_{sc}(\lambda h_{sc} \cos\theta W) u_{front}, \tag{4.49}$$

where ρ_{sc} is the snow cover density, h_{sc} is the snow cover depth, $\lambda \in [0,1]$ is the fraction of the snow cover layer entrained into the PSL, θ is the slope, W is the section width of the front region which the eruption flows through, and u_{front} is the front velocity.

Bartelt *et al.* (2016) breaks down the formation of the powder snow cloud into two processes: *air intake* and *ice-dust blow-out*. Both processes happen simultaneously but at different locations of the avalanche. As particles in the DSL collide with the ground, the *dispersive pressure* causes the DSL to expand, which causes air intake. Then, the downward motion of heavy particles displaces the enclosed air, causing the compression of the DSL. Therefore, the velocity of expansion/compression w_h causes the variation in the DSL height h_{dsl}:

$$\frac{\partial h_{dsl}}{\partial t} + \nabla \cdot (h_{dsl}\mathbf{u}_{dsl}) = w_h \quad [m \cdot s^{-1}], \tag{4.50}$$

where $\mathbf{u}_{dsl}$ is the DSL two-dimensional velocity parallel to the terrain. The variation rate of the DSL height, w_h, is a one-dimensional velocity perpendicular to the terrain and has its own formulation; w_h results from the mechanical energy caused by the sharing in the DSL body, leading to its variation in height. During the blow-out, i.e. the compression of the DSL, the mass flow into the PSL is defined as

$$F_{inj} = \begin{cases} (\rho \mathbf{u}_{inj}) \cdot (A\mathbf{n}_b), & w_h < 0, \\ 0, & otherwise, \end{cases} \tag{4.51}$$
$$\mathbf{u}_{inj} \cdot \mathbf{n}_b = 2w_h.$$

Recently, Ivanova *et al.* (2021) proposed a depth-averaged model with turbulence applied to powder–snow avalanches simulations. The model splits the velocity along the depth $u = U + u'$ into mean velocity U and fluctuation velocity u' components. The mass balance for the depth-averaged model due to entrainment is

$$\frac{\partial \hat{h}_{psl}}{\partial t} + \frac{\partial (\hat{h}_{psl} U)}{\partial x} = S_e + S_a, \tag{4.52}$$

where $\hat{h}_{psl}$ is the cloud height with entrainment (the model distinguishes the cloud height without air entrainment h_{psl}, and with air entrainment $\hat{h}_{psl}$), S_e and S_a are the snow and air entrainment souce terms, respectively. The air entrainment, caused by turbulence, is described as

$$S_a = \begin{cases} (\alpha_U U + \alpha_T \sqrt{\langle u'^2 \rangle}) \frac{\hat{\rho}}{\rho}, & \hat{\rho} > 2\rho_a, U > 0 \\ 0, & otherwise, \end{cases} \tag{4.53}$$

where $\langle u'^2 \rangle = \frac{1}{h} \int_0^h u'^2 dz$ is the variance of velocity fluctuations representing the turbulent kinetic energy, $\alpha_U \in [0,1]$ is the steady entrainment coefficient, $\alpha_T \in [0,1]$ is the turbulent entrainment coefficient, and $\hat{\rho}$ is the mean density of the cloud and follows the relationship $\rho h = \hat{\rho}\hat{h}$. The snow entrainment follows an alternative approach by defining an oscillatory injection velocity $U_e(x,t)$ based on a Gaussian pulse of half-length L_0 and amplitude A_0,

$$U_e = A_0 \exp\left[-\frac{(x - x_0 - S_0 t)^2}{2 \cdot L_0^2} \right], \tag{4.54}$$

where S_0 is the propagation velocity of the pulse and x_0 is the starting position of core at time $t = 0$. The suggested values for the densities are $\rho = 7\ kg/m^3$ and $\rho_0 = 10\ kg/m^3$. The final snow entrainment term is given by

$$S_e = \frac{\rho}{\rho_0} U_e. \tag{4.55}$$

The methods described above are only a few examples of a diversity of entrainment models proposed by researchers throughout the years — see subsection 3.4.4 on page 98. The remaining section proposes the method adopted in this project, supported by the concepts presented by the methods listed above.

Injection Velocity ($\mathbf{u}_{inj}$)

The injection velocity is responsible for an increase in the momentum of the PSL by injecting kinetic energy into the system. The acceleration of the fluid at the front has numerous sources, such as the displacement of air caused by the ejection of snow mass from the ground (snow blow-out) and air intake. These factors produce the violent suspension process that forms the snow cloud.

The ejection of snow mass upwards is proportional to the velocity of change in the DSL's height, $2w_h$, listed in Equation 4.51. The acceleration caused by the entrainment air follows the front velocity $\mathbf{u}_{front}$. Therefore, the injection velocity is the combination of both:

$$\mathbf{u}_{inj} = (2w_h + \omega_{\mathbf{u}} \parallel \mathbf{u}_{front} \parallel)(-\mathbf{n}_b), \tag{4.56}$$

where $\mathbf{u}_{front}$ is the front velocity vector. Note that $\mathbf{u}_{inj}$ has the same direction of $(-\mathbf{n}_b)$[11], parallel to the normal of the terrain.

The term $\omega_{\mathbf{u}}$ accounts for air intake and turbulent motion from the intermittent region. Due to the turbulent nature of the PSL, this factor is generalized as a random perturbation:

$$\omega_{\mathbf{u}} \approx \omega_s + \omega_t, \tag{4.57}$$

where ω_s is a steady factor and ω_t is a perturbation factor caused by turbulence.

As later detailed in subsection 5.1.3, $\omega_{\mathbf{u}}$ is further reduced into a noise function. Note also that the boundary conditions for the velocity field must include the DSL motion, so the velocity at the boundary is defined as

$$(\mathbf{u})_b = \mathbf{u}_{inj} + \mathbf{u}_{dsl}. \tag{4.58}$$

Concentration of Volume Injection (α_{inj})

As mentioned earlier, the concentration of volume α_{inj} builds from the volume and the total amount of mass entrained at a given time. Analogous to Bartelt's w_h term in Equation 4.50, the variation rate in the DSL's height h_{dsl} can be extracted from the right-hand side of

[11] Recall that $\mathbf{n}_b$ points outwards the PSL volume, i.e. downwards into the terrain.

Equation 4.11

$$\frac{\partial h'}{\partial t} + \nabla \cdot (h' \bar{\mathbf{u}}) = \frac{q_e}{\rho}$$

of the DSL model presented in section 4.2. Let Q_e represent such term, respective to w_h, so

$$Q_e = \frac{q_e}{\rho_{dsl}}. \tag{4.59}$$

The total mass m_e entrained over the period Δt through an area A is given by:

$$m_e = Q_e \rho_{dsl} A \Delta t, \tag{4.60}$$

which is converted for the correspondent volume V as a volume concentration as

$$\alpha^v_{inj} = \frac{m_e}{M^v}, \tag{4.61}$$

where M^v is total mass capacity of the PSL volume V defined as

$$M^v = \rho_{psl} V. \tag{4.62}$$

4.3.2 Numerical Model

This section describes the numerical treatment of the core system of the governing equations described in section 4.3. The finite volume method, introduced in the appendix section B.1 on page 205, solves the equations by discretizing them over the decomposition of the physical domain into cells called *finite volumes* — see Figure 39. The FVM integrates the equations for each cell volume and uses the cell boundary fluxes to discretize the volume integrals[12]. A detailed description of the discretization process is presented in Appendix B, section B.1 on page 205. Therefore, this section only briefly and directly discusses the numerical model used to solve the equations.

Each cell in the grid spans an equation that composes the final system of numerical equations. For a given cell C with center C_c, the flux of a quantity ϕ passing through the cell face f_i is computed in the face center f_{ci} and is represented by $(\phi \cdot \mathbf{u})_{f_{ci}} \cdot \mathbf{S}_{\mathbf{f}i}$, where $\mathbf{S}_{\mathbf{f}i}$ is the face area vector pointing outwards the cell — see Figure 39. The following equations are written in terms of C, where the subscripts $(\bigstar)_{C_c}$ and $(\bigstar)_{f_{ci}}$ represent quantities evaluated at the cell center C_c and the face center f_{ci}, respectively.

The iterative numerical method uses the PIMPLE algorithm, see section C.3 on page 227, which loops through a *prediction-correction* pair of phases that build up the solution for each time step in the simulation. In this case, the PIMPLE algorithm is adapted to include Equation 4.43, the equation for α_s. Source code 2 describes the final algorithm of the PSL model, and the following list details the functions in the code. In the equations, the superscript $(\bigstar)^o$ refers to values from previous time steps or loop iterations.

[12] See the Divergence theorem in subsection B.1.1 on page 207.

Figure 39 – The FMV splits the physical domain into a volumetric mesh where the equations are discretized in each grid cell. The discretization process uses the fluxes passing through the faces of each cell. The flux in a face is defined by $(\phi\mathbf{u})_{f_c} \cdot \mathbf{S_f}$, where $\mathbf{S_f}$ is the face area vector pointing outward the cell, and ϕ is the quantity being transported by the velocity $\mathbf{u}$.

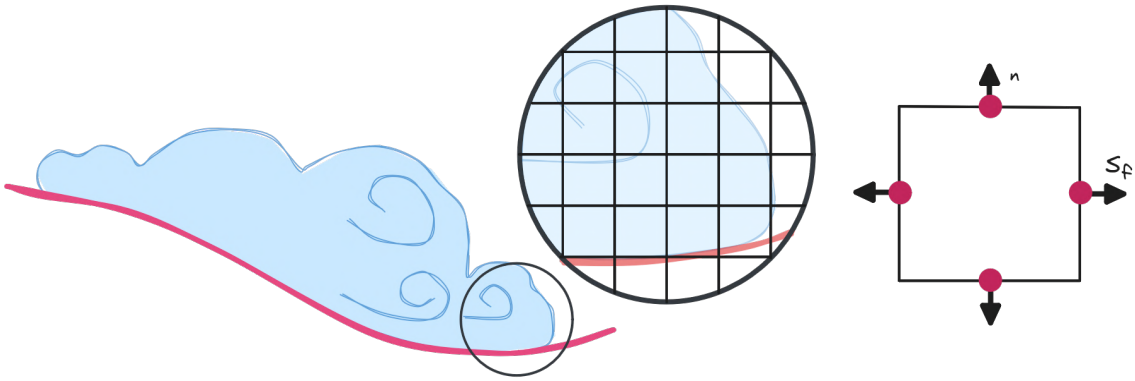

Source: Elaborated by the author.

Source code 2 – PSL Algorithm.

```
1:      u = u_0; p = p_0; rho = rho_0;
2:      for(t = t_0; t < t_final; t += dt) {
3:          // solve alpha equation and update rho
4:          rho = updateMixtureDensity(u);
5:          while(PIMPLE.loop()) {
6:              u_star = predictMomentum(rho, u, p);
7:              while(PIMPLE.correct()) {
8:                  p = correct(u_star, p);
9:              }
10:         }
11:     }
```

- `updateMixtureDensity`($\mathbf{u}^o$, α_s^o)

  The first action in every new time step iteration, right before the PIMPLE loop, is the computation of a new value of ρ. The mixture density ρ, recalling Equation 4.27,

$$\rho = \alpha_s \rho_s + \alpha_a \rho_a,$$

  is required by the momentum equation, Equation 4.41, and is computed through α_s, solved by Equation 4.44:

$$\frac{\partial \alpha_s}{\partial t} + \nabla \cdot (\mathbf{u}^o \alpha_s) = \nabla \cdot \left(D_{AB} \nabla \alpha_s \right).$$

Here, a sequential operator splitting similar to Greenshields *et al.* (2010) can be used[13]. First, just the inviscid portion of the equation is explicitly solved for α_s^I (with the superscript $(\bigstar)^I$ referring to as the inviscid solution), given by

$$\frac{\partial \alpha_s^I}{\partial t} + \underbrace{\nabla \cdot (\mathbf{u}^o \alpha_s^o)}_{\text{advection}} = 0. \tag{4.63}$$

In order to guarantee boundedness in the solution of the advective term marked above, advection is solved explicitly by a *flux-correction transport method*[14], which provides a bounded value for the fluxes $(\alpha_s^o \mathbf{u}^o)_{fci}$. The resulting α_s^I is assigned to α_s and a second equation containing the diffusion contribution is built:

$$\underbrace{\frac{\partial \alpha_s}{\partial t}}_{1} - \underbrace{\frac{\partial \alpha_s^I}{\partial t}}_{2} = \underbrace{\nabla \cdot \left(D_{AB} \nabla \alpha_s \right)}_{3}. \tag{4.64}$$

The equation above is solved by the numerical system

$$\mathbf{A}_\alpha [\alpha_s] = \mathbf{b}_\alpha, \tag{4.65}$$

where each numbered term in Equation 4.64 is translated into the system by the corresponding discretization:

1. $\boxed{\frac{\partial \alpha_s}{\partial t}}$

   The transient term is descritized by the first-order implicit Euler:

   $$\frac{C_V}{\Delta t} (\alpha_s - \alpha_s^o)_{C_c}, \tag{4.66}$$

   where C_V is the volume of the cell. Here and in the following equations, the coefficients multiplying α_s are entries in the matrix $\mathbf{A}_\alpha$[15], and coefficients multiplying known values $(\bigstar)^o$ are components of $\mathbf{b}_\alpha$.

2. $\boxed{\frac{\partial \alpha_s^I}{\partial t}}$

   The explicit transient term is descritized by the first-order implicit Euler and contributes only to the right-hand side:

   $$\frac{C_V}{\Delta t} (\alpha_s^I - \alpha_s^o)_{C_c}. \tag{4.67}$$

[13] The idea is to split the equation into two equations: the *inviscid equation*, that accounts only for inviscid contributions and the *diffusion correction equation* that includes the diffusion term and the rest.

[14] See MULES in Appendix C, section C.2

[15] Terms related to $(\bigstar)_{C_c}$ correspond to diagonal entries of $\mathbf{A}_\alpha$, while the remaining correspond to off-diagonal entries.

3.

$$\boxed{\nabla \cdot \left(D_{AB} \nabla \alpha_s \right)}$$

Considering the coefficients above constant, the laplacian term follows the same procedure detailed in subsection B.1.6 on page 218 in Appendix B:

$$\begin{aligned}
\Gamma \triangle \alpha_s &\approx \sum_{f_i \in S} (\nabla_{\mathbf{n}_i} \alpha_s)_{f_{ci}} S_{f_i} \\
&\approx a_C (\alpha_s)_{C_c} + \sum_{f_i \in S} a_{N_i} (\alpha_s)_{N_{ci}} + b_C, \\
a_C &= \Gamma \sum_{f_i \in S} \not\perp_{corr_i} S_{f_i}, \\
a_{N_i} &= -\Gamma \not\perp_{corr_i} S_{f_i}, \\
b_C &= \Gamma \sum_{f_i \in S} (\nabla \alpha_s^o)_{f_{ci}} \cdot (\mathbf{n}_i - \not\perp_{corr_i} \mathbf{d}_i) S_{f_i} \\
\Gamma &= D_{AB},
\end{aligned} \tag{4.68}$$

where $\mathbf{d}_i = N_{ci} - C_c$, and $\not\perp_{corr_i}$ is a non-orthogonal correction factor as described in subsection B.1.4 on Appendix B.

The resulting value of α_s provides the new value for ρ[16].

- $\mathbf{u}^\star \leftarrow$ `predictMomentum`$(\rho, \mathbf{u}^o, p^o)$

  In the **momentum prediction** phase, an intermediary velocity field $\mathbf{u}^\star$ is computed from the new value of ρ and previous values of velocity and pressure $(\rho, \mathbf{u}^o, p^o)$. This field is the solution of the the numerical system

$$\mathbf{A}\mathbf{u}^\star = \mathbf{b}, \tag{4.69}$$

  built from the FVM discretization of the momentum equation, Equation 4.41:

$$\underbrace{\frac{\partial \rho^o \mathbf{u}^\star}{\partial t}}_{1} + \underbrace{\nabla \cdot (\rho^o \mathbf{u}^o \otimes \mathbf{u}^\star)}_{2} = \underbrace{-\nabla p^o_{rgh} - \mathbf{g} \cdot \mathbf{h} \nabla \rho^o}_{3} + \underbrace{\nabla \cdot \tau^\star}_{4}, \tag{4.70}$$

  where each term in the equation translates as:

1.

$$\boxed{\frac{\partial \rho^o \mathbf{u}^\star}{\partial t}}$$

The transient term is descritized by the first-order implicit Euler:

$$\frac{C_V}{\Delta t} (\rho^o)_{C_c} \mathbf{u}^\star = \frac{C_V}{\Delta t} (\rho^o \mathbf{u}^o)_{C_c}. \tag{4.71}$$

[16] Recall $\alpha_a = 1 - \alpha_s$, therefore $\rho = \alpha_s \rho_s + (1 - \alpha_s) \rho_a$.

2.

$$\boxed{\nabla \cdot (\rho^o \mathbf{u}^o \otimes \mathbf{u}^\star)}$$

The convective term follows the usual choice for large eddy simulations, the linear scheme, sacrificing boundedness for accuracy:

$$\sum_{f_i \in S} (w_i \Phi^o)_{f_{ci}} \otimes (\mathbf{u}^\star)_{C_c} + \sum_{f_i \in S} (-w_i \Phi^o + \Phi^o)_{f_{ci}} \otimes (\mathbf{u}^\star)_{N_{ci}}, \tag{4.72}$$

where $\Phi^o = \rho^o \mathbf{u}^o$ is the mass flux, and w_i is the interpolation weight based on the cell center to face centers distances, $\mathbf{d}_C = f_{ci} - C_c$ and $\mathbf{d}_{Ni} = N_{ci} - f_{ci}$:

$$w_i = \frac{\mathbf{n} \cdot \mathbf{d}_{Ni}}{\mathbf{n} \cdot (\mathbf{d}_C + \mathbf{d}_{Ni})}. \tag{4.73}$$

3.

$$\boxed{-\nabla p^o_{rgh} - \mathbf{g} \cdot \mathbf{h} \nabla \rho^o}$$

The scalar gradient discretization for the source terms produce the following contributions to the right hand side of the system:

$$-\sum_{f_i \in S} (p^o_{rgh})_{f_{ci}} \mathbf{S}_{\mathbf{f}i} - \mathbf{g} \cdot \mathbf{h} \sum_{f_i \in S} (\rho^o)_{f_{ci}} \mathbf{S}_{\mathbf{f}i}, \tag{4.74}$$

where $\mathbf{h} = C_c$.

4.

$$\boxed{\nabla \cdot \tau^\star}$$

The expansion of the tensor term is[17]:

$$\begin{aligned} \nabla \cdot \tau^\star &= \mu \triangle \mathbf{u}^\star + \mu \nabla \cdot \mathbf{Dev}^o, \\ \mathbf{Dev}^o &= (\nabla \otimes \mathbf{u}^o)^T - \frac{2}{3} \mathrm{tr}((\nabla \otimes \mathbf{u}^o)^T) \mathbf{I}, \end{aligned} \tag{4.75}$$

where the explicit terms are discretized as

$$\begin{aligned} (\nabla \otimes \mathbf{u}^o)_{C_c} &\approx \frac{1}{C_V} \sum_{f_i \in S} (\mathbf{u}^o)_{f_{ci}} \otimes \mathbf{S}_{\mathbf{f}i}, \\ (\nabla \cdot \mathbf{Dev}^o)_{C_c} &\approx \frac{1}{C_V} \sum_{f_i \in S} (\mathbf{Dev}^o)_{f_{ci}} \cdot \mathbf{S}_{\mathbf{f}i}. \end{aligned} \tag{4.76}$$

[17] Recalling the definition of τ by Equation 4.33, and noting that for any matrix $\mathbf{M}$

$$\mathrm{tr}(\frac{1}{2}(\mathbf{M} + \mathbf{M}^T)) = \mathrm{tr}(\mathbf{M}) = \mathrm{tr}(\mathbf{M}^T),$$

the term expands as:

$$\begin{aligned} \nabla \cdot \tau &= \nabla \cdot (\underbrace{2\mu \mathbf{D}}_{\text{expand}} - \frac{2}{3} \mu \underbrace{\mathrm{tr}(\mathbf{D})}_{\text{expand}} \mathbf{I}) \\ &= \nabla \cdot (\overbrace{\mu \nabla \otimes \mathbf{u} + \mu (\nabla \otimes \mathbf{u})^T}^{} - \frac{2}{3} \mu \overbrace{\mathrm{tr}((\nabla \otimes \mathbf{u})^T)}^{} \mathbf{I}) \\ &= \mu \triangle \mathbf{u} + \mu \nabla \cdot ((\nabla \otimes \mathbf{u})^T - \frac{2}{3} \mathrm{tr}((\nabla \otimes \mathbf{u})^T) \mathbf{I}) \end{aligned}$$

Note that assuming the mixture incompressible, recalling Equation 4.37, the deviatoric term becomes

$$\mathbf{Dev}^o = (\nabla \otimes \mathbf{u}^o)^T.$$

The laplacian term $\mu \triangle \mathbf{u}^\star$ follows the same procedure detailed in subsection B.1.6 on page 218 in Appendix B:

$$\begin{aligned}
\mu \triangle \mathbf{u}^\star &\approx \sum_{f_i \in S} (\nabla_{\mathbf{n}_i} \otimes \mathbf{u}^\star)_{f_{ci}} S_{f_i} \\
&\approx a_C(\mathbf{u}^\star)_{C_c} + \sum_{f_i \in S} a_{N_i}(\mathbf{u}^\star)_{N_i} + b_C, \\
a_C &= \mu \sum_{f_i \in S} \not\perp_{corr_i} S_{f_i}, \\
a_{N_i} &= -\mu \not\perp_{corr_i} S_{f_i}, \\
b_C &= \mu \sum_{f_i \in S} (\nabla \otimes \mathbf{u}^o)_{f_{ci}} \cdot (\mathbf{n}_i - \not\perp_{corr_i} \mathbf{d}_i) S_{f_i}.
\end{aligned} \tag{4.77}$$

The final form of the discretization in the system becomes:

$$-a_C(\mathbf{u}^\star)_{C_c} - \sum_{f_i \in S} a_{N_i}(\mathbf{u}^\star)_{N_i} = b_C + (\nabla \cdot \mathbf{Dev}^o)_{C_c}. \tag{4.78}$$

- `correct`$(\mathbf{u}^\star, p^o_{rgh})$

  The momentum prediction step provides an estimate for the velocity $\mathbf{u}^\star$ by solving the system

  $$\mathbf{A}\mathbf{u}^\star = \mathbf{b}.$$

  However, the system above does not include the continuity equation, $\nabla \cdot \mathbf{u} = 0$, and therefore, $\mathbf{u}^\star$ is not a divergence-free field. Also, the system does not compute the coupled pressure field p_{rgh}; instead, it uses a previous pressure field p^o_{rgh}. A new pressure field p computed from $\mathbf{u}^\star$ completes the coupled solution and fixes $\mathbf{u}^\star$.

  The pressure equation is constructed by substituting the continuity equation into the divergence of the momentum equation, see section C.3 on page 227. In FVM, the **pressure equation** is defined as

  $$\underbrace{\nabla \cdot \frac{1}{A_{diag}} \nabla p_{rgh}}_{1} = \underbrace{\nabla \cdot \left(\frac{\mathbf{B}(\mathbf{u}^\star)}{A_{diag}} \right)}_{2}. \tag{4.79}$$

  The terms A_{diag} and $\mathbf{B}(\mathbf{u}^\star)$ come from the system

  $$A_{diag}\mathbf{u}^\star = \mathbf{B}(\mathbf{u}^\star) - \nabla p_{rgh}, \tag{4.80}$$

  where the pressure term is separated from the original system, $\mathbf{A}_{diag}$ contains only the diagonal entries of the resulting system without the pressure term, and $\mathbf{B}(\mathbf{u}^\star)$ contains all off-diagonal elements and source terms:

  $$\mathbf{B}(\mathbf{u}^\star) = -(\mathbf{A} - A_{diag})\mathbf{u}^\star + b. \tag{4.81}$$

Equation 4.79 is solved by the system

$$\mathbf{A}_p[p_{rgh}] = \mathbf{b}_p, \tag{4.82}$$

and each numbered term in the equation translates into the system as:

1. $$\boxed{\nabla \cdot \frac{1}{A_{diag}} \nabla p_{rgh}}$$

   The laplacian of the pressure is discretized as in Equation 4.77, resulting in

   $$-a_C(p_{rgh})_{C_c} - \sum_{f_i \in S} a_{N_i}(p_{rgh})_{N_i} = b_C, \tag{4.83}$$

   with appropriate coefficient values.

2. $$\boxed{\nabla \cdot \left(\frac{\mathbf{B}(\mathbf{u}^\star)}{A_{diag}}\right)}$$

   The divergence term is explicitly solved, i.e. it becomes a source term discretized as

   $$\sum_{f_i \in S} \left(\frac{\mathbf{B}(\mathbf{u}^\star)}{A_{diag}}\right)_{f_{ci}} \cdot \mathbf{S}_{\mathbf{f}i}, \tag{4.84}$$

   where the terms bellow come from the momentum equation discretization described earlier:

   $$\left(\frac{\mathbf{B}(\mathbf{u}^\star)}{A_{diag}}\right)_{C_c} = \frac{1}{A_{diag}} \Big(\underbrace{\frac{C_V}{\Delta t}(\rho^o \mathbf{u}^o)_{C_c}}_{\text{Equation 4.71}} + \underbrace{-\mathbf{g} \cdot \mathbf{h} \sum_{f_i \in S} (\rho^o)_{f_{ci}} \mathbf{S}_{\mathbf{f}i}}_{\text{Equation 4.74}} + \underbrace{b_C + (\nabla \cdot \mathbf{Dev}^o)_{C_c}}_{\text{Equation 4.78}} \Big). \tag{4.85}$$

With the new value of p_{rgh}, the velocity field $\mathbf{u}^\star$ can be corrected with

$$\mathbf{u} \leftarrow \frac{\mathbf{B}(\mathbf{u}^\star)}{A_{diag}} - \frac{\nabla p_{rgh}}{A_{diag}}, \tag{4.86}$$

where $\mathbf{u}$ is the new divergence-free velocity field.

4.4 Remarks

- The DSL model consists of Equation 4.11, Equation 4.6, and Equation 4.7, respectively:

$$\frac{\partial h'}{\partial t} + \nabla \cdot (h' \bar{\mathbf{u}}) = \frac{q_e}{\rho},$$

$$\frac{\partial (h' \bar{\mathbf{u}})}{\partial t} + \nabla_S \cdot (h' \bar{\mathbf{u}} \otimes \bar{\mathbf{u}}) = -\frac{\tau_b}{\rho} + h' \mathbf{g}_S - \frac{1}{2\rho} \nabla_S (h' p_b),$$

$$\nabla_n \cdot (h' \bar{\mathbf{u}} \otimes \bar{\mathbf{u}}) = h' \mathbf{g}_n - \frac{1}{2\rho} \nabla_n (h' p_b) - \frac{1}{\rho} \mathbf{n} p_b,$$

where q_e is given by Equation 4.9 and τ_b is given by Equation 4.13.

- The PSL model consists of Equation 4.28, Equation 4.41, and Equation 4.43, respectively:

$$\nabla \cdot \mathbf{u} = 0,$$

$$\frac{\partial \rho \mathbf{u}}{\partial t} + \nabla \cdot (\rho \mathbf{u} \otimes \mathbf{u}) = -\nabla p_{rgh} - \mathbf{g} \cdot \mathbf{h} \nabla \rho + \nabla \cdot \tau,$$

$$\frac{\partial \alpha_s}{\partial t} + \nabla \cdot (\mathbf{u} \alpha_s) = \nabla \cdot \left(D_{AB} \nabla \alpha_s \right),$$

  where τ is given by Equation 4.36.

- Table 6 lists the terms and constants in the DSL and PSL models.

Table 6 – Model parameters values.

Model	Parameter	Description
DSL	ρ	Snow density $[kg \cdot m^{-3}]$
	μ	Voellmy's dry friction
	ξ	Voellmy's dynamic friction $[m \cdot s^{-2}]$
	e_b	Erosion energy
PSL	ρ_a	Air density $[kg \cdot m^{-3}]$
	μ_a	Air viscosity $[m^2 \cdot s^{-1}]$
	ρ_s	Powder-snow density $[kg \cdot m^{-3}]$
	μ_s	Powder-snow viscosity $[m^2 \cdot s^{-1}]$
	D_{ab}	Molecular diffusivity
	ν_t	Turbulent eddy viscosity
	S_C	Turbulent Schmidt number

- The PSL model builds upon the simplifaction that the mixture fluid of snow and air is incompressible.

- The PSL model is agnostic of the DSL model used, which means that other DSL models serving the same type of information can replace the presented DSL model. The PSL model requires only the DSL height field $h_{dsl}(\mathbf{x})$, surface-tangential field $\mathbf{u}_{dsl}(\mathbf{x})$, and the height variation rate $w_h(\mathbf{x})$.

- The transition layer becomes a set of Dirichlet boundary conditions for the PSL's bottom boundary, particularly for the PSL velocity field $\mathbf{u}$ and volume concentration of snow field α.

- An extra oscillatory term applied to the resulting quantities of the transition layer emulates the intermittent behavior caused by turbulence in the front of the avalanche.

CHAPTER

5

RESULTS

This chapter describes the final pieces to build the system for producing animations of powder-snow avalanches, which includes the creation of the numerical meshes, choosing the values for the parameters of the models, and exporting animation data.

The following section describes all remaining numerical details to complete the simulation workflow. A discussion and analysis of the method is presented in section 5.2 on page 142. Before presenting the final results, section 5.3 on page 151 quickly describes how simulation data is converted into renderable geometry. The chapter finalizes with section 5.4 on page 157, presenting the final results of avalanches simulated on natural terrain surfaces.

5.1 Numerical Setup

As described in the previous chapter, the numerical solutions require discretizing the governing equations over decomposing the physical domain into a set of discrete cells for each simulation. Each cell contains estimates of physical quantities, such as the velocity field $\mathbf{u}$ or the concentration of volume α_s. The transport of such quantities between the cells manifests as fluxes through their boundaries. Each cell spans a discrete version of the governing equation based on its fluxes and cell values, and the set of such equations produces a numerical system. The system produces new values for the physical fields that evolve over simulation time, generating data for each animation frame.

The following subsections detail the process described above for each PSA layer. Each subsection describes the remaining pieces for each simulation: the numerical grid, the *boundary conditions*[1], and the numerical solvers. One extra subsection discusses the implementation of the transition layer.

[1] As mentioned, the fluxes used in the discretizations require a pair of cells. However, cells at the mesh's boundary lack neighbors and need boundary conditions to complete their discretizations. Refer to subsection B.1.7 on how the FVM discretizes such boundary conditions.

5.1.1 DSL

Numerical Grid

The numerical grid used in the simulation of the DSL is a three-dimensional discrete surface represented by a set of two-dimensional flat[2] polygonal cells individually bounded by straight edges.

In simulation setups where the terrain is a plane, a set of regular cells poses no difficulties for the numerical solution. However, in natural terrains with high curvatures, other polygonal alternatives, such as triangular meshes, can produce mesh elements that better adapt to the terrain. Particularly, the **pMesh**[3] structure provided by OpenFOAM offers a flexible solution. The **pMesh** fills a triangular mesh volume with a polyhedral mesh, composed mainly of hexahedra, providing various benefits for subdivision and adaptiveness. The boundary surface of a **pMesh** may be used as the DSL numerical grid. Figure 40 shows the two types of mesh described above.

Figure 40 – Two examples of meshes tessellating the same patch of terrain. On the left is a regular quadrangular mesh. On the right is a polyhedral mesh that is well adapted for terrains with complex geometries.

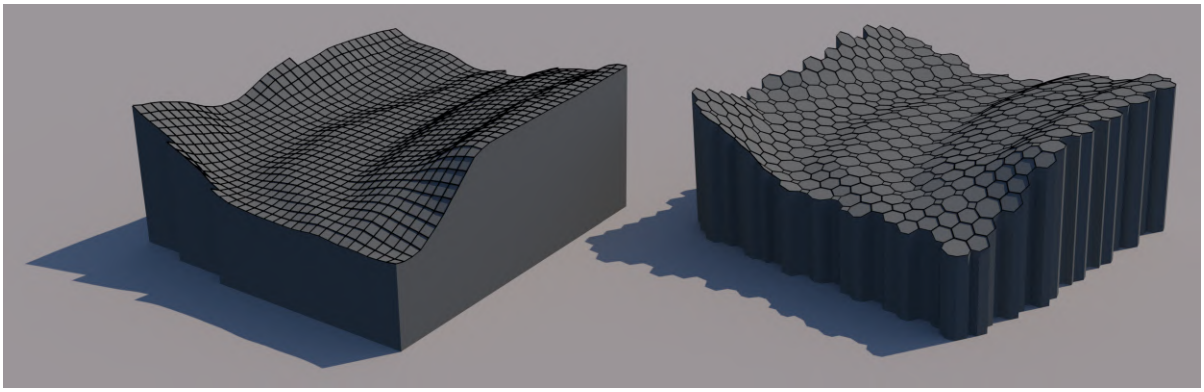

Source: Elaborated by the author.

Boundary Conditions

The DSL model consists of Equation 4.11, Equation 4.6, Equation 4.7. The equations contain three unknown variables: the velocity field $\bar{\mathbf{u}}(\mathbf{x})$, the basal pressure field $p_b(\mathbf{x})$, and the DSL height field $h'(\mathbf{x})$. Since the basal pressure is explicitly solved inside the momentum equation, the method needs boundary conditions for only the velocity and the avalanche height fields. As listed in Table 7[4], a Neumann condition is used in all boundary edges for all fields.

[2] Note that in practice, the vertices of a cell may not be coplanar.

[3] The **pMesh** is a meshing option of the meshing library called *cfMesh*, incorporated in OpenFOAM. See <https://cfmesh.com/>.

[4] Recall the normal gradient $\nabla_{\mathbf{m}}$ along the direction edge bi-normal vector $\mathbf{m}$. See section B.2 in Appendix B.

Table 7 – DSL Boundary Conditions.

Variable	Boundary	Condition
$\bar{\mathbf{u}}$	All	$\nabla_{\mathbf{m}}\bar{\mathbf{u}} = 0$
h'	All	$\nabla_{\mathbf{m}}h' = 0$

Accuracy

The following tables give information on the solution of the numerical method described in subsection 4.2.1. Table 8 lists the numerical schemes for interpolation used in each discretization term, and Table 9 shows the numerical solvers for each numerical system.

The *upwind* scheme was used to compute all convection terms, while all transient terms were discretized with the *backward* Euler scheme. The gradient terms were directly discretized via the Divergence theorem, where all variables were computed at face centers by linear interpolation. The *boundedness* column in Table 8 indicates if the scheme produces resulting values within the original bounds of their respective fields in the cells.

Table 8 – DSL Numerical Schemes.

Term	Scheme	Boundedness	Accuracy
$\nabla_S \cdot (h^o \bar{\mathbf{u}}^o \otimes \bar{\mathbf{u}})$	Upwind	Bounded	First-Order
$\nabla \cdot (h \bar{\mathbf{u}}^o)$	Upwind	Bounded	First-Order
$\partial \bigstar / \partial t$	Backward Time	-	Second-Order
$\nabla_S (h^o p_b^o)$	Gauss w/ Linear Interpolation	Unbounded	Second-Order

Both numerical systems were solved with Preconditioned bi-conjugate gradient (PBiCGStab)[5] (VORST, 1992) along with the Diagonal-based Incomplete LU (DILU) preconditioner.

Table 9 – DSL Numerical Solvers.

System	Solver	Preconditioner
$\mathbf{A}\bar{\mathbf{u}} = \mathbf{b}$	PBiCGStab	DILU
$\mathbf{A}_h[h] = \mathbf{b}_h$	PBiCGStab	DILU

5.1.2 PSL

Numerical Grid

The numerical grid used in the simulation of the PSL is a three-dimensional discrete volume represented by a set of three-dimensional cells individually bounded by flat faces.

Similar to DSL surface decompositions, the three-dimensional cells in the PSL grid may consist of regular aligned boxes or more complex polygonal shapes. Note that regardless of the choice of element type, mesh generation algorithms may still produce non-planar faces and

[5] The PBiCGStab is designed for numerical systems with an assymetric matrix $\mathbf{A}$, usually produced by terms like the advection.

concave cells. Figure 41 shows two examples of three-dimensional meshes, one consisting of axis-aligned boxes and the second resulting from the **pMesh** structure mentioned earlier.

Figure 41 – Examples of PSL numerical grids. On the left, a mesh consisting of axis-aligned boxes extruded from a quadrangular surface mesh. On the right, a polyhedral mesh with varying element types and sizes.

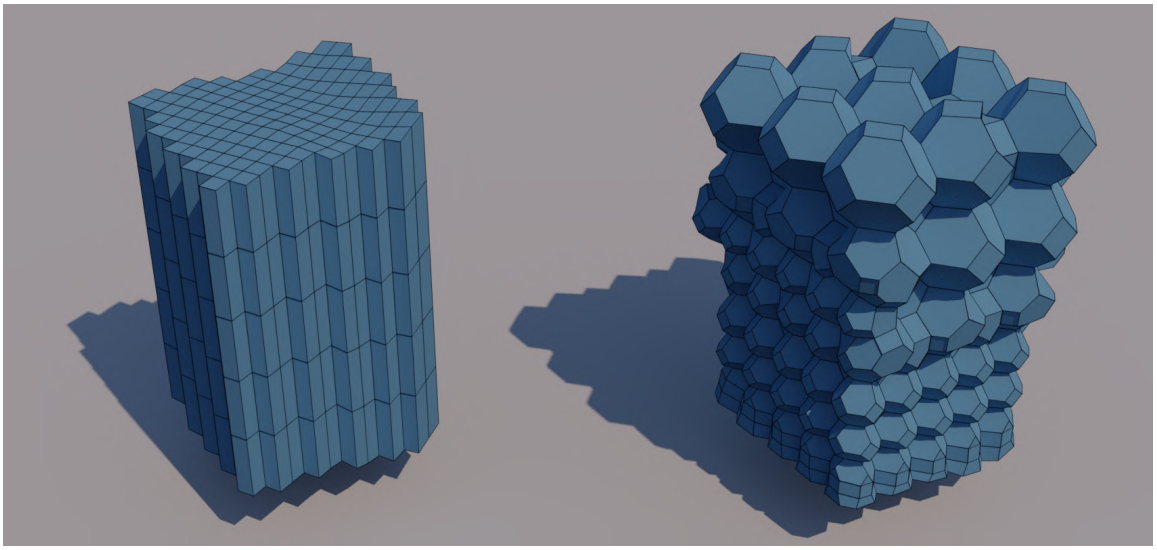

Source: Elaborated by the author.

Boundary Conditions

The PSL model consists of Equation 4.28, Equation 4.41, and Equation 4.43. The equations contain three unknown variables: the velocity field $\mathbf{u}(\mathbf{x})$, the concentration of volume for the snow phase field $\alpha_s(\mathbf{x})$, and the hydrostatic pressure $p_{rgh}(\mathbf{x})$.

As shown by Figure 42, the boundary of the simulation domain is decomposed into six patches, one for each direction of the coordinates axis. Therefore, a boundary condition is defined for each variable over each patch. In particular, the **terrain** patch receives the boundary conditions for $\mathbf{u}$ and α_s that represent the transition layer.

The following list presents the considered options for boundary conditions, where $\bigstar$ denotes any field mentioned earlier, $\bigstar_b$ represents a defined value for this field at the boundary, and $\mathbf{n}_b$ is the normal of the boundary face pointing outwards the cell. Some conditions depend on the direction of the flow, dictated by $\mathbf{u} \cdot \mathbf{n}_b$, that characterizes *inflow* and *outflow* from the domain:

$$\begin{aligned} \mathbf{u} \cdot \mathbf{n}_b < 0 &\rightarrow \text{Inflow}, \\ \mathbf{u} \cdot \mathbf{n}_b > 0 &\rightarrow \text{Outflow}. \end{aligned} \tag{5.1}$$

- **Zero Gradient** — The Neumann boundary condition for zero flow.

$$\nabla_{\mathbf{n}_b} \bigstar = 0. \tag{5.2}$$

Figure 42 – Regardless of the shape of the simulation terrain, six patches comprise the boundaries of the numerical domain. Considering the slope alignment with the Cartesian axis x, each axis associates a pair of patches respectively: **Back** and **Front** in $\pm y$ directions, **Top** and **Terrain** in $\pm z$, and **Right** and **Left** in $\pm x$.

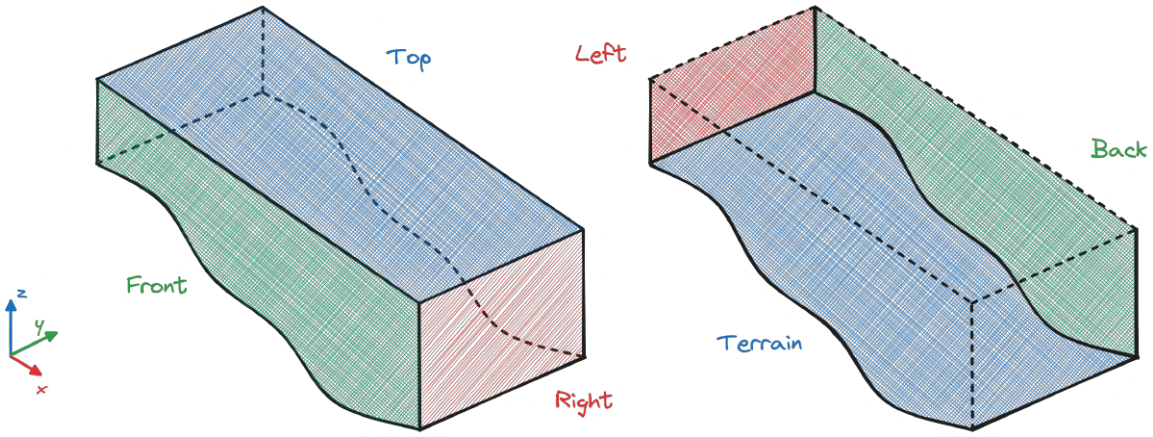

Source: Elaborated by the author.

- **Dirichlet** — Uses a known value $\bigstar_b$ for the field.

$$\bigstar = \bigstar_b. \tag{5.3}$$

- **Free** — Allows inflow and outflow.

$$\begin{cases} \bigstar = \bigstar_b, & \text{Inflow}, \\ \nabla_{\mathbf{n}_b} \bigstar = 0, & \text{Outflow}. \end{cases} \tag{5.4}$$

- **Free Velocity** — Allows velocity inflow and outflow on boundaries with Dirichlet condition for pressure.

$$\begin{cases} \mathbf{u} = -\mathbf{u} \cdot \mathbf{n}_b, & \text{Inflow}, \\ \nabla_{\mathbf{n}_b} \mathbf{u} = 0, & \text{Outflow}. \end{cases} \tag{5.5}$$

- **Slip** — Allows only tangential velocities at the boundary.

$$(\mathbf{u})_{\mathbf{n}_b} = 0. \tag{5.6}$$

- **No Slip**

$$\mathbf{u} = 0. \tag{5.7}$$

- **Total Pressure**

$$\begin{cases} p_{rgh} = p_0 - \frac{1}{2}|\mathbf{u}|^2, & \text{Inflow}, \\ p_{rgh} = p_0, & \text{Outflow}, \end{cases} \tag{5.8}$$

where p_0 is a reference pressure value.

- **Fixed Flux Pressure** — Ensures no flux

$$\nabla p_{rgh} = \frac{\phi_{H/A} - \phi}{|S_f| D_p}. \tag{5.9}$$

The choices of the different types of boundary conditions listed above have an impact not only on the physical modeling of the problem but also on the stability of the numerical solution. The cubical shape of the physical domain described earlier, given by the six boundary patches, provides some combination options for boundary conditions. A natural choice is to consider all five patches, besides the *terrain* patch, as **open free** boundaries where mass can freely flow inwards and outwards — as in a large mountain. However, adding some constraints, such as wall boundaries, might increase the method's stability.

Figure 43 – Boundary patches can be modeled as closed or open boundaries. Mass will flow through open boundaries, which can be free (allowing inflow and outflow) or restricted to inflow or outflows. Although making all boundaries *free* makes sense (left), adding additional flow restrictions, such as the solid top on the right, may help the numerical method.

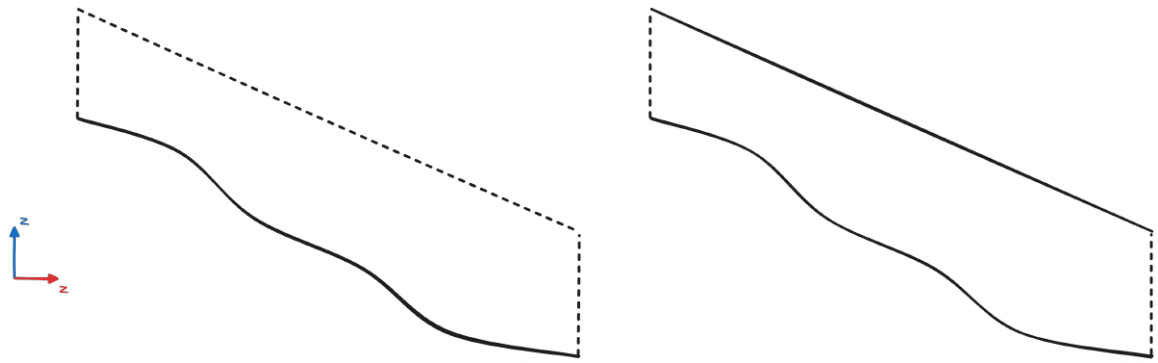

Source: Elaborated by the author.

Figure 43 depicts two possible configurations, which model the domain as an open box and a tunnel. Open boundaries are classified as **free**, **inlet**, and **outlet** boundaries. Inlet boundaries allow only inflow, and outlet boundaries allow only outflow. From our experiments, fixing a small velocity $\mathbf{u}_\varepsilon$ at the *left* and *right* patches, like a *wind tunnel*, produced more stable results. Table 10 details the wind tunnel approach described above, where front and back patches are modeled as walls. The values used in the terrain boundary condition are detailed later in subsection 5.1.3.

Table 10 – "Wind Tunnel" PSL Boundary Conditions.

		α_s	$\mathbf{u}$	p_{rgh}
Front/Back	wall	0	Slip	Zero Gradient
Left	outflow	Zero Gradient	$\mathbf{u}_\varepsilon$	Zero Gradient
Right	inflow	0	$\mathbf{u}_\varepsilon$	Zero Gradient
Top	free	Free	Free (with p_b)	Total Pressure
Terrain	-	α_{inj}	$\mathbf{u}_{inj}$	Fixed Flux Pressure

Accuracy

The following tables give information on the solution of the numerical method described in subsection 4.3.2. Table 11 lists the numerical schemes for interpolation used in each discretization term, and Table 12 shows the numerical solvers for each numerical system. The *vanLeer01* scheme listed in Table 11 is a TVD advection scheme[6], introduced by van Leer (1974), that uses limiter function to bound the results — in this case, to $[0,1]$, indicated by the *01* suffix.

Table 11 – PSL Numerical Schemes.

Term	Scheme	Boundedness	Accuracy
$\nabla\cdot(\rho\Phi\bar{\mathbf{u}})$	vanLeer	Unbounded	Second-Order
$\nabla\cdot(\Phi\alpha)$	vanLeer01	Bounded	Second-Order
$\partial\bigstar/\partial t$	Implicit Euler	-	First-Order
$\nabla(\mathbf{u})$	Cell limited Gauss w/ Linear Interpolation 1.0	Unbounded	Second-Order

The numerical systems were mainly solved by the PBiCGStab method along with the DILU preconditioner for $\mathbf{u}$ and the symmetric equivalent preconditioner, the Faster version of the Diagonal-based Incomplete Cholesky (FDIC), for α_s and p.

Table 12 – PSL Numerical Solvers.

Term	Solver	Preconditioner
$\mathbf{A}_\alpha[\alpha_s]=\mathbf{b}_\alpha$	PBiCGStab	FDIC
$\mathbf{A}\mathbf{u}^\star=\mathbf{b}$	PBiCGStab	DILU
$\mathbf{A}_p[p_{rgh}]=\mathbf{b}_p$	PBiCGStab	FDIC

5.1.3 Transition Layer

As presented in subsection 4.3.1, the transition layer manifests as boundary conditions for the mass and velocity fields, α_s and $\mathbf{u}_{psl}$ (the subscripts $\bigstar_{dsl}$ and $\bigstar_{psl}$ will be used in this section to facilitate the distinction of DSL and PSL values, respectively). Such conditions are defined by direct value assignment, characterizing the Dirichlet boundary condition listed for the *terrain* patch on Table 10 in the previous section.

The boundary values of α_s and $\mathbf{u}_{psl}$ are defined for each *terrain* patch face f_b on every time step. These values are mainly based on temporal DSL fields, such as the DSL velocity field $\mathbf{u}_{dsl}(\mathbf{x},t)$. Therefore, the *terrain* patch geometry represents the interface between both layers, since each face f_b will carry the state of the DSL at its location for a particular time t — see Figure 44.

Note that the DSL grid and the PSL's terrain patch may not share the same geometry or topology. Moreover, since the simulation of the DSL is independent of the PSL's simulation, it may even use a different value of time steps — see Figure 44. Therefore, the interface between

[6] See subsection B.1.5.

Figure 44 – The DSL and PSL simulations can share different geometry, topology, or time steps. The transition layer requires the transference of information between both layers. The example below considers a DSL simulated in a hexagonal mesh registered at times $[...,t_m,t_{m+1},...]$. The terrain patch of the PSL grid is a quadrangular mesh and follows a different set of time steps $[...,t_n,t_{n+1},...]$. When simulating the PSL, the DSL state is needed at time t_n, which falls between times t_{m-1} and t_m; therefore, DSL values are interpolated temporally and spatially between cell centers.

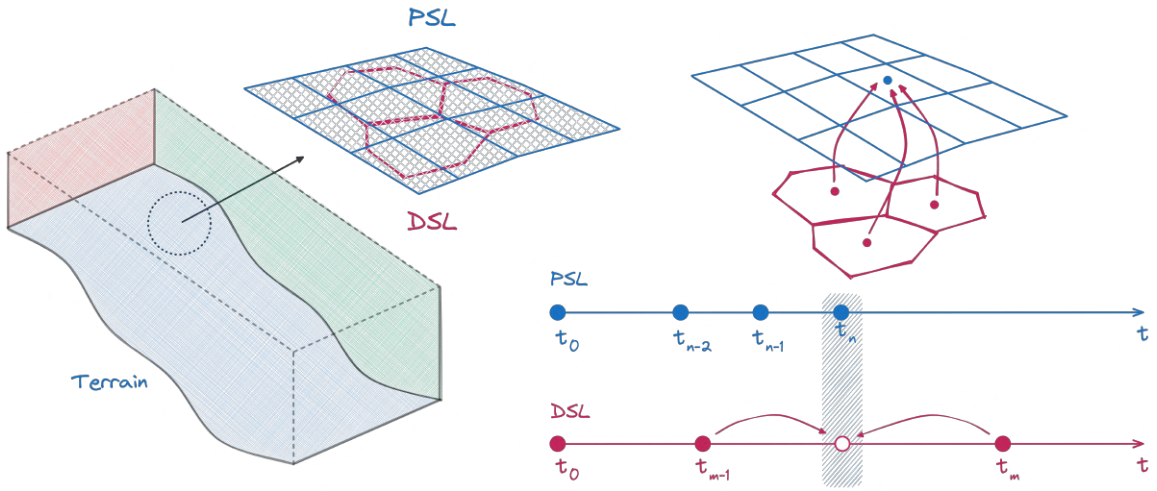

Source: Elaborated by the author.

the original DSL fields and their counterparts in the PSL's terrain patch must map the values spatially and temporally, so

$$\bigstar_{psl}(\mathbf{x},t) \approx \bigstar_{dsl}(\mathbf{x},t), \tag{5.10}$$

for any DSL field $\bigstar_{dsl}(\mathbf{x},t)$ at any spatial location $\mathbf{x}$ and time t. As shown in Figure 44, such approximation is performed by linearly interpolating values between DSL time steps and from DSL face center positions.

Velocity Trigger

In an avalanche, the suspension of snow particles occurs after the DSL achieves enough velocity and intensifies as the velocity increases. The intensification of the suspension, manifested by the entrainment processes, can be defined by a function of the velocity, here emulated by a sigmoid-like function:

$$w_s(\mathbf{x}) = \frac{1}{1+\exp(-\mathbf{u}(\mathbf{x})+U_{min})}, \tag{5.11}$$

where U_{min} controls the minimum velocity required for the formation of the powder cloud. All experiments in this chapter use $U_{min} = 10\ m \cdot s^{-1}$.

Front Distance

The front region of the snow avalanche comprises the eruption entrainment process and is where most of the mass and momentum exchanges happen — the closer to the front position $\mathbf{x}_f$, the higher the intensity of such dynamic. Therefore, α_{inj} and $\mathbf{u}_{inj}$ injection amounts at the position $\mathbf{x}$ depend on its distance to $\mathbf{x}_f$. Such dependence can be emulated by the weight function

$$w_{front}(\mathbf{x}, \mathbf{x}_f) = \exp\Big(-\frac{\| \mathbf{x} - \mathbf{x}_f \|}{L_{front}}\Big), \tag{5.12}$$

that decreases from 1 towards 0 as the distance $\| \mathbf{x} - \mathbf{x}_f \|$ increases. The term L_{front} roughly represents the size of the region in meters that defines the front region — i.e., the first L_{front} meters after the leading edge of the avalanche.

The distances $\| \mathbf{x} - \mathbf{x}_f \|$ are *surface distances*. The surface distance function $Sd(\mathbf{x}, \mathbf{x}_f)$ defines the shortest path between two points on a surface, restricted to the surface (like the geodesic distance). As the front position $\mathbf{x}_f$ advances, the distance field $d(\mathbf{x})$ is calculated every time step via a *front-propagation* algorithm.

Source code 3 – Algorithm for computing front distance in the DSL.

```
front_cells = detectFrontCells(DSL_mesh);
dist(front_cells) = 0;
q.push(front_cells);
while(!q.empty()) {
    cell = q.front();
    q.pop();
    for(neighbor : cell.neighborsInDirection(-u(cell))) {
        new_dist = dist(cell) + distance(cell, neighbor);
        if(h(neighbor) > h_min &&
            dist(neighbor) > new_dist) {
            dist(neighbor) = new_dist;
            q.push(neighbor);
        }
    }
}
```

The algorithm, listed in Source code 3, works on the DSL grid cells by (1) first detecting cells that contain the front leading edge, named *front cells*, and (2) then constructing the distance field:

1. **Front Cells Detection**:

   Front cells are cells that intersect the front line of the DSL at a given time. The front line is defined by the DSL's height h and velocity $\mathbf{u}_{dsl}$. A cell C is considered to intersect the

front if there is a neighbor cell N downhill ($C_z > N_z$), at the direction of $\mathbf{u}_{dsl}(C)$, that is empty ($h(N) < h_{min}$).

2. **Distance Propagation**:

   The distance field computation starts by setting all front cell distances to zero and putting them into a queue (lines 2-3). While the queue is not empty, the next cell in the queue is taken, and any *affected* neighbor is pushed into the queue. A neighbor is affected if its distance value must be updated. Each cell will hold the smallest distance propagated into it.

   For a given cell C, only non-empty neighbors in the upwind direction, $-\mathbf{u}_{dsl}(C)$, are considered.

In the algorithm described above, a neighbor of a cell in the direction $\mathbf{d}$ is the neighbor cell for which the shared face intersects with the ray cast from the cell's center with direction $\mathbf{d}$ — see Figure 45.

Figure 45 – The injection of mass and velocity depends on the distance from the avalanche's leading edge. On the left, front cells represent the leading edge, whose velocity *directional neighbors* are empty (no DSL height). A directional neighbor is a neighbor whose shared face intersects the direction ray $\mathbf{d}$ originated from the cell's center (middle). On the right is the distance field propagated from the front cells. The propagation follows the negative direction of velocity.

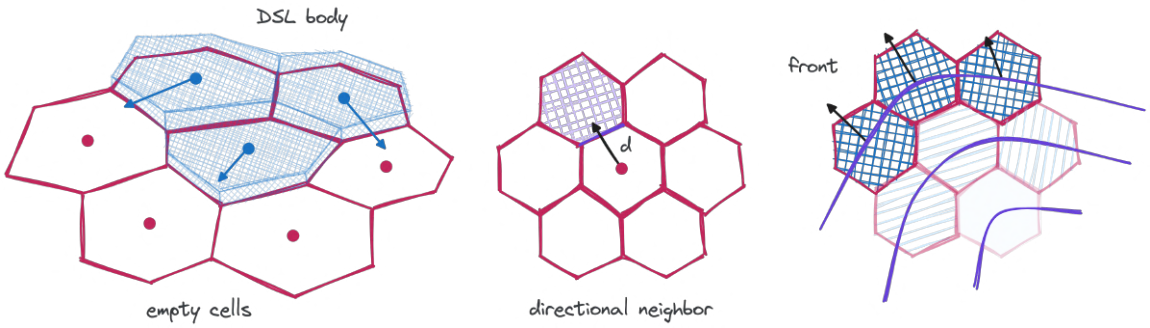

Source: Elaborated by the author.

Velocity Injection

The velocity injection occurs in the normal direction of the terrain and depends directly on the front velocity, as described by Equation 4.56:

$$\mathbf{u}_{inj} = (2w_h + \omega_{\mathbf{u}} \parallel \mathbf{u}_{front} \parallel)(-\mathbf{n}_b)$$

Since the front region extends for at least L_{front} meters, a convenient assumption is to use the DSL velocity as the front velocity $\mathbf{u}_{front} \approx \mathbf{u}_{dsl}$ in every boundary point $\mathbf{x}$, so the injection velocity becomes:

$$\mathbf{u}_{inj}(\mathbf{x}) = (2w_h(\mathbf{x}) + \omega_{\mathbf{u}} \parallel \mathbf{u}_{dsl}(\mathbf{x}) \parallel)(-\mathbf{n}_b(\mathbf{x})). \tag{5.13}$$

The term $\omega_{\mathbf{u}}$ summarizes the intermittent behavior at the front region. The many factors that lead to the turbulent motion at the front include the eruption entrainment process, the air intake from the ambient air, and the violent release of trapped air underneath. Also, the entrainment of snow depends significantly on the constitutive properties of the snow cover.

The snow cover comprises multiple layers of snow of different densities, constituting a heterogeneous body of snow. As such layers interact with the avalanche, they affect the entrainment processes differently.

A practical solution to mimic the effects mentioned above is to use a spatial noise function $\Omega(\mathbf{x})$ for $\omega_{\mathbf{u}}$, so

$$\omega_{\mathbf{u}}(\mathbf{x}) = \Omega(\mathbf{x}), \tag{5.14}$$

which causes random perturbations into the injection velocity associated with the complexity of the snow cover body. Random surges of velocity represent chunks of weak layers being entrained rapidly. In particular, the family of cellular noise functions, such as the Worley Noise (WORLEY, 1996), produces distinct space regions resembling natural patterns. As shown in Figure 46, once computed over the terrain surface, these regions can be seen as chunks of snow packs of variable densities.

Figure 46 – Cellular noise functions produce natural-like patterns that can compose the complex internal structure of the snow cover. Such random variations in the term $\omega_{\mathbf{u}}\mathbf{u}$ produce surges of velocity that mimic the turbulent nature of entrainment processes.

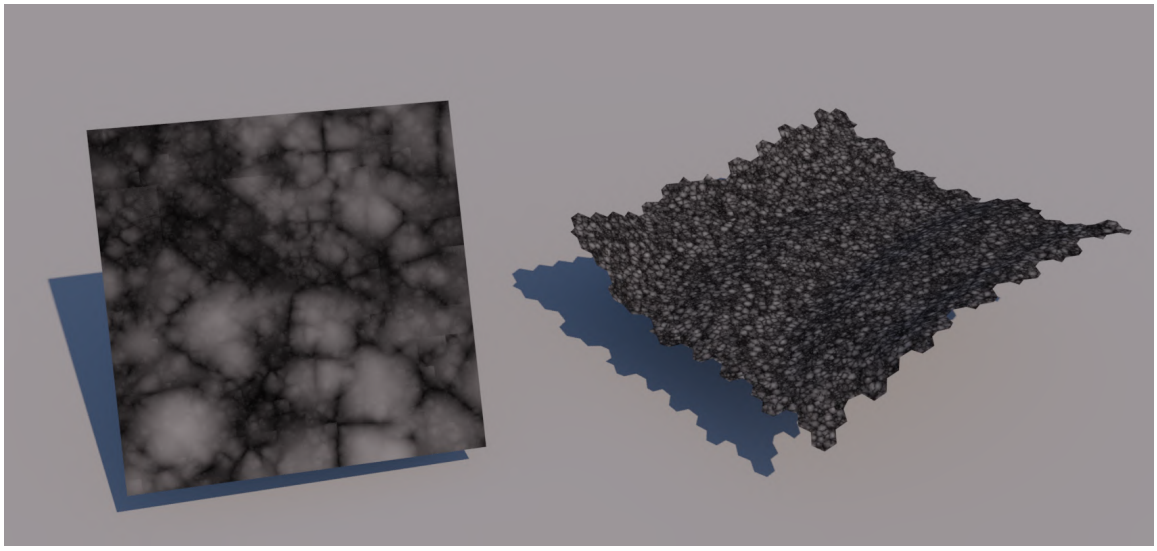

Source: Elaborated by the author.

The combination of all factors described above now integrates the term $\mathbf{u}_{inj}$. Additionally, an scalar factor $\gamma_{\mathbf{u}}$ can be used to modulate the injection velocity. Considering the front weight explained earlier, the final form of the boundary condition of the velocity becomes:

$$(\mathbf{u})_b = w_s w_{front} \gamma_{\mathbf{u}} \mathbf{u}_{inj} + \mathbf{u}_{dsl}, \tag{5.15}$$

where w_s is the suspension factor and w_{front} is the front weight described earlier.

Mass Injection

From Equation 4.61 in subsection 4.3.1, α_{inj} is computed from the mass concentration

$$\alpha_{inj}^{v} = \frac{m_e}{M^v}$$

for the volume V in the boundary cell. However, the entrainment mass m_e defined in the previous chapter takes the full entrainment of the DSL, which considers injecting the same mass entrained by the DSL into the PSL. Although it does not harm the final animation, a more realistic approach is to consider that only a portion of the snow cover gets into the PSL.

Therefore, a constant $\gamma_\alpha \in [0,1]$ can adjust the injection value to consider only a fraction of the entrained mass. The final form of the boundary condition for α_s is

$$(\alpha_s)_b = w_s w_{front} \gamma_\alpha \omega_a \alpha_{inj}^{v}, \tag{5.16}$$

where ω_a is similar to $\omega_{\mathbf{u}}$ and emulates the variable density of the snow cover.

5.2 Discussions

This section explores the influence of the terrain geometry and the model's parameters on the resulting animation. Although the principal goal of this project is the visual realism of a powder-snow avalanche animation, which is, to some extent, subjective, this section brings some quantitative analysis of the results. Each of the following results explores a particular discussion in order to build a better understanding of the method:

- The influence of slope — page 143;
- The terrain topography — page 145;
- The model parameters — page 146;
- The numerical mesh — page 150.

All simulations consider the powder-snow avalanche triggered by the detachment of a body of snow cover defined by a release area. Initially at rest, $\mathbf{u}_{dsl} = 0$, the triggered body gets into motion and composes the DSL, which induces the PSL. Unless otherwise specified, the simulations presented in this section use the set of parameter values listed in Table 13. All DSL simulations presented in this section are three-dimensional, and two-dimensional PSLs used a cross section of their respective DSL.

Some of the following analyses use measurements of mass and energy. The discrete approximation of such quantities in a given discrete PSL mesh results from the summation of the individual cell measurements. Given the set of cells C_i containing the fields of velocity $\mathbf{u}$ and concentration of volume α_s, the total measurements are defined as:

Table 13 – Model parameters values.

Simulation	Parameter	Description	Value
DSL	ρ	Snow density $[kg \cdot m^{-3}]$	1500
	μ	Voellmy's dry friction	0.155
	ξ	Voellmy's dynamic friction $[m \cdot s^{-2}]$	5000
	e_b	Erosion energy	50
Transition Layer	γ_α	Mass injection factor	0.1
	$\gamma_\mathbf{u}$	Velocity injection factor	1.6
	L_{front}	Front extension $[m]$	40
PSL	ρ_a	Air density $[kg \cdot m^{-3}]$	1.2
	μ_a	Air viscosity $[m^2 \cdot s^{-1}]$	$1.4 \cdot 10^{-5}$
	ρ_s	Powder-snow density $[kg \cdot m^{-3}]$	1.4
	μ_s	Powder-snow viscosity $[m^2 \cdot s^{-1}]$	$1 \cdot 10^{-4}$
	D_{ab}	Molecular diffusivity	$2 \cdot 10^{-4}$

- **Cell Mass**

$$m_i = \alpha_{si} V_i \rho_s, \tag{5.17}$$

where V_i is the volume of cell C_i;

- **Total Mass**

$$M = \sum_i m_i; \tag{5.18}$$

Slope

The influence of the slope is studied using the simplified case of an avalanche descending a ramp with a constant slope. This analysis considers a set of ramps and the fixed set of parameter values in Table 13; only the slope varies between simulations.

In each simulation, a rectangular region on the top of the ramp represents the release area of the DSL as depicted in Figure 47. The release area is constructed from the projection of a rectangular region, defined in the xy plane, onto the ramp. The size of the release area is adjusted so that the mass of the DSL is approximately the same across the different simulations.

After a fixed time interval t_n, each avalanche may achieve a different velocity and mass due to the influence of the slope. The different velocities result directly from the action of gravity, expressed in Equation 4.6 in section 3, as the source term given by the surface-tangential component $h'\mathbf{g}_S$. The greater the angle, the bigger the tangential acceleration. The curves in Figure 48 represent the front position and velocity evolution for a given set of ramps. The angles vary from 20 to 35 degrees, and it is clear how higher angles produce greater velocities and, therefore, greater runout distances over time.

The velocity of the DSL directly impacts the PSL's entrainment — recall the velocity injection from Equation 5.15; Therefore, the slope affects the powder cloud formation process. Figure 49 shows the profiles of cloud formations in the avalanche cases described above. Note

Figure 47 – Scheme representing the initial conditions for each slope simulation. The initial release area is defined by the projection of a rectangular region defined in the xy plane onto the ramp (left). The plane region is adapted to each slope value so the initial mass is the approximately the same for all simulations (right). Each simulation considers a ramp with a constant slope and fixed model parameters.

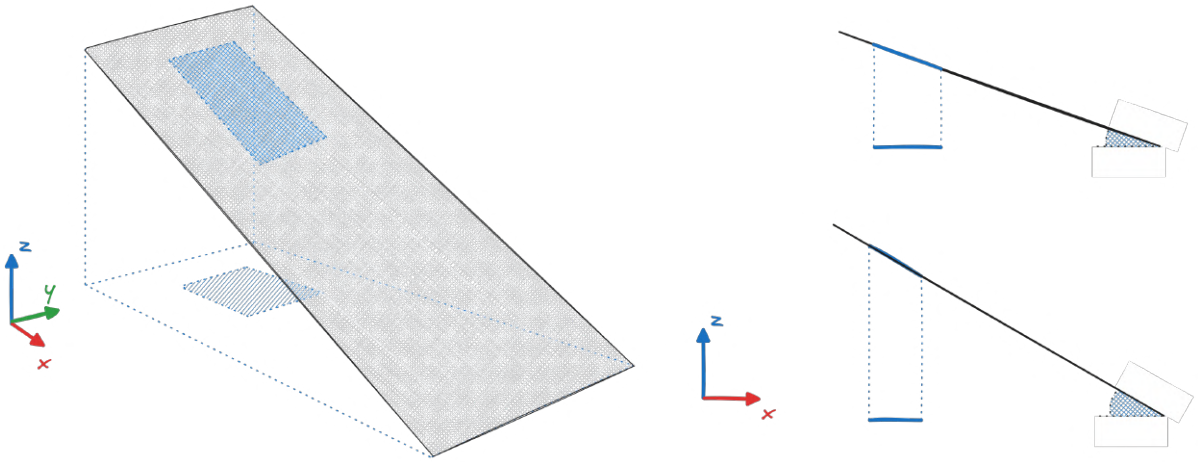

Source: Elaborated by the author.

Figure 48 – The graph on the left shows the distances covered by four avalanches in terrains with different slopes. After 30 seconds, the avalanche on a 35-degree slope covers more than 500 meters, five times more than on a 20-degree slope. The right graph shows the evolution of the front velocity for the same avalanches, where the steepest case achieves 30 $m \cdot s^{-1}$, and the flattest keeps a constant speed. The oscillations in the front velocity curves are caused by the method of front extraction and the effects of the interpolation between the PSL and DSL meshes.

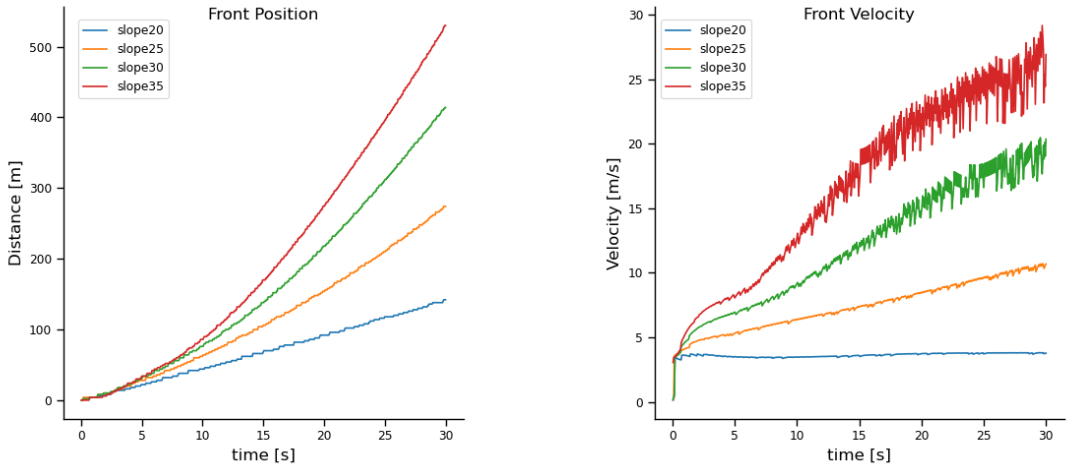

Source: Elaborated by the author.

how the 20-degree slope case does not develop enough velocity to inject mass into the PSL. The figure also shows the total mass of the powder cloud. Figure 50 on page 145 shows the resulting clouds.

Figure 49 – The graph on the left depicts the profile of the plume heights produced in avalanches descending different slopes. Higher slopes produce higher clouds, up to 40 *m*, in this experiment due to higher velocities. Greater velocities induce more significant mass injections into the PSL. The graph on the right shows the evolution of the total mass of the powder clouds.

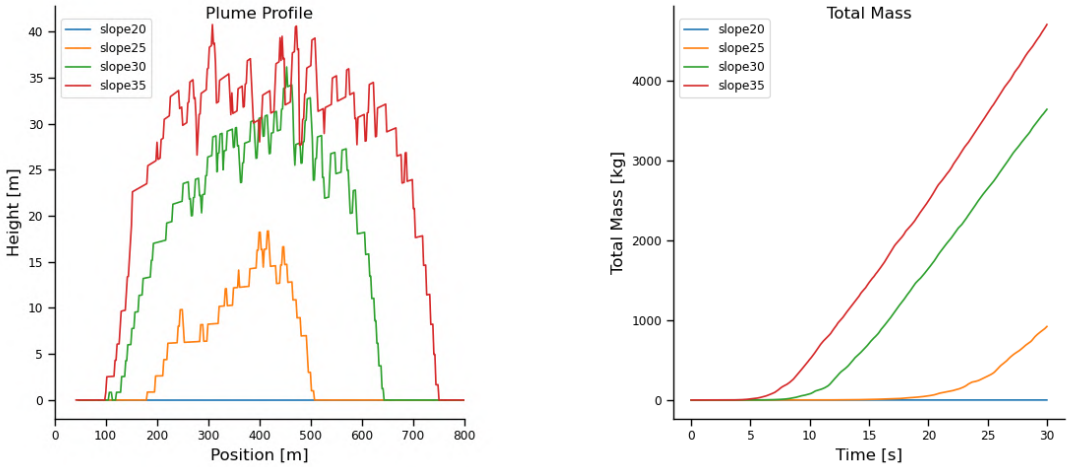

Source: Elaborated by the author.

Figure 50 – Resulting clouds 30 seconds after release for 35, 30, and 25-degree slopes, from top to bottom, respectively. Steeper slopes generate faster and bigger avalanches.

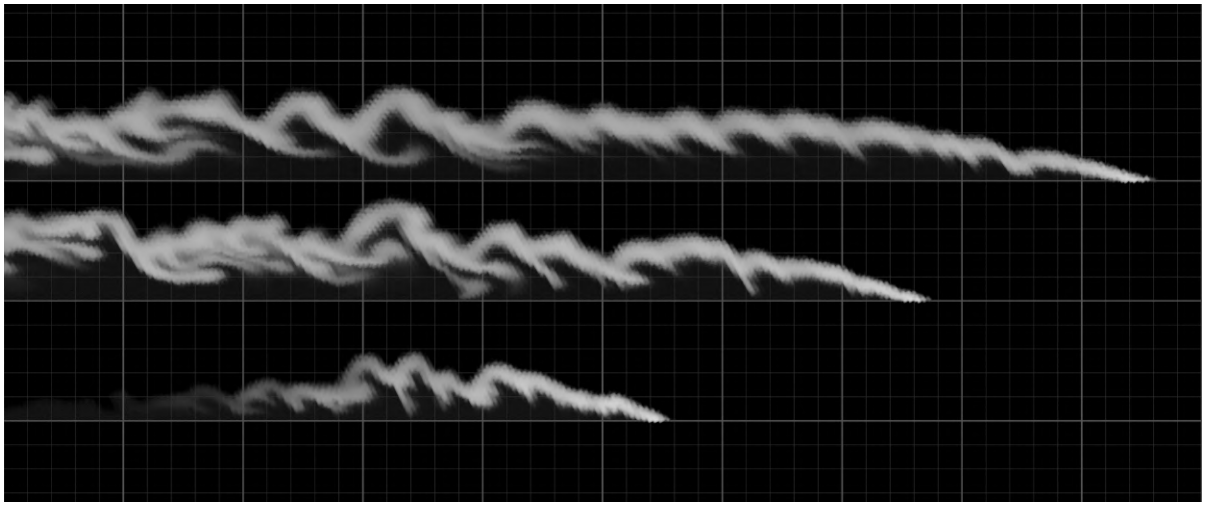

Source: Elaborated by the author.

Terrain Topography

The inherent complexity of natural terrains shapes the path taken by an avalanche. The DSL follows the terrain's topography, tunneling into fissures, bifurcating over sharp protuberances, and spreading across open areas. Although the powder cloud does not hover over the small terrain features, this source is the DSL, and its overall motion resembles the final path of the dense avalanche. The following result explores such characteristics of the snow avalanche flow by releasing a mass on a river bed-like terrain followed by bumps, as depicted in Figure 51 on page 146.

Figure 51 – The figure below shows a modified ramp featuring a channel descending the terrain. The channel descends straightly in the first section of the course and enters into a sine-like shape. The channel flows into a series of bumps in the third and final stage.

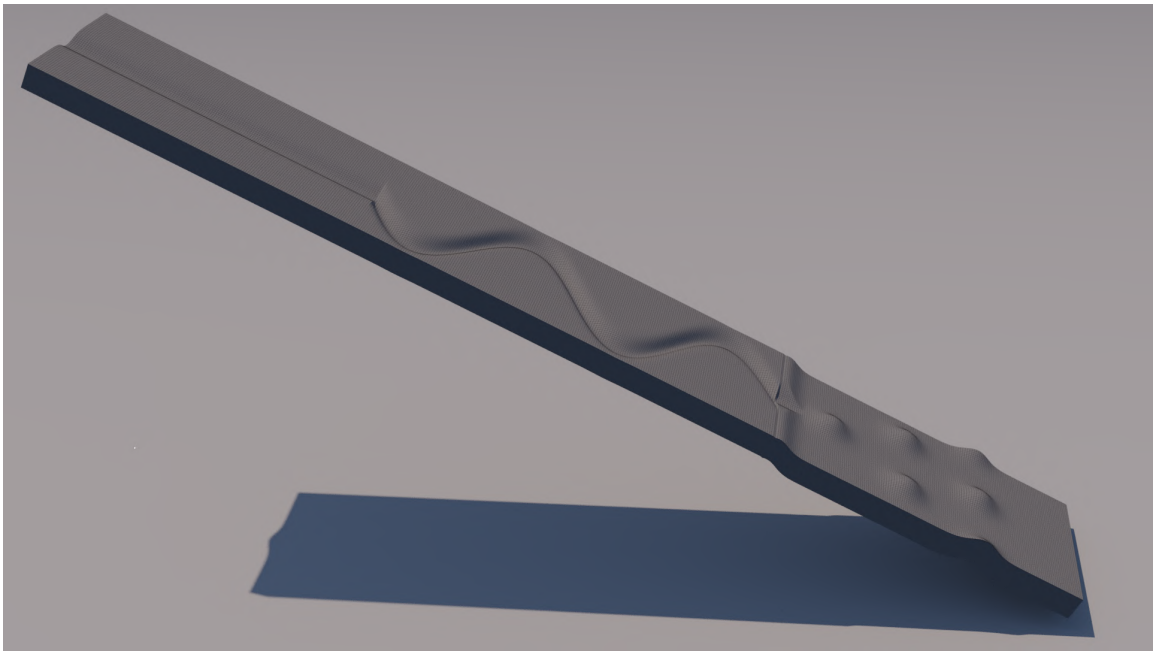

Source: Elaborated by the author.

Figure 52 on page 147 presents the resulting simulation of a dense snow avalanche triggered for the modified ramp mesh above. The three pictures depict the avalanche's state passing by the terrain's three stages. In the first stage, the release area covers a channel section. The image of the second stage, characterized by the curved channel, shows how the flow follows the curved geometry. Although the DSL overflows the curves, most of its mass is channeled. The last stage shows how the bumps in the terrain bifurcate the flow, and the avalanche accumulates on their upper sides.

The behavior of the DSL flow over the complexities of the terrain has a direct impact on the appearance of the front region of the powder cloud. Such an implication happens due to the influence of the velocity and entrainment of snow, which depend on the DSL and the snow cover. Figure 53 on page 148 visually compares the resulting front of the experiment described above with an avalanche descending a flat ramp with similar initial conditions.

Model Parameters

The mixture density of the PSL, ρ_s, plays a central role in the motion of the powder cloud. From the momentum equation of the PSL model, Equation 4.41 on page 118, the gradient of the density field scales the action of gravity. Higher density differences induce higher accelerations and increase the velocity while carrying more inertia. Moreover, high-density volumes have stronger momentum and may displace more surrounding fluid. The following experiment lists avalanches with powder snow densities varying from near-air density to higher values.

Figure 52 – The figure below shows the DSL of an avalanche release in a channeled terrain. The color map represents the height of the DSL, with brighter colors meaning greater heights. The three images show the state of the DSL at each of the three terrain sections: the release in a straight channel, a curved channel, and a plane region with bumps. Note how the bright colors mark the terrain features.

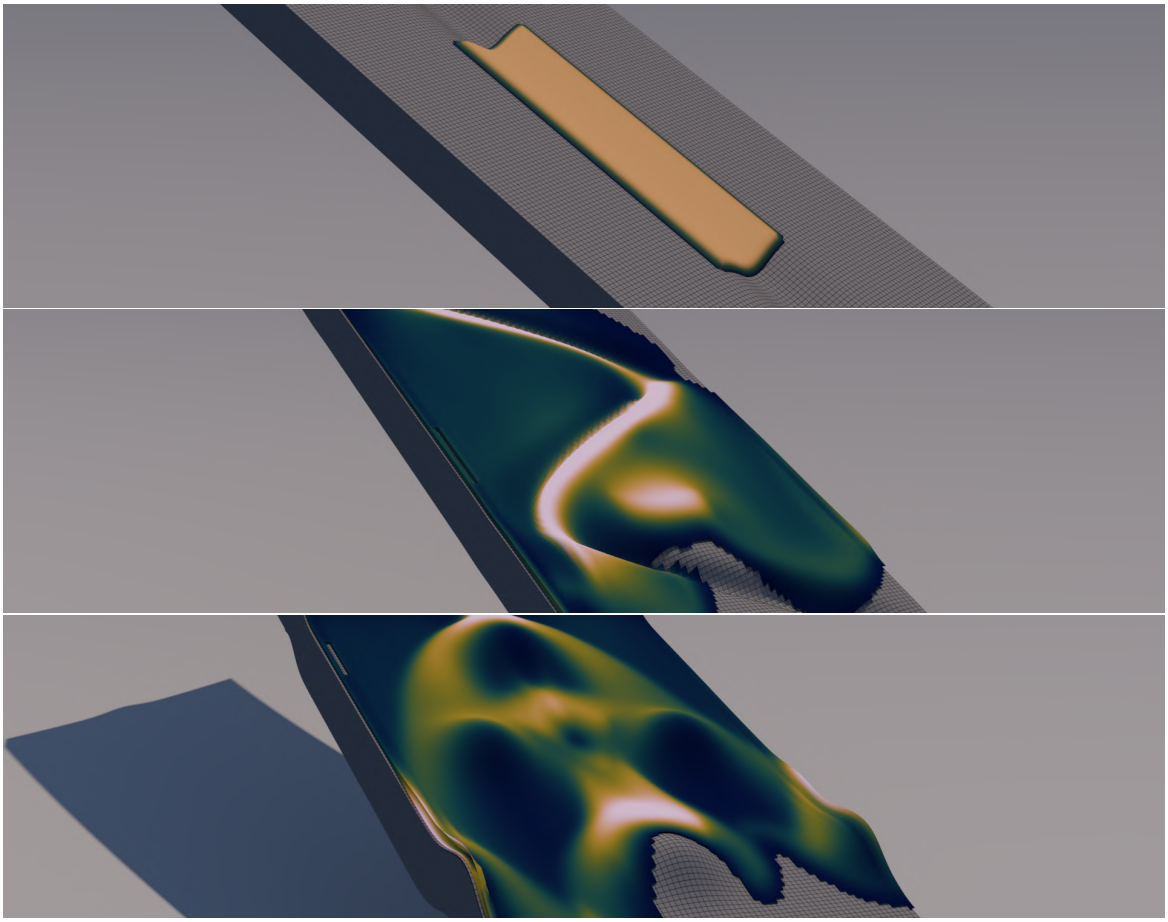

Source: Elaborated by the author.

For a given DSL simulation data descending a flat 25-degree slope, Figure 54 on page 148 shows the resulting PSL 50 seconds after release time for four density values: 1.4, 2.5, 5.0, and 7.0 $kg \cdot m^{-3}$. Note how the cloud distribution concentrates towards the head of the PSL as the density value increases and how lower densities lead to more complex patterns. Figure 55 on page 149 shows the total mass of the powder cloud along with the plume profiles developed by the experiments listed above.

In the DSL model, the erosion energy e_b modulates the entrainment rate. Higher values lead to lower entrainment rates. The erosion energy value represents the energy required to detach mass from the snow cover. The entrainment process maintains the avalanche motion by introducing mass into the body, increasing the momentum. Therefore, higher entrainment rates contribute to the acceleration of the avalanche. Figure 56 on page 150 shows the front position, total mass, plume profile, and maximum velocities of DSL simulations using erosion energy values, 15, 25, 100, and 400, respectively — Figure 57 shows the resulting PSL clouds.

Figure 53 – On the left is an avalanche's powder cloud descending the modified ramp; on the right is an equivalent avalanche in a flat ramp. Note how the features of the underlying terrain geometry manifest in the PSL. The left side clearly shows the sine-like structure from the second section of the terrain.

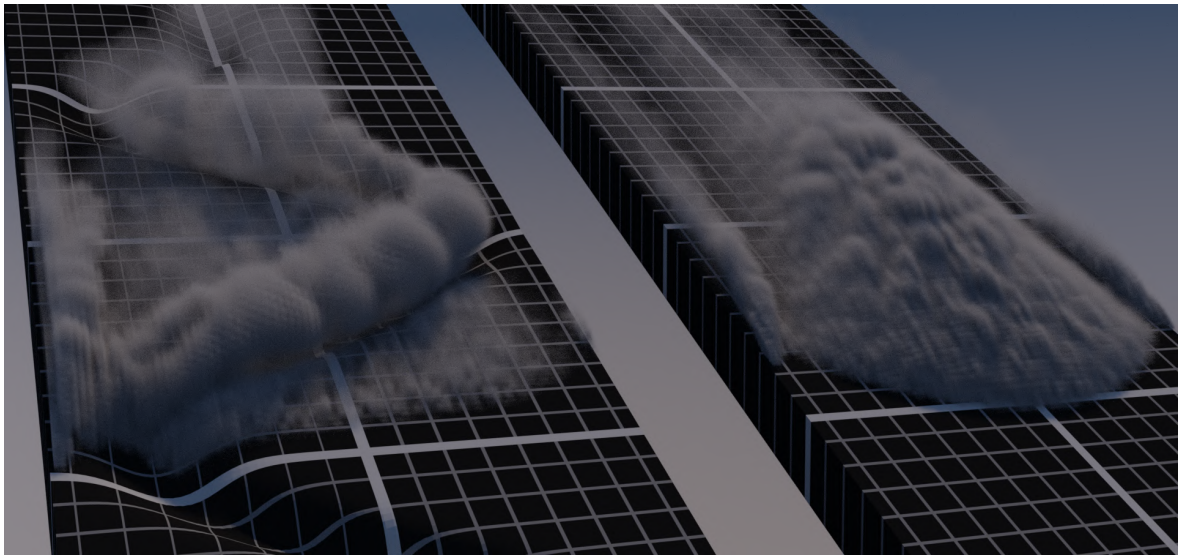

Source: Elaborated by the author.

Figure 54 – Resulting clouds 50 seconds after release for four powder snow density ρ_s values, 1.4, 2.5, 5.0, and 7.0 $kg \cdot m^{-3}$, from top to bottom, respectively. All triggered from the same DSL simulation in a 25-degree slope.

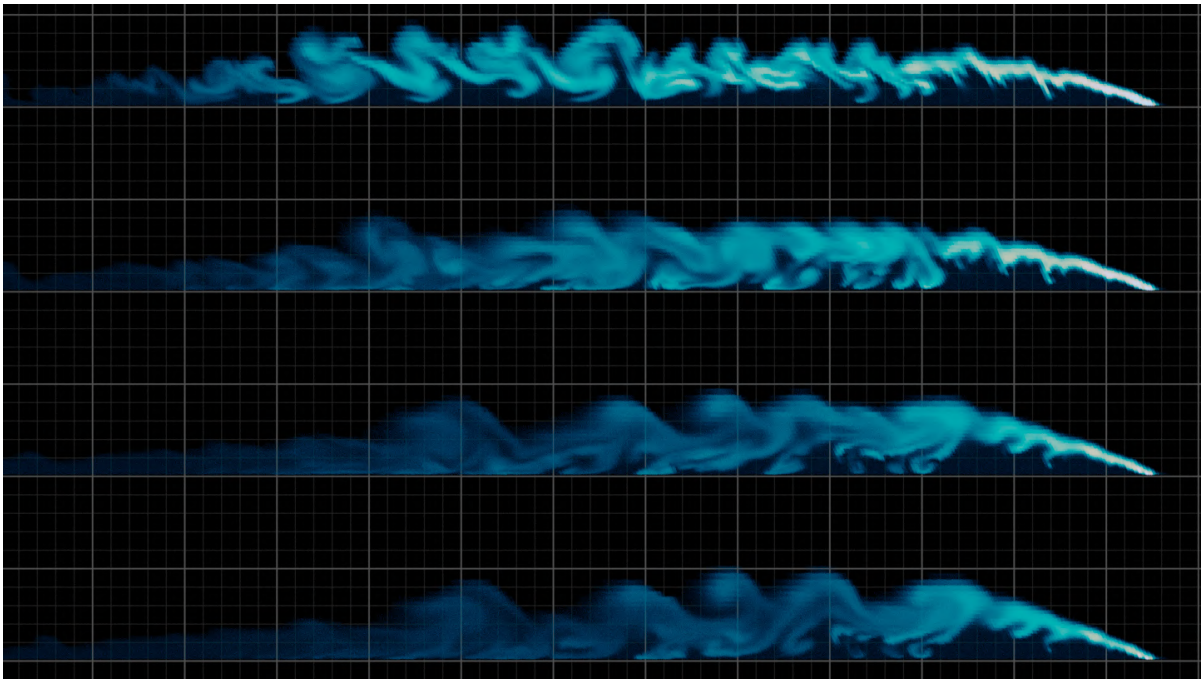

Source: Elaborated by the author.

Mass and Momentum Injections

The injection of mass and velocity into the PSL contains some parametrization that dictates the final shape of the cloud. From equations Equation 5.12, Equation 5.15, and Equa-

Figure 55 – Measurements of 50 seconds-long PSL simulations for four powder snow density ρ_s values, 1.4, 2.5, 5.0, and 7.0 $kg \cdot m^{-3}$. On the left is the evolution of the total mass of the powder cloud. On the right the profile of the plume heights.

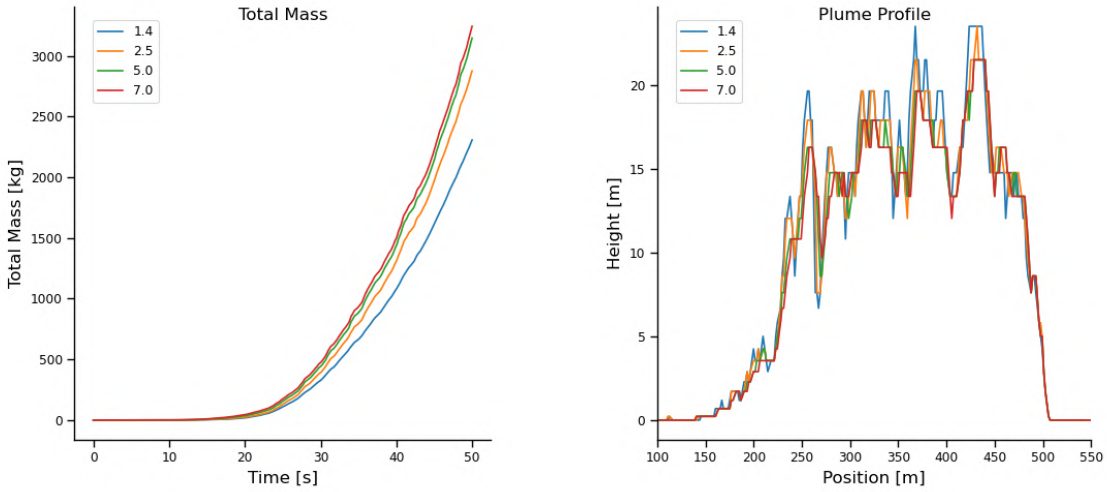

Source: Elaborated by the author.

tion 5.16, the four parameters considered are:

- **Mass Injection Factor**: γ_α controls the percent of mass entrained by the DSL that gets into the PSL. Therefore, $\gamma_\alpha \in [0, 1]$; Figure 58 on page 152 shows the powder clouds colored by the concentration of volume α_s for four values of γ_α: 0.01, 0.1, 0.4, and 0.9. The highest values concentrate in the front, where injection occurs, and flow in distinct patterns. Lower values of γ_α produce visible structures, while higher values smooth out and fill the cloud volume. Such differences result from the diffusion equation, Equation 4.43 on page 119, driven by the gradient of α_s; as greater gradient values induce higher diffusion rates.

- **Velocity Injection Factor**: $\gamma_\mathbf{u}$ scales the combined effect of air intake and snowpack ejection displacement translated into velocity surges. Figure 59 on page 153 shows the powder clouds produced with four values of $\gamma_\mathbf{u}$: 1.0, 2.0, 4.0, and 8.0. The injection velocity has an apparent effect on the size of the cloud. Higher velocities lead to higher plumes and turbulent motion. Figure 60 presents graphs of the total mass and maximum velocity values of the PSL over a 50 s simulation.

- **Front Extension**: L_{front} controls the size of the avalanche front, i.e., the region where the two parameters above have a more significant effect. L_{front} is considered to be in the range of $10 \sim 40m$. Figure 61 on page 155 shows the powder clouds produced with four values of L_{front}: 10, 20, 40, and 80. Smaller front regions result in short injection times from the same terrain location, leading to smaller plume heights. Also, separate plumes become more evident away from the front in such cases due to the spatial noise distribution in the terrain. Extensive front regions inject mass from the same terrain position longer, giving enough time to mix. Additionally, the overall height of the cloud increases as the injection

Figure 56 – Measurements of 30 seconds-long DSL simulations for different values of erosion energy e_b values, 15, 25, 100, and 400. Note how the high-value avalanches accelerate faster but stay behind at the end. The variations in the velocity curves result from the higher entrainemt velocity term $2w_h$ for smaller erosion energy values.

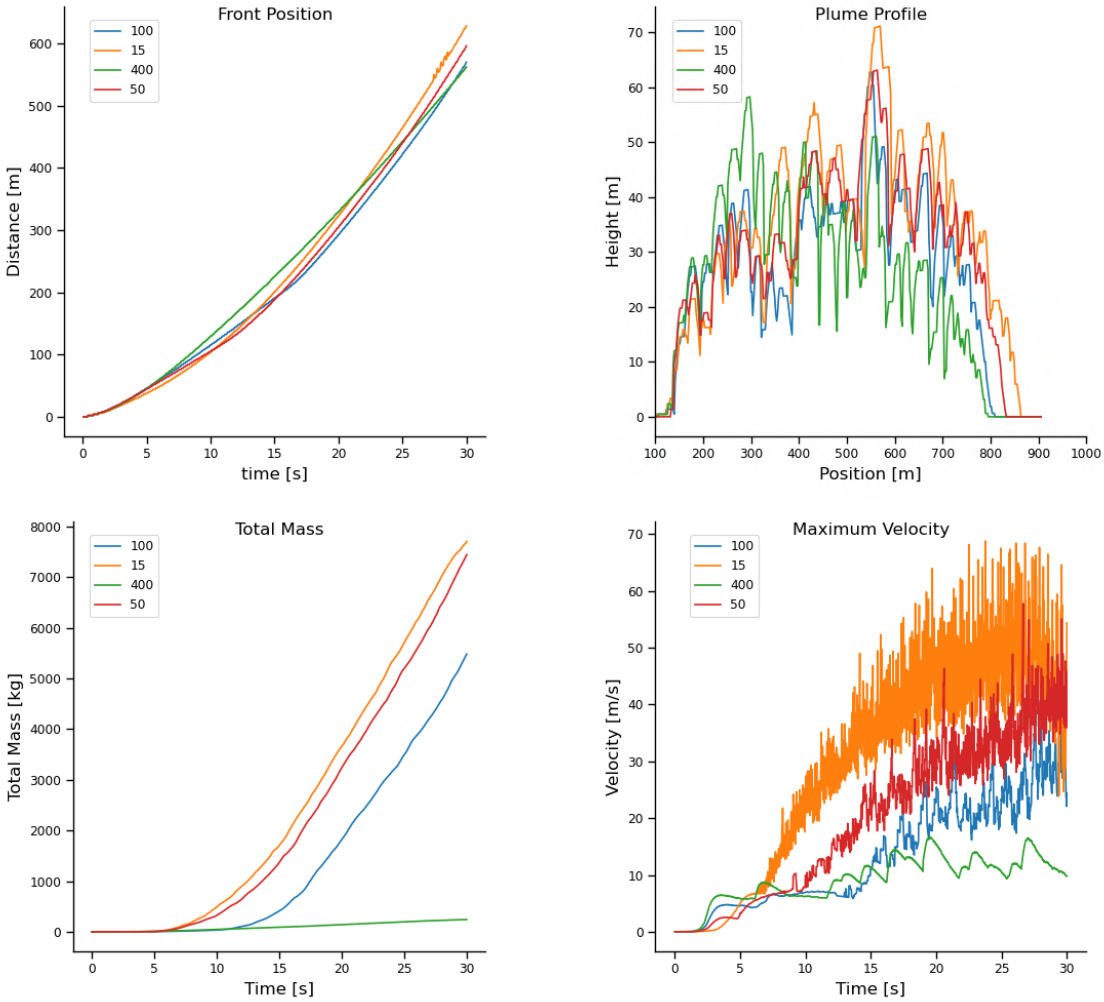

Source: Elaborated by the author.

velocities act longer. Figure 62 shows that although the total mass does not diverge much, the curve profiles are notably different.

- **Noise Factor**: The coefficients $\omega_\bigstar$ introduce random oscillations into the entrainment of the PSL. Such oscillations emulate the intermittent region's turbulent nature and the snow cover's heterogeneous constitution. The turbulence plays a crucial role in the formation of the plumes. In the constant slope case used in the previous experiments, the entrainment sources, $2w_h$ and $\mathbf{u}_{dsl}$, vary slowly with the acceleration of the avalanche, leading to a steady injection. The omission of an oscillatory factor results in a smooth PSL cloud, as shown in Figure 63 on page 156.

Numerical Method

Figure 57 – Resulting clouds 30 seconds after release for four erosion energy values, 15, 25, 100, and 400, from top to bottom, respectively. All triggered from their respective DSL simulations in a 25-degree slope. Higher energy values lead to smaller α_s fields (the last PSL is hardly visible in the figure).

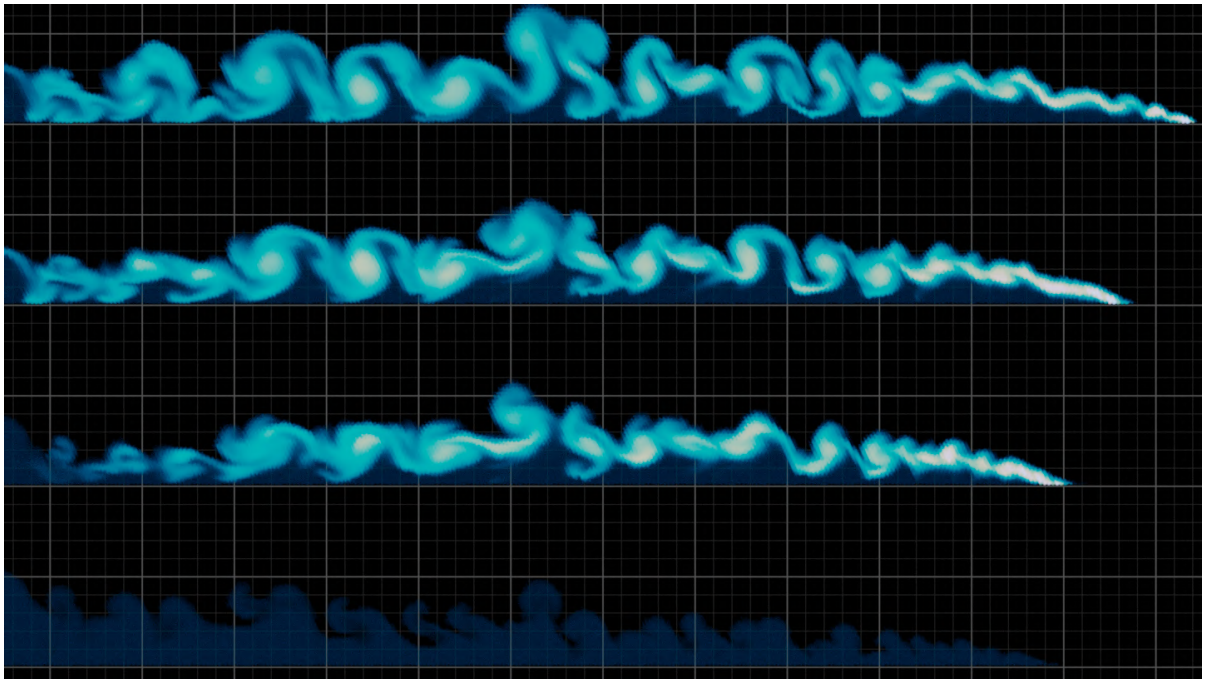

Source: Elaborated by the author.

The experiments presented in this section utilize ramps up to 1 *km* long. Natural terrains, used at this chapter's end, can present avalanche tracks of many kilometers. Such large scales inevitably bring computational challenges for the numerical methods since the precision of the results depends directly on the resolution of the grid.

Typical fluid simulations use cell grids a few centimeters wide, if not smaller. However, compared to avalanche sizes, such resolutions can quickly increase the number of cells to hundreds of millions. Therefore, cells in the order of meters become necessary. The following experiments explore the convergence of the PSL model given a different set of two-dimensional grid resolutions.

Figure 64 on page 156 depicts a series of powder snow clouds different numerical grids with decreasing resolutions. As the cell sizes increases the higher numerical diffusivity becomes apparent and lead to fewer flow details. Figure 65 presents the variation on the mean Courant values and the time steps extracted from each simulation.

5.3 Rendering

Both simulations of the DSL and PSL produce data for rendering, where each time step of the simulations provides the data for a respective frame in the final animation. Therefore, for

Figure 58 – Resulting clouds 50 seconds after release for four mass injection factor γ_α values, 0.01, 0.1, 0.4, and 0.9, from top to bottom, respectively. All triggered from the same DSL simulation in a 25-degree slope.

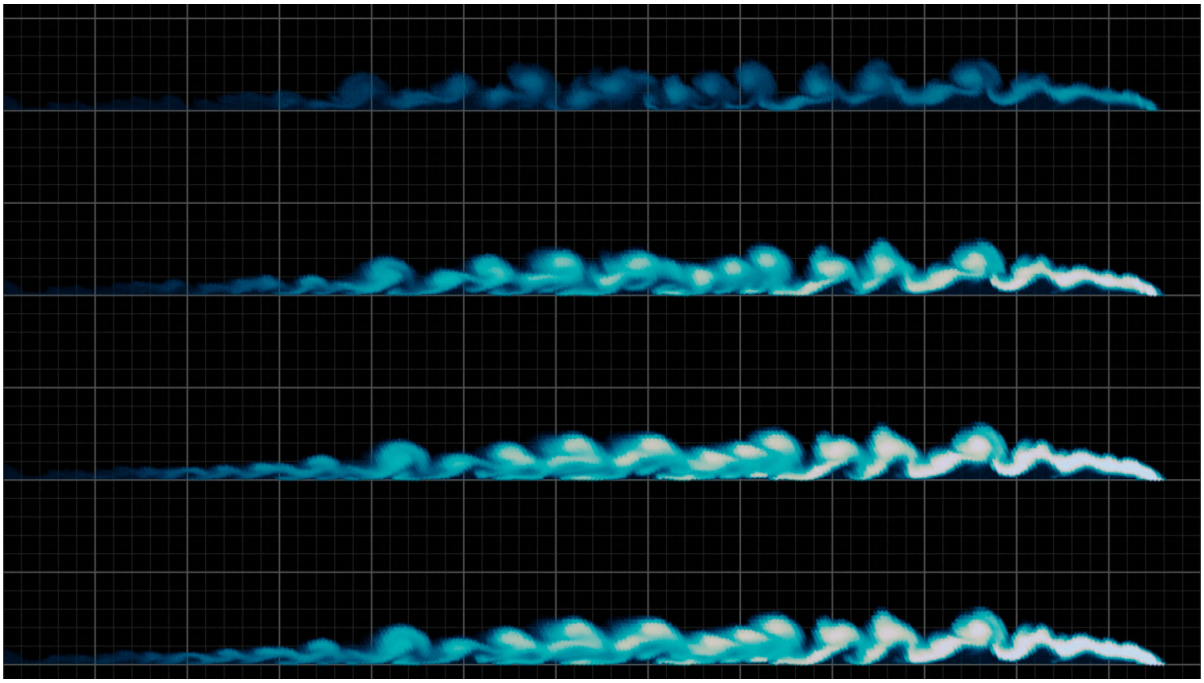

Source: Elaborated by the author.

an animation of 20 frames per second, the simulations must output data at intervals of $0.05s$.

Given the inherent nature of their resulting fields, the rendering of each layer uses a different type of data:

- The resulting field of the DSL simulation is the height of the dense avalanche at each numerical cell in the terrain surface, which can be used to build a **polygonal mesh** to represent the DSL surface.
- The PSL data is a scalar volume field representing the powder-snow concentration in every numerical cell, thus a **sparse volumetric density field** can be used to represent the powder-snow cloud.

DSL Surface

The surface render mesh of the DSL covers the set of two-dimensional cells S_{dsl} that contains enough moving mass, defined as

$$S_{dsl} = \{C_k \forall k | h_k > H_\varepsilon\},$$

where h_k is the height of the avalanche in cell C_k, and H_ε represents the minimum height required for a cell to be considered an avalanche cell. The cells consist of the set of vertices V_{dsl}, where each vertex $v_i \in V_{dsl}$ is shared by a set of incident cells N_i.

Figure 59 – Resulting clouds 50 seconds after release for four velocity injection factor $\gamma_{\mathbf{u}}$ values, 1.0, 2.0, 4.0, and 8.0, from top to bottom, respectively. All triggered from the same DSL simulation in a 25-degree slope. Greenish colors (at the front) represent higher velocities.

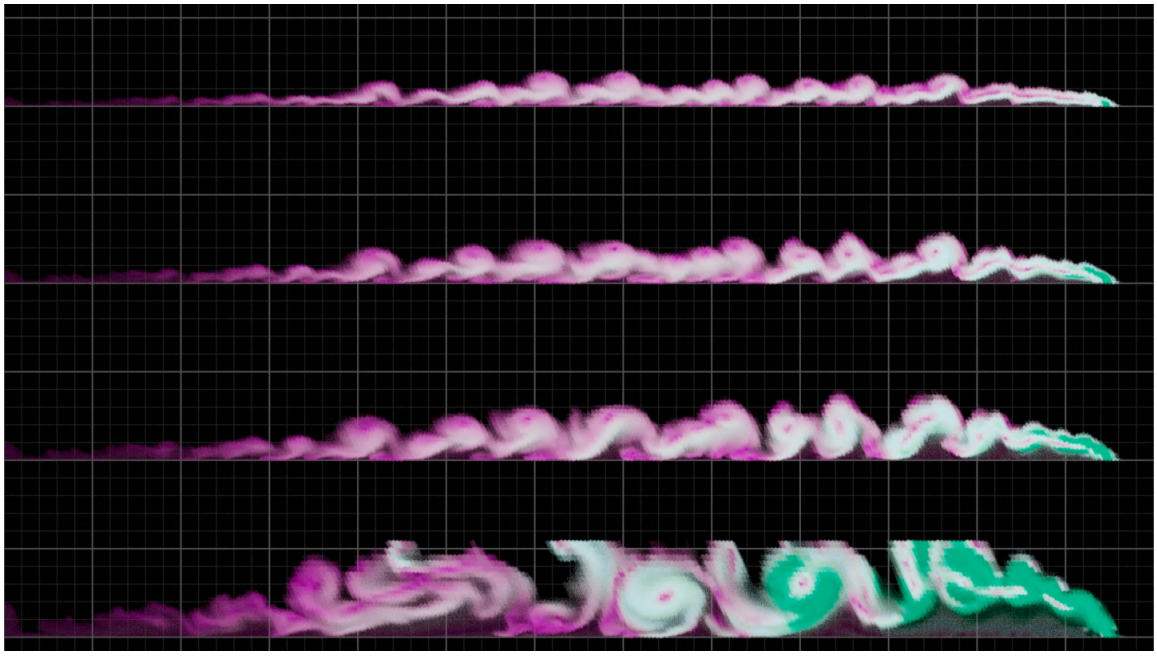

Source: Elaborated by the author.

The construction of the render mesh M_{dsl} and its vertices V_M is defined by the direct map $E : V_{dsl} \rightarrow V_M$, defined as

$$m_i = v_i + h_i \mathbf{n}_i, \tag{5.19}$$

where $m_i \in V_M$ is the corresponding vertex in V_M for the vertex v_i, h_i is the DSL height value at v_i, and $\mathbf{n}_i$ is the terrain normal vector at v_i. The computation of h_i is done by averaging the cell values from the incident cells in N_i:

$$h_i = \frac{1}{|N_i|} \sum_{c \in N_i} h_c. \tag{5.20}$$

The process results in the extrusion of S_{dsl} by displacing each vertex in the normal direction of the terrain surface by an amount computed from the mean height values from the neighboring cells; see left in Figure 66. Note in the same figure that it is different from extruding the cells individually, which could lead to discontinuities in the edges by producing steps between cells with different height values.

PSL Cloud

As mentioned, a *volumetric density field* can represent the PSL cloud, meaning the final result will be rendered as a volume of a three-dimensional scalar field $\phi(\mathbf{x})$. Generally, the field representation considers a regular grid of cubic cells, called *voxels*, where a value of ϕ is defined for each voxel **ijk**. This section will refer to the volumetric density field grid as the *voxel grid*.

Figure 60 – Measurements of 50 seconds-long PSL simulations for four velocity injection factor $\gamma_{\mathbf{u}}$ values, 1.0, 2.0, 4.0, and 8.0. On the left is the evolution of the total mass of the powder cloud. On the right are the maximum velocity values over time. The oscillation present in the velocity curves come from the noise factor in the entrainment process.

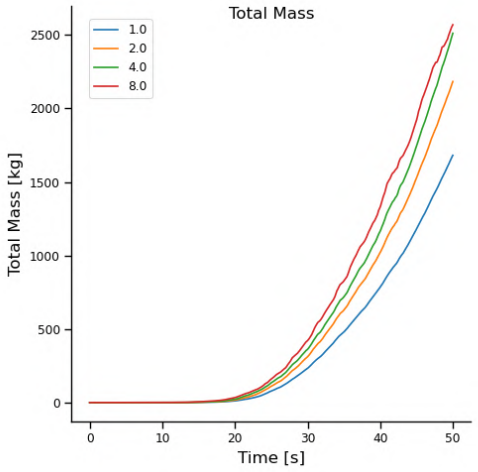

Source: Elaborated by the author.

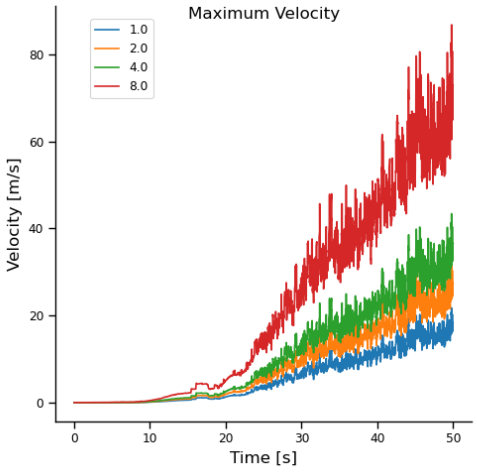

Source: Elaborated by the author.

The conversion of the simulation grid data into a voxel grid representing the PSL cloud comes from the natural translation of the volume concentration of the snow phase, $\alpha_s(\mathbf{x})$[7], into density values for the voxels[8] by a mapping function $\Gamma : \alpha_s \rightarrow \phi$ defined as

$$\Gamma(\mathbf{x}) = \gamma\alpha_s(\mathbf{x}), \tag{5.21}$$

where γ is a conversion factor that will be discussed later.

From the FVM, each simulation cell C contains a single value of α_s, localized at its center C_c, representing the mean value of the field over the cell volume C_V. Similarly, each voxel **ijk** contains a single density value, $\phi(\mathbf{ijk})$. Therefore, the output volume is an approximation of the original field and its accuracy depends directly on the resolution of the voxel grid — see Figure 67.

The data structure used for storing the voxels was the OpenVDB data structure (MUSETH *et al.*, 2013). OpenVDB, initially released by Dream Works Animation, is an open-source library that implements a hierarchical data structure highly optimized for manipulating sparse volumetric data. The data of each simulation step is converted into the OpenVDB and produces a single file for each animation frame. 3d software packages, such as Blender (COMMUNITY, 2018), widely support OpenVDB files.

All rendered images presented in this chapter were produced with a high-end renderer called *RenderMan*®(CHRISTENSEN *et al.*, 2018), particularly with the *Non-Commercial Ren-*

[7] See section 4.3 on page 116.

[8] Note that the density in the volumetric density field represented by the voxel grid is not related to the physical property of density of the PSL. The term *density* in this rendering context refers to the concentration of matter that will interact with light, analogous to smoke density.

Figure 61 – Resulting clouds 50 seconds after release for four front extension factor L_{front} values, 10, 20, 40, and 80 m, from top to bottom, respectively. All triggered from the same DSL simulation in a 25-degree slope. Brighter colors represent higher α_s values.

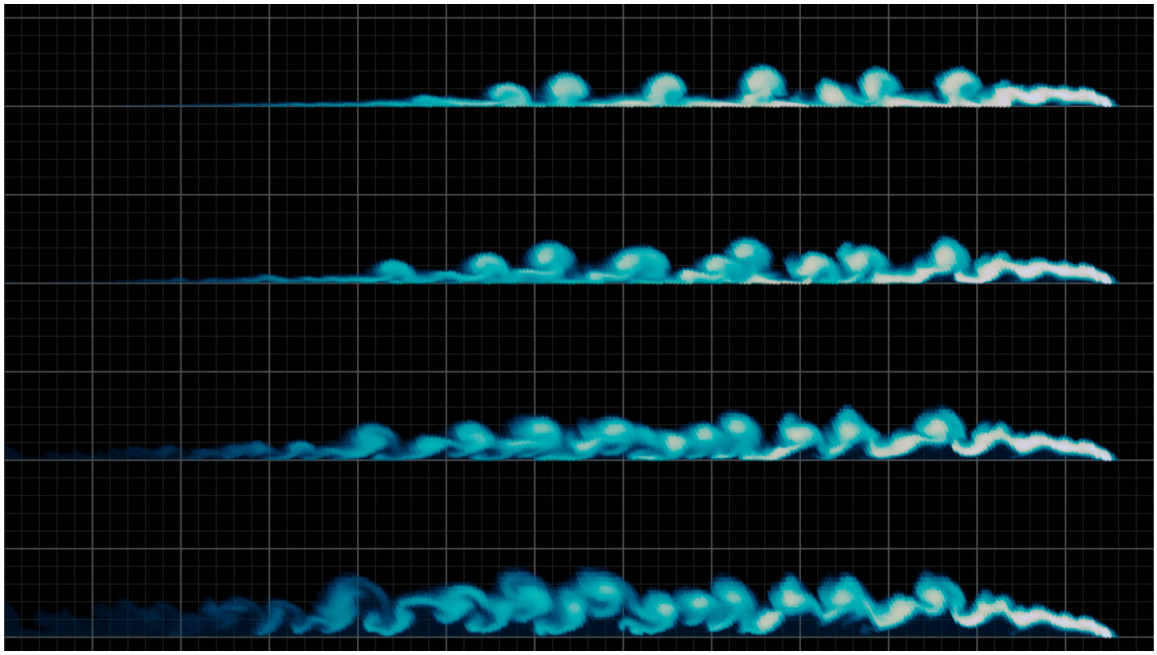

Source: Elaborated by the author.

Figure 62 – Measurements of 50 seconds-long PSL simulations for four front extension factor L_{front} values, 10, 20, 40, and 80 m. On the left is the evolution of the total mass of the powder cloud. On the right the profile of the plume heights.

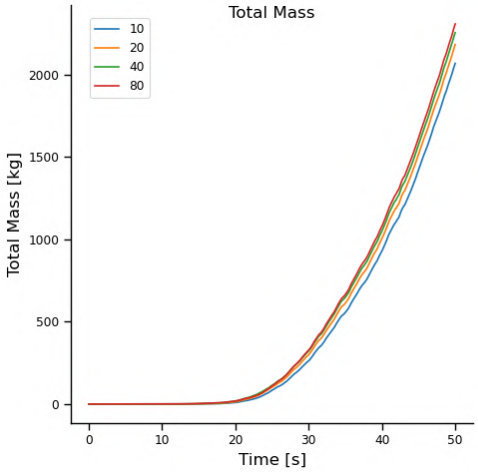

Source: Elaborated by the author.

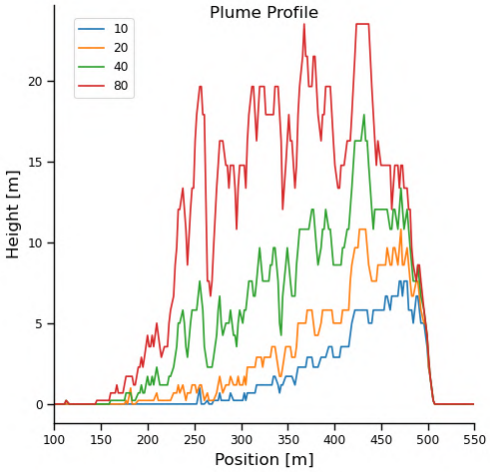

Source: Elaborated by the author.

derMan®25 version[9]. RenderMan®is a photorealistic rendering software based on physical rendering models developed by Pixar Animation Studios. Due to the visual resemblance of the powder-snow cloud with sky clouds, the strategy presented in *RenderMan*®'s documenta-

[9] <https://renderman.pixar.com/store>

Figure 63 – On top, the resulting powder cloud simulated with noise factors $\omega_{\mathbf{u}}$ and ω_a. On the bottom, no noise factor was used. The constant injection value leads to a smooth cloud surface, opposite to the turbulent pattern generated by the oscillating injection.

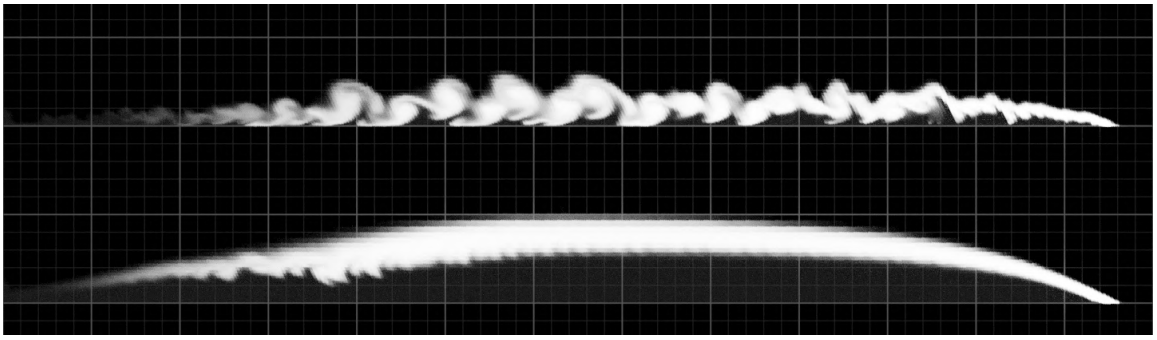

Source: Elaborated by the author.

Figure 64 – Powder clouds generated from the same parameters and initial conditions for different grid resolutions. From top to bottom, the grids contain cell sizes of 0.1, 0.5, 1.0, 5.0, and 10.0. Note how the sharp features, such as vortices and curved shapes, smooth out as the cell size increases. Only the general shape of the flow remains for larger cell sizes.

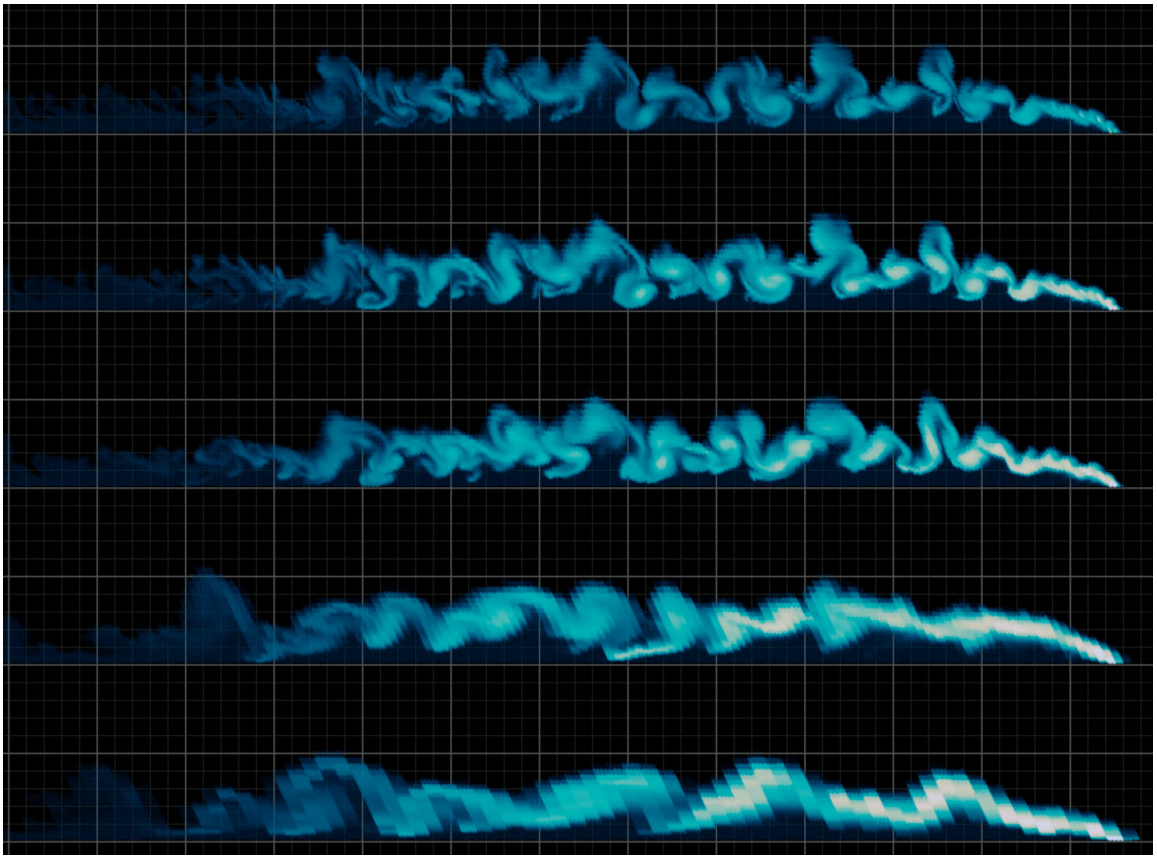

Source: Elaborated by the author.

tion[10] guided the configuration of the rendering. For text completeness, Table 14 lists the main configurations used in the final results.

[10] <https://rmanwiki.pixar.com/display/REN25/Rendering+Clouds+with+Aggregate+Volumes>

Figure 65 – The distribution of the Courant numbers and sub-time steps registered in the different resolution cases of cell sizes of 0.1, 0.5, 1.0, 5.0, and 10.0 (x-axis in the plots). As expected, larger cells lead to smaller Courant numbers and allow larger time steps.

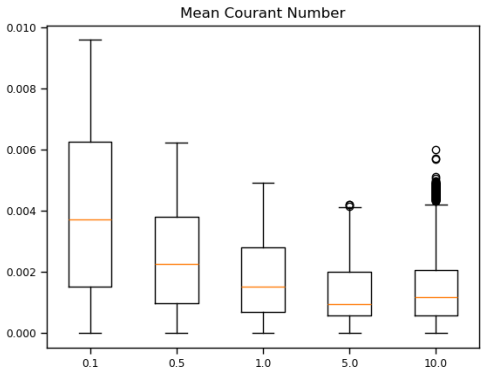

Source: Elaborated by the author.

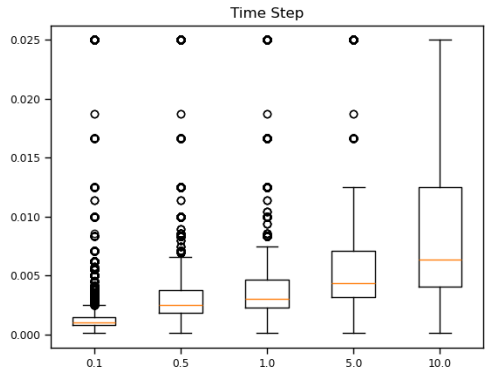

Source: Elaborated by the author.

Figure 66 – The render mesh that represents the DSL surface, blue in the figure, can be constructed by extruding the elements of the simulation mesh, red in the figure. On the left, the extrusion happens on the vertices defined by the DSL height values of the incident cells. On the right, cells are extruded individually by their height values.

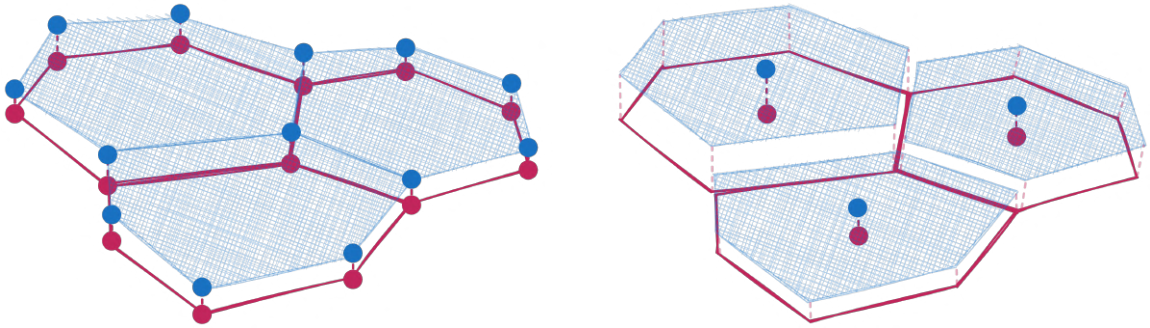

Source: Elaborated by the author.

Table 14 – Renderer configuration.

Parameter	Value
Max Path Length	256
Multi-Scattering Approx. Bleed	0.9
Primary Anisotropy	0.8
Secondary Anisotropy	−0.2
Lobe Blend Factor	0.2

5.4 Natural Terrain Examples

This section lists some examples of powder-snow avalanches simulated in complex terrain geometries. Generally, the three-dimensional terrain geometry is constructed from two-dimensional height maps, which may originate from:

- **Procedural generation techniques:** manipulate noise functions, such as the Perlin-noise,

Figure 67 – Consider a hexagonal cell from the simulation grid containing a single value of α_s. The voxel grid contains samples of α_s from the underlying cell. Since the density field is defined only on the lattice points **ijk**, the voxels' resolution has a direct impact on the final result.

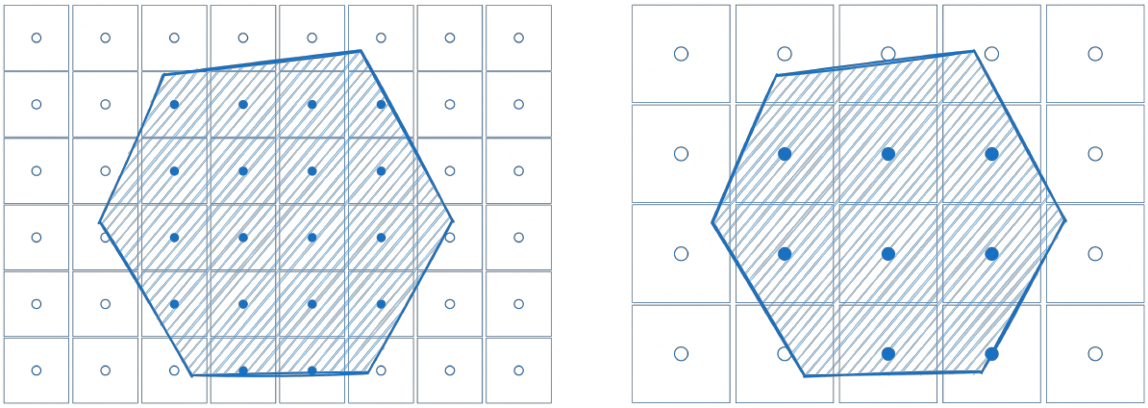

Source: Elaborated by the author.

Figure 68 – A cloud asset rendered with the workflow considered for the powder-snow cloud.

Source: RenderMan25 (2023).

to generate natural-like landscapes.

- **Real-world topographical data:** usually represented by Digital Elevation Models (DEMs), with files in Geographical Information Systems (GIS) format.

The construction of the terrain geometry proceeds by projecting the map into a three-dimensional plane and extruding each vertex of the plane by the corresponding height information of the map.

Given the regular distribution of the texels in the texture, a regular grid of quadrangular cells represents the three-dimensional mesh. The grid initially lies in the XY plane, and the vertices z coordinate is set to the height value of the terrain. Then, the mesh may be manipulated

to attend to the numerical grid requirements, such as being converted to a triangular mesh or going through a smoothing process.

5.4.1 Wolfsgrube Mountain

The Wolfsgrube Mountain is a 1641 m high mountain in the Bavarian Forest National Park in southeastern Germany. It is part of the Lusen Ridge, the second-highest mountain range in the Bavarian Forest after the Rachel Ridge.

This section utilizes a digital elevation model of the Wolfsgrube region to generate the three-dimensional surface terrain — see Figure 69. The initial conditions of the dense snow avalanche, such as the release area, follow the same conditions presented by Rauter and Tukovi (2018) — see Figure 70a. The conditions reproduce the catastrophic event on 13 March 1988, with a large release area of 196255 m^2 and a vertical descent of 984 m (FISCHER *et al.*, 2015). The avalanche path starts with a 36.5-degree slope, falls into a gully 100 m wide, and opens into the mountain base.

Figure 69 – A real photography of the Wolfsgrube mountain and the respective terrain surface generated from the DEM.

(a) Picture of the Wolfsgrube.

Source: Federal Ministry Republic of Austria (2023).

(b) Surface mesh topography.

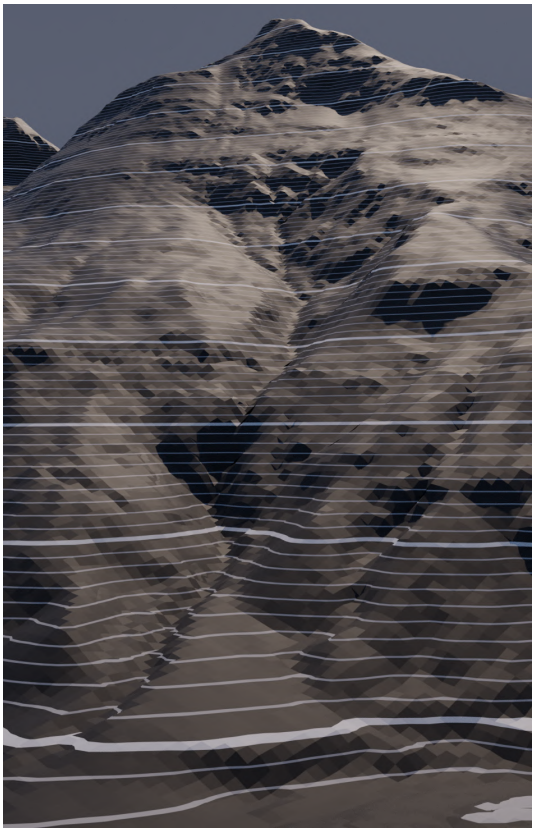

Source: Elaborated by the author.

Figure 70 shows the resulting DSL that descends in the Wolfsgrube terrain. The terrain

topography drives the body of snow, characterized by a slab avalanche, through its channel and renders a clear runout area. The PSL triggered is shown in Figure 71 at different moments of the descent. Note how the powder cloud follows the terrain features by being channeled in the middle of the track.

Figure 70 – Start and end states of the DSL. Note how the DSL stretches through the gully and deposit at the base of the mountain. The topographic lines represent the vertical height of the terrain with a bold line every 100 *m*.

(a) Initial slab release.

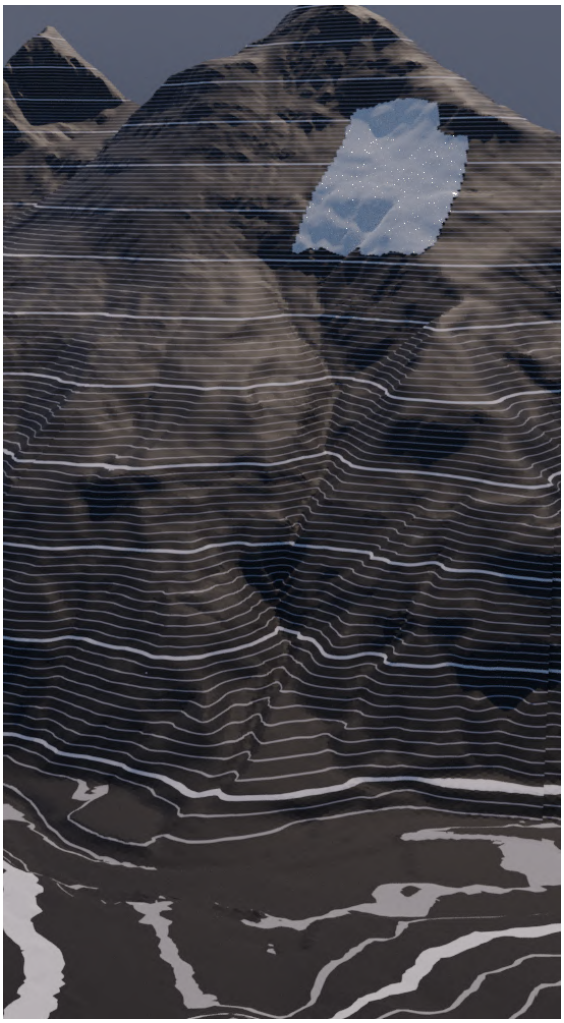

Source: Elaborated by the author.

(b) Run-out area.

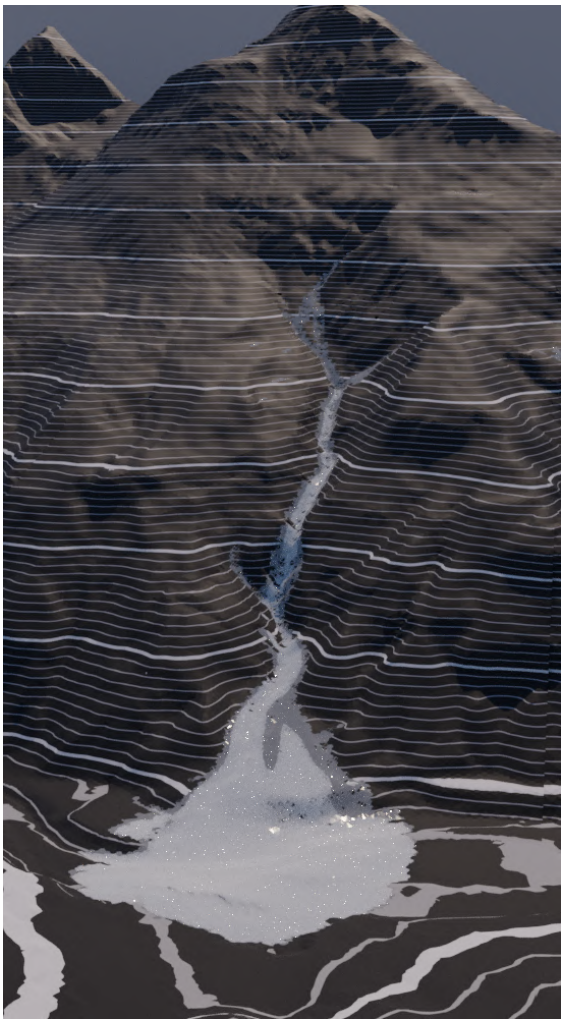

Source: Elaborated by the author.

From a distance, it is possible to distinguish the plumes. However, the characteristics billows do not appear. The main reason is that the method does not simulate turbulence, although the noise factor introduced in the entrainment processes does generate instabilities in the cloud similar to turbulence effects. Moreover, the resolution of the PSL grid in this particular simulation is 5 *m* per cell, which induces smooth results and erases details, as shown in Figure 64.

Figure 71 – Sequential frames of the full animation of the powder-snow avalanche triggered by the DSL depicted in Figure 70.

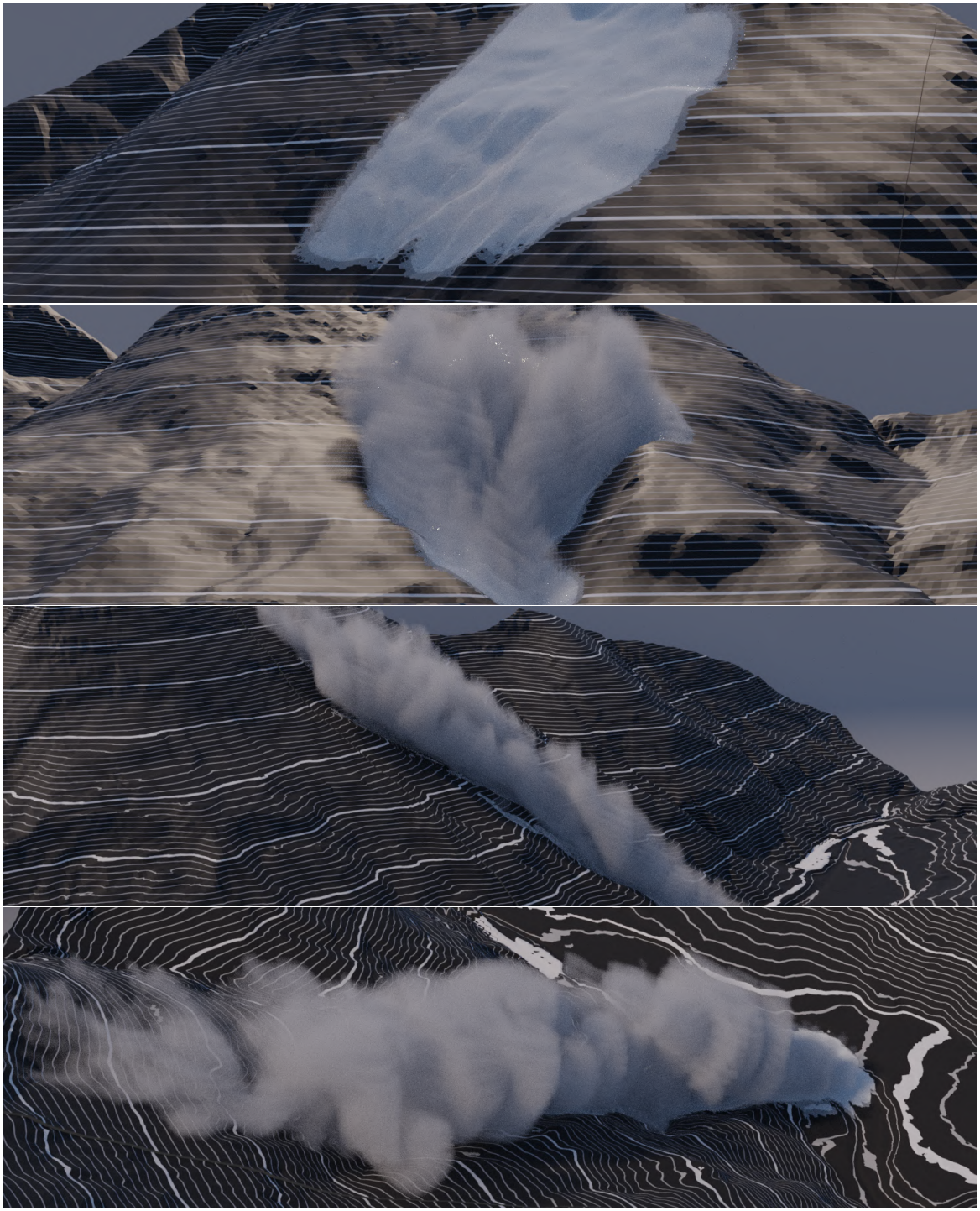

Source: Elaborated by the author.

5.5 Computational Performance

This section presents some performance measurements from the results presented in this chapter. The numerical simulations utilized the OpenFOAM v2026 core library based on the CPU. The simulations ran in parallel — up to 20 threads. The equipment utilized was an

Intel®Core™ i9 13900k with 64 GB of RAM.

Table 15 lists the processing times for each simulation presented in this chapter. The table presents the average time for simulations presented in groups, such as the four simulations of density values. The name of the simulations characterizes which parameter was being studied to facilitate identification. The first set of numbers, for the different slope angles, presents one pair (column) of times and cell counts for each angle. All DSL simulations utilized three-dimensional grids, oposed to PSL simulation, which utilized two-dimensional grids. Animations were produced at 20 fps. Therefore, simulations of 30 seconds contain 600 frames, 50 seconds contain 1000 frames, and 90 seconds contain 1800 frames.

Table 15 – Memory and time measurements of the simulations presented in this chapter.

Figure	Simulations	Type	Duration [s]	Total Time [s]	Cell Count
Figure 50	Angles	DSL	30	180 210 237 239	33450 32250 30825 29175
		PSL		103 159 158 156	22300 21500 20550 19450
Figure 52	Modified	DSL	30	24	32250
	ramp	PSL		17287	1612500
Figure 53	Ramp	DSL		28	32250
		PSL		11036	1612500
		DSL	50	57	32250
Figure 54	ρ_s	PSL		138	18734
Figure 57	e_b	DSL		34	32250
Figure 57	e_b	PSL		100	21500
Figure 58	γ_α	PSL		145	18734
Figure 59	$\gamma_{\mathbf{u}}$	PSL		168	18734
Figure 61	L_{front}	PSL		143	18734
Figure 64	$\Delta x = 0.1$	PSL		19393	375122
Figure 64	$\Delta x = 0.5$	PSL		887	75004
Figure 64	$\Delta x = 1.0$	PSL		350	37502
Figure 64	$\Delta x = 5.0$	PSL		87	7480
Figure 64	$\Delta x = 10.0$	PSL		65	3740
Figure 70	Wolfsgrube	DSL	90	218	40895
Figure 71		PSL		24662	1516800

CHAPTER

6

CONCLUSIONS

This chapter presents the conclusions and general discussions about the proposed method for producing physically-based digital animations of powder snow avalanches. The previous chapters explored existing research on the general topic of snow avalanches, predominantly from engineering and geological sciences, which compose the mathematical and physical background of the method.

The text presented a one-way coupling model for the animation of mixed-type avalanches. The method performs two sequential simulations such that the first feed the second. Therefore, the PSL simulation is agnostic to the DSL simulation method as long as the output data from the DSL is compatible. Such an approach is particularly appealing to Computer Graphics systems.

The primary motivation for this work was to bring the study of avalanche-like phenomena to the realm of computer graphics. Large-scale physical phenomena are complex events that are not fully understood and are the subject of intense research across various disciplines. Although there are well-known mathematical models for describing such phenomena, little can be found in computer graphics literature.

Although the text presents a complete workflow for animating powder-snow avalanches, it also represents an initial step into the subject. The extensive research presented in Chapter 3 brings a rich literature that offers numerous opportunities for new applications in Computer Graphics. However, it also points out many challenges and open problems avalanche science faces, consequently challenging Computer Graphics approaches.

6.1 Limitations

During the experiments, the numerical stability of the simulations became challenging. Although the FVM offers reasonable flexibility regarding the grid's topology, it proved very sensitive to the geometry. The input mesh, produced from the DEM, usually carries sharp edges

and non-planar faces, leading to concave grid cells. The numerical method must use orthogonal correctors to mitigate such problems. Therefore, most terrain meshes had to be pre-processed with smoothing methods and re-meshing algorithms to produce better-quality grids.

The current DSL method is limited to mildly curved terrains due to the nature of SWE. Such a model requires small flow heights compared to the curvature. However, other alternatives exist, such as the recent use of the MPM method for dense snow flows (LI *et al.*, 2022). Moreover, hybrid methods can bring solutions for both the DSL and the PSL simulations.

The method presented in section 5.3 for generating the volumetric field of the powder-snow cloud for rendering is analogous to pixel rasterization schemes and brings inherent problems such as aliasing. However, given the large size of simulation cells compared to voxel sizes, increasing the resolution of the voxel grid or applying anti-aliasing techniques to it does not necessarily solve the problem. The current method is purely dependent on the numerical grid resolution regarding aliasing effects.

6.2 Future Work

The resolution of the PSL simulation is the principal factor for the visual quality of the result. However, the simulation domains are inherently too large to utilize desirable cell sizes. Although machine resources limit the code and can handle parallel runs efficiently, performance optimization was not deeply explored. A natural and appealing path for future developments is using GPUs to solve numerical systems or handle mesh element computations such as interpolation of fields.

An alternative to avoid the increase in cell count is to employ post-processing techniques to enhance the visual quality and realism of the resulting data. One possible approach to handle the aliasing effects mentioned earlier is the use of interpolation techniques, such as the *radial basis functions Hermite interpolation* (FASSHAUER, 2007), to compute voxel values.

The PSL model equations provide a convenient approach for describing the mixture of fluids with a smaller set of equations. However, the equations used in the model bring simplifications that should be explored in the future. For example, air drag is critical in shaping the powder cloud, mainly the head of the snow avalanche.

Indeed, the leading edge of the PSL is one of its mesmerizing and distinct features. However, the appearance of the front suffers directly and intensely from the effects of the low resolution of the numerical grid. In future work, adaptive structures will be explored to develop solutions that provide outstanding details on the surface of the cloud, mainly in the front. The adaptivity should be able to provide dynamic refinement close to the evolving interface between air and powder snow.

Turbulence is the core phenomenon in such avalanches. Although the noise factors in the

entrainment model agitate the flow and lead to billow shapes, the method does not handle interior flows and fluctuations caused by the intermittent region. The next step would be introducing a turbulent model or exploring procedural turbulent models rooted back to *wavelet turbulence* (KIM *et al.*, 2008b).

Finally, future developments should consider the dual-coupling systems between avalanches and physical objects, such as trees and buildings. Other than the base terrain, the interaction with the surroundings perceptually integrates the scene and ensures realism. Physical interaction is of utmost importance in the animation of physical phenomena.

BIBLIOGRAPHY

ABDELRAZEK, A.; KIMURA, I.; SHMIZU, Y. Numerical simulation of a small-scale snow avalanche tests using non-newtonian sph model. **Journal of Japan Society of Civil Engineers, Ser. A2 (Applied Mechanics (AM))**, v. 70, p. I_681–I_690, 01 2014. Citation on page 86.

ABRAHAM, M. T.; SATYAM, N.; PRADHAN, B.; TIAN, H. Debris flow simulation 2d (dfs 2d): Numerical modelling of debris flows and calibration of friction parameters. **Journal of Rock Mechanics and Geotechnical Engineering**, 2022. ISSN 1674-7755. Available: <https://www.sciencedirect.com/science/article/pii/S1674775522000403>. Citation on page 72.

AKIYAMA, J.; URA, M. Motion of 2d buoyant clouds downslope. **Journal of Hydraulic Engineering**, American Society of Civil Engineers, v. 125, n. 5, p. 474–480, 1999. Citation on page 93.

ALBABA, A.; LAMBERT, S.; FAUG, T. Dry granular avalanche impact force on a rigid wall: Analytic shock solution versus discrete element simulations. **Phys. Rev. E**, American Physical Society, v. 97, p. 052903, 5 2018. Available: <https://link.aps.org/doi/10.1103/PhysRevE.97.052903>. Citation on page 100.

ALDUáN, I.; OTADUY, M. A. Sph granular flow with friction and cohesion. In: **Proceedings of the 2011 ACM SIGGRAPH/Eurographics Symposium on Computer Animation**. New York, NY, USA: Association for Computing Machinery, 2011. (SCA '11), p. 25–32. ISBN 9781450309233. Available: <https://doi.org/10.1145/2019406.2019410>. Citation on page 104.

ANCEY, C. **Snow Avalanches. Selected topics in geological and geomorphological fluid mechanics**. [S.l.]: Springer, Berlin, 2001. Citations on pages 78 and 92.

____. Powder snow avalanches: Approximation as non-boussinesq clouds with a richardson numberdependent entrainment function. **Journal of Geophysical Research: Earth Surface**, v. 109.0, n. F1, 2004. Available: <https://onlinelibrary.wiley.com/doi/abs/10.1029/2003JF000052>. Citations on pages 64 and 92.

____. **Snow Avalanches**. Oxford University Press, 2016. Available: <https://oxfordre.com/naturalhazardscience/view/10.1093/acrefore/9780199389407.001.0001/acrefore-9780199389407-e-17>. Citations on pages 58, 59, 60, 72, 87, and 92.

ANCEY, C.; GERVASONI, C.; MEUNIER, M. Computing extreme avalanches. **Cold Regions Science and Technology**, v. 39, n. 2, p. 161–180, 2004. ISSN 0165-232X. Snow And Avalanches: Papers Presented At The European Geophysical Union Conference, Nice, April 2003. Dedicated To The Avalanche Dynamics Pioneer Dr. B. Salm. Available: <https://www.sciencedirect.com/science/article/pii/S0165232X04000436>. Citations on pages 68 and 86.

ANCEY, C.; MEUNIER, M. Estimating bulk rheological properties of flowing snow avalanches from field data. **Journal of Geophysical Research: Earth Surface**, v. 109, n. F1, 2004. Available: <https://agupubs.onlinelibrary.wiley.com/doi/abs/10.1029/2003JF000036>. Citation on page 78.

ANCEY, C.; MEUNIER, M.; RICHARD, D. Inverse problem in avalanche dynamics models. **Water Resources Research**, v. 39, n. 4, 2003. Available: <https://agupubs.onlinelibrary.wiley.com/doi/abs/10.1029/2002WR001749>. Citation on page 86.

ANDREOTTI, B.; FORTERRE, Y.; POULIQUEN, O. **Granular media: between fluid and solid**. [S.l.]: Cambridge University Press, 2013. Citation on page 96.

ARENSON, L. U.; COLGAN, W.; MARSHALL, H. P. Chapter 2 - physical, thermal, and mechanical properties of snow, ice, and permafrost. In: SHRODER, J. F.; HAEBERLI, W.; WHITEMAN, C. (Ed.). **Snow and Ice-Related Hazards, Risks, and Disasters**. Boston: Academic Press, 2015, (Hazards and Disasters Series). p. 35–75. ISBN 978-0-12-394849-6. Available: <https://www.sciencedirect.com/science/article/pii/B9780123948496000020>. Citation on page 78.

ARENSON, L. U.; SPRINGMAN, S. M.; SEGO, D. C. The rheology of frozen soils. **Applied Rheology**, v. 17, n. 1, p. 12147–1–12147–14, 2007. Available: <https://doi.org/10.1515/arh-2007-0003>. Citation on page 77.

ARMANINI, A.; FRACCAROLLO, L.; ROSATTI, G. Two-dimensional simulation of debris flows in erodible channels. **Computers & Geosciences**, v. 35, n. 5, p. 993–1006, 2009. ISSN 0098-3004. Modelling and Simulation of Dangerous Phenomena for Hazard Mapping. Available: <https://www.sciencedirect.com/science/article/pii/S009830040800068X>. Citation on page 104.

ATKIN, R.; CRAINE, R. Continuum theories of mixtures: basic theory and historical development. **The Quarterly Journal of Mechanics and Applied Mathematics**, Oxford University Press, v. 29.0, n. 2, p. 209–244, 1976. Citations on pages 96 and 203.

AVAL-1D, WSL. **AVAL-1D**. 2022. [Online; accessed September 26, 2022]. Available: <https://www.wsl.ch/en/services-et-produits/logiciels-sites-internets-et-apps/aval-1d.html>. Citations on pages 102 and 103.

AVALANCHE.ORG. **Avalanche.org**. 2023. [Online; accessed September 09, 2023]. Available: <https://avalanche.org/avalanche-encyclopedia/#avalanche>. Citation on page 51.

BAGNOLD, R. A. Experiments on a gravity-free dispersion of large solid spheres in a newtonian fluid under shear. **Proceedings of the Royal Society of London. Series A. Mathematical and Physical Sciences**, The Royal Society London, v. 225, n. 1160, p. 49–63, 1954. Citations on pages 79 and 87.

____. Auto-suspension of transported sediment; turbidity currents. **Proceedings of the Royal Society of London. Series A. Mathematical and Physical Sciences**, The Royal Society London, v. 265, n. 1322, p. 315–319, 1962. Citation on page 87.

BAINES, P. G. Mixing in flows down gentle slopes into stratified environments. **Journal of Fluid Mechanics**, Cambridge University Press, v. 443, p. 237–270, 2001. Citation on page 91.

BAKER, J. L.; BARKER, T.; GRAY, J. M. N. T. A two-dimensional depth-averaged $\mu(i)$-rheology for dense granular avalanches. **Journal of Fluid Mechanics**, Cambridge University Press, v. 787, p. 367–395, 2016. Citation on page 85.

BAKHVALOV, N. S.; ÉGLIT, M. É. Investigation of the one-dimensional motion of a snow avalanche along a flat slope. **Fluid Dynamics**, v. 8, n. 5, p. 683–689, 9 1973. ISSN 1573-8507. Available: <https://doi.org/10.1007/BF01023564>. Citation on page 74.

BARALE, L. Footstep-triggered grain flows on the lee side of a desert sand dune (erg chebbi, morocco). **International Journal of Earth Sciences**, v. 104, n. 8, p. 2213–2214, Nov 2015. ISSN 1437-3262. Available: <https://doi.org/10.1007/s00531-015-1246-3>. Citation on page 47.

BARBOLINI, M.; BIANCARDI, A.; CAPPABIANCA, F.; NATALE, L.; PAGLIARDI, M. Laboratory study of erosion processes in snow avalanches. **Cold Regions Science and Technology**, v. 43, n. 1, p. 1–9, 2005. ISSN 0165-232X. Snow and Avalanches. Available: <https://www.sciencedirect.com/science/article/pii/S0165232X05000807>. Citation on page 66.

BARBOLINI, M.; GRUBER, U.; KEYLOCK, C.; NAAIM, M.; SAVI, F. Application of statistical and hydraulic-continuum dense-snow avalanche models to five real european sites. **Cold Regions Science and Technology**, v. 31, n. 2, p. 133–149, 2000. ISSN 0165-232X. Available: <https://www.sciencedirect.com/science/article/pii/S0165232X00000082>. Citation on page 86.

BARDOLINI, M.; ISSLER, D.; JÓHANNESSON, T.; HÁKONARDÓTTIR, K.; LIED, K.; GAUER, P.; NAAIM, M.; FAUG, T.; NATALE, L.; CAPPABIANCA, F. *et al.* Avalanche test sites and research equipment in europe. v. 8, 2005. Citation on page 60.

BARTELT, P.; BÜHLER, Y.; BUSER, O.; GINZLER, C. Plume formation in powder snow avalanches. In: . [S.l.: s.n.], 2013. Citations on pages 54, 58, 61, and 63.

BARTELT, P.; BUSER, O.; PLATZER, K. Fluctuation-dissipation relations for granular snow avalanches. **Journal of Glaciology**, Cambridge University Press, v. 52, n. 179, p. 631–643, 2006. Citations on pages 74 and 86.

BARTELT, P.; BUSER, O.; VALERO, C. V.; BüHLER, Y. Configurational energy and the formation of mixed flowing/powder snow and ice avalanches. **Annals of Glaciology**, Cambridge University Press, v. 57, n. 71, p. 179–188, 2016. Citations on pages 62, 97, 99, and 121.

BARTELT, P.; CHRISTEN, M.; BÜHLER, Y.; CAVIEZEL, A.; BUSER, O. Snow entrainment: Avalanche interaction with an erodible substrate. In: **Proceedings of the International Snow Science Workshop**. [S.l.: s.n.], 2018. p. 716–720. Citation on page 99.

BARTELT, P.; KERN, M.; CHRISTEN, M. A mixed flowing/powder snow avalanche model. In: **Proceeding of the International Snow Science Workshop: a merging between theory and practice (ISSW 2000)**. [S.l.: s.n.], 2000. p. 280–289. Citations on pages 97 and 99.

BARTELT, P.; MCARDELL, B. W. Granulometric investigations of snow avalanches. **Journal of Glaciology**, Cambridge University Press, v. 55, n. 193, p. 829–833, 2009. Citation on page 76.

BARTELT, P.; SALM, B.; GRUBER, U. Calculating dense-snow avalanche runout using a voellmy-fluid model with active/passive longitudinal straining. **Journal of Glaciology**, Cambridge University Press, v. 45, n. 150, p. 242–254, 1999. Citations on pages 72, 74, 76, 84, and 102.

BARTELT, P.; VALERO, C. V.; FEISTL, T.; CHRISTEN, M.; BüHLER, Y.; BUSER, O. Modelling cohesion in snow avalanche flow. **Journal of Glaciology**, Cambridge University Press, v. 61, n. 229, p. 837–850, 2015. Citation on page 80.

BARTHOLOMEW, P.; DESKOS, G.; FRANTZ, R. A.; SCHUCH, F. N.; LAMBALLAIS, E.; LAIZET, S. Xcompact3d: An open-source framework for solving turbulence problems on a cartesian mesh. **SoftwareX**, v. 12.0, p. 100550, 2020. ISSN 2352-7110. Available: <https://www.sciencedirect.com/science/article/pii/S2352711019303620>. Citation on page 104.

BARTHOLOMEW, P.; LAIZET, S. A new highly scalable, high-order accurate framework for variable-density flows: Application to non-boussinesq gravity currents. **Computer Physics Communications**, v. 242.0, p. 83–94, 2019. ISSN 0010-4655. Available: <https://www.sciencedirect.com/science/article/pii/S0010465519301006>. Citation on page 88.

BEGHIN, P. **Etude des bouffées bidimensionnelles de densité en écoulement sur pente avec application aux avalanches de neige poudreuse**. Phd Thesis (PhD Thesis), 1979. Citation on page 92.

BEGHIN, P.; BRUGNOT, G. Contribution of theoretical and experimental results to powder-snow avalanche dynamics. **Cold Regions Science and Technology**, v. 8, n. 1, p. 67–73, 1983. ISSN 0165-232X. Available: <https://www.sciencedirect.com/science/article/pii/0165232X83900186>. Citation on page 92.

BEGHIN, P.; HOPFINGER, E. J.; BRITTER, R. E. Gravitational convection from instantaneous sources on inclined boundaries. **Journal of Fluid Mechanics**, Cambridge University Press, v. 107, p. 407–422, 1981. Citation on page 92.

BEGHIN, P.; OLAGNE, X. Experimental and theoretical study of the dynamics of powder snow avalanches. **Cold Regions Science and Technology**, v. 19.0, n. 3, p. 317–326, 1991. ISSN 0165-232X. Available: <https://www.sciencedirect.com/science/article/pii/0165232X9190046J>. Citations on pages 64 and 65.

BEGNUDELLI, L.; SANDERS, B. F. Unstructured grid finite-volume algorithm for shallow-water flow and scalar transport with wetting and drying. **Journal of Hydraulic Engineering**, v. 132.0, n. 4, p. 371–384, 2006. Available: <https://ascelibrary.org/doi/abs/10.1061/%28ASCE%290733-9429%282006%29132%3A4%28371%29>. Citation on page 83.

BELL, N.; YU, Y.; MUCHA, P. J. Particle-based simulation of granular materials. In: **Proceedings of the 2005 ACM SIGGRAPH/Eurographics Symposium on Computer Animation**. New York, NY, USA: Association for Computing Machinery, 2005. (SCA '05), p. 77–86. ISBN 1595931988. Available: <https://doi.org/10.1145/1073368.1073379>. Citation on page 104.

BENJAMIN, T. B. Gravity currents and related phenomena. **Journal of Fluid Mechanics**, Cambridge University Press, v. 31, n. 2, p. 209248, 1968. Citations on pages 59 and 89.

BENKHALDOUN, F.; SEAD, M. A simple finite volume method for the shallow water equations. **Journal of Computational and Applied Mathematics**, v. 234.0, n. 1, p. 58–72, 2010. ISSN 0377-0427. Available: <https://www.sciencedirect.com/science/article/pii/S0377042709008139>. Citation on page 83.

BINGHAM, E. C. **The History of the Society of Rheology from 1924-1944**. [S.l.: s.n.], 1944. Citation on page 76.

BIRMAN, V.; MEIBURG, E. High-resolution simulations of gravity currents. **Journal of the Brazilian Society of Mechanical Sciences and Engineering**, SciELO Brasil, v. 28.0, n. 2, p. 169–173, 2006. Citation on page 88.

BORDEN, Z.; MEIBURG, E. Circulation based models for boussinesq gravity currents. **Physics of Fluids**, v. 25, n. 10, p. 101301, 2013. Available: <https://doi.org/10.1063/1.4825035>. Citation on page 90.

BORIS, J. P.; BOOK, D. L. Flux-corrected transport. i. shasta, a fluid transport algorithm that works. **Journal of Computational Physics**, v. 11, n. 1, p. 38–69, 1973. ISSN 0021-9991. Available: <https://www.sciencedirect.com/science/article/pii/0021999173901472>. Citation on page 217.

BOUCHUT, F.; MANGENEY-CASTELNAU, A.; PERTHAME, B.; VILOTTE, J.-P. A new model of saint venant and savagehutter type for gravity driven shallow water flows. **Comptes Rendus Mathematique**, v. 336.0, n. 6, p. 531–536, 2003. ISSN 1631-073X. Available: <https://www.sciencedirect.com/science/article/pii/S1631073X03001171>. Citation on page 83.

BOUSSINESQ, J. **Théorie Analytique de la Chaleur Mise en Harmonie Avec la Thermodynamique Et Avec la Théorie Mécanique de la Lumière: Refroidissement et échauffement par rayonnement, conductibilité des tiges, lames et masses cristallines, courants de convection, théorie mécanique de la lumière. 1903. xxxii, 625,[1] p**. [S.l.]: Gauthier-Villars, 1903. Citation on page 87.

BOVET, E.; CHIAIA, B.; PREZIOSI, L. A new model for snow avalanche dynamics based on non-newtonian fluids. **Meccanica**, v. 45, n. 6, p. 753–765, 12 2010. ISSN 1572-9648. Available: <https://doi.org/10.1007/s11012-009-9278-z>. Citation on page 86.

BOZHINSKIY, A.; LOSEV, K.; BARTELT, C. **The Fundamentals of Avalanche Science**. Eidgenöss. Inst. für Schnee- und Lawinenforschung, Bibliothek, 1998. (Eidgenössisches Institut für Schnee- und Lawinenforschung Weißfluhjoch: Mitteilungen des Eidgenössischen Institutes für Schnee- und Lawinenforschung). ISBN 9783905620719. Available: <https://books.google.com.br/books?id=n0MkGQAACAAJ>. Citations on pages 60, 74, 76, and 92.

BRIDSON, R.; HOURIHAM, J.; NORDENSTAM, M. Curl-noise for procedural fluid flow. **ACM Trans. Graph.**, Association for Computing Machinery, New York, NY, USA, v. 26.0, n. 3, p. 46es, 7 2007. ISSN 0730-0301. Available: <https://doi.org/10.1145/1276377.1276435>. Citation on page 105.

BRITTER, R. E.; LINDEN, P. F. The motion of the front of a gravity current travelling down an incline. **Journal of Fluid Mechanics**, Cambridge University Press, v. 99, n. 3, p. 531–543, 1980. Citation on page 90.

BROCK, R. R. Development of roll waves in open channels. California Institute of Technology, 1967. Citation on page 90.

BUSER, O.; BARTELT, P. Production and decay of random kinetic energy in granular snow avalanches. **Journal of Glaciology**, Cambridge University Press, v. 55, n. 189, p. 3–12, 2009. Citation on page 86.

BUTTINGER-KREUZHUBER, A.; HORVTH, Z.; NOELLE, S.; BLSCHL, G.; WASER, J. A fast second-order shallow water scheme on two-dimensional structured grids over abrupt topography. **Advances in Water Resources**, v. 127.0, p. 89–108, 2019. ISSN 0309-1708. Available: <https://www.sciencedirect.com/science/article/pii/S0309170818305335>. Citation on page 83.

CALGARO, C.; CREUSÉ, E.; GOUDON, T. Modeling and Simulation of Mixture Flows :Application to Powder-Snow Avalanches. **Computers and Fluids**, Elsevier, v. 107, p. 100–122, 2015. Available: <https://hal.archives-ouvertes.fr/hal-00732112>. Citation on page 97.

CAMPBELL, C. S. Rapid granular flows. **Annual Review of Fluid Mechanics**, v. 22, n. 1, p. 57–90, 1990. Available: <https://doi.org/10.1146/annurev.fl.22.010190.000421>. Citation on page 79.

CARROLL, C. S.; LOUGE, M. Y.; TURNBULL, B. Frontal dynamics of powder snow avalanches. **Journal of Geophysical Research: Earth Surface**, v. 118.0, n. 2, p. 913–924, 2013. Available: <https://agupubs.onlinelibrary.wiley.com/doi/abs/10.1002/jgrf.20068>. Citations on pages 99 and 120.

CARROLL, C. S.; TURNBULL, B.; LOUGE, M. Y. Role of fluid density in shaping eruption currents driven by frontal particle blow-out. **Physics of Fluids**, v. 24, n. 6, p. 066603, 2012. Available: <https://doi.org/10.1063/1.4725538>. Citation on page 99.

CHAWDHARY, S.; KHOSRONEJAD, A.; CHRISTODOULOU, G.; SOTIROPOULOS, F. Large eddy simulation of density current on sloping beds. **International Journal of Heat and Mass Transfer**, v. 120, p. 1374–1385, 2018. ISSN 0017-9310. Available: <https://www.sciencedirect.com/science/article/pii/S0017931017336529>. Citations on pages 101 and 102.

CHEN, C. P.; WOOD, P. E. A turbulence closure model for dilute gas-particle flows. **The Canadian Journal of Chemical Engineering**, v. 63, n. 3, p. 349–360, 1985. Available: <https://onlinelibrary.wiley.com/doi/abs/10.1002/cjce.5450630301>. Citation on page 96.

CHEREPANOV, G. P.; ESPARRAGOZA, I. E. A fracture-entrainment model for snow avalanches. **Journal of Glaciology**, Cambridge University Press, v. 54, n. 184, p. 182–188, 2008. Citation on page 86.

CHLDEK, M.; URIKOVI, R. Particle-based shallow water simulation for irregular and sparse simulation domains. **Computers & Graphics**, v. 53.0, p. 170 – 176, 2015. ISSN 0097-8493. Available: <http://www.sciencedirect.com/science/article/pii/S0097849315000412>. Citation on page 104.

CHRISTEN, M.; BARTELT, P.; GRUBER, U. Aval-1d: An avalanche dynamics program for the practice. In: **International congress interpraevent**. [S.l.: s.n.], 2002. p. 715–725. Citation on page 102.

CHRISTEN, M.; KOWALSKI, J.; BARTELT, P. Ramms: Numerical simulation of dense snow avalanches in three-dimensional terrain. **Cold Regions Science and Technology**, v. 63.0, n. 1, p. 1–14, 2010. ISSN 0165-232X. Available: <https://www.sciencedirect.com/science/article/pii/S0165232X10000844>. Citations on pages 73, 86, and 103.

CHRISTENSEN, P.; FONG, J.; SHADE, J.; WOOTEN, W.; SCHUBERT, B.; KENSLER, A.; FRIEDMAN, S.; KILPATRICK, C.; RAMSHAW, C.; BANNISTER, M.; RAYNER, B.; BROUILLAT, J.; LIANI, M. Renderman: An advanced path-tracing architecture for movie rendering. **ACM Trans. Graph.**, Association for Computing Machinery, New York, NY, USA, v. 37, n. 3, aug 2018. ISSN 0730-0301. Available: <https://doi.org/10.1145/3182162>. Citation on page 154.

Christian Kröner. **Experimental and numerical description of rapid granular flows and some baseline constraints for simulating 3-dimensional granular flow dynamics**. Phd Thesis (PhD Thesis) — Rheinische Friedrich-Wilhelms-Universität Bonn, 7 2014. Available: <https://hdl.handle.net/20.500.11811/6138>. Citations on pages 81 and 82.

COAZ, J. W. F. Die lawinen der schweizer alpen. p. 171, 1881. Citation on page 58.

COMMUNITY, B. O. **Blender - a 3D modelling and rendering package**. Stichting Blender Foundation, Amsterdam, 2018. Available: <http://www.blender.org>. Citation on page 154.

CORDONNIER, G.; ECORMIER, P.; GALIN, E.; GAIN, J.; BENES, B.; CANI, M.-P. Interactive generation of time-evolving, snow-covered landscapes with avalanches. In: ACM. **Proceedings of the 17th ACM SIGGRAPH/Eurographics Symposium on Computer Animation**. [S.l.], 2018. Citation on page 105.

CORTEN, H. Chapter 9 - fracture mechanics of composites. In: LIEBOWITZ, H. (Ed.). **Fracture of Nonmetals and Composites**. Academic Press, 1972. p. 675–769. ISBN 978-0-12-449707-8. Available: <https://www.sciencedirect.com/science/article/pii/B9780124497078500130>. Citation on page 86.

CRASTER, R. V.; MATAR, O. K. Dynamics and stability of thin liquid films. **Rev. Mod. Phys.**, American Physical Society, v. 81, p. 1131–1198, 8 2009. Available: <https://link.aps.org/doi/10.1103/RevModPhys.81.1131>. Citation on page 83.

DAI, A.; HUANG, Y.-L. Boussinesq and non-boussinesq gravity currents propagating on unbounded uniform slopes in the deceleration phase. **Journal of Fluid Mechanics**, Cambridge University Press, v. 917, p. A23, 2021. Citation on page 64.

DAMIAN, S. M. An extended mixture model for the simultaneous treatment of short and long scale interfaces (phd thesis). **National University of the Littoral**, 2013. Citation on page 227.

DAMIáN, S. M.; NIGRO, N. M. An extended mixture model for the simultaneous treatment of small-scale and large-scale interfaces. **International Journal for Numerical Methods in Fluids**, v. 75, n. 8, p. 547–574, 2014. Available: <https://onlinelibrary.wiley.com/doi/abs/10.1002/fld.3906>. Citation on page 227.

DARWISH, M.; MOUKALLED, F. **The finite volume method in computational fluid dynamics: an advanced introduction with OpenFOAM® and Matlab®**. [S.l.]: Springer, 2016. Citations on pages 205, 213, and 223.

DASGUPTA, P. Sediment gravity flow—the conceptual problems. **Earth-Science Reviews**, v. 62, n. 3, p. 265–281, 2003. ISSN 0012-8252. Available: <https://www.sciencedirect.com/science/article/pii/S0012825202001605>. Citation on page 48.

DECKELNICK, K.; DZIUK, G.; ELLIOTT, C. M. Computation of geometric partial differential equations and mean curvature flow. **Acta Numerica**, Cambridge University Press, v. 14, p. 139–232, 2005. Citations on pages 83 and 111.

DELLINO, P.; DIOGUARDI, F.; DORONZO, D. M.; MELE, D. The entrainment rate of non-boussinesq hazardous geophysical gas-particle flows: An experimental model with application to pyroclastic density currents. **Geophysical Research Letters**, v. 46, n. 22, p. 12851–12861, 2019. Available: <https://agupubs.onlinelibrary.wiley.com/doi/abs/10.1029/2019GL084776>. Citation on page 64.

DENLINGER, R. P.; IVERSON, R. M. Granular avalanches across irregular three-dimensional terrain: 1. theory and computation. **Journal of Geophysical Research: Earth Surface**, v. 109, n. F1, 2004. Available: <https://agupubs.onlinelibrary.wiley.com/doi/abs/10.1029/2003JF000085>. Citation on page 82.

DENT, J.; BURRELL, K.; SCHMIDT, D. S.; LOUGE, M.; ADAMS, E.; JAZBUTIS, T. Density, velocity and friction measurements in a dry-snow avalanche. **Annals of Glaciology**, Cambridge University Press, v. 26, p. 247–252, 1998. Citations on pages 61 and 66.

DENT, J.; LANG, T. Experiments on mechanics of flowing snow. **Cold Regions Science and Technology**, v. 5, n. 3, p. 253–258, 1982. ISSN 0165-232X. Available: <https://www.sciencedirect.com/science/article/pii/0165232X82900180>. Citation on page 76.

DONG, J.; LI, D. F. A new second-order modified hydrostatic reconstruction for the shallow water flows with a discontinuous topography. **Applied Numerical Mathematics**, v. 161.0, p. 408–424, 2021. ISSN 0168-9274. Available: <https://www.sciencedirect.com/science/article/pii/S016892742030369X>. Citation on page 83.

DOYLE, E. E.; HOGG, A. J.; MADER, H. M. A two-layer approach to modelling the transformation of dilute pyroclastic currents into dense pyroclastic flows. **Proceedings of the Royal Society A: Mathematical, Physical and Engineering Sciences**, The Royal Society Publishing, v. 467, n. 2129, p. 1348–1371, 2011. Citation on page 83.

DREIER, L.; BüHLER, Y.; GINZLER, C.; BARTELT, P. Comparison of simulated powder snow avalanches with photogrammetric measurements. **Annals of Glaciology**, Cambridge University Press, v. 57, n. 71, p. 371–381, 2016. Citations on pages 60 and 61.

DRUCKER, D. C.; PRAGER, W. Soil mechanics and plastic analysis or limit design. **Quarterly of Applied Mathematics**, Brown University, v. 10, n. 2, p. 157–165, 1952. ISSN 0033569X, 15524485. Available: <http://www.jstor.org/stable/43633942>. Citation on page 78.

DURAN, A.; LIANG, Q.; MARCHE, F. On the well-balanced numerical discretization of shallow water equations on unstructured meshes. **Journal of Computational Physics**, v. 235.0, p. 565–586, 2013. ISSN 0021-9991. Available: <https://www.sciencedirect.com/science/article/pii/S0021999112006365>. Citation on page 83.

DUTYKH, D.; ACARY-ROBERT, C.; BRESCH, D. Numerical simulation of powder-snow avalanche interaction with an obstacle. **Submitted to Applied Mathematical Modelling**, Citeseer, v. 21, 2009. Citation on page 96.

_____. Mathematical modeling of powder-snow avalanche flows. **Studies in Applied Mathematics**, Wiley Online Library, v. 127, n. 1, p. 38–66, 2011. Citation on page 97.

ECKART MCELWAINE JIM, K. B. M. Turbidity currents and powder snow avalanches. In: _____. **Handbook of Environmental Fluid Dynamics**. CRC Press, 2012. chap. chapter42. Available: <https://www.routledgehandbooks.com/doi/10.1201/b14241-46>. Citations on pages 59, 60, 63, and 88.

EDWARDS, A.; VIROULET, S.; JOHNSON, C.; GRAY, J. Erosion-deposition dynamics and long distance propagation of granular avalanches. **Journal of Fluid Mechanics**, Cambridge University Press, v. 915, p. A9, 2021. Citations on pages 66 and 85.

EGLIT, M. Some mathematical models of snow avalanches. **Advances in the Mechanics and the Flow of Granular Materials**, Clausthal-Zellerfeld, Trans Tech Publications Germany, v. 2, p. 577–588, 1983. Citation on page 94.

____. Mathematical and physical modelling of powder-snow avalanches in russia. **Annals of Glaciology**, Cambridge University Press, v. 26, p. 281–284, 1998. Citations on pages 94 and 95.

____. Mathematical modeling of dense avalanches. In: **Proceedings of the Anniversary Conference**. [S.l.: s.n.], 1998. v. 25, p. 15–18. Citation on page 74.

EGLIT, M.; DEMIDOV, K. Mathematical modeling of snow entrainment in avalanche motion. **Cold Regions Science and Technology**, v. 43, n. 1, p. 10–23, 2005. ISSN 0165-232X. Snow and Avalanches. Available: <https://www.sciencedirect.com/science/article/pii/S0165232X05000790>. Citations on pages 84 and 92.

EGLIT, M.; YAKUBENKO, A.; ZAYKO, J. A review of russian snow avalanche modelsfrom analytical solutions to novel 3d models. **Geosciences**, v. 10, n. 77, 2020. ISSN 2076-3263. Available: <https://www.mdpi.com/2076-3263/10/2/77>. Citations on pages 60, 71, 72, 76, 84, 92, and 94.

ELLISON, T. H.; TURNER, J. S. Turbulent entrainment in stratified flows. **Journal of Fluid Mechanics**, Cambridge University Press, v. 6, n. 3, p. 423448, 1959. Citations on pages 58, 61, 90, and 91.

EPFL. **SLAB: EPFL Snow and Avalanche Simulation Laboratory**. 2022. [Online; accessed July 26, 2022]. Available: <https://www.epfl.ch/labs/slab/>. Citation on page 101.

Erik Klemetti. **Annotated Volcano: Exploring Pinatubo's Devastating Eruption, 25 Years Later**. 2016. [Online; accessed January 6, 2024]. Available: <https://www.wired.com/2016/06/annotated-volcano-exploring-pinatubos-devastating-eruption-25-years-later/>. Citation on page 40.

ETH, Zürich. **Artikel: Über die Zerstörungskraft von Lawinen**. 2022. [Online; accessed August 02, 2022]. Available: <https://www.e-periodica.ch/digbib/view?pid=sbz-002:1955:73::175#1891l>. Citation on page 72.

Failes, Ian. **Behind 'Black Widow': A helicopter, a prison, an avalanche and a digital pig**. 2021. [Online; accessed October 6, 2022]. Available: <https://beforesandafters.com/2021/07/30/behind-black-widow-a-helicopter-a-prison-an-avalanche-and-a-digital-pig/>. Citations on pages 40 and 105.

FAILLETTAZ, J.; LOUCHET, F.; GRASSO, J.; DAUDON, D.; DENDIEVEL, R. Scale invariance of snow avalanche triggering mechanisms. In: **Stevens JR ed Proceedings of the International Snow Science Workshop**. [S.l.: s.n.], 2002. v. 29, p. 528–531. Citation on page 64.

FARIN, M.; MANGENEY, A.; ROCHE, O. Fundamental changes of granular flow dynamics, deposition, and erosion processes at high slope angles: Insights from laboratory experiments. **Journal of Geophysical Research: Earth Surface**, v. 119, n. 3, p. 504–532, 2014. Available: <https://agupubs.onlinelibrary.wiley.com/doi/abs/10.1002/2013JF002750>. Citation on page 66.

FASSHAUER, G. E. **Meshfree approximation methods with MATLAB**. [S.l.]: World Scientific, 2007. Citation on page 164.

FAVIER, L.; DAUDON, D.; DONZÉ, F.-V.; MAZARS, J. Predicting the drag coefficient of a granular flow using the discrete element method. **Journal of Statistical Mechanics: Theory and Experiment**, IOP Publishing, v. 2009, n. 06, p. P06012, 6 2009. Available: <https://doi.org/10.1088/1742-5468/2009/06/p06012>. Citation on page 100.

Federal Ministry Republic of Austria. **Association pour l'amélioration et le partage de connaissances sur les avalanches.** 2023. [Online; accessed December 5, 2023]. Available: <https://info.bml.gv.at/en/topics/forests/forest-and-natural-hazards/what-is-an-avalanche.html>. Citation on page 159.

FEI, J. bo; JIE, Y. xin; ZHANG, B. yin; FU, X. dong. A shallow constitutive law-based granular flow model for avalanches. **Computers and Geotechnics**, v. 68, p. 109–116, 2015. ISSN 0266-352X. Available: <https://www.sciencedirect.com/science/article/pii/S0266352X15000786>. Citation on page 82.

FICK, A. Ueber diffusion. **Annalen der Physik**, v. 170, n. 1, p. 59–86, 1855. Available: <https://onlinelibrary.wiley.com/doi/abs/10.1002/andp.18551700105>. Citation on page 203.

FISCHER, J.-T. A novel approach to evaluate and compare computational snow avalanche simulation. **Natural Hazards and Earth System Sciences**, v. 13, n. 6, p. 1655–1667, 2013. Available: <https://nhess.copernicus.org/articles/13/1655/2013/>. Citation on page 103.

FISCHER, J.-T.; KOFLER, A.; FELLIN, W.; GRANIG, M.; KLEEMAYR, K. Multivariate parameter optimization for computational snow avalanche simulation. **Journal of Glaciology**, Cambridge University Press, v. 61, n. 229, p. 875–888, 2015. Citations on pages 85, 87, 103, 112, and 159.

FRANTZ, R. A.; DESKOS, G.; LAIZET, S.; SILVESTRINI, J. H. High-fidelity simulations of gravity currents using a high-order finite-difference spectral vanishing viscosity approach. **Computers & Fluids**, v. 221.0, p. 104902, 2021. ISSN 0045-7930. Available: <https://www.sciencedirect.com/science/article/pii/S0045793021000682>. Citations on pages 101, 102, and 104.

FUKUSHIMA, Y. Analytical study of powder snow avalanches. **Journal of the Japanese Society of Snow and Ice**, The Japanese Society of Snow and Ice, v. 48, n. 4, p. 189–197, 1986. Citation on page 93.

FUKUSHIMA, Y.; HAGIHARA, T.; SAKAMOTO, M. Dynamics of inclined suspension thermals. **Fluid Dynamics Research**, v. 26, n. 5, p. 337–354, 2000. ISSN 0169-5983. Available: <https://www.sciencedirect.com/science/article/pii/S0169598399000313>. Citation on page 93.

FUKUSHIMA, Y.; HAYAKAWA, N. Analysis of powder-snow avalanches using three-dimensional topographic data. **Annals of Glaciology**, Cambridge University Press, v. 18, p. 102106, 1993. Citation on page 93.

FUKUSHIMA, Y.; PARKER, G. Discontinuous turbidity currents and powder snow avalanches. In: **Unknown Host Publication Title**. [S.l.]: Am. Soc. Civ. Engrs, 1984. Citation on page 93.

____. Numerical simulation of powder-snow avalanches. **Journal of Glaciology**, Cambridge University Press, v. 36.0, n. 123, p. 229237, 1990. Citations on pages 59 and 93.

FURDADA, G.; MARGALEF, A.; TRAPERO, L.; PONS, M.; ARENY, F.; BARó, M.; REYES, A.; GUINAU, M. The avalanche of les fonts d'arinsal (andorra): An example of a pure powder, dry snow avalanche. **Geosciences**, v. 10, n. 4, 2020. ISSN 2076-3263. Available: <https://www.mdpi.com/2076-3263/10/4/126>. Citation on page 60.

GAO, M.; PRADHANA, A.; HAN, X.; GUO, Q.; KOT, G.; SIFAKIS, E.; JIANG, C. Animating fluid sediment mixture in particle-laden flows. **ACM Trans. Graph.**, Association for Computing Machinery, New York, NY, USA, v. 37, n. 4, jul 2018. ISSN 0730-0301. Available: <https://doi.org/10.1145/3197517.3201309>. Citation on page 105.

GAO, M.; TAMPUBOLON, A. P.; JIANG, C.; SIFAKIS, E. An adaptive generalized interpolation material point method for simulating elastoplastic materials. **ACM Transactions on Graphics (TOG)**, ACM, v. 36.0, n. 6, p. 223, 2017. Citation on page 104.

GAUER, P. Comparison of avalanche front velocity measurements and implications for avalanche models. **Cold Regions Science and Technology**, v. 97, p. 132–150, 2014. ISSN 0165-232X. Available: <https://www.sciencedirect.com/science/article/pii/S0165232X1300147X>. Citation on page 60.

GAUER, P.; ISSLER, D. Possible erosion mechanisms in snow avalanches. **Annals of Glaciology**, Cambridge University Press, v. 38, p. 384392, 2004. Citations on pages 66 and 84.

GAUER, P.; ISSLER, D.; LIED, K.; KRISTENSEN, K.; SANDERSEN, F. On snow avalanche flow regimes: Inferences from observations and measurements. In: **Proceedings Whistler 2008 International Snow Science Workshop September 21-27, 2008**. [S.l.: s.n.], 2008. p. 717. Citation on page 63.

GAUME, J.; CHAMBON, G.; REIWEGER, I.; HERWIJNEN, A. van; SCHWEIZER, J. On the failure criterion of weak-snow layers using the discrete element method. In: **Proceedings ISSW**. [S.l.: s.n.], 2014. p. 681–688. Citation on page 100.

GAUME, J.; GAST, T.; TERAN, J.; HERWIJNEN, A. van; JIANG, C. Dynamic anticrack propagation in snow. **Nature Communications**, v. 9, n. 1, p. 3047, 8 2018. ISSN 2041-1723. Available: <https://doi.org/10.1038/s41467-018-05181-w>. Citations on pages 58, 101, and 105.

GAUME, J.; van Herwijnen, A.; GAST, T.; TERAN, J.; JIANG, C. Investigating the release and flow of snow avalanches at the slope-scale using a unified model based on the material point method. **Cold Regions Science and Technology**, v. 168, p. 102847, 2019. ISSN 0165-232X. Available: <https://www.sciencedirect.com/science/article/pii/S0165232X19302149>. Citations on pages 78 and 101.

GAVRILYUK, S.; IVANOVA, K.; FAVRIE, N. Multi-dimensional shear shallow water flows: Problems and solutions. **Journal of Computational Physics**, v. 366, p. 252–280, 2018. ISSN 0021-9991. Available: <https://www.sciencedirect.com/science/article/pii/S0021999118302250>. Citation on page 102.

GEORGE, D. L.; IVERSON, R. M. A depth-averaged debris-flow model that includes the effects of evolving dilatancy. ii. numerical predictions and experimental tests. **Proceedings of the Royal Society A: Mathematical, Physical and Engineering Sciences**, The Royal Society Publishing, v. 470, n. 2170, p. 20130820, 2014. Citations on pages 82 and 83.

GISSLER, C.; HENNE, A.; BAND, S.; PEER, A.; TESCHNER, M. An implicit compressible sph solver for snow simulation. **ACM Trans. Graph.**, Association for Computing Machinery, New York, NY, USA, v. 39.0, n. 4, 7 2020. ISSN 0730-0301. Available: <https://doi.org/10.1145/3386569.3392431>. Citation on page 104.

GOES, F. de; WALLEZ, C.; HUANG, J.; PAVLOV, D.; DESBRUN, M. Power particles: An incompressible fluid solver based on power diagrams. **ACM Trans. Graph.**, Association for Computing Machinery, New York, NY, USA, v. 34.0, n. 4, 7 2015. ISSN 0730-0301. Available: <https://doi.org/10.1145/2766901>. Citation on page 104.

GONZALEZ, O.; STUART, A. M. **A first course in continuum mechanics**. [S.l.]: Cambridge University Press, 2008. Citations on pages 77, 205, and 213.

GRAY, J.; WIELAND, M.; HUTTER, K. Gravity-driven free surface flow of granular avalanches over complex basal topography. **Proceedings of the Royal Society of London. Series A: Mathematical, Physical and Engineering Sciences**, The Royal Society, v. 455.0, n. 1985, p. 1841–1874, 1999. Citation on page 82.

GRAY, J. M. N. T.; EDWARDS, A. N. A depth-averaged $\mu(i)$-rheology for shallow granular free-surface flows. **Journal of Fluid Mechanics**, Cambridge University Press, v. 755, p. 503–534, 2014. Citations on pages 78 and 82.

GRAY, J. M. N. T.; TAI, Y.-C.; NOELLE, S. Shock waves, dead zones and particle-free regions in rapid granular free-surface flows. **Journal of Fluid Mechanics**, Cambridge University Press, v. 491, p. 161–181, 2003. Citation on page 82.

GREENSHIELDS, C. J.; WELLER, H. G. Notes on computational fluid dynamics: General principles. **(No Title)**, 2022. Citations on pages 217 and 230.

GREENSHIELDS, C. J.; WELLER, H. G.; GASPARINI, L.; REESE, J. M. Implementation of semi-discrete, non-staggered central schemes in a colocated, polyhedral, finite volume framework, for high-speed viscous flows. **International Journal for Numerical Methods in Fluids**, v. 63, n. 1, p. 1–21, 2010. Available: <https://onlinelibrary.wiley.com/doi/abs/10.1002/fld.2069>. Citation on page 125.

GREVE, R.; HUTTER, K. Motion of a granular avalanche in a convex and concave curved chute: experiments and theoretical predictions. **Philosophical Transactions of the Royal Society of London. Series A: Physical and Engineering Sciences**, v. 342, n. 1666, p. 573–600, 1993. Available: <https://royalsocietypublishing.org/doi/abs/10.1098/rsta.1993.0033>. Citations on pages 64 and 82.

GREVE, R.; KOCH, T.; HUTTER, K. Unconfined flow of granular avalanches along a partly curved surface. i. theory. **Proceedings of the Royal Society of London. Series A: Mathematical and Physical Sciences**, The Royal Society London, v. 445, n. 1924, p. 399–413, 1994. Citation on page 82.

GRIGORIAN, S.; EGLIT, M.; IAKIMOV, I. L. New statement and solution of the problem of the motion of snow avalanche. **Snow, Avalanches & Glaciers. Tr. Vysokogornogo Geofizich Inst**, v. 12, p. 104–113, 1967. Citation on page 74.

GRIGORIAN, S.; OSTROUMOV, A. The mathematical model for slope processes of avalanche type (in russian). scientific report 1955. **Institute for Mechanics, Moscow State University, Moscow, Russia**, 1977. Citation on page 74.

GRIGORIAN, S. S.; OSTROUMOV, A. V. On a continuum model for avalanche flow and its simplified variants. **Geosciences**, v. 10, n. 1, 2020. ISSN 2076-3263. Available: <https://www.mdpi.com/2076-3263/10/1/35>. Citations on pages 58, 76, 84, and 85.

GRIGORYAN, S. A new law of friction and mechanism for large-scale avalanches and landslides. In: **Soviet Physics Doklady**. [S.l.: s.n.], 1979. v. 24, p. 110. Citation on page 75.

GRöBELBAUER, H. P.; FANNELøP, T. K.; BRITTER, R. E. The propagation of intrusion fronts of high density ratios. **Journal of Fluid Mechanics**, Cambridge University Press, v. 250, p. 669–687, 1993. Citation on page 90.

GUBLER, H. Comparison of three models of avalanche dynamics. **Annals of Glaciology**, Cambridge University Press, v. 13, p. 82–89, 1989. Citation on page 73.

____. **Swiss avalanche-dynamics procedures for dense flow avalanches**. [S.l.]: AlpuG Davos, 2005. Citations on pages 29, 73, and 74.

GÜÇER, D.; ÖZGÜÇ, H. B. Simulation of a flowing snow avalanche using molecular dynamics. **Turkish Journal of Electrical Engineering & Computer Sciences**, The Scientific and Technological Research Council of Turkey, v. 22.0, n. 6, p. 1596–1610, 2014. Citation on page 105.

GURJAR, S. **Numerical Simulation of a Powder Snow Avalanche**. Phd Thesis (PhD Thesis) — ETH Zurich, 2023. Citations on pages 97 and 101.

HAERI, A.; SKONIECZNY, K. Three-dimensionsal granular flow continuum modeling via material point method with hyperelastic nonlocal granular fluidity. **Computer Methods in Applied Mechanics and Engineering**, v. 394, p. 114904, 2022. ISSN 0045-7825. Available: <https://www.sciencedirect.com/science/article/pii/S0045782522001876>. Citation on page 101.

HAFF, P. K. Grain flow as a fluid-mechanical phenomenon. **Journal of Fluid Mechanics**, Cambridge University Press, v. 134, p. 401–430, 1983. Citations on pages 74 and 79.

HARBITZ, C. **A survey of computational models for snow avalanche motion**. [S.l.]: NGI report, Oslo, 1998. Citations on pages 59 and 60.

HARBITZ, C. B.; ISSLER, D.; KEYLOCK, C. J. Conclusions from a recent survey of avalanche computational models. In: . [S.l.: s.n.], 1998. Citations on pages 59, 60, 66, and 67.

HEIMGARTNER, M. On the flow of avalanching snow. **Journal of Glaciology**, Cambridge University Press, v. 19, n. 81, p. 357–363, 1977. Citation on page 73.

HERGARTEN, S.; ROBL, J. Modelling rapid mass movements using the shallow water equations in cartesian coordinates. **Natural Hazards and Earth System Sciences**, v. 15.0, p. 671–685, 2015. Citation on page 83.

HERMANN, F.; HUTTER, K. Laboratory experiments on the dynamics of powder-snow avalanches in the run-out zone. **Journal of Glaciology**, Cambridge University Press, v. 37, n. 126, p. 281295, 1991. Citations on pages 64 and 65.

HILL, S. **1/9 Debris Flow**. 2019. [Online; accessed September 09, 2023]. Available: <https://sbbucketbrigade.org/timeline/1-9-debris-flow/>. Citation on page 47.

HOLZMANN, T. Mathematics, numerics, derivations and openfoam®. **Loeben, Germany: Holzmann CFD**, 2016. Citation on page 223.

HOPFINGER, E. J. Snow avalanche motion and related phenomena. **Annual Review of Fluid Mechanics**, v. 15, n. 1, p. 47–76, 1983. Available: <https://doi.org/10.1146/annurev.fl.15.010183.000403>. Citations on pages 59, 60, 84, 88, and 90.

HOPFINGER, E. J.; TOCHON-DANGUY, J.-C. A model study of powder-snow avalanches. **Journal of Glaciology**, Cambridge University Press, v. 19.0, n. 81, p. 343356, 1977. Citation on page 90.

HOU, J.; LIANG, Q.; SIMONS, F.; HINKELMANN, R. A 2d well-balanced shallow flow model for unstructured grids with novel slope source term treatment. **Advances in Water Resources**, v. 52.0, p. 107–131, 2013. ISSN 0309-1708. Available: <https://www.sciencedirect.com/science/article/pii/S0309170812002230>. Citation on page 83.

____. A stable 2d unstructured shallow flow model for simulations of wetting and drying over rough terrains. **Computers & Fluids**, v. 82.0, p. 132–147, 2013. ISSN 0045-7930. Available: <https://www.sciencedirect.com/science/article/pii/S0045793013001552>. Citation on page 83.

HUANG, Z.; AODE, H. A laboratory study of rheological properties of mudflows in hangzhou bay, china. **International Journal of Sediment Research**, v. 24, n. 4, p. 410–424, 2009. ISSN 1001-6279. Available: <https://www.sciencedirect.com/science/article/pii/S1001627910600145>. Citation on page 77.

HUBBARD, M. Multidimensional slope limiters for muscl-type finite volume schemes on unstructured grids. **Journal of Computational Physics**, v. 155.0, n. 1, p. 54–74, 1999. ISSN 0021-9991. Available: <https://www.sciencedirect.com/science/article/pii/S0021999199963295>. Citation on page 83.

HUI, W.; LI, P.; LI, Z. A unified coordinate system for solving the two-dimensional euler equations. **Journal of Computational Physics**, v. 153, n. 2, p. 596–637, 1999. ISSN 0021-9991. Available: <https://www.sciencedirect.com/science/article/pii/S0021999199962952>. Citation on page 83.

HUNGR, O. A model for the runout analysis of rapid flow slides, debris flows, and avalanches. **Canadian Geotechnical Journal**, v. 32, n. 4, p. 610–623, 1995. Available: <https://doi.org/10.1139/t95-063>. Citations on pages 72 and 82.

HUPPERT, H. E. Gravity currents: a personal perspective. **Journal of Fluid Mechanics**, Cambridge University Press, v. 554, p. 299–322, 2006. Citations on pages 87 and 90.

HUSSIN, H. Y.; LUNA, B. Q.; WESTEN, C. J. van; CHRISTEN, M.; MALET, J.-P.; ASCH, T. W. J. van. Parameterization of a numerical 2-d debris flow model with entrainment: a case study of the faucon catchment, southern french alps. **Natural Hazards and Earth System Sciences**, v. 12, n. 10, p. 3075–3090, 2012. Available: <https://nhess.copernicus.org/articles/12/3075/2012/>. Citation on page 72.

HUTTER, K. Avalanche dynamics. In: ____. **Hydrology of Disasters**. Dordrecht: Springer Netherlands, 1996. p. 317–394. ISBN 978-94-015-8680-1. Available: <https://doi.org/10.1007/978-94-015-8680-1_11>. Citation on page 77.

HUTTER, K.; KOCH, T. Motion of a granular avalanche in an exponentially curved chute: experiments and theoretical predictions. **Philosophical Transactions of the Royal Society of London. Series A: Physical and Engineering Sciences**, The Royal Society London, v. 334, n. 1633, p. 93–138, 1991. Citations on pages 80 and 82.

HUTTER, K.; RAJAGOPAL, K. R. On flows of granular materials. **Continuum Mechanics and Thermodynamics**, v. 6, n. 2, p. 81–139, 6 1994. ISSN 1432-0959. Available: <https://doi.org/10.1007/BF01140894>. Citation on page 79.

HUTTER, K.; SAVAGE, S. B.; NOHGUCHI, Y. Numerical, analytical, and laboratory experimental studies of granular avalanche flows. **Annals of Glaciology**, Cambridge University Press, v. 13, p. 109–116, 1989. Citation on page 80.

HUTTER, K.; WANG, Y.; PUDASAINI, S. P. The savage–hutter avalanche model: how far can it be pushed? **Philosophical Transactions of the Royal Society A: Mathematical, Physical and Engineering Sciences**, The Royal Society London, v. 363, n. 1832, p. 1507–1528, 2005. Citations on pages 81 and 82.

HWANG, H.; HUTTER, K. A new kinetic model for rapid granular flow. **Continuum Mechanics and Thermodynamics**, Springer, v. 7, n. 3, p. 357–384, 1995. Citation on page 82.

imageworks. **Mulan**. 2020. [Online; accessed October 6, 2022]. Available: <https://www.imageworks.com/our-craft/vfx/movies/mulan>. Citation on page 105.

ISSA, R. Solution of the implicitly discretised fluid flow equations by operator-splitting. **Journal of Computational Physics**, v. 62, n. 1, p. 40–65, 1986. ISSN 0021-9991. Available: <https://www.sciencedirect.com/science/article/pii/0021999186900999>. Citation on page 228.

ISSLER, D. Modelling of snow entrainment and deposition in powder-snow avalanches. **Annals of Glaciology**, Cambridge University Press, v. 26, p. 253258, 1998. Citations on pages 98, 99, and 102.

____. Experimental information on the dynamics of dry-snow avalanches. In: ____. **Dynamic Response of Granular and Porous Materials under Large and Catastrophic Deformations**. Berlin, Heidelberg: Springer Berlin Heidelberg, 2003. p. 109–160. ISBN 978-3-540-36565-5. Available: <https://doi.org/10.1007/978-3-540-36565-5_4>. Citation on page 63.

____. Dynamically consistent entrainment laws for depth-averaged avalanche models. **Journal of Fluid Mechanics**, Cambridge University Press, v. 759, p. 701738, 2014. Citations on pages 53, 66, and 84.

____. The 2017 rigopiano avalanchedynamics inferred from field observations. **Geosciences**, v. 10, n. 466, 2020. ISSN 2076-3263. Available: <https://www.mdpi.com/2076-3263/10/11/466>. Citation on page 60.

ISSLER, D.; ERRERA, A.; PRIANO, S.; GUBLER, H.; TEUFEN, B.; KRUMMENACHER, B. Inferences on flow mechanisms from snow avalanche deposits. **Annals of Glaciology**, Cambridge University Press, v. 49, p. 187–192, 2008. Citation on page 66.

ISSLER, D.; GAUER, P.; BARBOLINI, M.; BALEAN, R. Continuum models of particle entrainment and deposition in snow drift and avalanche dynamics. In: **Models of Continuum Mechanics in Analysis and Engineering. Proc. of a conference held at the Technische Universität Darmstadt, Sept**. [S.l.: s.n.], 2000. v. 30, p. 58–80. Citations on pages 96 and 102.

ISSLER, D.; GAUER, P.; SCHAER, M.; KELLER, S. Inferences on mixed snow avalanches from field observations. **Geosciences**, v. 10, n. 1, 2020. ISSN 2076-3263. Available: <https://www.mdpi.com/2076-3263/10/1/2>. Citations on pages 60 and 66.

ISSLER, D.; JENKINS, J. T.; MCELWAINE, J. N. Comments on avalanche flow models based on the concept of random kinetic energy. **Journal of Glaciology**, Cambridge University Press, v. 64, n. 243, p. 148–164, 2018. Citation on page 86.

ISSLER, D.; JÓHANNESSON, T. Dynamically consistent entrainment and deposition rates in depth-averaged gravity mass flow models. **Norwegian Geotechnical Institute, 0slo, Technial hlte U**, v. 111, p. 1200–1, 2011. Citation on page 66.

ISSLER, D.; PéREZ, M. P. Interplay of entrainment and rheology in snow avalanches: a numerical study. **Annals of Glaciology**, Cambridge University Press, v. 52, n. 58, p. 143–147, 2011. Citation on page 83.

IVANOVA, K.; CAVIEZEL, A.; BHLER, Y.; BARTELT, P. Numerical modeling of turbulent geophysical flows using a hyperbolic shear shallow water model: Application to powder snow avalanches. **Computers & Fluids**, p. 105211, 2021. ISSN 0045-7930. Available: <https://www.sciencedirect.com/science/article/pii/S004579302100325X>. Citations on pages 59, 99, 102, and 121.

IVERSON, R. M. The physics of debris flows. **Reviews of geophysics**, Wiley Online Library, v. 35.0, n. 3, p. 245–296, 1997. Citations on pages 82 and 83.

IVERSON, R. M.; DENLINGER, R. P. Flow of variably fluidized granular masses across three-dimensional terrain: 1. coulomb mixture theory. **Journal of Geophysical Research: Solid Earth**, v. 106, n. B1, p. 537–552, 2001. Available: <https://agupubs.onlinelibrary.wiley.com/doi/abs/10.1029/2000JB900329>. Citations on pages 78 and 82.

IVERSON, R. M.; GEORGE, D. L. A depth-averaged debris-flow model that includes the effects of evolving dilatancy. i. physical basis. **Proceedings of the Royal Society A: Mathematical, Physical and Engineering Sciences**, The Royal Society Publishing, v. 470, n. 2170, p. 20130819, 2014. Citations on pages 82 and 83.

IVERSON, R. M.; OUYANG, C. Entrainment of bed material by earth-surface mass flows: Review and reformulation of depth-integrated theory. **Reviews of Geophysics**, v. 53, n. 1, p. 27–58, 2015. Available: <https://agupubs.onlinelibrary.wiley.com/doi/abs/10.1002/2013RG000447>. Citation on page 85.

JAMIESON, B.; MARGRETH, S.; JONES, A. Application and limitations of dynamic models for snow avalanche hazard mapping. In: **Proceedings Whistler 2008 International Snow Science Workshop September 21-27, 2008**. [S.l.: s.n.], 2008. p. 730. Citations on pages 74 and 102.

JASAK, H.; JEMCOV, A.; TUKOVIĆ Željko. Openfoam: A c++ library for complex physics simulations. In: . [s.n.], 2007. Available: <https://api.semanticscholar.org/CorpusID:35226827>. Citation on page 223.

JIANG, C.; GAST, T.; TERAN, J. Anisotropic elastoplasticity for cloth, knit and hair frictional contact. **ACM Transactions on Graphics (TOG)**, ACM, v. 36.0, n. 4, p. 152, 2017. Citation on page 104.

JIANG, C.; SCHROEDER, C.; SELLE, A.; TERAN, J.; STOMAKHIN, A. The affine particle-in-cell method. **ACM Transactions on Graphics (TOG)**, ACM, v. 34.0, n. 4, p. 51, 2015. Citation on page 104.

JONTHAN, Å.; DANIEL, C. **Slab and Powder-Snow avalanche animation on the GPU**. 2021. Citation on page 104.

JUEZ, C.; MURILLO, J.; GARCíA-NAVARRO, P. 2d simulation of granular flow over irregular steep slopes using global and local coordinates. **Journal of Computational Physics**, v. 255, p. 166–204, 2013. ISSN 0021-9991. Available: <https://www.sciencedirect.com/science/article/pii/S0021999113005275>. Citation on page 83.

KABORE, B. W.; PETERS, B.; MICHAEL, M.; NICOT, F. A discrete element framework for modeling the mechanical behaviour of snow—part i: Mechanical behaviour and numerical model. **Granular Matter**, v. 23, n. 2, p. 42, 4 2021. ISSN 1434-7636. Available: <https://doi.org/10.1007/s10035-020-01083-1>. Citation on page 100.

KAPLER, A. Avalanche! snowy fx for xxx. In: ACM. **ACM SIGGRAPH 2003 Sketches & Applications**. [S.l.], 2003. p. 1–1. Citation on page 105.

KARMAN, T. V. The engineer grapples with nonlinear problems. **Bulletin of the American Mathematical Society**, American Mathematical Society, v. 46, n. 8, p. 615–683, 1940. Citations on pages 59 and 89.

KAY, M. **Practical Hydraulics and Water Resources Engineering (3rd ed.)**. [S.l.]: CRC Press., 2017. ISBN 9781315380674. Citation on page 72.

KAZHIKHOV, A. V.; SMAGULOV, S. The correctness of boundary-value problems in a diffusion model of an inhomogeneous liquid. In: **Soviet Physics Doklady**. [S.l.: s.n.], 1977. v. 22, p. 249. Citation on page 97.

KELLER, S. Measurements of powder snow avalanches-laboratory. **Surveys in Geophysics**, Springer, v. 16, n. 5, p. 661–670, 1995. Citation on page 64.

KERN, M.; BARTELT, P.; SOVILLA, B.; BUSER, O. Measured shear rates in large dry and wet snow avalanches. **Journal of Glaciology**, Cambridge University Press, v. 55, n. 190, p. 327–338, 2009. Citation on page 66.

KERN, M.; TIEFENBACHER, F.; MCELWAINE, J. The rheology of snow in large chute flows. **Cold Regions Science and Technology**, v. 39, n. 2, p. 181–192, 2004. ISSN 0165-232X. Snow And Avalanches: Papers Presented At The European Geophysical Union Conference, Nice, April 2003. Dedicated To The Avalanche Dynamics Pioneer Dr. B. Salm. Available: <https://www.sciencedirect.com/science/article/pii/S0165232X04000230>. Citation on page 96.

KIM, T.; THüREY, N.; JAMES, D.; GROSS, M. Wavelet turbulence for fluid simulation. **ACM Trans. Graph.**, Association for Computing Machinery, New York, NY, USA, v. 27.0, n. 3, p. 16, 9 2008. ISSN 0730-0301. Available: <https://doi.org/10.1145/1360612.1360649>. Citation on page 105.

____. Wavelet turbulence for fluid simulation. **ACM Trans. Graph.**, Association for Computing Machinery, New York, NY, USA, v. 27, n. 3, p. 1–6, aug 2008. ISSN 0730-0301. Available: <https://doi.org/10.1145/1360612.1360649>. Citation on page 165.

KIM, T.-Y.; FLORES, L. Snow avalanche effects for mummy 3. In: **ACM SIGGRAPH**. [S.l.: s.n.], 2008. p. 11–15. Citation on page 105.

KOCH, T.; GREVE, R.; HUTTER, K. Unconfined flow of granular avalanches along a partly curved surface. ii. experiments and numerical computations. **Proceedings of the Royal Society of London. Series A: Mathematical and Physical Sciences**, The Royal Society London, v. 445, n. 1924, p. 415–435, 1994. Citations on pages 82 and 111.

KONOPLIV, N. A.; SMITH, S. G. L.; MCELWAINE, J. N.; MEIBURG, E. Modelling gravity currents without an energy closure. **Journal of Fluid Mechanics**, Cambridge University Press, v. 789, p. 806–829, 2016. Citation on page 90.

KULIKOVSKII, A.; SVESHNIKOVA, E. A model for simulation of a powder snow avalanche. **Mater. Glyatsiologicheskikh Issled.(Data Glaciol. Stud.)**, v. 53, p. 108–112, 1977. Citation on page 92.

KYROUSI, F.; LEONARDI, A.; ROMAN, F.; ARMENIO, V.; ZANELLO, F.; ZORDAN, J.; JUEZ, C.; FALCOMER, L. Large eddy simulations of sediment entrainment induced by a lock-exchange gravity current. **Advances in Water Resources**, v. 114, p. 102–118, 2018. ISSN 0309-1708. Available: <https://www.sciencedirect.com/science/article/pii/S0309170817307698>. Citations on pages 101 and 102.

KöHLER, A.; MCELWAINE, J. N.; SOVILLA, B. Geodar data and the flow regimes of snow avalanches. **Journal of Geophysical Research: Earth Surface**, v. 123, n. 6, p. 1272–1294, 2018. Available: <https://agupubs.onlinelibrary.wiley.com/doi/abs/10.1002/2017JF004375>. Citation on page 63.

LABUZ JOSEPH F.AND ZANG, A. Mohr–coulomb failure criterion. **Rock Mechanics and Rock Engineering**, v. 45, n. 6, p. 975–979, Nov 2012. ISSN 1434-453X. Available: <https://doi.org/10.1007/s00603-012-0281-7>. Citation on page 78.

LACHAPELLE, E. R. Snow avalanches: A review of current research and applications. **Journal of Glaciology**, Cambridge University Press, v. 19, n. 81, p. 313324, 1977. Citations on pages 58 and 72.

LAGOTALA, H. Étude de l'avalanche des pèlerins (chamonix) 10-11 avril 1924. **Le Globe. Revue genevoise de géographie**, Persée-Portail des revues scientifiques en SHS, v. 66, n. 1, p. 37–85, 1927. Citation on page 71.

LAIZET, S.; LAMBALLAIS, E. **Xcompact3d in turbulence we trust**. 2022. [Online; accessed September 26, 2022]. Available: <https://www.incompact3d.com/>. Citation on page 104.

LAUNDER, B.; SPALDING, D. The numerical computation of turbulent flows. **Computer Methods in Applied Mechanics and Engineering**, v. 3, n. 2, p. 269–289, 1974. ISSN 0045-7825. Available: <https://www.sciencedirect.com/science/article/pii/0045782574900292>. Citation on page 96.

Lê, L.; PITMAN, E. B. A model for granular flows over an erodible surface. **SIAM Journal on Applied Mathematics**, v. 70, n. 5, p. 1407–1427, 2010. Available: <https://doi.org/10.1137/060677501>. Citation on page 83.

LEMONS, D. S. An introduction to stochastic processes in physics. **American Journal of Physics**, v. 71, n. 2, p. 191–191, 2003. Available: <https://doi.org/10.1119/1.1526134>. Citation on page 86.

LEPERA, R. Modeling and simulation of rapid granular flows. application to powder snow avalanches. 2020. Citation on page 96.

LEVEQUE, R. J. **Finite Volume Methods for Hyperbolic Problems**. [S.l.]: Cambridge University Press, 2002. (Cambridge Texts in Applied Mathematics). Citation on page 83.

LI, R.; ZHANG, X. **A Finite Volume Scheme for Savage-Hutter Equations on Unstructured Grids**. 2019. Citation on page 82.

LI, X.; SOVILLA, B.; JIANG, C.; GAUME, J. The mechanical origin of snow avalanche dynamics and flow regime transitions. **The Cryosphere**, v. 14, n. 10, p. 3381–3398, 2020. Available: <https://tc.copernicus.org/articles/14/3381/2020/>. Citation on page 101.

____. Three-dimensional and real-scale modeling of flow regimes in dense snow avalanches. **Landslides**, Springer, v. 18, n. 10, p. 3393–3406, 2021. Citations on pages 58 and 101.

LI, X.; SOVILLA, B.; LIGNEAU, C.; JIANG, C.; GAUME, J. Different erosion and entrainment mechanisms in snow avalanches. **Mechanics Research Communications**, v. 124, p. 103914, 2022. ISSN 0093-6413. Available: <https://www.sciencedirect.com/science/article/pii/S0093641322000647>. Citations on pages 85, 86, 101, and 164.

LIANG, Q.; MARCHE, F. Numerical resolution of well-balanced shallow water equations with complex source terms. **Advances in Water Resources**, v. 32.0, n. 6, p. 873–884, 2009. ISSN 0309-1708. Available: <https://www.sciencedirect.com/science/article/pii/S0309170809000396>. Citation on page 83.

LIED, K.; BAKKEHøI, K. Empirical calculations of snow–avalanche run–out distance based on topographic parameters. **Journal of Glaciology**, Cambridge University Press, v. 26, n. 94, p. 165–177, 1980. Citation on page 68.

LIED, K.; WEILER, C.; BAKKEHOI, S.; HOPF, J. Calculation methods for avalanche run-out distance for the austrian alps. In: **Les apports de la recherche scientifique à la sécurité neige glace et avalanche**. [S.l.: s.n.], 1995. Citation on page 74.

LIGNEAU, C.; SOVILLA, B.; GAUME, J. Numerical investigation of the effect of cohesion and ground friction on snow avalanches flow regimes. **PloS one**, Public Library of Science San Francisco, CA USA, v. 17, n. 2, p. e0264033, 2022. Citations on pages 74 and 78.

LINDEN, P. F.; SIMPSON, J. E. Gravity-driven flows in a turbulent fluid. **Journal of Fluid Mechanics**, Cambridge University Press, v. 172, p. 481–497, 1986. Citation on page 64.

LIU, W.; HE, S.-m.; ONYANG, C.-j. Dynamic process simulation with a savage-hutter type model for the intrusion of landslide into river. **Journal of Mountain Science**, v. 13, n. 7, p. 1265–1274, 7 2016. ISSN 1993-0321. Available: <https://doi.org/10.1007/s11629-015-3439-4>. Citation on page 83.

LIU, X.; CHEN, Y.; ZHANG, H.; ZOU, Y.; WANG, Z.; PENG, Q. Physically based modeling and rendering of avalanches. **The Visual Computer**, v. 37, n. 9, p. 2619–2629, Sep 2021. ISSN 1432-2315. Available: <https://doi.org/10.1007/s00371-021-02215-1>. Citation on page 105.

LIU, Y.; ZHOU, J.; SONG, L.; ZOU, Q.; LIAO, L.; WANG, Y. Numerical modelling of free-surface shallow flows over irregular topography with complex geometry. **Applied Mathematical Modelling**, v. 37.0, n. 23, p. 9482–9498, 2013. ISSN 0307-904X. Available: <https://www.sciencedirect.com/science/article/pii/S0307904X13003077>. Citation on page 83.

LOUCHET, F. **Snow Avalanches: Beliefs, Facts, and Science**. [S.l.]: Oxford University Press, USA, 2021. Citation on page 60.

LOUGE, M. Y.; CARROLL, C. S.; TURNBULL, B. Role of pore pressure gradients in sustaining frontal particle entrainment in eruption currents: The case of powder snow avalanches. **Journal of Geophysical Research: Earth Surface**, v. 116, n. F4, 2011. Available: <https://agupubs.onlinelibrary.wiley.com/doi/abs/10.1029/2011JF002065>. Citation on page 99.

LOWE, D. R. Subaqueous liquefied and fluidized sediment flows and their deposits. **Sedimentology**, v. 23, n. 3, p. 285–308, 1976. Available: <https://onlinelibrary.wiley.com/doi/abs/10.1111/j.1365-3091.1976.tb00051.x>. Citation on page 46.

____. Sediment Gravity Flows: Their Classification and Some Problems of Application to Natural Flows and Deposits. In: **Geology of Continental Slopes**. SEPM Society for Sedimentary Geology, 1979. ISBN 9781565761575. Available: <https://doi.org/10.2110/pec.79.27.0075>. Citation on page 47.

LUCA, I.; HUTTER, K.; TAI, Y. C.; KUO, C. Y. A hierarchy of avalanche models on arbitrary topography. **Acta Mechanica**, v. 205, n. 1, p. 121–149, 6 2009. ISSN 1619-6937. Available: <https://doi.org/10.1007/s00707-009-0165-4>. Citation on page 82.

MAHAJAN, P.; BROWN, R. L. A microstructure-based constitutive law for snow. **Annals of Glaciology**, Cambridge University Press, v. 18, p. 287–294, 1993. Citation on page 78.

MAJOR, J. J.; PIERSON, T. C. Debris flow rheology: Experimental analysis of fine-grained slurries. **Water resources research**, Wiley Online Library, v. 28, n. 3, p. 841–857, 1992. Citation on page 77.

MANGENEY-CASTELNAU, A.; VILOTTE, J.-P.; BRISTEAU, M. O.; PERTHAME, B.; BOUCHUT, F.; SIMEONI, C.; YERNENI, S. Numerical modeling of avalanches based on saint venant equations using a kinetic scheme. **Journal of Geophysical Research: Solid Earth**, v. 108, n. B11, 2003. Available: <https://agupubs.onlinelibrary.wiley.com/doi/abs/10.1029/2002JB002024>. Citations on pages 82 and 83.

Matt Reeves (20th Century Fox). **War for the Planet of the Apes**. 2017. [Online; accessed January 6, 2024]. Available: <https://www.wetafx.co.nz/films/filmography/war-for-the-planet-of-the-apes/>. Citation on page 39.

MCCLUNG, D.; LIED, K. Statistical and geometrical definition of snow avalanche runout. **Cold Regions Science and Technology**, v. 13, n. 2, p. 107–119, 1987. ISSN 0165-232X. Available: <https://www.sciencedirect.com/science/article/pii/0165232X87900498>. Citation on page 68.

MCCLUNG, D.; MEARS, A.; SCHAERER, P. Extreme avalanche run-out: Data from four mountain ranges. **Annals of Glaciology**, Cambridge University Press, v. 13, p. 180–184, 1989. Citation on page 68.

MCCLUNG, D. M. Extreme avalanche runout in space and time. **Canadian Geotechnical Journal**, v. 37, n. 1, p. 161–170, 2000. Available: <https://doi.org/10.1139/t99-081>. Citation on page 68.

MCCLUNG, D. M.; MEARS, A. I. Dry-flowing avalanche run-up and run-out. **Journal of Glaciology**, Cambridge University Press, v. 41, n. 138, p. 359–372, 1995. Citation on page 74.

MCELWAINE, J.; NISHIMURA, K. Ping-pong ball avalanche experiments. **Annals of Glaciology**, Cambridge University Press, v. 32, p. 241–250, 2001. Citation on page 64.

MCGILL, Z. **The Nine Avalanche Problems Explained**. 2023. [Online; accessed September 09, 2023]. Available: <https://www.bakermountainguides.com/avalanche-problems/>. Citation on page 51.

MEIBURG, E.; RADHAKRISHNAN, S.; NASR-AZADANI, M. Modeling Gravity and Turbidity Currents: Computational Approaches and Challenges. **Applied Mechanics Reviews**, v. 67, n. 4, 7 2015. ISSN 0003-6900. 040802. Available: <https://doi.org/10.1115/1.4031040>. Citations on pages 87 and 102.

MELLOR, M. **Avalanches**. [S.l.]: Cold Regions Research and Engineering Laboratory (US), 1968. Citations on pages 59 and 60.

____. **A review of basic snow mechanics**. [S.l.]: US Army Cold Regions Research and Engineering Laboratory Hanover, NH, 1974. Citation on page 78.

____. Chapter 23 - dynamics of snow avalanches. In: VOIGHT, B. (Ed.). **Rockslides and Avalanches, 1**. Elsevier, 1978, (Developments in Geotechnical Engineering, v. 14). p. 753–792. Available: <https://www.sciencedirect.com/science/article/pii/B9780444415073500313>. Citations on pages 59 and 60.

MEUNIER, M.; ANCEY, C. Towards a conceptual approach to predetermining long-return-period avalanche run-out distances. **Journal of Glaciology**, Cambridge University Press, v. 50, n. 169, p. 268–278, 2004. Citations on pages 68 and 86.

MIDDLETON, G. V.; HAMPTON, M. A. Part i. sediment gravity flows: mechanics of flow and deposition. Pacific section SEPM, 1973. Citation on page 46.

MISHRA, A.; MAHAJAN, P. A constitutive law for snow taking into account the compressibility. **Annals of Glaciology**, Cambridge University Press, v. 38, p. 145–149, 2004. Citation on page 78.

MORTON, B. R.; TAYLOR, G. I.; TURNER, J. S. Turbulent gravitational convection from maintained and instantaneous sources. **Proceedings of the Royal Society of London. Series A. Mathematical and Physical Sciences**, v. 234, n. 1196, p. 1–23, 1956. Available: <https://royalsocietypublishing.org/doi/abs/10.1098/rspa.1956.0011>. Citation on page 90.

MOSHER, D.; CAMPBELL, D.; GARDNER, J.; PIPER, D.; CHAYTOR, J.; REBESCO, M. The role of deep-water sedimentary processes in shaping a continental margin: The northwest atlantic. **Marine Geology**, v. 393, p. 245–259, 2017. ISSN 0025-3227. Advancements in Understanding Deep-Sea Clastic Sedimentation Processes. Available: <https://www.sciencedirect.com/science/article/pii/S0025322717304073>. Citation on page 89.

MOUGIN, P. Les avalanches en savoie, vol. iv. **Ministère de lAgriculture, Direction Générale des Eaux et Forêts, Service des Grandes Forces Hydrauliques, Paris**, 1922. Citations on pages 58 and 71.

MULAK, D.; GAUME, J. Numerical investigation of the mixed-mode failure of snow. **Computational Particle Mechanics**, v. 6, n. 3, p. 439–447, 7 2019. ISSN 2196-4386. Available: <https://doi.org/10.1007/s40571-019-00224-5>. Citation on page 100.

MUSETH, K.; LAIT, J.; JOHANSON, J.; BUDSBERG, J.; HENDERSON, R.; ALDEN, M.; CUCKA, P.; HILL, D.; PEARCE, A. Openvdb: an open-source data structure and toolkit for high-resolution volumes. In: **Acm siggraph 2013 courses**. [S.l.: s.n.], 2013. p. 1–1. Citation on page 154.

NAAIM, M. Modélisation numérique des avalanches aérosols. **La Houille Blanche**, EDP Sciences, n. 5-6, p. 56–62, 1995. Citation on page 96.

NAAIM, M.; DURAND, Y.; ECKERT, N.; CHAMBON, G. Dense avalanche friction coefficients: influence of physical properties of snow. **Journal of Glaciology**, Cambridge University Press, v. 59, n. 216, p. 771–782, 2013. Citations on pages 78 and 85.

NAAIM, M.; GURER, I. Two-phase numerical model of powder avalanche theory and application. **Natural Hazards**, Springer, v. 17.0, n. 2, p. 129–145, 1998. Citation on page 96.

NAAIM, M.; MARTINEZ, H. Experimental and theoretical determination of concentration profiles and influence of particle characteristics in blowing snow. **Surveys in Geophysics**, v. 16, n. 5, p. 695–710, Nov 1995. ISSN 1573-0956. Available: <https://doi.org/10.1007/BF00665749>. Citation on page 65.

NAAIM, M.; NAAIM-BOUVET, F.; FAUG, T.; BOUCHET, A. Dense snow avalanche modeling: flow, erosion, deposition and obstacle effects. **Cold Regions Science and Technology**, v. 39, n. 2, p. 193–204, 2004. ISSN 0165-232X. Snow And Avalanches: Papers Presented At The European Geophysical Union Conference, Nice, April 2003. Dedicated To The Avalanche Dynamics Pioneer Dr. B. Salm. Available: <https://www.sciencedirect.com/science/article/pii/S0165232X04000643>. Citation on page 85.

NARAIN, R.; SEWALL, J.; CARLSON, M.; LIN, M. C. Fast animation of turbulence using energy transport and procedural synthesis. In: **ACM SIGGRAPH Asia 2008 Papers**. Association for Computing Machinery, 2008. (SIGGRAPH Asia '08). ISBN 9781450318310. Available: <https://doi.org/10.1145/1457515.1409119>. Citation on page 105.

NAVAS-MONTILLA, A.; JUEZ, C.; FRANCA, M.; MURILLO, J. Depth-averaged unsteady rans simulation of resonant shallow flows in lateral cavities using augmented weno-ader schemes. **Journal of Computational Physics**, v. 395, p. 511–536, 2019. ISSN 0021-9991. Available: <https://www.sciencedirect.com/science/article/pii/S0021999119304450>. Citation on page 102.

NAZAROV, A. N. Mathematical modeling of a snow-powder avalanche in the framework of the equations of two-layer shallow water. **Fluid Dynamics**, v. 26, n. 1, p. 70–75, Jan 1991. ISSN 1573-8507. Available: <https://doi.org/10.1007/BF01050115>. Citation on page 94.

NI, Y.; CAO, Z.; LIU, Q. Mathematical modeling of shallow-water flows on steep slopes. **Journal of Hydrology and Hydromechanics**, Sciendo, v. 67.0, n. 3, p. 252–259, 2019. Citation on page 83.

NICOT, F. Constitutive modelling of snow as a cohesive-granular material. **Granular Matter**, v. 6, n. 1, p. 47–60, 6 2004. ISSN 1434-7636. Available: <https://doi.org/10.1007/s10035-004-0159-9>. Citation on page 78.

NISHIMURA, K.; BARPI, F.; ISSLER, D. Perspectives on snow avalanche dynamics research. **Geosciences**, v. 11, n. 2, 2021. ISSN 2076-3263. Available: <https://www.mdpi.com/2076-3263/11/2/57>. Citation on page 60.

NISHIMURA, K.; MAENO, N.; SANDERSEN, F.; KRISTENSEN, K.; NOREM, H.; LIED, K. Observations of the dynamic structure of snow avalanches. **Annals of Glaciology**, Cambridge University Press, v. 18, p. 313–316, 1993. Citation on page 65.

NOREM, H.; IRGENS, F.; SCHIELDROP, B. Simulation of snow-avalanche flow in run-out zones. **Annals of Glaciology**, Cambridge University Press, v. 13, p. 218–225, 1989. Citation on page 74.

OLLER, P.; JANERAS, M.; de Buen, H.; ARNó, G.; CHRISTEN, M.; GARCíA, C.; MARTíNEZ, P. Using aval-1d to simulate avalanches in the eastern pyrenees. **Cold Regions Science and Technology**, v. 64, n. 2, p. 190–198, 2010. ISSN 0165-232X. International Snow Science Workshop 2009 Davos. Available: <https://www.sciencedirect.com/science/article/pii/S0165232X10001576>. Citation on page 102.

OUILLON, R.; MEIBURG, E.; SUTHERLAND, B. R. Turbidity currents propagating down a slope into a stratified saline ambient fluid. **Environmental Fluid Mechanics**, Springer, v. 19, n. 5, p. 1143–1166, 2019. Citation on page 87.

PAIVA, A.; PETRONETTO, F.; LEWINER, T.; TAVARES, G. Particle-based viscoplastic fluid/-solid simulation. **Computer-Aided Design**, Elsevier, v. 41.0, n. 4, p. 306–314, 2009. Citation on page 104.

PANTIN, H. Interaction between velocity and effective density in turbidity flow: Phase-plane analysis, with criteria for autosuspension. **Marine Geology**, v. 31, n. 1, p. 59–99, 1979. ISSN 0025-3227. Available: <https://www.sciencedirect.com/science/article/pii/0025322779900574>. Citation on page 87.

PARKER, G. Conditions for the ignition of catastrophically erosive turbidity currents. **Marine Geology**, v. 46, n. 3, p. 307–327, 1982. ISSN 0025-3227. Available: <https://www.sciencedirect.com/science/article/pii/002532278290086X>. Citation on page 87.

PARKER, G.; FUKUSHIMA, Y.; PANTIN, H. M. Self-accelerating turbidity currents. **Journal of Fluid Mechanics**, Cambridge University Press, v. 171.0, p. 145181, 1986. Citations on pages 59, 91, 93, and 97.

PARSONS, J. D.; FRIEDRICHS, C. T.; TRAYKOVSKI, P. A.; MOHRIG, D.; IMRAN, J.; SYVITSKI, J. P. M.; PARKER, G.; PUIG, P.; BUTTLES, J. L.; GARCíA, M. H. The mechanics of marine sediment gravity flows. In: ____. **Continental Margin Sedimentation**. John Wiley & Sons, Ltd, 2007. p. 275–337. ISBN 9781444304398. Available: <https://onlinelibrary.wiley.com/doi/abs/10.1002/9781444304398.ch6>. Citation on page 87.

PATANKAR, S. V.; SPALDING, D. B. A calculation procedure for heat, mass and momentum transfer in three-dimensional parabolic flows. In: **Numerical prediction of flow, heat transfer, turbulence and combustion**. [S.l.]: Elsevier, 1983. p. 54–73. Citation on page 228.

PATRA, A.; BAUER, A.; NICHITA, C.; PITMAN, E.; SHERIDAN, M.; BURSIK, M.; RUPP, B.; WEBBER, A.; STINTON, A.; NAMIKAWA, L.; RENSCHLER, C. Parallel adaptive numerical simulation of dry avalanches over natural terrain. **Journal of Volcanology and Geothermal Research**, v. 139, n. 1, p. 1–21, 2005. ISSN 0377-0273. Modeling and Simulation of Geophysical Mass Flows. Available: <https://www.sciencedirect.com/science/article/pii/S0377027304002288>. Citation on page 104.

PATRA, A.; BEVILACQUA, A.; AKHAVAN-SAFAEI, A.; PITMAN, E. B.; BURSIK, M.; HYMAN, D. Comparative analysis of the structures and outcomes of geophysical flow models and modeling assumptions using uncertainty quantification. **Frontiers in Earth Science**, Frontiers, v. 8, p. 275, 2020. ISSN 2296-6463. Citation on page 104.

PERLA, R.; CHENG, T. T.; MCCLUNG, D. A twoparameter model of snowavalanche motion. **Journal of Glaciology**, Cambridge University Press, v. 26, n. 94, p. 197207, 1980. Citation on page 74.

PERLA, R.; LIED, K.; KRISTENSEN, K. Particle simulation of snow avalanche motion. **Cold Regions Science and Technology**, v. 9, n. 3, p. 191–202, 1984. ISSN 0165-232X. Available: <https://www.sciencedirect.com/science/article/pii/0165232X84900661>. Citation on page 74.

PETROFF, M. **A picture of Morning Glory Clouds, from Gulf of Carpentaria, Australia**. 2009. [Online; accessed September 09, 2023]. Available: <https://commons.wikimedia.org/wiki/File:Morning_glory_clouds.jpg>. Citation on page 49.

PIERSON, T. C.; COSTA, J. E. A rheologic classification of subaerial sediment-water flows. **Debris flows/avalanches: process, recognition, and mitigation. Reviews in Engineering Geology**, v. 7.0, p. 1–12, 1987. Citation on page 48.

PIRULLI, M.; SORBINO, G. Assessing potential debris flow runout: a comparison of two simulation models. **Natural Hazards and Earth System Sciences**, v. 8, n. 4, p. 961–971, 2008. Available: <https://nhess.copernicus.org/articles/8/961/2008/>. Citation on page 72.

PITMAN, E. B.; NICHITA, C. C.; PATRA, A.; BAUER, A.; SHERIDAN, M.; BURSIK, M. Computing granular avalanches and landslides. **Physics of Fluids**, v. 15, n. 12, p. 3638–3646, 2003. Available: <https://doi.org/10.1063/1.1614253>. Citations on pages 83, 85, and 104.

PLAPP, J. E.; MITCHELL, J. P. A hydrodynamic theory of turbidity currents. **Journal of Geophysical Research (1896-1977)**, v. 65, n. 3, p. 983–992, 1960. Available: <https://agupubs.onlinelibrary.wiley.com/doi/abs/10.1029/JZ065i003p00983>. Citations on pages 59 and 87.

POPOVA, E.; POPOV, V. L. The research works of coulomb and amontons and generalized laws of friction. **Friction**, v. 3, n. 2, p. 183–190, 6 2015. ISSN 2223-7704. Available: <https://doi.org/10.1007/s40544-015-0074-6>. Citation on page 72.

PROSPERETTI, A.; TRYGGVASON, G. **Computational Methods for Multiphase Flow**. [S.l.]: Cambridge University Press, 2007. Citation on page 93.

PUDASAINI, S. P.; HUTTER, K. Rapid shear flows of dry granular masses down curved and twisted channels. **Journal of Fluid Mechanics**, Cambridge University Press, v. 495, p. 193–208, 2003. Citation on page 82.

____. **Avalanche dynamics: dynamics of rapid flows of dense granular avalanches**. [S.l.]: Springer Science & Business Media, 2007. Citations on pages 29, 49, 50, 60, 74, 77, and 100.

RAM, D.; GAST, T.; JIANG, C.; SCHROEDER, C.; STOMAKHIN, A.; TERAN, J.; KAVEHPOUR, P. A material point method for viscoelastic fluids, foams and sponges. In: ACM. **Proceedings of the 14th ACM SIGGRAPH/Eurographics Symposium on Computer Animation**. [S.l.], 2015. p. 157–163. Citation on page 105.

RAMMS, WSL. **RAMMS - Rapid Mass Movement Simulation**. 2022. [Online; accessed September 26, 2022]. Available: <https://ramms.slf.ch/en/modules/avalanche.html>. Citation on page 103.

RANKINE, W. J. M. Ii. on the stability of loose earth. **Philosophical transactions of the Royal Society of London**, The Royal Society London, n. 147, p. 9–27, 1857. Citation on page 73.

RASTELLO, M.; HOPFINGER, E. J. Sediment-entraining suspension clouds: a model of powder-snow avalanches. **Journal of Fluid Mechanics**, Cambridge University Press, v. 509.0, p. 181206, 2004. Citation on page 93.

RAUTER, M.; KOFLER, A.; HUBER, A.; FELLIN, W. fasavagehutterfoam 1.0: depth-integrated simulation of dense snow avalanches on natural terrain with openfoam. **Geoscientific Model Development**, v. 11.0, n. 7, p. 2923–2939, 2018. Available: <https://gmd.copernicus.org/articles/11/2923/2018/>. Citations on pages 58, 82, 83, and 112.

RAUTER, M.; KöHLER, A. Constraints on entrainment and deposition models in avalanche simulations from high-resolution radar data. **Geosciences**, v. 10, n. 1, 2020. ISSN 2076-3263. Available: <https://www.mdpi.com/2076-3263/10/1/9>. Citation on page 87.

RAUTER, M.; TUKOVI, . A finite area scheme for shallow granular flows on three-dimensional surfaces. **Computers & Fluids**, v. 166.0, p. 184–199, 2018. ISSN 0045-7930. Available: <https://www.sciencedirect.com/science/article/pii/S0045793018300732>. Citations on pages 83, 87, 111, and 159.

REIWEGER, I.; GAUME, J.; SCHWEIZER, J. A new mixed-mode failure criterion for weak snowpack layers. **Geophysical Research Letters**, v. 42, n. 5, p. 1427–1432, 2015. Available: <https://agupubs.onlinelibrary.wiley.com/doi/abs/10.1002/2014GL062780>. Citation on page 78.

RenderMan25. **Association pour l'amélioration et le partage de connaissances sur les avalanches.** 2023. [Online; accessed December 5, 2023]. Available: <https://rmanwiki.pixar.com/display/REN25/Rendering+Clouds+with+Aggregate+Volumes>. Citation on page 158.

ROCHE, O.; ATTALI, M.; MANGENEY, A.; LUCAS, A. On the run-out distance of geophysical gravitational flows: Insight from fluidized granular collapse experiments. **Earth and Planetary Science Letters**, v. 311, n. 3, p. 375–385, 2011. ISSN 0012-821X. Available: <https://www.sciencedirect.com/science/article/pii/S0012821X11005371>. Citation on page 64.

RODRIGUEZ-PAZ, M.; BONET, J. A corrected smooth particle hydrodynamics formulation of the shallow-water equations. **Computers & Structures**, v. 83.0, n. 17, p. 1396 – 1410, 2005. ISSN 0045-7949. Advances in Meshfree Methods. Available: <http://www.sciencedirect.com/science/article/pii/S0045794905000714>. Citation on page 83.

ROHANIZADEGAN, M.; PETRONE, R. M.; POMEROY, J. W.; KOSOVIC, B.; MUñOZ-ESPARZA, D.; HELGASON, W. D. High-resolution large-eddy simulations of flow in the complex terrain of the canadian rockies. **Earth and Space Science**, v. 10, n. 10, p. e2023EA003166, 2023. E2023EA003166 2023EA003166. Available: <https://agupubs.onlinelibrary.wiley.com/doi/abs/10.1029/2023EA003166>. Citation on page 101.

ROMANOVA, D. I. 3d avalanche flow modeling using openfoam. **Proceedings of the Institute for System Programming of the RAS**, Institute for System Programming of the Russian Academy of Sciences, v. 29.0, n. 1, p. 85–100, 2017. Citation on page 96.

ROTTMAN, J. W.; LINDEN, P. F. Gravity currents. In: ____. **Environmental Stratified Flows**. Boston, MA: Springer US, 2002. p. 89–117. ISBN 978-0-306-48024-9. Available: <https://doi.org/10.1007/0-306-48024-7_4>. Citation on page 89.

SALM, B. Contribution to avalanche dynamics. **IASH-AIHS Pub.**, v. 69, p. 199–214, 1966. Citation on page 73.

____. **On nonuniform, steady flow of avalanching snow**. [S.l.]: Ceuterick, 1967. Citation on page 73.

____. Grundlagen des lawinenverbaus. **Bündnerwald**, v. 9, p. 67–81, 1972. Citation on page 73.

____. Mechanical properties of snow. **Reviews of Geophysics**, v. 20, n. 1, p. 1–19, 1982. Available: <https://agupubs.onlinelibrary.wiley.com/doi/abs/10.1029/RG020i001p00001>. Citation on page 78.

____. Flow, flow transition and runout distances of flowing avalanches. **Annals of Glaciology**, Cambridge University Press, v. 18, p. 221–226, 1993. Citation on page 73.

____. A short and personal history of snow avalanche dynamics. **Cold Regions Science and Technology**, v. 39, n. 2, p. 83–92, 2004. ISSN 0165-232X. Snow And Avalanches: Papers Presented At The European Geophysical Union Conference, Nice, April 2003. Dedicated To The Avalanche Dynamics Pioneer Dr. B. Salm. Available: <https://www.sciencedirect.com/science/article/pii/S0165232X04000588>. Citations on pages 58 and 73.

SALM, B.; BURKARD, A.; GUBLER, H. **Berechnung von Fliesslawinen: eine Anleitung für Praktiker mit Beispielen**. [S.l.]: Eidgenössisches Institut für Schnee-und Lawinenforschung, Weissfluhjoch/Davos, 1990. Citation on page 73.

SALM, B.; GUBLER, H. Measurement and analysis of the motion of dense flow avalanches. **Annals of Glaciology**, Cambridge University Press, v. 6, p. 26–34, 1985. Citations on pages 73, 74, and 75.

SAMPL, P.; GRANIG, M. Avalanche simulation with samos-at. **ISSW 09 - International Snow Science Workshop, Proceedings**, p. 519–523, 1 2009. Citations on pages 98, 103, and 107.

SAMPL, P.; ZWINGER, T. Avalanche simulation with samos. **Annals of Glaciology**, Cambridge University Press, v. 38.0, p. 393398, 2004. Citations on pages 98 and 103.

SANZ-RAMOS, M.; BLADÉ, E.; OLLER, P.; ANDRADE, C. A.; FURDADA, G. Role of friction terms in two-dimensional modelling of dense snow avalanches. **Natural Hazards and Earth System Sciences Discussions**, Copernicus GmbH, p. 1–31, 2020. Citation on page 78.

SARTORIS, G.; BARTELT, P. Upwinded finite difference schemes for dense snow avalanche modeling. **International Journal for Numerical Methods in Fluids**, v. 32, n. 7, p. 799–821, 2000. Available: <https://onlinelibrary.wiley.com/doi/abs/10.1002/%28SICI%291097-0363%2820000415%2932%3A7%3C799%3A%3AAID-FLD989%3E3.0.CO%3B2-2>. Citation on page 84.

SAVAGE, S. B. The mechanics of rapid granular flows. In: HUTCHINSON, J. W.; WU, T. Y. (Ed.). Elsevier, 1984, (Advances in Applied Mechanics, v. 24). p. 289–366. Available: <https://www.sciencedirect.com/science/article/pii/S0065215608700474>. Citation on page 79.

SAVAGE, S. B.; HUTTER, K. The motion of a finite mass of granular material down a rough incline. **Journal of Fluid Mechanics**, Cambridge University Press, v. 199.0, p. 177215, 1989. Citations on pages 58 and 80.

____. The dynamics of avalanches of granular materials from initiation to runout. part i: Analysis. **Acta Mechanica**, Springer, v. 86.0, n. 1, p. 201–223, 1991. Citations on pages 80, 82, and 110.

SAVAGE, S. B.; SAYED, M. Stresses developed by dry cohesionless granular materials sheared in an annular shear cell. **Journal of Fluid Mechanics**, Cambridge University Press, v. 142, p. 391–430, 1984. Citation on page 66.

SCHEIWILLER, T. **Dynamics of powder-snow avalanches**. Phd Thesis (PhD Thesis) — ETH Zurich, 1986. Citation on page 95.

SCHRAML, K.; THOMSCHITZ, B.; MCARDELL, B. W.; GRAF, C.; KAITNA, R. Modeling debris-flow runout patterns on two alpine fans with different dynamic simulation models. **Natural Hazards and Earth System Sciences**, v. 15, n. 7, p. 1483–1492, 2015. Available: <https://nhess.copernicus.org/articles/15/1483/2015/>. Citation on page 72.

SCHWEIZER, J.; BARTELT, P.; van Herwijnen, A. Chapter 12 - snow avalanches. In: HAEBERLI, W.; WHITEMAN, C. (Ed.). **Snow and Ice-Related Hazards, Risks, and Disasters (Second Edition)**. Second edition. Elsevier, 2021, (Hazards and Disasters Series). p. 377–416. ISBN 978-0-12-817129-5. Available: <https://www.sciencedirect.com/science/article/pii/B9780128171295000019>. Citation on page 68.

SELIGMAN, G.; SELIGMAN, G. A.; DOUGLAS, C. **Snow structure and ski fields: being an account of snow and ice forms met with in nature, and a study on avalanches and snowcraft**. [S.l.]: Macmillan and Company, limited, 1936. Citation on page 58.

SHIN, J. O.; DALZIEL, S. B.; LINDEN, P. F. Gravity currents produced by lock exchange. **Journal of Fluid Mechanics**, Cambridge University Press, v. 521, p. 1–34, 2004. Citation on page 64.

SIMAKOV, N. A.; JONES-IVEY, R. L.; AKHAVAN-SAFAEI, A.; AGHAKHANI, H.; JONES, M. D.; PATRA, A. K. Modernizing titan2d, a parallel amr geophysical flow code to support multiple rheologies and extendability. In: SPRINGER. **International Conference on High Performance Computing**. [S.l.], 2019. p. 101–112. Citation on page 104.

SIMPSON, J. E. **Gravity currents: In the environment and the laboratory**. [S.l.]: Cambridge university press, 1999. Citations on pages 49 and 87.

SINGH, A. K.; SRIVASTAVA, P.; KUMAR, N.; MAHAJAN, P. A fabric tensor based small strain constitutive law for the elastoplastic behavior of snow. **Mechanics of Materials**, v. 165, p. 104182, 2022. ISSN 0167-6636. Available: <https://www.sciencedirect.com/science/article/pii/S0167663621003938>. Citation on page 78.

SINICKAS, A. **Field-based statistical modelling of snow avalanche runout**. PRISM, 2013. Available: <https://prism.ucalgary.ca/handle/11023/953>. Citation on page 68.

SLF. **WSL Institute of Snow and Avalanche Research SLF**. 2022. [Online; accessed July 26, 2022]. Available: <https://www.slf.ch/en/index.html>. Citations on pages 50, 73, and 102.

SOLENTHALER, B.; BUCHER, P.; CHENTANEZ, N.; MLLER, M.; GROSS, M. SPH Based Shallow Water Simulation. In: BENDER, J.; ERLEBEN, K.; GALIN, E. (Ed.). **Workshop in Virtual Reality Interactions and Physical Simulation "VRIPHYS" (2011)**. [S.l.]: The Eurographics Association, 2011. ISBN 978-3-905673-87-6. Citation on page 104.

Song, L.; Zhou, J.; Zou, Q.; Guo, J.; Liu, Y. Two-dimensional dam-break flood simulation on unstructured meshes. In: **2010 International Conference on Parallel and Distributed Computing, Applications and Technologies**. [S.l.: s.n.], 2010. p. 465–469. Citation on page 83.

SOVILLA, B. **Field experiments and numerical modelling of mass entrainment and deposition processes in snow avalanches**. Phd Thesis (PhD Thesis) — ETH Zurich, 2004. Citations on pages 61, 76, and 85.

Sovilla, B.; Bartelt, P. Observations and modelling of snow avalanche entrainment. **Natural Hazards and Earth System Sciences**, v. 2, p. 169–179, Jan. 2002. Citations on pages 66 and 73.

SOVILLA, B.; BURLANDO, P.; BARTELT, P. Field experiments and numerical modeling of mass entrainment in snow avalanches. **Journal of Geophysical Research: Earth Surface**, v. 111, n. F3, 2006. Available: <https://agupubs.onlinelibrary.wiley.com/doi/abs/10.1029/2005JF000391>. Citations on pages 53, 60, 61, 84, and 85.

SOVILLA, B.; MARGRETH, S.; BARTELT, P. On snow entrainment in avalanche dynamics calculations. **Cold Regions Science and Technology**, v. 47.0, n. 1, p. 69–79, 2007. ISSN 0165-232X. A Selection of papers presented at the International Snow Science Workshop, Jackson Hole, Wyoming, September 19-24, 2004. Available: <https://www.sciencedirect.com/science/article/pii/S0165232X06001261>. Citation on page 85.

SOVILLA, B.; MCELWAINE, J. N.; KHLER, A. The intermittency regions of powder snow avalanches. **Journal of Geophysical Research: Earth Surface**, v. 123, n. 10, p. 2525–2545, 2018. Available: <https://agupubs.onlinelibrary.wiley.com/doi/abs/10.1029/2018JF004678>. Citations on pages 54 and 63.

SOVILLA, B.; MCELWAINE, J. N.; LOUGE, M. Y. The structure of powder snow avalanches. **Comptes Rendus Physique**, v. 16.0, n. 1, p. 97–104, 2015. ISSN 1631-0705. Granular physics / Physique des milieux granulaires. Available: <https://www.sciencedirect.com/science/article/pii/S1631070514001844>. Citation on page 62.

SOVILLA, B.; MCELWAINE, J. N.; SCHAER, M.; VALLET, J. Variation of deposition depth with slope angle in snow avalanches: Measurements from valle de la sionne. **Journal of Geophysical Research: Earth Surface**, v. 115, n. F2, 2010. Available: <https://agupubs.onlinelibrary.wiley.com/doi/abs/10.1029/2009JF001390>. Citation on page 61.

SOVILLA, B.; SCHAER, M.; RAMMER, L. Measurements and analysis of full-scale avalanche impact pressure at the vallée de la sionne test site. **Cold Regions Science and Technology**, v. 51, n. 2, p. 122–137, 2008. ISSN 0165-232X. International Snow Science Workshop (ISSW) 2006. Available: <https://www.sciencedirect.com/science/article/pii/S0165232X07001188>. Citations on pages 60 and 62.

St. Lawrence, W.; LANG, T. A constitutive relation for the deformation of snow. **Cold Regions Science and Technology**, v. 4, n. 1, p. 3–14, 1981. ISSN 0165-232X. Available: <https://www.sciencedirect.com/science/article/pii/0165232X81900264>. Citation on page 78.

STACEY, M. W.; BOWEN, A. J. The vertical structure of density and turbidity currents: Theory and observations. **Journal of Geophysical Research: Oceans**, v. 93, n. C4, p. 3528–3542, 1988. Available: <https://agupubs.onlinelibrary.wiley.com/doi/abs/10.1029/JC093iC04p03528>. Citation on page 91.

STEINKOGLER, W.; GAUME, J.; LöWE, H.; SOVILLA, B.; LEHNING, M. Granulation of snow: From tumbler experiments to discrete element simulations. **Journal of Geophysical Research: Earth Surface**, v. 120, n. 6, p. 1107–1126, 2015. Available: <https://agupubs.onlinelibrary.wiley.com/doi/abs/10.1002/2014JF003294>. Citation on page 64.

STEINKOGLER, W.; SOVILLA, B.; LEHNING, M. Influence of snow cover properties on avalanche dynamics. **Cold Regions Science and Technology**, v. 97, p. 121–131, 2014. ISSN 0165-232X. Available: <https://www.sciencedirect.com/science/article/pii/S0165232X13001535>. Citation on page 66.

STEWART, J. **Incredible Photos of Massive Dust Storm Taken From Fleeing News Helicopter**. 2018. [Online; accessed September 09, 2023]. Available: <https://mymodernmet.com/arizona-dust-storm-news-helicopter/>. Citation on page 49.

STOMAKHIN, A.; SCHROEDER, C.; CHAI, L.; TERAN, J.; SELLE, A. A material point method for snow simulation. **ACM Transactions on Graphics (TOG)**, ACM, v. 32.0, n. 4, p. 102, 2013. Citation on page 104.

STOMAKHIN, A.; SCHROEDER, C.; JIANG, C.; CHAI, L.; TERAN, J.; SELLE, A. Augmented mpm for phase-change and varied materials. **ACM Transactions on Graphics (TOG)**, ACM, v. 33.0, n. 4, p. 138, 2014. Citation on page 105.

SULSKY, D.; ZHOU, S.-J.; SCHREYER, H. L. Application of a particle-in-cell method to solid mechanics. **Computer physics communications**, Elsevier, v. 87.0, n. 1-2, p. 236–252, 1995. Citation on page 101.

TAI, Y.-C.; HUTTER, K.; GRAY, J. Dense granular avalanches: Mathematical description and experimental validation. In: ____. **Geomorphological Fluid Mechanics**. Berlin, Heidelberg: Springer Berlin Heidelberg, 2001. p. 339–366. ISBN 978-3-540-45670-4. Available: <https://doi.org/10.1007/3-540-45670-8_14>. Citation on page 78.

TAI, Y. C.; KUO, C. Y. A new model of granular flows over general topography with erosion and deposition. **Acta Mechanica**, v. 199, n. 1, p. 71–96, Aug 2008. ISSN 1619-6937. Available: <https://doi.org/10.1007/s00707-007-0560-7>. Citation on page 83.

TAKAHASHI, T. **Debris flow: mechanics, prediction and countermeasures**. [S.l.]: CRC press, 2014. Citation on page 48.

TAKAHASHI, T.; TSUJIMOTO, H. Granular flow model of avalanche and its application. **Proceedings of Hydraulic Engineering**, Japan Society of Civil Engineers, v. 42, p. 907–912, 1998. Citation on page 82.

TALLING, P. J.; BAKER, M. L.; POPE, E. L.; RUFFELL, S. C.; JACINTO, R. S.; HEIJNEN, M. S.; HAGE, S.; SIMMONS, S. M.; HASENHÜNDL, M.; HEEREMA, C. J.; MCGHEE, C.; APPRIOUAL, R.; FERRANT, A.; CARTIGNY, M. J. B.; PARSONS, D. R.; CLARE, M. A.; TSHIMANGA, R. M.; TRIGG, M. A.; CULA, C. A.; FARIA, R.; GAILLOT, A.; BOLA, G.; WALLANCE, D.; GRIFFITHS, A.; NUNNY, R.; URLAUB, M.; PEIRCE, C.; BURNETT, R.; NEASHAM, J.; HILTON, R. J. Longest sediment flows yet measured show how major rivers

connect efficiently to deep sea. **Nature Communications**, v. 13, n. 1, p. 4193, Jul 2022. ISSN 2041-1723. Available: <https://doi.org/10.1038/s41467-022-31689-3>. Citation on page 47.

TAMPUBOLON, A. P.; GAST, T.; KLÁR, G.; FU, C.; TERAN, J.; JIANG, C.; MUSETH, K. Multi-species simulation of porous sand and water mixtures. **ACM Transactions on Graphics (TOG)**, ACM, v. 36.0, n. 4, p. 105, 2017. Citation on page 105.

THIBERT, E.; BELLOT, H.; RAVANAT, X.; OUSSET, F.; PULFER, G.; NAAIM, M.; HAGENMULLER, P.; NAAIM-BOUVET, F.; FAUG, T.; NISHIMURA, K.; ITO, Y.; BAROUDI, D.; PROKOP, A.; SCHöN, P.; SORUCO, A.; VINCENT, C.; LIMAM, A.; HéNO, R. The full-scale avalanche test-site at lautaret pass (french alps). **Cold Regions Science and Technology**, v. 115, p. 30–41, 2015. ISSN 0165-232X. Available: <https://www.sciencedirect.com/science/article/pii/S0165232X15000622>. Citation on page 60.

TIEFENBACHER, F.; KERN, M. Experimental devices to determine snow avalanche basal friction and velocity profiles. **Cold Regions Science and Technology**, v. 38, n. 1, p. 17–30, 2004. ISSN 0165-232X. Available: <https://www.sciencedirect.com/science/article/pii/S0165232X03000600>. Citation on page 66.

TILLGREN, S. **Generating 3D Avalanche Slabs with Voronoi Tessellation in Real-Time on the CPU**. 2020. 38 p. Citation on page 105.

TOCHON-DANGUY, J.; HOPFINGER, E. Simulation of the dynamics of powder avalanches. In: **Snow Mechanics Symposium**. [S.l.: s.n.], 1975. Citation on page 90.

TROTTET, B.; SIMENHOIS, R.; BOBILLIER, G.; BERGFELD, B.; HERWIJNEN, A. van; JIANG, C.; GAUME, J. Transition from sub-rayleigh anticrack to supershear crack propagation in snow avalanches. **Nature Physics**, 7 2022. ISSN 1745-2481. Available: <https://doi.org/10.1038/s41567-022-01662-4>. Citation on page 101.

Trésorier, Marc. **Association pour l'amélioration et le partage de connaissances sur les avalanches.** 2021. [Online; accessed June 29, 2022]. Available: <http://www.data-avalanche.org/>. Citation on page 60.

TSUDA, Y.; YUE, Y.; DOBASHI, Y.; NISHITA, T. Visual simulation of mixed-motion avalanches with interactions between snow layers. **The Visual Computer**, Springer, v. 26.0, n. 6-8, p. 883–891, 2010. Citation on page 105.

TSUNEMATSU, K.; MAENO, F.; NISHIMURA, K. Application of an inertia dependent flow friction model to snow avalanches: Exploration of the model using a ping-pong ball experiment. **Geosciences**, v. 10, n. 11, 2020. ISSN 2076-3263. Available: <https://www.mdpi.com/2076-3263/10/11/436>. Citation on page 65.

TUKOVI, .; JASAK, H. A moving mesh finite volume interface tracking method for surface tension dominated interfacial fluid flow. **Computers & Fluids**, v. 55.0, p. 70–84, 2012. ISSN 0045-7930. Available: <https://www.sciencedirect.com/science/article/pii/S0045793011003380>. Citation on page 83.

TUKOVIĆ, Ž. **Metoda kontrolnih volumena na domenama promjenjivog oblika**. Phd Thesis (PhD Thesis) — Sveučilište u Zagrebu, Fakultet strojarstva i brodogradnje, 2005. Citation on page 220.

TURNBULL, B.; BARTELT, P. Mass and momentum balance model of a mixed flowing/powder snow avalanche. **Surveys in geophysics**, Springer, v. 24, n. 5, p. 465–477, 2003. Citation on page 93.

TURNBULL, B.; MCELWAINE, J. A comparison of powder-snow avalanches at vallée de la sionne, switzerland, with plume theories. **Journal of Glaciology**, Cambridge University Press, v. 53, n. 180, p. 30–40, 2007. Citations on pages 61 and 64.

TURNBULL, B.; MCELWAINE, J. N. Experiments on the non-boussinesq flow of self-igniting suspension currents on a steep open slope. **Journal of Geophysical Research: Earth Surface**, v. 113, n. F1, 2008. Available: <https://agupubs.onlinelibrary.wiley.com/doi/abs/10.1029/2007JF000753>. Citation on page 64.

TURNBULL, B.; MCELWAINE, J. N.; ANCEY, C. Kulikovskiy–sveshnikova–beghin model of powder snow avalanches: Development and application. **Journal of Geophysical Research: Earth Surface**, v. 112, n. F1, 2007. Available: <https://agupubs.onlinelibrary.wiley.com/doi/abs/10.1029/2006JF000489>. Citation on page 93.

TURNER, J. S. **Buoyancy Effects in Fluids**. [S.l.]: Cambridge University Press, 1973. (Cambridge Monographs on Mechanics). Citation on page 90.

UNGARISH, M. **An introduction to gravity currents and intrusions**. [S.l.]: CRC press, 2009. Citation on page 87.

VACONDIO, R.; ROGERS, B. D.; STANSBY, P. K. Accurate particle splitting for smoothed particle hydrodynamics in shallow water with shock capturing. **International Journal for Numerical Methods in Fluids**, v. 69.0, n. 8, p. 1377–1410, 2012. Available: <https://onlinelibrary.wiley.com/doi/abs/10.1002/fld.2646>. Citation on page 83.

VALERO, C. V.; JONES, K. W.; BüHLER, Y.; BARTELT, P. Release temperature, snow-cover entrainment and the thermal flow regime of snow avalanches. **Journal of Glaciology**, Cambridge University Press, v. 61, n. 225, p. 173–184, 2015. Citation on page 86.

VALERO, C. V.; WEVER, N.; CHRISTEN, M.; BARTELT, P. Modeling the influence of snow cover temperature and water content on wet-snow avalanche runout. **Natural Hazards and Earth System Sciences**, v. 18, n. 3, p. 869–887, 2018. Available: <https://nhess.copernicus.org/articles/18/869/2018/>. Citation on page 80.

VALLET, J.; TURNBULL, B.; JOLY, S.; DUFOUR, F. Observations on powder snow avalanches using videogrammetry. **Cold Regions Science and Technology**, v. 39, n. 2, p. 153–159, 2004. ISSN 0165-232X. Snow And Avalanches: Papers Presented At The European Geophysical Union Conference, Nice, April 2003. Dedicated To The Avalanche Dynamics Pioneer Dr. B. Salm. Available: <https://www.sciencedirect.com/science/article/pii/S0165232X04000461>. Citations on pages 60 and 61.

van Leer, B. Towards the ultimate conservative difference scheme. ii. monotonicity and conservation combined in a second-order scheme. **Journal of Computational Physics**, v. 14, n. 4, p. 361–370, 1974. ISSN 0021-9991. Available: <https://www.sciencedirect.com/science/article/pii/0021999174900199>. Citation on page 137.

VARNES, D. J. Slope movement types and processes. **Special report**, v. 176.0, p. 11–33, 1978. Citation on page 48.

VÉDRINE, L.; LI, X.; GAUME, J. Detrainment and braking of snow avalanches interacting with forests. **Natural Hazards and Earth System Sciences**, v. 22, n. 3, p. 1015–1028, 2022. Available: <https://nhess.copernicus.org/articles/22/1015/2022/>. Citation on page 101.

VENANT, B. D. S. Theorie du mouvement non-permanent des eaux avec application aux crues des rivers et a l'introduntion des marees dans leur lit. **Academic de Sci. Comptes Redus**, v. 73, n. 99, p. 148–154, 1871. Citations on pages 58 and 72.

VENKATASAWMY, R. **The Digitization of Cinematic Visual Effects: Hollywood's Coming of Age**. [S.l.]: Lexington Books, 2012. Citation on page 40.

VIDIC, L. **Half-mile avalanche shaves snow from Bald Mountain**. 2022. [Online; accessed September 09, 2023]. Available: <https://www.summitdaily.com/news/half-mile-avalanche-shaves-snow-from-bald-mountain/>. Citation on page 51.

VIONNET, V.; MARTIN, E.; MASSON, V.; LAC, C.; NAAIM-BOUVET, F.; GUYOMARC'H, G. High-resolution large eddy simulation of snow accumulation in alpine terrain. **Journal of Geophysical Research: Atmospheres**, v. 122, n. 20, p. 11,005–11,021, 2017. Available: <https://agupubs.onlinelibrary.wiley.com/doi/abs/10.1002/2017JD026947>. Citation on page 101.

VIROULET, S.; BAKER, J. L.; EDWARDS, A. N.; JOHNSON, C. G.; GJALTEMA, C.; CLAVEL, P.; GRAY, J. M. N. T. Multiple solutions for granular flow over a smooth two-dimensional bump. **Journal of Fluid Mechanics**, Cambridge University Press, v. 815, p. 77–116, 2017. Citation on page 82.

VOELLMY, A. Uber die zerstorungskraft von lawinen. **Schweizerische Bauzeitung, Jahrg.**, v. 73, p. 159–162, 1955. Citations on pages 58 and 72.

VORST, H. A. van der. Bi-cgstab: A fast and smoothly converging variant of bi-cg for the solution of nonsymmetric linear systems. **SIAM Journal on Scientific and Statistical Computing**, v. 13, n. 2, p. 631–644, 1992. Available: <https://doi.org/10.1137/0913035>. Citation on page 133.

VRIEND, N. M.; MCELWAINE, J. N.; SOVILLA, B.; KEYLOCK, C. J.; ASH, M.; BRENNAN, P. V. High-resolution radar measurements of snow avalanches. **Geophysical Research Letters**, v. 40, n. 4, p. 727–731, 2013. Available: <https://agupubs.onlinelibrary.wiley.com/doi/abs/10.1002/grl.50134>. Citations on pages 60 and 61.

Wallner, Chris. **Lyngen Alps Avalanche**. 2017. [Online; accessed March 6, 2018]. Available: <https://snowbrains.com/lyngen-alps-avalanche-buried-two-italian-tourists/>. Citation on page 40.

WANG, C.; ZHANG, Q.; KONG, F.; GAO, Y. Fast animation of debris flow with mixed adaptive grid refinement. **Computer Animation and Virtual Worlds**, v. 26.0, n. 1, p. 3–14, 2015. Available: <https://onlinelibrary.wiley.com/doi/abs/10.1002/cav.1542>. Citation on page 104.

WANG, X.; LIU, S.; BAN, X.; XU, Y.; ZHOU, J.; KOSINKA, J. Robust turbulence simulation for particle-based fluids using the rankine vortex model. **The Visual Computer**, Springer, v. 36.0, n. 10, p. 2285–2298, 2020. Citation on page 105.

WANGER, R. E-periodica: die plattform für digitalisierte schweizer zeitschriften. In: ____. **Bibliotheken der Schweiz: Innovation durch Kooperation; Festschrift für Susanna Bliggenstorfer anlässlich ihres Rücktrittes als Direktorin der Zentralbibliothek Zürich**. Berlin: De Gruyter, 2018. p. 401 – 413. ISBN 978-3-11-055182-2. Citation on page 72.

WELLS, M. G.; DORRELL, R. M. Turbulence processes within turbidity currents. **Annual Review of Fluid Mechanics**, v. 53, n. 1, p. 59–83, 2021. Available: <https://doi.org/10.1146/annurev-fluid-010719-060309>. Citation on page 87.

WIELAND, M.; GRAY, J. M. N. T.; HUTTER, K. Channelized free-surface flow of cohesionless granular avalanches in a chute with shallow lateral curvature. **Journal of Fluid Mechanics**, Cambridge University Press, v. 392, p. 73–100, 1999. Citation on page 82.

WOLPER, J.; CHEN, Y.; LI, M.; FANG, Y.; QU, Z.; LU, J.; CHENG, M.; JIANG, C. Anisompm: Animating anisotropic damage mechanics. **ACM Trans. Graph.**, Association for Computing Machinery, New York, NY, USA, v. 39, n. 4, aug 2020. ISSN 0730-0301. Available: <https://doi.org/10.1145/3386569.3392428>. Citation on page 105.

WORLEY, S. A cellular texture basis function. In: **Proceedings of the 23rd annual conference on Computer graphics and interactive techniques**. [S.l.: s.n.], 1996. p. 291–294. Citation on page 141.

XIA, X.; LIANG, Q. A gpu-accelerated smoothed particle hydrodynamics (sph) model for the shallow water equations. **Environmental Modelling & Software**, v. 75, p. 28–43, 2016. ISSN 1364-8152. Available: <https://www.sciencedirect.com/science/article/pii/S1364815215300608>. Citation on page 104.

_____. A new depth-averaged model for flow-like landslides over complex terrains with curvatures and steep slopes. **Engineering Geology**, v. 234.0, p. 174 – 191, 2018. ISSN 0013-7952. Available: <http://www.sciencedirect.com/science/article/pii/S0013795217306324>. Citation on page 83.

YEH, T.-h.; CANTERO, M.; CANTELLI, A.; PIRMEZ, C.; PARKER, G. Turbidity current with a roof: Success and failure of rans modeling for turbidity currents under strongly stratified conditions. **Journal of Geophysical Research: Earth Surface**, v. 118, n. 3, p. 1975–1998, 2013. Available: <https://agupubs.onlinelibrary.wiley.com/doi/abs/10.1002/jgrf.20126>. Citation on page 101.

YNDESTAD, L. K. H. **Particle-based Powder-snow Avalanche Simulation Using GPU**. Master's Thesis (Master's Thesis) — Institutt for datateknikk og informasjonsvitenskap, 2011. Citation on page 104.

YU, M.-h. Advances in strength theories for materials under complex stress state in the 20th century. **Appl. Mech. Rev.**, v. 55, n. 3, p. 169–218, 2002. Citation on page 77.

YUAN, L.; LIU, W.; ZHAI, J.; WU, S. F.; PATRA, A. K.; PITMAN, E. B. Refinement on non-hydrostatic shallow granular flow model in a global cartesian coordinate system. **Computational Geosciences**, v. 22, n. 1, p. 87–106, 2 2018. ISSN 1573-1499. Available: <https://doi.org/10.1007/s10596-017-9672-x>. Citation on page 83.

YUE, Y.; SMITH, B.; BATTY, C.; ZHENG, C.; GRINSPUN, E. Continuum foam: A material point method for shear-dependent flows. **ACM Transactions on Graphics (TOG)**, ACM, v. 34.0, n. 5, p. 160, 2015. Citation on page 105.

ZAHIBO, N.; PELINOVSKY, E.; TALIPOVA, T.; NIKOLKINA, I. Savage-hutter model for avalanche dynamics in inclined channels: Analytical solutions. **Journal of Geophysical Research: Solid Earth**, v. 115, n. B3, 2010. Available: <https://agupubs.onlinelibrary.wiley.com/doi/abs/10.1029/2009JB006515>. Citation on page 82.

ZHAI, J.; YUAN, L.; LIU, W.; ZHANG, X. Solving the savage–hutter equations for granular avalanche flows with a second-order godunov type method on gpu. **International Journal for Numerical Methods in Fluids**, v. 77, n. 7, p. 381–399, 2015. Available: <https://onlinelibrary.wiley.com/doi/abs/10.1002/fld.3988>. Citation on page 82.

ZHANG, S.; KONG, F.; LI, C.; WANG, C.; QIN, H. Hybrid modeling of multiphysical processes for particle-based volcano animation. **Computer Animation and Virtual Worlds**, v. 28, n. 3-4, p. e1758, 2017. E1758 cav.1758. Available: <https://onlinelibrary.wiley.com/doi/abs/10.1002/cav.1758>. Citation on page 104.

ZHAO, J.; CHEN, Y.; ZHANG, H.; XIA, H.; WANG, Z.; PENG, Q. Physically based modeling and animation of landslides with mpm. **The Visual Computer**, v. 35, n. 9, p. 1223–1235, 9 2019. ISSN 1432-2315. Available: <https://doi.org/10.1007/s00371-019-01709-3>. Citations on pages 101 and 105.

ZHAO, J.; ZGEN, I.; LIANG, D.; HINKELMANN, R. Improved multislope muscl reconstruction on unstructured grids for shallow water equations. **International Journal for Numerical Methods in Fluids**, v. 87.0, n. 8, p. 401–436, 2018. Available: <https://onlinelibrary.wiley.com/doi/abs/10.1002/fld.4499>. Citation on page 83.

ZHOU, G. G.; DU, J.; SONG, D.; CHOI, C. E.; HU, H.; JIANG, C. Numerical study of granular debris flow run-up against slit dams by discrete element method. **Landslides**, Springer, v. 17, n. 3, p. 585–595, 2020. Citation on page 100.

ZHU, B.; LU, W.; CONG, M.; KIM, B.; FEDKIW, R. A new grid structure for domain extension. **ACM Transactions on Graphics (TOG)**, ACM, v. 32.0, n. 4, p. 63, 2013. Citation on page 104.

ZHU, K.; HE, X.; LI, S.; WANG, H.; WANG, G. Shallow sand equations: Real-time height field simulation of dry granular flows. **IEEE Computer Architecture Letters**, IEEE Computer Society, n. 01, p. 1–1, 2019. Citation on page 104.

ZUGLIANI, D.; ROSATTI, G. Trent2d: An accurate numerical approach to the simulation of two-dimensional dense snow avalanches in global coordinate systems. **Cold Regions Science and Technology**, v. 190, p. 103343, 2021. ISSN 0165-232X. Available: <https://www.sciencedirect.com/science/article/pii/S0165232X21001245>. Citation on page 104.

ZWINGER, T.; KLUWICK, A.; SAMPL, P. Numerical simulation of dry-snow avalanche flow over natural terrain. In: ____. **Dynamic Response of Granular and Porous Materials under Large and Catastrophic Deformations**. Berlin, Heidelberg: Springer Berlin Heidelberg, 2003. p. 161–194. ISBN 978-3-540-36565-5. Available: <https://doi.org/10.1007/978-3-540-36565-5_5>. Citations on pages 95, 97, and 103.

ÉTIENNE, J.; SARAMITO, P.; HOPFINGER, E. J. Numerical simulations of dense clouds on steep slopes: application to powder-snow avalanches. **Annals of Glaciology**, Cambridge University Press, v. 38, p. 379–383, 2004. Citations on pages 97 and 98.

Appendix

APPENDIX

A

BACKGROUND CONCEPTS

A.1 Continum Mixture Theory

The Continuum Mixture Theory (CMT) (ATKIN; CRAINE, 1976), which has long roots in the work of Fick (1855), deals with substances in nature whose materials consist of more than one constituent. The CMT characterizes the mixture as a superposition of multiple single continua representing the different constituents whose particles can occupy each domain location simultaneously.

Let the subscript $(\cdot)_\gamma$ indicate a field of constituent $\mathscr{C}_\gamma$, then for a set of n constituents and the position function ϕ_t^γ for $\mathscr{C}_\gamma$, the motion of the mixture is described by n equations

$$\mathbf{x} = \phi_t^\gamma(\mathbf{X}_\gamma, t), \quad 1 \leq \gamma \leq n, \tag{A.1}$$

The equation comes from a Continuum Mechanics perspective, which considers a body under deformation over time. The reference state, with material point locations represented in Lagrangian coordinates $\mathbf{X}$, and the deformed state, with locations represented in Eulerian coordinates $\mathbf{x}$, are mapped by the deformation function ϕ_t^γ. For each location $\mathbf{X}$, ϕ gives the spatial location $\mathbf{x}$ that characterizes the deformed state of the body for constituent $\mathscr{C}_\gamma$ after a given time t. Consequently, the velocity field $\mathbf{v}_\gamma$ of constituent $\mathscr{C}_\gamma$ is

$$\mathbf{u}_\gamma = \frac{\partial \phi_t^\gamma}{\partial t}. \tag{A.2}$$

The material derivatives for constituent $\mathscr{C}_\gamma$, $\frac{D^\gamma}{D_t}$, for an arbitrary scalar function $s(\mathbf{x},t)$ and an arbitrary vector function $\mathbf{w}(\mathbf{x},t)$ are

$$\frac{D^\gamma s}{D_t} = \frac{\partial s}{\partial t} + \mathbf{u}_\gamma \cdot \nabla s \tag{A.3}$$

and

$$\frac{D^\gamma \mathbf{w}}{D_t} = \frac{\partial \mathbf{w}}{\partial t} + (\nabla \mathbf{w})\mathbf{u}_\gamma. \tag{A.4}$$

The motion of the mixture can be computed by defining a mean velocity $\mathbf{u}$ of the mixture following the requirement that the total mass flow is the sum of the individual flows so that

$$\rho\mathbf{u} = \sum_{\gamma} \rho_{\gamma}\mathbf{u}_{\gamma}, \tag{A.5}$$

where ρ_{γ} represents the average density of $\mathscr{C}_{\gamma}$ over a small volume of the mixture and the mass density of the mixture, ρ, is given by

$$\rho = \sum_{\gamma} \rho_{\gamma}. \tag{A.6}$$

APPENDIX

B

NUMERICAL METHODS

B.1 Finite Volume Method

Finite Volume Methods (FVMs) are derived directly from the integral form of conservation laws. The FVM subdivides the physical domain into cells, named *finite volumes*, and keeps track of the fluxes of physical quantities between cells — see Figure 72. Applying the Gauss theorem connects the surface fluxes to volume quantities, allowing the discretization of the governing equations over the finite volumes. This chapter is heavily based on (GONZALEZ; STUART, 2008) and (DARWISH; MOUKALLED, 2016), refer to these books for a complete discussion on the FVM.

Figure 72 – The FVM decomposes the physical domain into finite volumes (left). The figure on the right illustrates mass fluxes between cells as the water flow between two tanks. From a conservation perspective, the mass in a finite volume will change only due to fluxes at the boundaries.

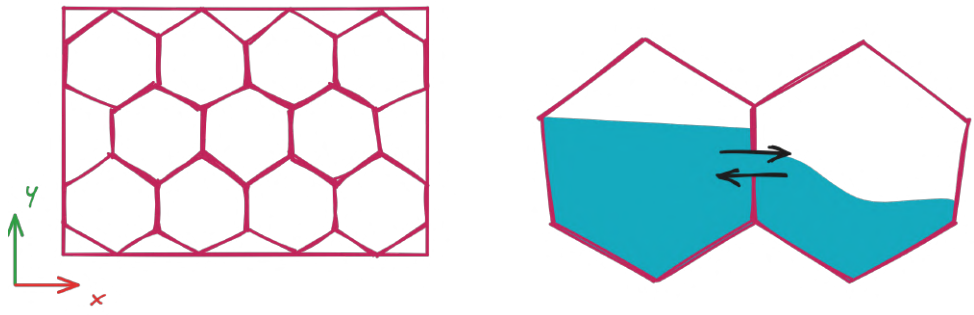

Source: Elaborated by the author.

Consider the one-dimensional case for an arbitrary quantity specified by the unknown function $q(x,t)$ at a given location x and time t. If this quantity represents the density of a substance, the sum

$$\int_{x_a}^{x_b} q(x,t)dx \tag{B.1}$$

gives the total mass of the substance in the section between x_a and x_b at a particular time t. As the flow evolve, the mass of the substance in $[x_a, x_b]$ might change over time due to the flux of matter at the endpoints x_a and x_b. If we know the flow velocity function $u(x,t)$, then the flux of mass $f(x,t)$ can be defined as

$$f(x,t) = u(x,t)q(x,t). \tag{B.2}$$

The following *integral form* gives the change of mass over time:

$$\frac{d}{dt}\int_{x_a}^{x_b} q(x,t)dx = -f(x,t)\Big|_{x_a}^{x_b}. \tag{B.3}$$

In particular, if q and f are smooth, the equation above can be written in the *differential form*

$$\begin{aligned}
\frac{d}{dt}\int_{x_a}^{x_b} q(x,t)dx &= -\int_{x_a}^{x_b} \frac{\partial}{\partial x} f(x,t)dx \\
\therefore \int_{x_a}^{x_b} \left[\frac{\partial}{\partial t} q(x,t) + \frac{\partial}{\partial x} f(x,t) \right] dx &= 0 \\
\therefore \frac{\partial}{\partial t} q(x,t) + \frac{\partial}{\partial x} f(x,t) &= 0.
\end{aligned} \tag{B.4}$$

Figure 73 – The continuous field $q(x,t)$ represents the distribution of a physical quantity over the physical domain at a given time t. The FVM decomposes the domain into cells C_i centered at positions x_i. Cell faces at $x_{i\pm\frac{1}{2}}$ represent the boundaries through which q flows. The average value Q_i approximates q inside C_i, and $F_{i\pm\frac{1}{2}}$ approximate the flux at faces in $x_{i\pm\frac{1}{2}}$.

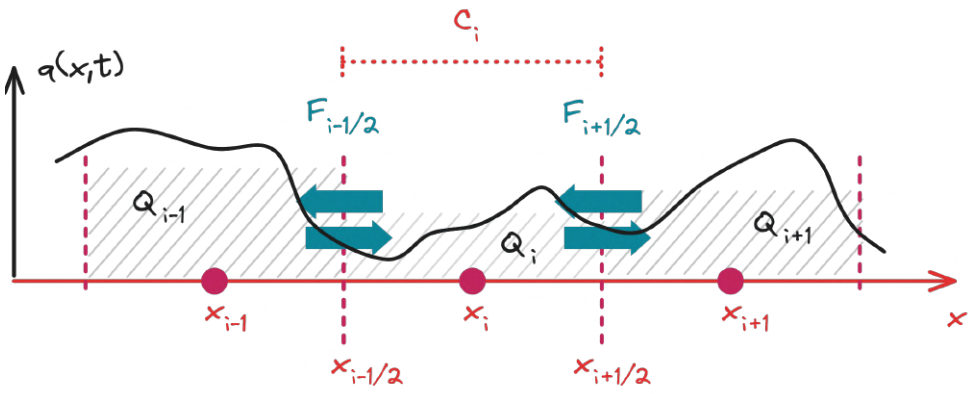

Source: Elaborated by the author.

The 1D domain decomposition in Figure 73 defines cells centered at x_i locations with faces at $x_{i\pm\frac{1}{2}}$ locations. The value Q_i is the approximation of q in the cell centered at x_i and is the average value of q over the interval $C_i = (x_{i-\frac{1}{2}}, x_{i+\frac{1}{2}})$:

$$Q_i \approx \frac{1}{\Delta x_i}\int_{C_i} q(x,t)dx, \tag{B.5}$$

where $\Delta x_i = |C_i|$. Similarly, the functions

$$\begin{aligned}
F_{i-\frac{1}{2}}(Q_{i-1}, Q_i) &\approx \frac{1}{\Delta t}\int_{t_n}^{t_{n+1}} f(x_{i-\frac{1}{2}}, t)dt \\
F_{i+\frac{1}{2}}(Q_i, Q_{i+1}) &\approx \frac{1}{\Delta t}\int_{t_n}^{t_{n+1}} f(x_{i+\frac{1}{2}}, t)dt
\end{aligned} \tag{B.6}$$

approximate the fluxes of q at the face locations $x_{i\pm\frac{1}{2}}$. Notice that F depends only on the neighboring values Q_i and $Q_{i\pm1}$ over the time interval $\Delta t = t_{n+1} - t_n$. By time integrating Equation B.3 over the time interval Δt, the approximations above, Q_i and $F_{i\pm\frac{1}{2}}$, can be used directly to approximate *Equation B.3* entirely[1]. This procedure illustrates the essence of the FVM: *approximate differential equations by using just volume quantities and boundary fluxes.*

B.1.1 The Divergence Theorem

Figure 74 – The visual illustration of the Divergence Theorem: The total divergence of a vector field $\mathbf{u}$ inside a volume Ω equals the total net flux of $\mathbf{u}$ passing through the boundary surface $\partial\Omega$ with the unit vector field $\mathbf{n}$ pointing outwards $\partial\Omega$.

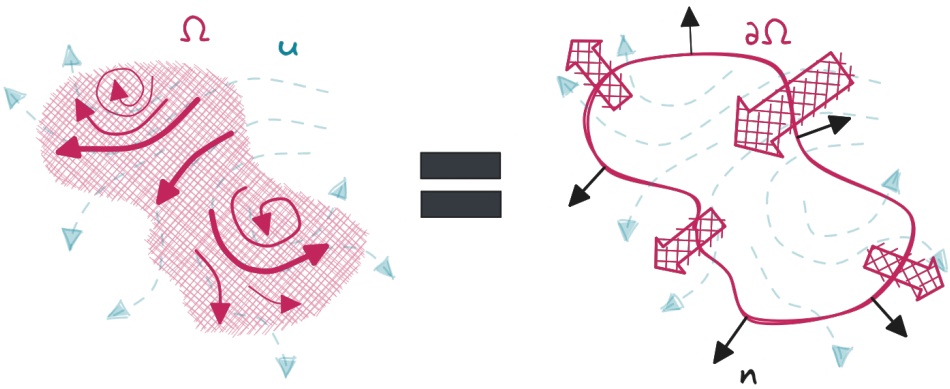

Source: Elaborated by the author.

The central tool of the FVM is the Gauss theorem, also known as the *Divergence Theorem*. For a given bounded region Ω with boundary $\partial\Omega$, the theorem connects the total volume divergence of a vector field $\mathbf{u}(\mathbf{x},t)$ inside Ω with the net flux of $\mathbf{u}$ through $\partial\Omega$ – see Figure 74. Let $\mathbf{n}(\mathbf{x})$ be the field of unit vectors normal to $\partial\Omega$; the divergence theorem reads:

$$\int_{\Omega} (\nabla \cdot \mathbf{u}) d\Omega = \oint_{\partial\Omega} (\mathbf{u} \cdot \mathbf{n}) d\partial\Omega. \tag{B.7}$$

In the discrete setting, the boundary surface $\partial\Omega$ is approximated by a set of polygonal faces $S \approx \partial\Omega$. The following sum approximates the integral in the right-hand side of Equation B.7:

$$\oint_{\partial\Omega} (\mathbf{u} \cdot \mathbf{n}) d\partial\Omega \approx \sum_{f_i \in S} \int_{f_i} (\mathbf{u} \cdot \mathbf{n}) dS \tag{B.8}$$

where f_i, with index $i \in [1, |S|]$, represents each face in S. The Gauss quadrature can approximate the solution of the face integral inside the sum in Equation B.8. Using the trapezoidal rule in any face f_i, only one integration point located at f_i's center f_{ci} results in second-order accuracy.

[1] Let the superscript $(\cdot)^n$ denote the time step index, then it is possible to obtain the following explicit form for Equation B.3: $Q_i^{n+1} = Q_i^n + \frac{\Delta t}{\Delta x}(F^n_{i-\frac{1}{2}} - F^n_{i+\frac{1}{2}})$.

Thus, for the face area vector $\mathbf{S_f}_i$ that points outwards the finite volume at face f_i, the integral is approximated by

$$\int_{f_i} (\mathbf{u}\cdot\mathbf{n})dS \approx (\mathbf{u})_{f_{ci}} \cdot \mathbf{S_f}_i = \mathbf{J}_i \cdot \mathbf{S_f}_i, \tag{B.9}$$

where the subscript $(\bigstar)_\mathbf{p}$ indicates the value of the quantity realized in the point $\mathbf{p}$. The symbol $\mathbf{J}_i$ will be used for now on to represent the quantity transported on the flux evaluated at f_{ci}. The final definition of $\mathbf{J}_i \cdot \mathbf{S_f}_i$, discussed later in subsection B.1.6, will produce the linear system of equations that will provide the numerical solution for the PDEs. As represented in Figure 75, applying Equation B.9 in Equation B.8 gives the approximated solution of the total flux passing through the surface S:

$$\oint_{\partial\Omega} (\mathbf{u}\cdot\mathbf{n})d\partial\Omega \approx \sum_{f_i \in S} \mathbf{J}_i \cdot \mathbf{S_f}_i. \tag{B.10}$$

Figure 75 – The total surface flux passing through the boundary surface $\partial\Omega$ can be approximated by the sum of the individual face fluxes $\mathbf{J}_i \cdot \mathbf{S_f}_i$ in the discrete surface S.

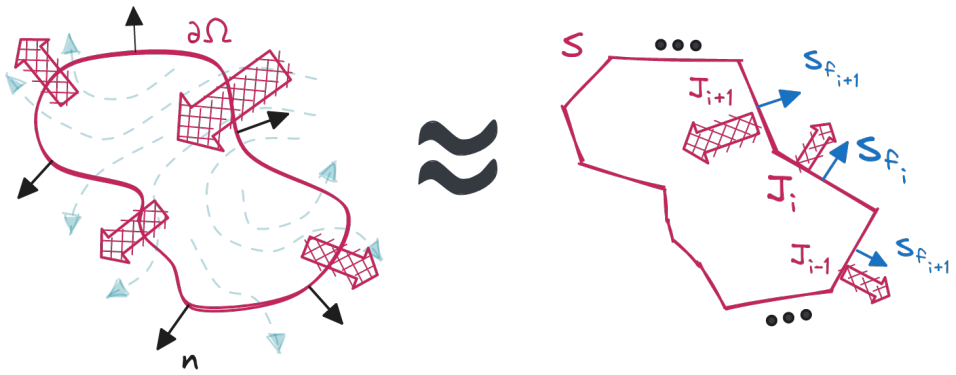

Source: Elaborated by the author.

The single-point Gauss quadrature could also be applied to approximate the volume integral in Equation B.7. For the mid-point c, and Ω volume V, the volume integral is approximated by

$$\int_\Omega (\nabla\cdot\mathbf{u})d\Omega \approx (\nabla\cdot\mathbf{u})_c V, \tag{B.11}$$

which combined to Equation B.10, gives the approximation for $\nabla\cdot\mathbf{u}$ over Ω:

$$(\nabla\cdot\mathbf{u})_c \approx \frac{1}{V}\sum_{f_i \in S} \mathbf{J}_i \cdot \mathbf{S_f}_i. \tag{B.12}$$

The Gauss theorem is not restricted to vector fields such as $\mathbf{u}$ and the internal product $(\cdot)$. The general form of the theorem is

$$\int_\Omega (\nabla * \Psi)d\Omega = \oint_{\partial\Omega} (\Psi * \mathbf{n})d\partial\Omega, \tag{B.13}$$

where Ψ is a generic tensor field that accepts any particular product operation $*$. This generalization enables the discretization of most differential terms in the Partial-Differential Equations (PDEs) commonly solved by FVMs. The following section details the discretization process of such equations, including the terms that do not accept the divergence theorem.

B.1.2 Spatial Discretization

This section lists the types of terms that appear in common physical models solved by FVMs, such as the velocity divergent term $\nabla \cdot \mathbf{u}$ in the previous section. In this section, $\rho(\mathbf{x},t)$, $p(\mathbf{x},t)$, $q(\mathbf{x},t)$, and $\phi(\mathbf{x},t)$ are scalar fields, $\mathbf{f}_b(\mathbf{x},t)$ and $\mathbf{u}(\mathbf{x},t) = (u_x, u_y, u_z)$ are vector fields, and Γ, μ, and ν are constants. Some equations decouple $\mathbf{n}$ from $\mathbf{S_f}$ by recalling

$$\mathbf{S_f} = (S_{fx}, S_{fy}, S_{fz}) = \mathbf{n} \parallel \mathbf{S_f} \parallel = \mathbf{n} S_f$$

- **Divergent term** $\nabla \cdot \mathbf{u}$:

$$\int_\Omega \nabla \cdot \mathbf{u} d\Omega = \oint_{\partial\Omega} (\mathbf{u} \cdot \mathbf{n}) d\partial\Omega \approx \sum_{f_i \in S} (\mathbf{u})_{f_{ci}} \cdot \mathbf{S_f}_i. \tag{B.14}$$

- **Convective term** $\nabla \cdot (\rho \mathbf{u} \phi)$:

$$\int_\Omega \nabla \cdot (\rho \mathbf{u} \phi) d\Omega = \oint_{\partial\Omega} ((\rho \mathbf{u} \phi) \cdot \mathbf{n}) d\partial\Omega \approx \sum_{f_i \in S} (\rho \mathbf{u} \phi)_{f_{ci}} \cdot \mathbf{S_f}_i. \tag{B.15}$$

- **Convective term** $\nabla \cdot (\rho \mathbf{u} \otimes \mathbf{u})$:

$$\int_\Omega \nabla \cdot (\rho \mathbf{u} \otimes \mathbf{u}) d\Omega = \oint_{\partial\Omega} ((\rho \mathbf{u} \otimes \mathbf{u}) \cdot \mathbf{n}) d\partial\Omega \approx \sum_{f_i \in S} (\rho \mathbf{u} \otimes \mathbf{u})_{f_{ci}} \cdot \mathbf{S_f}_i. \tag{B.16}$$

$$(\rho \mathbf{u} \otimes \mathbf{u})_{f_c} \cdot \mathbf{S_f} = \rho \begin{pmatrix} u_x u_x & u_x u_y & u_x u_z \\ u_y u_x & u_y u_y & u_y u_z \\ u_z u_x & u_z u_y & u_z u_z \end{pmatrix}_{f_c} \cdot \mathbf{S_f} = \rho \begin{pmatrix} u_x u_x S_{fx} + u_x u_y S_{fy} + u_x u_z S_{fz} \\ u_y u_x S_{fx} + u_y u_y S_{fy} + u_y u_z S_{fz} \\ u_z u_x S_{fx} + u_z u_y S_{fy} + u_z u_z S_{fz} \end{pmatrix}_{f_c}. \tag{B.17}$$

- **Diffusion term** $\nabla \cdot (\Gamma \nabla \phi)$:

$$\int_\Omega \nabla \cdot (\Gamma \nabla \phi) d\Omega = \oint_{\partial\Omega} (\Gamma \nabla_{\mathbf{n}} \phi) d\partial\Omega \approx \sum_{f_i \in S} (\Gamma \nabla_{\mathbf{n}} \phi)_{f_{ci}} S_{f_i}, \tag{B.18}$$

where $S_{f_i} = \parallel \mathbf{S_f}_i \parallel$. The computation of the gradient of ϕ is discussed in subsection B.1.4.

- **Diffusion term** $\nabla \cdot (\nu \nabla \otimes \mathbf{u})$:

$$\int_\Omega \nabla \cdot (\nu \nabla \otimes \mathbf{u}) d\Omega = \oint_{\partial\Omega} ((\nu \nabla \otimes \mathbf{u}) \cdot \mathbf{n}) d\partial\Omega \approx \sum_{f_i \in S} (\nu \nabla \otimes \mathbf{u})_{f_{ci}} \cdot \mathbf{S_f}_i. \tag{B.19}$$

$$(\nu \nabla \otimes \mathbf{u})_{f_c} \cdot \mathbf{S_f} = \nu \begin{pmatrix} \frac{\partial u_x}{\partial x} & \frac{\partial u_y}{\partial x} & \frac{\partial u_z}{\partial x} \\ \frac{\partial u_x}{\partial y} & \frac{\partial u_y}{\partial y} & \frac{\partial u_z}{\partial y} \\ \frac{\partial u_x}{\partial z} & \frac{\partial u_y}{\partial z} & \frac{\partial u_z}{\partial z} \end{pmatrix}_{f_c} \cdot \mathbf{S_f} = \nu \begin{pmatrix} \frac{\partial u_x}{\partial x} S_{fx} + \frac{\partial u_y}{\partial x} S_{fy} + \frac{\partial u_z}{\partial x} S_{fz} \\ \frac{\partial u_x}{\partial y} S_{fx} + \frac{\partial u_y}{\partial y} S_{fy} + \frac{\partial u_z}{\partial y} S_{fz} \\ \frac{\partial u_x}{\partial z} S_{fx} + \frac{\partial u_y}{\partial z} S_{fy} + \frac{\partial u_z}{\partial z} S_{fz} \end{pmatrix}_{f_c}. \tag{B.20}$$

- **Tensor term** $\nabla \cdot (\mu(\nabla \otimes \mathbf{u})^T)$:

$$\int_\Omega \nabla \cdot (\mu(\nabla \otimes \mathbf{u})^T) d\Omega = \oint_{\partial\Omega} ((\mu(\nabla \otimes \mathbf{u})^T) \cdot \mathbf{n}) d\partial\Omega \approx \sum_{f_i \in S} (\mu(\nabla \otimes \mathbf{u})^T)_{f_{ci}} \cdot \mathbf{S}_{\mathbf{f}i}. \quad \text{(B.21)}$$

$$(\mu(\nabla \otimes \mathbf{u})^T)_{f_c} \cdot \mathbf{S_f} = \mu \begin{pmatrix} \frac{\partial u_x}{\partial x} & \frac{\partial u_x}{\partial y} & \frac{\partial u_x}{\partial z} \\ \frac{\partial u_y}{\partial x} & \frac{\partial u_y}{\partial y} & \frac{\partial u_y}{\partial z} \\ \frac{\partial u_z}{\partial x} & \frac{\partial u_z}{\partial y} & \frac{\partial u_z}{\partial z} \end{pmatrix}_{f_c} \cdot \mathbf{S_f} = \mu \begin{pmatrix} \frac{\partial u_x}{\partial x} S_{fx} + \frac{\partial u_x}{\partial y} S_{fy} + \frac{\partial u_x}{\partial z} S_{fz} \\ \frac{\partial u_y}{\partial x} S_{fx} + \frac{\partial u_y}{\partial y} S_{fy} + \frac{\partial u_y}{\partial z} S_{fz} \\ \frac{\partial u_z}{\partial x} S_{fx} + \frac{\partial u_z}{\partial y} S_{fy} + \frac{\partial u_z}{\partial z} S_{fz} \end{pmatrix}_{f_c} . \quad \text{(B.22)}$$

- **Scalar gradient term** $\nabla\phi$:

  In this particular case, the Green-Gauss theorem[2] is used instead:

$$\int_\Omega \nabla\phi d\Omega = \oint_{\partial\Omega} (\phi \mathbf{n}) d\partial\Omega \approx \sum_{f_i \in S} (\phi)_{f_{ci}} \mathbf{S}_{\mathbf{f}i}. \quad \text{(B.23)}$$

Note that the discretizations above require evaluating values in face locations, such as the fields $\mathbf{u}$ and ϕ, and even a differential operator, as the gradient $\nabla\phi$ in Equation B.18. The computation of such values depends directly on how the fields are stored in the numerical mesh. Moreover, the mesh's geometry also affects the accuracy of the computations, as detailed in subsection B.1.4 on page 213.

The divergence theorem does not work for all terms found in equations. *Transient* and *source* terms, marked in the equations bellow, are examples of terms that do not need the transformation of their volume integrals into surface integrals. Their discretization comes directly from the approximation of volume integral:

$$\underbrace{\frac{\partial(\rho\phi)}{\partial t}}_{\text{transient}} + \nabla \cdot (\rho \mathbf{u} \phi) = \nabla \cdot (\Gamma \nabla\phi) + \underbrace{q}_{\text{source}}, \quad \text{(B.24)}$$

$$\underbrace{\frac{\partial \mathbf{u}}{\partial t}}_{\text{transient}} + \nabla \cdot (\mathbf{u} \otimes \mathbf{u}) - \nabla \cdot (\nu \nabla \otimes \mathbf{u}) = -\nabla p + \underbrace{\mathbf{f}_b}_{\text{source}} . \quad \text{(B.25)}$$

The following approximations consider the single-point volume integration with integration point located at the cell center C_c and cell volume C_V:

- **Source terms** q and $\mathbf{f}_b$:

$$\int_\Omega q d\Omega \approx (q)_{C_c} C_V \quad \text{and} \quad \int_\Omega \mathbf{f}_b d\Omega \approx (\mathbf{f}_b)_{C_c} C_V . \quad \text{(B.26)}$$

[2] The Green-Gauss theorem states that the surface integral of a scalar function ϕ is equal to the volume integral of the gradient of ϕ, $\nabla\phi$.

- **Transient terms** $\frac{\partial(\rho\phi)}{\partial t}$ and $\frac{\partial \mathbf{u}}{\partial t}$:

  Assuming that Ω does not change its volume in time, i.e. C_V is constant, then the transient term discretization can also be approximated by the Gauss quadrature for the volume integral:

$$\int_\Omega \frac{\partial(\rho\phi)}{\partial t} d\Omega \approx \frac{\partial(\rho\phi)_{C_c}}{\partial t} C_V \quad \text{and} \quad \frac{\partial(\mathbf{u})}{\partial t} d\Omega \approx \frac{\partial(\mathbf{u})_{C_c}}{\partial t} C_V. \tag{B.27}$$

To illustrate the process of the FVM, consider Equation B.24. The first step is to set the proper integration for each term:

$$\int_\Omega \frac{\partial(\rho\phi)}{\partial t} d\Omega + \oint_{\partial\Omega} ((\rho\mathbf{u}\phi)\cdot\mathbf{n}) d\partial\Omega = \oint_{\partial\Omega} ((\Gamma\nabla\phi)\cdot\mathbf{n}) d\partial\Omega + \int_\Omega q d\Omega, \tag{B.28}$$

and then perform the approximations

$$\overline{\frac{\partial(\rho\phi)_{C_c}}{\partial t} C_V} + \sum_{f_i \in S} (\rho\mathbf{u}\phi)_{f_{ci}} \cdot \mathbf{S}_{\mathbf{f}i} = \sum_{f_i \in S} (\Gamma\nabla\phi)_{f_{ci}} \cdot \mathbf{S}_{\mathbf{f}i} + (q)_{C_c} C_V. \tag{B.29}$$

The next step is to discretize the temporal derivative, marked in the equation above. The following section discusses the approximation of the transient term.

B.1.3 Time Integration

The process of temporal discretization follows the same approach taken until now, which consists of the integration over the time variable t. Like the one-dimensional spatial discretization presented earlier, temporal cells T_n of size Δt split the timeline, so the time index $n \in [0, +\infty)$ represents the *temporal cell* center $t_n = t_0 + n\Delta t$ — see Figure 76. Similarly, the *temporal face* location happens on indices $n \pm \frac{1}{2}$. The transient solution solves the equations in order $[t_0, \ldots, t_{n-1}, t_n, t_{n+1}, \ldots]$.

Figure 76 – The discretization in time splits the temporal line into temporal cells of size Δt. Similar to spatial flux computations, temporal face locations are also of interest in temporal discretization. The temporal dependency makes the computation of ϕ values follow the order $[\ldots, n-1, n, n+1, \ldots]$.

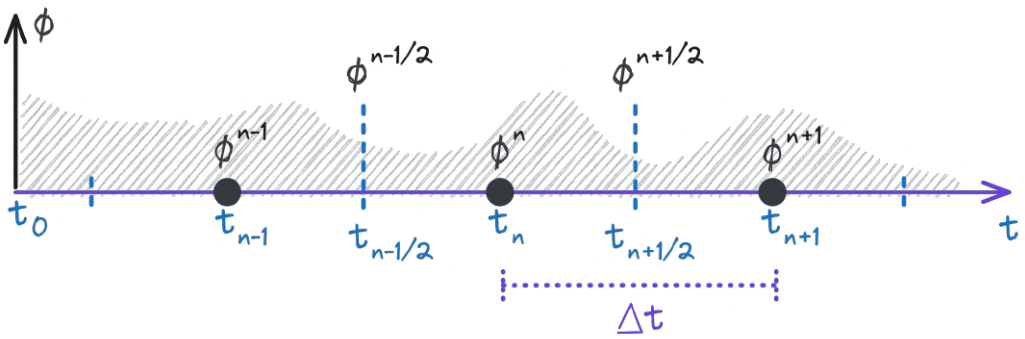

Source: Elaborated by the author.

In particular, the integration for the temporal cell T_n, i.e. for the time interval $[t_{n-\frac{1}{2}}, t_{n+\frac{1}{2}}]$, of Equation B.29 results in

$$\int_{t_n-\frac{\Delta t}{2}}^{t_n+\frac{\Delta t}{2}} \frac{\partial(\rho\phi)_{C_c}}{\partial t} C_V dt + \int_{t_n-\frac{\Delta t}{2}}^{t_n+\frac{\Delta t}{2}} \Big[\sum_{f_i\in S} (\rho \mathbf{u}\phi)_{f_{ci}} \cdot \mathbf{S}_{\mathbf{f}i}\Big] dt = \int_{t_n-\frac{\Delta t}{2}}^{t_n+\frac{\Delta t}{2}} \Big[\sum_{f_i\in S} (\Gamma\nabla\phi)_{f_{ci}} \cdot \mathbf{S}_{\mathbf{f}i}\Big] dt + \int_{t_n-\frac{\Delta t}{2}}^{t_n+\frac{\Delta t}{2}} \Big[(q)_{C_c} C_V\Big] dt \tag{B.30}$$

For simplicity, let $L(\phi)$ represent the sum of all spatially discretized terms except the transient term and rewrite the equation above as

$$\int_{t_n-\frac{\Delta t}{2}}^{t_n+\frac{\Delta t}{2}} \frac{\partial(\rho\phi)_{C_c}}{\partial t} C_V dt + \int_{t_n-\frac{\Delta t}{2}}^{t_n+\frac{\Delta t}{2}} L dt = 0. \tag{B.31}$$

One possible approach is to solve the second term with the mid point rule:

$$\int_{t_n-\frac{\Delta t}{2}}^{t_n+\frac{\Delta t}{2}} L dt \approx (L)^n \Delta t, \tag{B.32}$$

where the superscript $(\cdot)^n$ indicates the temporal location of the variables in L. In the FVM, the first term is approximated by the face fluxes in the same manner as in the previous sections:

$$\int_{t_n-\frac{\Delta t}{2}}^{t_n+\frac{\Delta t}{2}} \frac{\partial(\rho\phi)_{C_c}}{\partial t} C_V dt \approx C_V \Big((\rho\phi)_{C_c}^{n+\frac{1}{2}} - (\rho\phi)_{C_c}^{n-\frac{1}{2}}\Big). \tag{B.33}$$

Putting all together, Equation B.31 becomes

$$\frac{C_V}{\Delta t}\Big((\rho\phi)_{C_c}^{n+\frac{1}{2}} - (\rho\phi)_{C_c}^{n-\frac{1}{2}}\Big) + (L)^n = 0. \tag{B.34}$$

Note that the equation above contains samples from times $[t_{n-\frac{1}{2}}, t_n, t_{n+\frac{1}{2}}]$. The form of how these elements are computed will depend on the choice of interpolation for the temporal fluxes located at $t_{n-\frac{1}{2}}$ and $t_{n+\frac{1}{2}}$. Figure 77 illustrates the two common approaches listed here:

- **Implicit Euler Scheme**:

  The first-order implicit Euler scheme, or *first-order upwind*, considers the value of the element at t_k to be the same as the value at $t_{k+\frac{1}{2}}$. In other words, unknown values receive the same values of locations halfway backward. Therefore, the flux terms in Equation B.34 receive the same values of the respective cell centers:

  $$\frac{C_V}{\Delta t}\Big((\rho\phi)_{C_c}^{n} - (\rho\phi)_{C_c}^{n-1}\Big) + (L)^n = 0. \tag{B.35}$$

  Note that only the data from time t_{n-1} is available at this point. The time of the new values, t_n, is the same as the time of the spatial term $(L)^n$. It means that $(L)^n$ is not available yet, and the whole system of equations for both terms needs to be solved together.

- **Explicit Euler Scheme**:

  The first-order explicit Euler scheme considers the value of the element at t_k to be the same as the value at $t_{k-\frac{1}{2}}$. Therefore, face fluxes receive the same values of cell centers halfway forward:

$$\frac{C_V}{\Delta t}\left((\rho\phi)_{C_c}^{n+1} - (\rho\phi)_{C_c}^{n}\right) + (L)^n = 0. \tag{B.36}$$

  The spatial discretization lies in a previous time t_n regarding the new time t_{n+1}. All data is available for time t_n, meaning that the new step can be computed directly as:

$$(\rho\phi)_{C_c}^{n+1} = (\rho\phi)_{C_c}^{n} - \frac{\Delta t}{C_V}(L)^n. \tag{B.37}$$

Figure 77 – This figure visually represents implicit and explicit Euler schemes at step N in time t_n. Filled circles in the timeline represent data available for the computation. The dashed column represents the location in time of the spatial discretization L. In the case of the implicit Euler scheme, ϕ^n is unknown, then $(L)^n$ must be computed along with the new transient term.

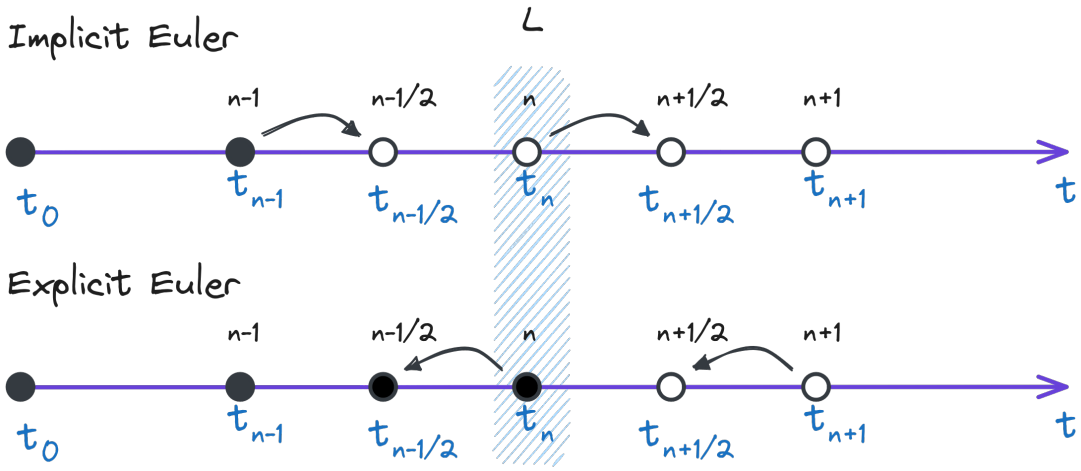

Source: Elaborated by the author.

The literature offers a variety of temporal discretization methods, including higher-order Euler schemes, the Crank-Nicholson method, which uses a central difference scheme, and methods that consider non-uniform time steps. Refer to Gonzalez and Stuart (2008) and Darwish and Moukalled (2016) for further information.

B.1.4 Face Computations

As mentioned earlier, the computation of the fluxes $\mathbf{J}_i \cdot \mathbf{S}_{\mathbf{f}i}$ requires the evaluation of values at the face centers f_{ci}. Some numerical settings conveniently store fields in face centers, the case of staggered grids with velocity components. However, values resulting from volume integrals are located at cell centers. In such cases, the interpolation of cell values must be interpolated to face locations.

Figure 78 depicts two pairs of cells, C and N_i, with respective centers C_c and N_{ci}, and volumes C_V and N_{Vi}, shared by a single face f_i with center f_{ci}. Let $\mathbf{d}_i = N_{ci} - C_c$ connect both

Figure 78 – The flux of a face f_i requires field values at the face center f_{ci}. Usually the field values are found in the cell centers, C_c and N_{ci}, and must be interpolated to the face locations. The usual approach is to interpolate along the line $\mathbf{d}_i$ that connects both cell centers at the intersection point f_{pi}. In skewed grids, f_{pi} deviates away from f_{ci} by $\bar{\mathbf{pc}}_i$, requiring further calculations for f_{ci}.

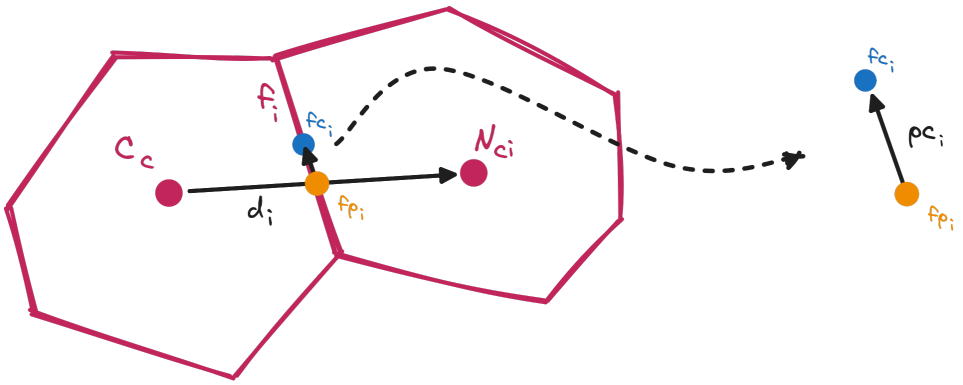

Source: Elaborated by the author.

cell centers and intersect the face f_i at point f_{pi}, where f_{pi} is not necessarily the same as f_{ci}[3], as shown in the figure. Suppose the cell values for the scalar field $\phi(\mathbf{x})$ for both cells are

$$\phi_C = (\phi)_{C_c} C_V \quad \text{and} \quad \phi_{Ni} = (\phi)_{N_{ci}} N_{Vi}. \tag{B.38}$$

The common approach is to assume that ϕ varies linearly along $\mathbf{d}_i$, meaning that the estimate at f_{pi} is the linear interpolation of ϕ_C and ϕ_N:

$$\phi_{f_{pi}} = \lambda_C \phi_C + \lambda_N \phi_N. \tag{B.39}$$

where λ_C and λ_N are interpolation coefficients. However, the second order accuracy of the flux discretization requires a value located at the face center f_{ci}. Therefore, a *skewness correction* must be performed in order to compute $\phi_{f_{ci}}$:

$$\phi_{f_{ci}} = \phi_{f_{pi}} + (\nabla_{\mathbf{d}_i} \phi)_{f_{pi}} \cdot \bar{\mathbf{pc}}_i, \tag{B.40}$$

where $\bar{\mathbf{pc}}_i = f_{ci} - f_{pi}$ and the gradient $(\nabla_{\mathbf{d}_i} \phi)_{f_{pi}}$ can be computed as

$$\left(\frac{\partial \phi}{\partial \mathbf{d}_i} \right)_{f_{pi}} = \frac{\phi_N - \phi_C}{\| \mathbf{d}_i \|}. \tag{B.41}$$

Some flux equations will contain differential operators, such as the gradient operator $\nabla\phi$ in the diffusion term described in Equation B.18 on page 209. Let $\Gamma = 1$ in the equation and the face normal vector $\mathbf{n}_i$ be decoupled from $\mathbf{S}_{\mathbf{f}i} = \mathbf{n}_i |\mathbf{S}_{\mathbf{f}i}| = \mathbf{n}_i S_{f_i}$, then:

$$\mathbf{J}_i \cdot \mathbf{S}_{\mathbf{f}i} = (\nabla\phi)_{f_{ci}} \cdot \mathbf{S}_{\mathbf{f}i} = (\nabla\phi \cdot \mathbf{n}_i)_{f_{ci}} S_{f_i} = (\nabla_{\mathbf{n}_i} \phi)_{f_{ci}} S_{f_i}{}^{4}. \tag{B.42}$$

[3] In *skewed* grids, $\mathbf{d}_i$ may not intersect the face at its mid-points.

[4] The operator $\nabla_{\mathbf{n}}$ is referred to as the *surface normal gradient*.

Figure 79 – Depending on the orthogonality of the grid, the connecting vector $\mathbf{d}_i$ deviates from $\mathbf{S}_{\mathbf{f}i}$. Both directions are equal on the left, and the vectors are colinear. In such a case, the direction of $\mathbf{d}_i$ fully represents the flux direction. The same cannot be said about the setting on the right, where the flux will contain a non-orthogonal component.

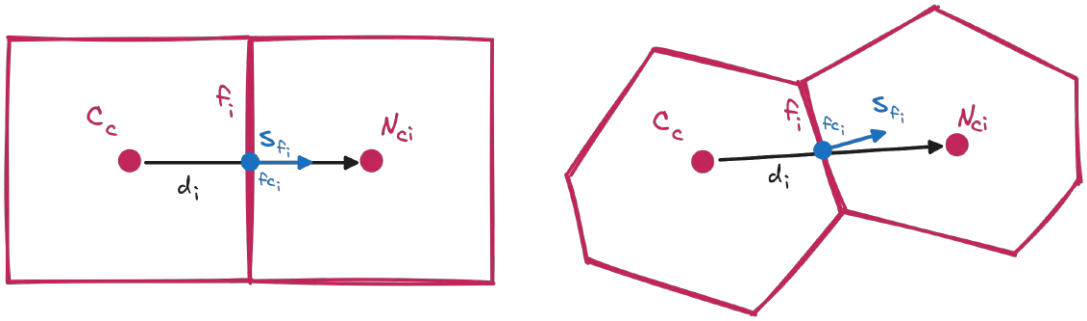

Source: Elaborated by the author.

In the track of the effects skewed grids produce on interpolation methods for face values, the non-orthogonality of grids will also directly impact flux computations. Figure 79 presents two cases that show the alignment of the vector $\mathbf{d}_i$ with $\mathbf{S}_{\mathbf{f}i}$. In the simpler case, where $\mathbf{d}_i$ aligns with $\mathbf{n}_i$, yielding

$$(\nabla_{\mathbf{n}_i}\phi)_{f_{ci}} = \left(\frac{\partial\phi}{\partial\mathbf{n}_i}\right)_{f_{ci}} = \left(\frac{\partial\phi}{\partial\mathbf{d}_i}\right)_{f_{ci}} = \frac{\phi_{Ni}-\phi_C}{\parallel \mathbf{d}_i \parallel}, \tag{B.43}$$

The equation above works because since the flux *flows* parallel to $\mathbf{d}_i$, and the fact that $\mathbf{d}_i$ is perpendicular to f_i implies that $\mathbf{J}_i \cdot \mathbf{S}_{\mathbf{f}i}$ describes the whole flux quantity. Therefore, the gradient along $\mathbf{d}_i$ is valid and sufficient.

For non-orthogonal cases, when there is an angle $\theta > 0$ between $\mathbf{n}_i$ and $\mathbf{d}_i$, the accuracy of Equation B.42 can be maintained by decomposing the discretization into two parts:

$$(\nabla_{\mathbf{n}_i}\phi)_{f_{ci}} = \underbrace{(\phi_{Ni}-\phi_C)\ \not\angle_{corr_i}}_{\text{orthogonal part}} + \underbrace{(\nabla\phi)_{f_{ci}} \cdot (\mathbf{n}_i - \not\angle_{corr_i}\,\mathbf{d}_i)}_{\text{correction}}. \tag{B.44}$$

where the *correction* half is computed from **known** values of ϕ. There are various strategies to define $\not\angle_{corr_i}$. The following three examples (a) enforce $\mathbf{d}_i \perp (\mathbf{n}_i - \mathbf{d}_i)$, (b) pretend the $\mathbf{d}_i$ direction is orthogonal to the face f_i, and (c) make $(\mathbf{n}_i - \mathbf{d}_i) \perp \mathbf{S}_{\mathbf{f}i}$:

a) *minimum correction*

$$\not\angle_{corr_i} = \frac{\cos\theta}{\parallel \mathbf{d}_i \parallel}. \tag{B.45}$$

b) *orthogonal correction*

$$\not\angle_{corr_i} = \frac{1}{\parallel \mathbf{d}_i \parallel}. \tag{B.46}$$

c) *over-relaxed*

$$\not\angle_{corr_i} = \frac{1}{\parallel \mathbf{d}_i \parallel \cos\theta}. \tag{B.47}$$

The next step is assembling a numerical system of equations from the resulting discretizations described so far. However, before proceeding to this final step in subsection B.1.6, the following section discusses further the discretization of convection terms.

B.1.5 Advection Schemes

The convective terms listed in subsection B.1.2, Equation B.15, and Equation B.16 model the transport of physical quantities by a velocity field. A more generic form is

$$\nabla \cdot (\mathbf{u} * \Psi)^{5}, \tag{B.48}$$

where Ψ can be a tensor of any rank field with its appropriate product $*$. The transport phenomenon described above is referred to as *advection*[6], and its physical meaning provides an alternative computation of the discretized term.

Consider the following example of a mass flux carrying a scalar property given by $\phi(\mathbf{x})$:

$$\begin{aligned}\int_{\Omega} \nabla \cdot (\rho \mathbf{u} \phi) d\Omega = \oint_{\partial\Omega} ((\rho \mathbf{u} \phi) \cdot \mathbf{n}) d\partial\Omega &\approx \sum_{f_i \in S} (\rho \mathbf{u} \phi)_{f_{ci}} \cdot \mathbf{S}_{\mathbf{f}i} \\ &\approx \sum_{f_i \in S} (\rho \mathbf{u})_{f_{ci}} \cdot \mathbf{S}_{\mathbf{f}i} \phi_{f_{ci}} \\ &\approx \sum_{f_i \in S} \Phi_{f_{ci}} \phi_{f_{ci}},\end{aligned} \tag{B.49}$$

where $\Phi_{f_{ci}} = (\rho \mathbf{u})_{f_{ci}} \cdot \mathbf{S}_{\mathbf{f}i}$ is the mass flux at f_{ci}, which can be computed via interpolation. Applying the same interpolation strategy for the computation of ϕ_{fci}, although as accurate as Φ_{fci}, may lead to an unstable numerical method. The solution should come from the physical interpretation of the transport phenomenon that carries ϕ along with the flux.

The idea is that the quantity ϕ_{fci} at the face must come only from one side of the face, the side against the flow direction, called the *upwind*. Conversely, the side along the flow direction is called the *downwind*. In other words, the value of ϕ_{fci} comes from the *upwind cell* and is given by an *upwind scheme*.

In the simple setting of the upwind scheme, the value of $\phi_{f_{ci}}$ is given by

$$\phi_{f_{ci}} = \begin{cases} \phi_u, & \Phi_{f_{ci}} \geq 0, \\ \phi_d, & \Phi_{f_{ci}} < 0, \end{cases} \tag{B.50}$$

where ϕ_u is the upwind cell value of ϕ, and ϕ_d is the downwind cell value. Figure 80 depicts both the interpolation and the upwind schemes; note how the linear interpolation scheme is numerically more accurate, but physically the upwind scheme makes more sense.

[5] Sometimes the form includes density as well, $\nabla(\rho \mathbf{u} * \Psi)$, implying a mass flux.

[6] In literature, advection and convection are used almost interchangeably, with the common difference that in convection, the transport is also caused by diffusion.

Figure 80 – A one-dimensional example comparing the results produced by linear interpolation and a simple upwind scheme, ϕ^L and ϕ^U. The former uses both upwind and downwind cell values, ϕ_u and ϕ_d, but is not physically accurate. The latter uses just ϕ_u, since it is carried by the flow in the right direction.

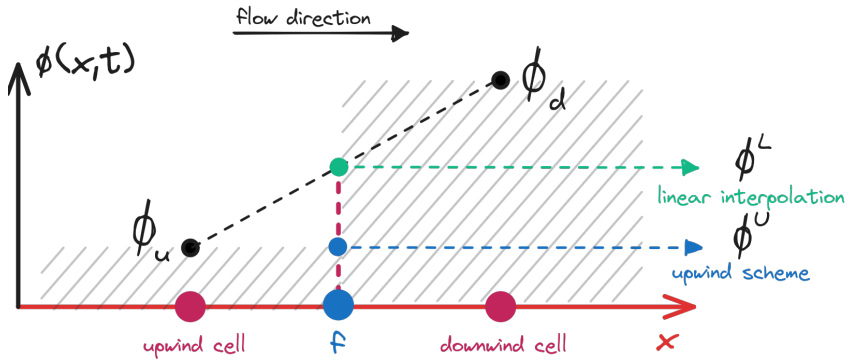

Source: Adapted from Greenshields and Weller (2022).

Despite its physical argument, however, the upwind scheme suffers from high diffusivity due to its low numerical accuracy. Therefore, diverse alternative upwind schemes try to diminish these issues, such as combining both methods:

$$\phi_{f_{ci}} = (1-\beta)\phi^U + \beta\phi^L, \tag{B.51}$$

where ϕ^L is the value provided by the interpolation method, and ϕ^U is given by the upwind scheme, Equation B.50. The interpolation factor β can be optimized for each face in the numerical grid and various schemes define formulations for β, such as the so-called Total Variation Diminishing (TVD) schemes. Refer to Greenshields and Weller (2022) for a introduction about TVD schemes and others.

The linear interpolation scheme does not guarantee bounded solutions for $\nabla \cdot \mathbf{u}\phi$, resulting in ϕ values outside the interval $[\min(\phi_u, \phi_d), \max(\phi_u, \phi_d)]$. Boundedness is particularly important when dealing with bounded properties, such as the concentration of volume $\alpha \in [0,1]$. The TVD schemes mentioned above try to diminish the unboundedness problem, but another class of schemes takes a different approach.

The Flux-Corrected Transport (FCT) methods, introduced by Boris and Book (1973), use low and high-order[7] methods to compute flux values, Φ^L and Φ^H, respectively, to produce a bounded flux. The final flux is given by

$$\Phi = \Phi^L + \lambda(\Phi^H - \Phi^L), \tag{B.52}$$

where $\lambda \in [0,1]$ is the weighting factor. The trick relies on the computation of λ, which takes into account all fluxes in a particular cell, instead of a single face. The desired result is that no new minima or maxima values of ϕ appear from one time step to the next.

[7] The reasoning comes the fact that low-order methods are bounded, but less accurate, while high-order methods are accurate but unbounded.

With all discretizations in place, it is now possible to construct a numerical system of equations that will provide the solution for the equations. The following section combines all the steps described so far and completes this introduction to FMVs.

B.1.6 Numerical Linear System

The last piece in the puzzle relies on finalizing the computation of the face fluxes. Consider a more general flux function $F(f) = F_f = \mathbf{J}_f \cdot \mathbf{S_f}$ for an arbitrary quantity $q(\mathbf{x},t)$. Different ways exist to compute F_f; however, the computation schemes generally rely on the values from the two neighboring cells. Like the one-dimensional flux functions $F_{i\pm1}$ on page 206, the idea is that the flux of any face will depend only on the values "Q_i" of the two connected cells. In particular, the flux $F(f)$ between two cells C and N connected by the face f is defined as

$$F(f) = \mathbf{J}_f \cdot \mathbf{S_f} = \alpha_C Q_C + \alpha_N Q_N + \beta, \tag{B.53}$$

where α_C and α_N are the linear coefficients for the averaged[8] values of q, named Q_C and Q_N, for cells C and N, respectively. The last term, β, is the non-linear term of the combination. The decomposition of $F(f)$ described above is called *flux linearization* and is the building block for the final system of discretized equations:

$$\mathbf{Ax} = \mathbf{b}, \tag{B.54}$$

where $\mathbf{A}$ is a matrix of coefficients provided by the discretization, $\mathbf{x}$ is the vector of unknown values for a particular variable, and $\mathbf{b}$ is a vector of the correspondent source and non-orthogonal values. This numerical system will provide an approximate solution for the original equations. Take as an example the diffusion equation for a scalar field ϕ with its source q:

$$-\nabla \cdot (\nabla \phi) = q. \tag{B.55}$$

From Equation B.18 and Equation B.26, the discretized form for the cell C with center C_c and volume C_V is

$$-\sum_{f_i \in S} (\nabla_{\mathbf{n}_i} \phi)_{f_{ci}} S_{f_i} = (q)_{C_c} C_V. \tag{B.56}$$

Using the flux solution for $(\nabla_{\mathbf{n}_i} \phi)_{f_{ci}} S_{f_i}$ given by Equation B.44 for non-orthogonal grids, the left hand side of the equation above expands as

$$\begin{aligned}
-\sum_{f_i \in S} (\nabla_{\mathbf{n}_i} \phi)_{f_{ci}} S_{f_i} &= -\sum_{f_i \in S} (\phi_{Ni} - \phi_C)\, \not\perp_{corr_i} S_{f_i} - \sum_{f_i \in S} (\nabla \phi)_{f_{ci}} \cdot (\mathbf{n}_i - \not\perp_{corr_i} \mathbf{d}_i) S_{f_i} \\
&= \sum_{f_i \in S} \phi_C \not\perp_{corr_i} S_{f_i} - \sum_{f_i \in S} \phi_{Ni} \not\perp_{corr_i} S_{f_i} - \sum_{f_i \in S} \underbrace{(\nabla \phi)_{f_{ci}} \cdot (\mathbf{n}_i - \not\perp_{corr_i} \mathbf{d}_i) S_{f_i}}_{\text{here we use known values of } \phi} \\
&= \Big(\sum_{f_i \in S} \alpha_{C_i} \Big) \phi_C + \sum_{f_i \in S} \alpha_{N_i} \phi_{N_i} + \sum_{f_i \in S} \beta_i,
\end{aligned} \tag{B.57}$$

[8] Similar to the one-dimensional example for density along a segment given by Equation B.5 on page 206, but for volumes.

where $(\nabla\phi)_{fci}$ is computed using Equation B.68 and

$$\begin{aligned}\alpha_{N_i} &= -\not\perp_{corr_i} S_{f_i},\\ \alpha_{C_i} &= -\alpha_{N_i},\\ \beta_i &= (\nabla\phi)_{f_{ci}} \cdot (\mathbf{n}_i - \not\perp_{corr_i} \mathbf{d}_i) S_{f_i}.\end{aligned} \tag{B.58}$$

Equation B.56 now becomes

$$\Big(\sum_{f_i \in S} \alpha_{C_i}\Big)\phi_C + \sum_{f_i \in S} \alpha_{N_i}\phi_{N_i} + \sum_{f_i \in S} \beta_i = (q)_{C_c} C_V, \tag{B.59}$$

which can be rewritten in the convenient form

$$a_C \phi_C + \sum_{f_i \in S} a_{N_i}\phi_{N_i} = b_C, \tag{B.60}$$

where

$$a_C = \sum_{f_i \in S} \alpha_{C_i}, \quad a_{N_i} = \alpha_{N_i}, \quad b_C = (q)_{C_c} C_V - \sum_{f_i \in S} \beta_i. \tag{B.61}$$

Note that the simplified form given by Equation B.60 resembles the system $\mathbf{Ax} = \mathbf{b}$ mentioned earlier. In particular, the system of numerical equations for the diffusion equation above is given by

$$\mathbf{A}[\phi] = \mathbf{b}, \tag{B.62}$$

where $\mathbf{A}$ is composed of diagonal values a_{C_j} and off-diagonal values $a_{N_{ji}}$, $[\phi]$ is the vector of all cell values ϕ_{C_j}, and $\mathbf{b}$ is the vector of all source terms b_{C_j}, with $j \in [1, \text{number of cells}]$.

B.1.7 Boundary Conditions

Figure 81 – Boundary faces of the numerical domain connect to a single cell. Therefore, boundary conditions specify field values at the face center f_{ci}. Note that the non-orthogonality may also appear in boundary faces since the connecting vector $\mathbf{d}_{fi}$ may not align to the face normal $\mathbf{n}_i$.

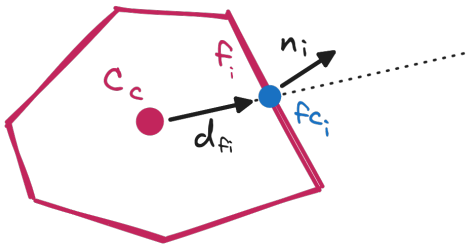

Source: Elaborated by the author.

The flux in faces that belong to the boundaries of the numerical domain requires special treatment. Mesh boundary faces have only one cell connected, requiring a direct substitution of values in Equation B.53. The value at the boundary must be specified at the face integration point f_c and use the direction vector $\mathbf{d}_{fi} = f_{ci} - C_c$, connecting the cell center to the face center, unlike the previous vector $\mathbf{d}_i$ that connected two cell centers – see Figure 81. Such specifications are called *boundary conditions*, and the two most common are:

- **Dirichlet Boundary Condition**:

  The Dirichlet boundary condition directly specifies the value of the field at the the face center f_c. In the case the diffusion equation discussed in the previous section, the fluxes in left hand side of Equation B.56 would have a specified value for $\phi(f_{ci}) = \phi_{fci}$:

$$\begin{aligned} -(\nabla_{\mathbf{n}_i}\phi)_{f_{ci}} S_{f_i} &= -(\phi_{fci} - \phi_C) \not\perp_{corr_{fi}} S_{f_i} - (\nabla\phi)_{f_{ci}} \cdot (\mathbf{n}_i - \not\perp_{corr_{fi}} \mathbf{d}_{fi}) S_{f_i} \\ &= \phi_C \not\perp_{corr_{fi}} S_{f_i} - \phi_{Ni} \not\perp_{corr_{fi}} S_{f_i} - (\nabla\phi)_{f_{ci}} \cdot (\mathbf{n}_i - \not\perp_{corr_{fi}} \mathbf{d}_{fi}) S_{f_i} \\ &= \alpha_{C_i}\phi_C + \beta_i \end{aligned} \tag{B.63}$$

  Note that since ϕ_{fci} is given, the term respective to α_N is merged to β.

- **Neumann Boundary Condition**:

  The Neumann boundary condition directly specifies the value $F_f = \mathbf{J}_f \cdot \mathbf{n}_f$ of the flux along the normal $\mathbf{n}_f$ of f:

$$\begin{aligned} \mathbf{J}_f \cdot \mathbf{S_f} &= \mathbf{J}_f \cdot \mathbf{n}_f S_f \\ &= F_f S_f \\ &= \beta \end{aligned} \tag{B.64}$$

  The Neumann Boundary condition is the same for non-orthogonal grids, the flux value becomes a source term β in the final system of equations.

B.2 Finite Area Method

The Finite Area Method (FAM), introduced by Tuković (2005), is a specialization of the FVM, described in the previous chapter, for solving PDEs on curved surfaces. Mainly, the FAM splits the surface domain into discrete cells, called finite areas, defined by flat polygonal areas bounded by straight edges — left side in Figure 82. Therefore, the area integral of a given cell C representing a surface area Γ can be approximated by the midpoint rule as

$$\int_\Gamma \phi d\Gamma \approx \phi_C C_A, \tag{B.65}$$

where C_A is the area of C and ϕ_C is the cell value of ϕ in C. The cell value comes from the midpoint approximation of the area integral, $(\phi)_{C_c}$, where C_c is the center point of C. In the following, the subscript $(\bigstar)_p$ indicates the value of a field at the location p, $(\bigstar)_A$ denotes the area of a cell, and $(\bigstar)_c$ denotes the center point.

Like FVMs, the discretization in the FAM also uses the divergence theorem[9] and analogously defines the fluxes in the edges. Each cell C may share its edge e_i with the neighbor cell N_i,

[9] See subsection B.1.1.

with index $i \in [0, \text{number of edges of } C]$. The flux through the edge e_i is computed in the center point of the edge, e_{ci}, and uses the edge length vector[10]

$$\mathbf{L_e}_i = \mathbf{m}_{ei}|\mathbf{L_e}_i| = \mathbf{m}_{ei}L_{ei}, \tag{B.66}$$

where $\mathbf{m}_{ei}$ is one of the bi-normal vectors associated with the edge e_i, along with $\mathbf{n}_{ei}$, and has the same direction of $e_{ci} - C_c$ — see right side of Figure 82.

Figure 82 – The FAM applies the strategy of FVMs on curved surface domains by discretizing the integrals over finite areas. These cells are polygonal areas bounded by edges. The flux between two neighbor cells, $\mathbf{C}$ and $\mathbf{N}_i$, passes through their shared edge, e_i. Each cell has a surface normal vector $\mathbf{n}_C$, and each edge has two bi-normal vectors, $\mathbf{n}_i$ and $\mathbf{m}_i$, which define the edge length vector $\mathbf{L_e}_i$.

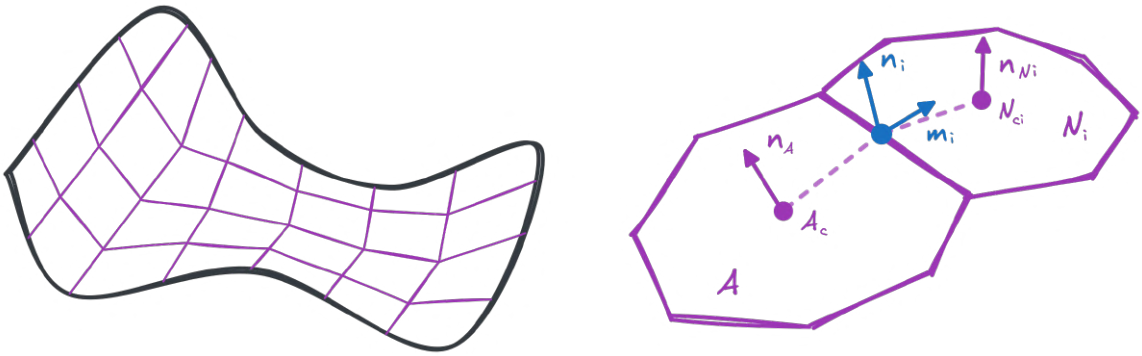

Source: Elaborated by the author.

The discretization under the FAM scheme is analogous to the FVM, and uses Equation B.66 to compute the fluxes. Here are some examples:

- **Divergent term $\nabla \cdot \mathbf{u}$**:

$$\int_\Gamma \nabla \cdot \mathbf{u} d\Gamma = \oint_{\partial\Gamma} (\mathbf{u} \cdot \mathbf{m}) d\partial\Gamma \approx \sum_{e_i \in E} (\mathbf{u})_{e_{ci}} \cdot \mathbf{L_e}_i, \tag{B.67}$$

  where $\mathbf{m}$ is the normal field pointing outward Γ, E is the set of edges that approximate $\partial\Gamma$, and $\mathbf{u}(\mathbf{x})$ is a vector field.

- **Scalar gradient term $\nabla\phi$**:

$$\int_\Gamma \nabla\phi d\Gamma = \oint_{\partial\Gamma} (\phi\mathbf{m}) d\partial\Gamma \approx \sum_{e_i \in E} (\phi)_{e_{ci}} \mathbf{L_e}_i, \tag{B.68}$$

  where $\phi(\mathbf{x})$ is a scalar field.

Note that the discretizations above require the value of fields at edge centers. For scalar fields, the value can be computed via linear interpolation or upwind schemes, as described in

[10] The length vector $\mathbf{L_e}$ is analogous to the face area vector $\mathbf{S_f}$ used in FVMs.

subsection B.1.4. However, the direct interpolation of vector quantities does not guarantee a resulting vector tangential to the domain surface.

In order to produce edge vectors that are tangential to the domain surface, the cell vector quantities are interpolated in their local cell coordinates. A different local coordinate system for each cell is defined based on the target edge. Figure 83 shows the local coordinate systems used in the interpolation between two cells, C and N_i. The local coordinates of the cell C is composed by the surface normal vector $\mathbf{n}_C$, and two tangential vectors, $\mathbf{t}_C = \frac{e_{ci}-C_c}{\|e_{ci}-C_c\|}$ and $\mathbf{v}_C = \mathbf{t}_C \times \mathbf{n}_C$.

Figure 83 – Interpolations of cell vector quantities to the center of edges use local coordinates defined in each point to guarantee surface-tangential resulting vectors.

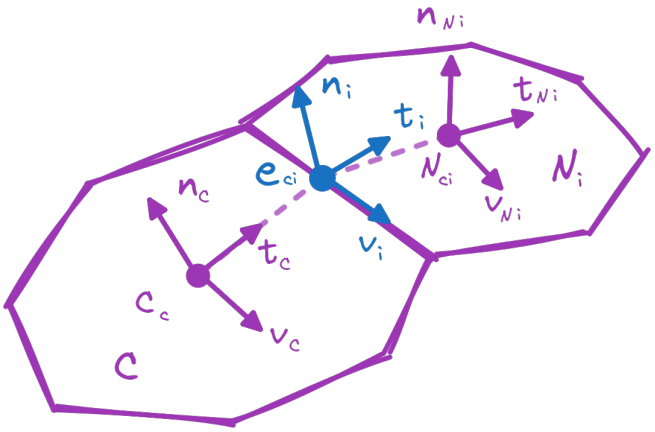

Source: Elaborated by the author.

Let $\mathbf{T}_\bigstar$ be the transformation into the local coordinates system of C, N_i, or e_i. Then the interpolation of the vector field $\mathbf{u}$ into the edge center e_{ci} is given by

$$(\mathbf{u})_{e_{ci}} = \mathbf{T}_{e_i}^{-1}(w_i \mathbf{T}_C \mathbf{u}_C + (1-w_i)\mathbf{T}_{N_i}\mathbf{u}_{N_i}), \tag{B.69}$$

where w_i is the interpolation factor.

APPENDIX

C

OPENFOAM

OpenFOAM[1] is an open-source software that serves as a C++ toolbox for developing numerical solutions for various CFD problems. The OpenFOAM Foundation maintains and distributes the source code under the GNU General Public License Version 3. Due to its open access, flexibility, and robustness, OpenFOAM established a large community of users and developers in academia, research institutions, and industry. Its success is because OpenFOAM provides convenient usage of its wide variety of solvers for users, and its architecture benefits developers who need to modify existing solvers or create new ones.

Primarily, OpenFOAM uses the Finite Volume Method to discretize and solve a given set of PDEs — see section B.1. Once a finite volume mesh representing the solution domain contains the fields of the variables for a given set of equations, OpenFOAM's discretization functions offer a direct way to express the equations in code. Take, for example, the equation:

$$\frac{\partial T}{\partial t} + \nabla \cdot (T\mathbf{u}) = 0, \tag{C.1}$$

for a scalar field T transported by a velocity field $\mathbf{u}$. In OpenFOAM the equation is transcribed to Source code 4. See section C.2 for a list of discretization functions.

Source code 4 – OpenFOAM's version of Equation C.1 for C++.

```
1: solve (
2:     fvm::ddt(T) + fvm::div(u, T)
3: );
```

This chapter introduces the concepts and pieces of OpenFOAM relevant to the project. Refer to Jasak, Jemcov and Tuković (2007) for a general introduction on the code design, Holzmann (2016) for mathematical derivations on OpenFoam, and Darwish and Moukalled (2016) for a comprehensive material on Finite Volume method applications in OpenFOAM.

[1] The name OpenFOAM stands for *Open-source Field Operation And Manipulation.*

C.1 Field Representations

OpenFOAM can represent dimensional and dimensionless scalar, vector, and tensor variable fields. Many field operations have convenient C++ operators, such as the dot-product for two vector fields listed in Source code 5.

Source code 5 – OpenFOAM provides operators for common operations. For example, the & operator performs the scalar product between two vector fields *a* and *b*.

```
1:      scalarField c = a & b;
```

OpenFOAM defines *Geometric Fields* as the spatial distribution of the physical quantities over the physical domain for which the solution is calculated. A geometrical mesh decomposes the domain into disjoint cells called volumes. Field values are then stored in specific locations inside each volume to possibilitate the numerical discretizations of the equations. Such locations describe the quantities of a particular field over the physical domain. The discretization defines the proper location of each field in the mesh, and fields can be assigned to vertex positions, face centers, or cell centers as shown in Figure 84.

Figure 84 – Common mesh locations for field spatial locations in the physical domain, from left to right, vertices, face centers, and cell centers.

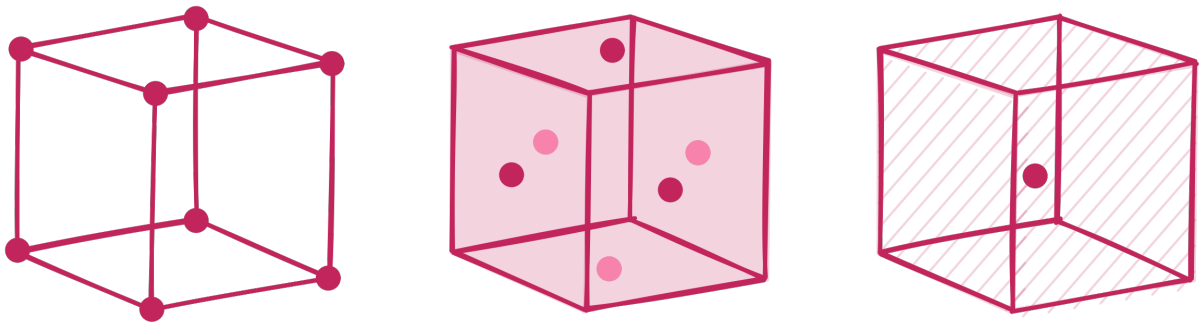

Source: Elaborated by the author.

In particular, OpenFOAM utilizes a data structure for the numerical mesh called *polyMesh*. The polyMesh structure can handle polyhedral cells bounded by arbitrary polygonal faces. This configuration allows unstructured meshes with different types of elements containing a variable amount of faces, however, with specific requirements:

- Cells must be convex;
- Every edge in the cell must be used by exactly two faces of the same cell;
- Cells must not overlap one another.

The central element in the polyMesh is the face, which provides the mesh's topology. Each face connects at most two cells and obligatorily belongs to one of the connecting cells,

called the *owner*. Thus, each face is associated with an owner and may or may not connect to a second cell called the *neighbor* — boundary faces do not have their neighbor cell. The orientation of a face determines which cell is its owner cell, producing consistent indexing throughout the mesh. In particular, the face's normal always points outwards the owner cell — see Figure 85.

Figure 85 – The polyMesh structure associates a owner cell and a neighbor cell for each face based on the face's orientation. The normal of a face always points outwards the owner cell, see the left figure. Consequently, the normals at the boundaries also point outwards the numerical domain, on the right.

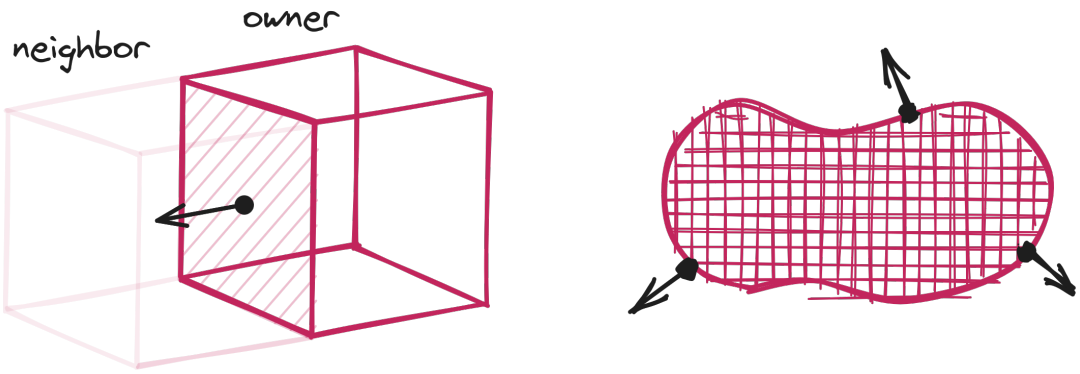

Source: Elaborated by the author.

OpenFOAM makes a distinction between *internal faces* and *boundary faces*. Boundary faces are faces that are connected to only a single cell, the owner cell. However, boundary faces additionally carry extra information that the solver uses to define the boundary conditions for the numerical system. Defining fields stored only by boundary or internal faces is also possible.

C.2 Discretizations

This section lists some of the discretization functions provided by OpenFOAM for the terms encountered in equations. As described in subsection B.1.6 on page 218, the discretizations compose the final system of numerical equations:

$$\mathbf{A}\mathbf{x} = \mathbf{b}, \tag{C.2}$$

where $\mathbf{x}$ is the set of unknowns, $\mathbf{A}$ is the matrix of discretized coefficients, referred to as *implicit terms*, and $\mathbf{b}$ contains the source terms, also referred to as *explicit terms*. Therefore, known values marked by the superscript $(\bigstar)^o$, including values from previous time steps i, $(\bigstar)^{n-i}$, are handled as explicit terms.

OpenFOAM provides two modules with discretization functions for implicit and explicit terms, called `fvm` and `fvc`, respectively. Values are naturally computed and stored in cell centers, marked in the equations by the subscripts $(\bigstar)_{C_c}$ and $(\bigstar)_{N_{ci}}$. Values computed at face centers are marked with the subscript $(\bigstar)_{f_{ci}}$. In the following, the discretizations consider a cell C with volume C_V and center C_c.

- `fmv::ddt(★)`
  - First-Order Implicit Euler

$$\left(\frac{\partial \bigstar}{\partial t}\right)_{C_c} \approx \frac{C_V}{\Delta t}((\bigstar)^n - (\bigstar)^{n-1})_{C_c}. \tag{C.3}$$

  - Second-Order Implicit Euler

$$\left(\frac{\partial \bigstar}{\partial t}\right)_{C_c} \approx \frac{C_V}{2\Delta t}\left(3(\bigstar)^n - 4(\bigstar)^{n-1} + (\bigstar)^{n-2}\right)_{C_c}. \tag{C.4}$$

- `fmv::div(`$\Phi^o, \bigstar$`)`

$$\nabla \cdot (\Phi^o \otimes \bigstar)_{C_c} \approx \sum_{f_i \in S} (\Phi^o \otimes \bigstar)_{f_{ci}}, \quad \text{where} \quad \Phi_{f_{ci}} = (\rho \mathbf{u})^o_{f_{ci}}. \tag{C.5}$$

  - Interpolation

$$\sum_{f_i \in S} (w_i \Phi^o)_{f_{ci}} \otimes (\bigstar)_{C_c} + \sum_{f_i \in S} ((1-w_i)\Phi^o)_{f_{ci}} \otimes (\bigstar)_{N_{ci}}, \tag{C.6}$$

    where w_i is the interpolation weight based on the cell center to face centers distances, $\mathbf{d}_C = f_{ci} - C_c$ and $\mathbf{d}_{Ni} = N_{ci} - f_{ci}$:

$$w_i = \frac{\mathbf{n} \cdot \mathbf{d}_{Ni}}{\mathbf{n} \cdot (\mathbf{d}_C + \mathbf{d}_{Ni})}. \tag{C.7}$$

  - Upwind

$$(\bigstar)_{f_{ci}} = \begin{cases} (\bigstar)_{C_c}, & \Phi^o_{f_{ci}} \geq 0, \\ (\bigstar)_{N_{ci}}, & \Phi^o_{f_{ci}} < 0. \end{cases} \tag{C.8}$$

- `fvm::laplacian(`$\bigstar$`)`[2]

$$\begin{aligned} (\triangle \bigstar)_{C_c} &\approx \sum_{f_i \in S} (\nabla_{\mathbf{n}_i} \otimes \bigstar)_{f_{ci}} S_{f_i} \\ &\approx a_C (\bigstar)_{C_c} + \sum_{f_i \in S} a_{N_i} (\bigstar)_{N_i} + b_C. \end{aligned} \tag{C.9}$$

- `fvc::flux(`$\bigstar$`)`

$$(\bigstar)_{f_c} \cdot \mathbf{S_f}. \tag{C.10}$$

- `fvc::interpolate(`$\bigstar$`)`

$$(\bigstar)_{f_c} = \lambda_C \bigstar_C + \lambda_N \bigstar_N. \tag{C.11}$$

- `fvc::grad(`$\bigstar$`)`

$$(\nabla \otimes \bigstar)_{C_c} \approx \frac{1}{C_V} \sum_{f_i \in S} (\bigstar)_{f_{ci}} \otimes \mathbf{S}_{\mathbf{f}i}. \tag{C.12}$$

[2] See subsection B.1.6.

- `fvc::div(★)`

$$(\nabla \cdot \bigstar)_{C_c} \approx \frac{1}{C_V} \sum_{f_i \in S} (\bigstar)_{fci} \cdot \mathbf{S}_{\mathbf{f}i}. \tag{C.13}$$

- `MULES::explicitSolve`

  OpenFOAM provides a Flux Corrected Transport (FCT)[3] method implementation called Multidimensional Universal Limiter for Explicit Solution (MULES) (DAMIáN; NIGRO, 2014). The FTC method guarantees boundedness in the solution of the convection equation by computing the flux Φ as Equation B.52

$$\Phi = \Phi^L + \lambda(\Phi^H - \Phi^L),$$

  where Φ^L and Φ^H are fluxes computed from low-order and high-order methods, respectively, and λ is computed iteratively. MULES solves explicitly the transport equation

$$\frac{\partial \phi}{\partial t} + \nabla \cdot \Phi = 0 \tag{C.14}$$

  for a scalar field ϕ through the discretization

$$\phi^{n+1} = \phi^n - \frac{\Delta t}{C_V} \sum_{f_i} (\Phi)^n_{fci}. \tag{C.15}$$

  The procedure for computing the values of λ uses local and global extrema for ϕ^n, as detailed by section 2.6.3 in Damian (2013).

An equivalent set of functions for the FAM is provided by OpenFOAM with the correspondent function namespaces `fam` and `fac`.

C.3 Numerical Algorithm

Physical models such as the Navier-Stokes Equations for imcompressible flows

$$\nabla \cdot \mathbf{u} = 0, \tag{C.16}$$

$$\frac{\partial \mathbf{u}}{\partial t} + \nabla \cdot (\mathbf{u} \otimes \mathbf{u}) = -\frac{1}{\rho} \nabla p - \nabla \cdot \tau + \mathbf{g}, \tag{C.17}$$

$$\tau = 2\mu \mathbf{D} - \frac{2}{3}\mu(\nabla \cdot \mathbf{u}) \quad \text{and} \quad \mathbf{D} = \frac{1}{2}(\nabla \otimes \mathbf{u} + (\nabla \otimes \mathbf{u})^T) \tag{C.18}$$

belong to the family of *coupling problems*. That is because Equation C.17 equation couples velocity and pressure, which poses an initial challenge to the solution of the problem[4]. The solution is only possible because Equation C.16 adds extra conditions for the velocity. Moreover, the non-linear nature of the equation requires iterative methods for this solution. The example of algorithm below splits the equations, so each iteration i performs the following steps:

[3] See subsection B.1.5.

[4] There are three momentum equations, one for each velocity component, but four unknown variables, the three velocity components, and the pressure.

1. Use the previously computed (or estimated) values $\mathbf{u}^{i-1}$ and p^{i-1}, and solve for $\mathbf{u}^\star$:

$$\begin{aligned} \frac{\partial \mathbf{u}^\star}{\partial t} + \nabla \cdot (\mathbf{u}^{i-1} \otimes \mathbf{u}^\star) &= -\frac{1}{\rho}\nabla p^{i-1} - \nabla \cdot \tau^\star + \mathbf{g}, \\ \tau^\star &= \nu \nabla \otimes \mathbf{u}^\star + \nu(\nabla \otimes \mathbf{u}^\star)^T - \frac{2}{3}\nu(\nabla \cdot \mathbf{u}^\star)\mathbf{I}, \\ \mathbf{A}\mathbf{u}^\star &= \mathbf{b} \end{aligned} \tag{C.19}$$

   where $\nu = \mu/\rho$. Note that the non-linearity of the advection term is solved by the use of $\mathbf{u}^{i-1}$, allowing the use of advection schemes (see subsection B.1.5). This step is generally referred to as *momentum prediction*.

2. Use the intermediary velocity field $\mathbf{u}^\star$ solve the pressure equation[5] for p^i:

$$\begin{aligned} \frac{1}{\rho}\nabla^2 p^i + \nabla \cdot (\nabla(\mathbf{u}^\star \otimes \mathbf{u}^\star)) &= 0, \\ \mathbf{A}[p^i] &= \mathbf{b}. \end{aligned} \tag{C.20}$$

3. Use $\mathbf{u}^\star$ and p^i to *correct* the values of $\mathbf{u}$ for the next step. As explained later, this process includes a *flux correction* and a *momentum correction*. The result is $\mathbf{u}^i$, which becomes the $\mathbf{u}^{i-1}$ in the next iteration, and the same happens to p^i.

The *prediction-correction* algorithm above follows the idea of the well known Semi-Implicit Method for Pressure-Linked Equations (SIMPLE) (PATANKAR; SPALDING, 1983) algorithm. However, the SIMPLE algorithm is primarily designed to only solve steady-state problems, which is not the case of the equations listed above. Transient solutions can be achieved through the variations of the SIMPLE algorithm called Pressure Implicit with Splitting of Operators (PISO) (ISSA, 1986), and the widely used combination of both, the PIMPLE algorithm. OpenFOAM provides the implementation for all the three algorithms.

[5] The equation above comes from applying the divergence operator on the momentum equation, Equation C.17, and using the continuity equation, Equation C.16, (assuming ν constant):

$$\cancel{\frac{\partial \nabla \cdot \mathbf{u}}{\partial t}}^{0} + \nabla \cdot (\nabla \cdot (\mathbf{u} \otimes \mathbf{u})) = -\frac{1}{\rho}\nabla \cdot (\nabla p) - \nabla \cdot (\underbrace{\nabla \cdot \tau}_{\text{expand}}) + \cancel{\nabla \cdot \mathbf{g}}^{0}$$

$$\nabla \cdot (\nabla \cdot (\mathbf{u} \otimes \mathbf{u})) = -\frac{1}{\rho}\nabla \cdot (\nabla p) - \nabla \cdot (\nabla \cdot (\nu \nabla \otimes \mathbf{u}) + \underbrace{\nabla \cdot (\nu(\nabla \otimes \mathbf{u})^T)}_{\equiv} - \cancel{\frac{2}{3}\nabla \cdot (\mu(\nabla \cdot \mathbf{u})\mathbf{I})}^{0})$$

$$\nabla \cdot (\nabla \cdot (\mathbf{u} \otimes \mathbf{u})) = -\frac{1}{\rho}\nabla \cdot (\nabla p) - \underbrace{\nabla \cdot (\nabla \cdot (\nu \nabla \otimes \mathbf{u}))}_{\equiv} - \nabla \cdot (\cancel{\nu \nabla (\nabla \cdot \mathbf{u})}^{0} + \cancel{(\nabla \nu)}^{0} \cdot (\nabla \otimes \mathbf{u}))$$

$$\frac{1}{\rho}\nabla^2 p + \nabla \cdot (\nabla \cdot (\mathbf{u} \otimes \mathbf{u})) = \cancel{\nabla^2 (\nabla \cdot \mathbf{u})}^{0}$$

The PISO algorithm repeats the steps 2 and 3 in order to improve the accuracy of the output values of velocity and pressure within each time step, which increases the accuracy of the transient term in step 1. In turn, The PIMPLE algorithm essentially adds another loop, including step 1 and the PISO loop, within each time step. The main advantage of the PIMPLE algorithm is that it can handle larger Courant numbers[6] $Co >> 1$, leading to larger simulation time steps.

In order to describe the PIMPLE algorithm, let us put the pressure term $-\nabla p$ aside from the momentum equation system $\mathbf{Au} = \mathbf{b}$ and separate the diagonal from the matrix $\mathbf{A}$, so $\mathbf{A} = \mathbf{A}_{diag} + \mathbf{A}_{off}$, where $\mathbf{A}_{diag}$ is the matrix containing the only the diagonal entries of $\mathbf{A}$ and $\mathbf{A}_{off}$ contains the off-diagonal entries. Let $\mathbf{B}(\mathbf{u})$ be a function of $\mathbf{u}$ representing all off-diagonal elements and source terms,

$$\mathbf{B}(\mathbf{u}) = -\mathbf{A}_{off}\mathbf{u} + \mathbf{b}, \tag{C.21}$$

so the original system, with the pressure term, is reconstructed as

$$\mathbf{A}_{diag}\mathbf{u} = \mathbf{B}(\mathbf{u}) - \nabla p. \tag{C.22}$$

Since $\mathbf{A}_{diag}$ is a diagonal matrix, it will be used as a scalar field A_{diag} in the following equations. The **momentum correction** is expressed as

$$\mathbf{u} \leftarrow \frac{\mathbf{B}(\mathbf{u}^o)}{A_{diag}} - \frac{\nabla p^o}{A_{diag}}, \tag{C.23}$$

where $\mathbf{u}^o$ and p^o represent previous (or intermediary) values, which are essentially explicit terms in the system above. The same procedure can be applied to the **flux correction** of Φ_f:

$$\Phi_f \leftarrow \mathbf{S_f} \cdot \left(\frac{\mathbf{B}(\mathbf{u})}{A_{diag}}\right)_f - \left(\frac{|\mathbf{S_f}|}{A_{diag}}\right)_f \nabla_{\mathbf{n}} p_f. \tag{C.24}$$

The **pressure equation**, Equation C.20, becomes

$$\nabla \cdot \frac{1}{A_{diag}} \nabla p = \nabla \cdot \left(\frac{\mathbf{B}(\mathbf{u})}{A_{diag}}\right), \tag{C.25}$$

and will use the previous equations. As characterized in the first step of the algorithm described earlier, the **momentum prediction**[7] computes an intermediary velocity field $\mathbf{u}^*$ from previous/initial states of $\mathbf{u}^o$ and p^o.

As mentioned, the PIMPLE algorithm loops over the *prediction-correction* scheme within each time step, where the correction half contains the PISO loop. The outer loop, called the PIMPLE loop, increases the system's overall accuracy and allows for $Co > 1$. For non-orthogonal meshes, an extra loop adds the non-orthogonal contribution $V_{corr}(\nabla p) = (\nabla p)_{f_c} \cdot \mathbf{V_f}$

[6] The Courant number $Co = \frac{u\Delta t}{\Delta x}$ measures how fast information travels through the numerical grid. A $Co > 1$ means that a fluid particle will move a distance greater than one cell length. The Co has direct relation to the convergence of the numerical algorithm.

[7] This text omits some details about the momentum prediction step. In reality, the system is partially solved first, through *under-relaxation*, using the momentum equation without the pressure term. Then, it is solved again with the pressure term included.

to the discretization of the pressure equation — see subsection B.1.4 on page 213. Essentially, the computed pressure p is fed back as p^o to the same equation as an explicit term for the non-orthogonal term:

$$\nabla \cdot \frac{1}{A_{diag}} \nabla p = \nabla \cdot \left(\frac{\mathbf{B}(\mathbf{u})}{A_{diag}} \right) + V_{corr}(\nabla p^o). \tag{C.26}$$

Figure 86 illustrates the description above and Source code 6 shows an example of the controls OpenFOAM provides for the PIMPLE algorithm. In OpenFOAM, the number `nCorrectors` correspond to the number of PISO loops, `nOuterCorrectors` to PIMPLE loops, and for the non-orthogonal correction loops described above, `nNonOrthogonalCorrectors`.

Source code 6 – Example of configuration of the PIMPLE algorithm in OpenFOAM.

```
1:      PIMPLE
2:      {
3:          momentumPredictor    yes;
4:          nOuterCorrectors     1;
5:          nCorrectors          2;
6:          nNonOrthogonalCorrectors 2;
7:      }
```

This section only briefly describes the type of numerical algorithm provided by OpenFOAM. Therefore, many details not mentioned deserve attention, such as solvers of linear systems of equations, accuracy, under-relaxation, and convergence. Refer to Greenshields and Weller (2022) for a comprehensive introduction on all topics.

Figure 86 – The PIMPLE algorithm alternates between prediction and correction phases by nested loops. The loops are executed within each main iteration, guaranteeing the method's accuracy and convergence for larger time steps.

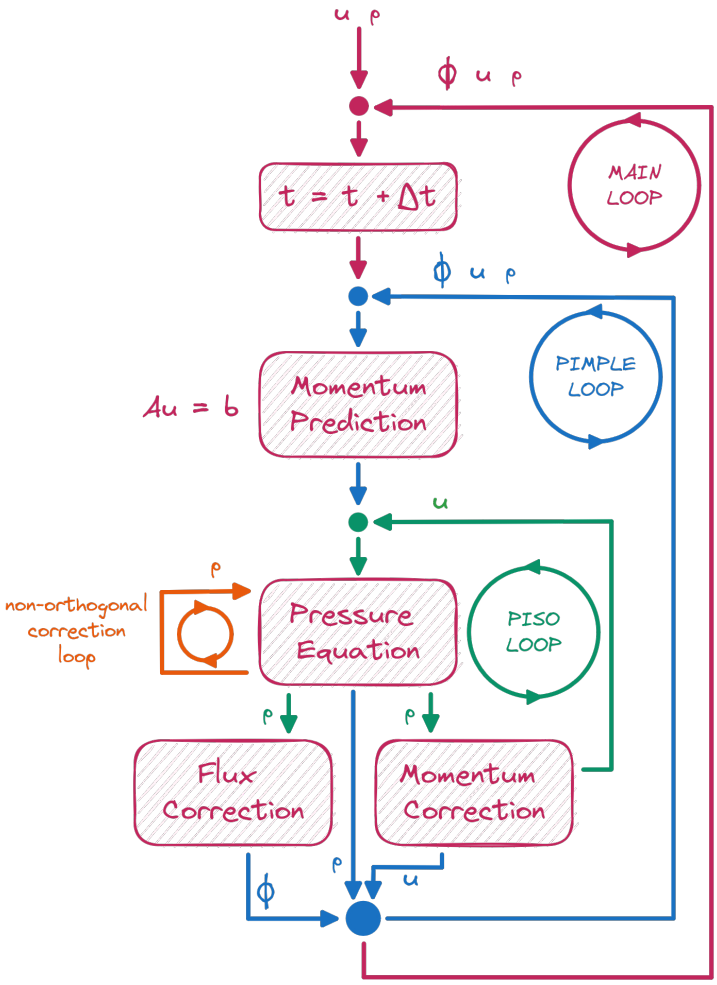

Source: Elaborated by the author.


ICMC
USP
SÃO CARLOS